

Aerotherm Final
Report No. 70-15

IMPROVED HEAT-SHIELD DESIGN
PROCEDURES FOR MANNED
ENTRY SYSTEMS

Part II
Application to Apollo

by
E. P. Bartlett, M. J. Abbett,
W. E. Nicolet, C. B. Moyer

[REDACTED]
[REDACTED]
(NASA-CR-108689) IMPROVED
HEAT-SHIELD DESIGN PROCEDURES FOR
MANNED ENTRY SYSTEMS. PART 2:
APPLICATION TO APOLLO Final Report
(Aerotherm Corp.) 217 p

N94-71373

Unclas

Z9/18 0204529

ORIGINAL PAGE IS
OF POOR QUALITY

CR108689

Aerotherm Final
Report No. 70-15
IMPROVED HEAT-SHIELD DESIGN
PROCEDURES FOR MANNED
ENTRY SYSTEMS
Part II
Application to Apollo
by
E. P. Bartlett, M. J. Abbett,
W. E. Nicolet, C. B. Moyer

Aerotherm Report No. 70-15, Part II
Copy No. _____

FINAL REPORT

IMPROVED HEAT-SHIELD DESIGN PROCEDURES
FOR MANNED ENTRY SYSTEMS

Part II
Application to Apollo

by

Eugene P. Bartlett, Michael J. Abbett
William E. Nicolet, Carl B. Moyer

Prepared for
National Aeronautics and Space Administration

June 22, 1970

Contract NAS9-9494

Technical Management
NASA Manned Spacecraft Center
Houston, Texas
Structures and Mechanics Division
Donald M. Curry
Emily W. Stephens

FOREWORD

This report was prepared by Aerotherm Corporation under NASA Manned Spacecraft Contract NAS9-9494. The contract period of performance was from 22 May 1969 through 22 May 1970. The report is published in two parts:

Part I: Executive Summary

Part II: Application to Apollo

A number of computer code user's manuals were also prepared and published as separate reports (see References 10 through 12).

The sponsor of the program was the Thermal Protection Section, Structures and Mechanics Division, Manned Spacecraft Center, National Aeronautics and Space Administration, Houston, Texas. Mr. Donald M. Curry and Miss Emily W. Stephens were the NASA/MSC technical monitors.

The Aerotherm program manager and principal investigator was Mr. Eugene P. Bartlett. While a number of people contributed directly and indirectly to the program, the major contributions were made by the following project engineers:

Inviscid Flow Field Studies	- M. J. Abbett
Heat Transfer Correlations	- E. P. Bartlett and M. J. Abbett
Incident Radiation Studies	- W. E. Nicolet
Coking Model	- C. B. Moyer and M. J. Abbett
Surface Ablation Model	- E. P. Bartlett
Apollo Flight Predictions	- M. J. Abbett and E. P. Bartlett

ABSTRACT

Procedures for the thermal design of a reentry vehicle heat shield are developed and applied to Apollo flight data. For the most part, predictions agree well with measured in-depth thermocouple response, in-depth material density profiles, surface recession and char penetration, and convective heating rates. The major advances in heat-shield prediction technology which are accomplished and used in the flight predictions are:

1. Nonsimilar boundary layer solutions are generated for Apollo at incidence based on the three-dimensional axisymmetric analogy which agree well with wind-tunnel convective heating data
2. Nonsimilar chemically-reacting boundary-layer solutions including transition to turbulent flow, with and without material ablation, are generated for Apollo at incidence
3. Simple and accurate correlations of stagnation-point heat- and mass-transfer coefficients including the effects of mass transfer and chemical reactions are developed and shown to apply to positions around the body for turbulent as well as laminar boundary layers
4. A simple and apparently accurate in-depth coking and surface thermochemical ablation model is developed for the Apollo heat-shield material
5. Apollo calorimeter and thermocouple data are used to develop a set of transitional heating criteria based on momentum thickness Reynolds number and normalized mass-transfer rate.

In addition, an independent calculation of radiation heating rates is made which compares favorably with flight radiometer measurements, and numerical experiments were initiated to attempt to extend a three-dimensional inviscid flow field program to Apollo at incidence.

TABLE OF CONTENTS

Section		Page
1	INTRODUCTION AND SUMMARY	1
2	INVISCID FLOW FIELD STUDIES	4
	2.1 Numerical Studies of Apollo Inviscid Flow Field	7
	2.2 Axisymmetric Analogy	9
	2.2.1 Analysis	9
	2.2.2 Results	13
	2.3 Summary of Inviscid Flow Field Studies	15
3	CONVECTIVE HEATING STUDIES	18
	3.1 Wind-Tunnel Correlations	19
	3.1.1 Results for Zero Incidence	19
	3.1.2 Results for Angle of Attack	22
	3.2 Convective Heating Flight Predictions	33
	3.2.1 Stagnation Point Boundary Layer	33
	3.2.2 Laminar Nonsimilar Boundary Layer	36
	3.2.3 Turbulent Nonsimilar Boundary Layer	41
	3.3 Mass-Transfer Correlations	47
	3.3.1 Stagnation Point	47
	3.3.2 Laminar Nonsimilar Boundary Layer	67
	3.3.3 Turbulent Nonsimilar Boundary Layer	75
	3.4 Summary of Convective Heating Studies	79
4	INCIDENT RADIATION STUDIES	82
	4.1 Review of NASA/MSC Procedures	82
	4.2 Verification of Reference Radiation Conditions	84
	4.2.1 Plane-Parallel Adiabatic Layer Fluxes	84
	4.2.2 Nonadiabatic Effects	84
	4.2.3 Spectral Effects	93
	4.3 Flight Predictions and Comparison with NASA/MSC Prediction and Flight Data	93
	4.4 Discussion and Conclusions	93
	4.4.1 Confidence Levels in the Predictions	93
	4.4.2 Conclusions	98
5	MATERIAL RESPONSE MECHANISM STUDIES	99
	5.1 Material Decomposition Model	100
	5.2 Char Layer Model Including Coking	102
	5.2.1 General	102
	5.2.2 Details of Analysis Modifications	109
	5.3 Material Thermal Properties Model	112
	5.4 Driver Temperature Calculations	115
	5.5 Surface Thermochemical Ablation Model	121
	5.6 Summary of Material Response Mechanism Studies	125
6	FLIGHT PREDICTIONS	127
	6.1 Approach Employed for Flight Predictions	127
	6.2 Flight Prediction Results	139
	6.2.1 In-Depth and Surface Temperatures	140
	6.2.2 Surface Ablation and Char Penetration	151
	6.2.3 Char Density	156
	6.2.4 Heat Transfer	162
	6.3 Summary of Flight Predictions	178

PRECEDING PAGE BLANK NOT FILMED

PRECEDING PAGE BLANK NOT FILMED

TABLE OF CONTENTS (concluded)

Section		Page
7	RECOMMENDED HEAT-SHIELD DESIGN PROCEDURE	179
8	RECOMMENDATIONS FOR FURTHER ANALYSIS AND PROGRAM IMPROVEMENTS	181
	REFERENCES	182
	APPENDIX A - SUMMARY OF COMPUTER CODES CONSTITUTING THE HEAT SHIELD DESIGN PROCEDURE	

LIST OF TABLES

Table		Page
1	Spreading Factor Distributions About Leeward Side of Apollo at 33° Incidence for Various Values of the Stagnation-Point Velocity-Gradient Ratio	14
2	Input Conditions to BLIMP program and Predicted Heating Rates for Apollo at Zero Incidence: JPL 21-Inch HWT at Nominal Mach 9 and High Reynolds Number	20
3	Pressure Distribution and Spreading Factors about Apollo at 25° Incidence	
	a. Windward Side	23
	b. Leeward Side	24
4	Pressure Distribution and Spreading Factors About Apollo at 33° Incidence	
	a. Windward Side	25
	b. Leeward Side	26
5	Streamwise Pressure Gradient Parameter Distribution About Windward Side of Apollo at 25° Incidence	27
6	Wall Temperature Correction for Nonablating Stagnation-Point Heat-Transfer Coefficient	35
7	Nonablating Laminar Heat-Transfer Coefficient Distributions About Apollo at 25° Incidence	
	a. Windward Side	37
	b. Leeward Side	38
8	Parameters Associated with the Momentum Thickness Reynolds Number About the Windward Side of Apollo at 25° Incidence: $H_T = 20,000 \text{ Btu/Lb}$, $P_{T2} = 1.0 \text{ Atm}$	44
9	Nonablating Laminar/Turbulent Heat-Transfer Coefficient Distributions About Apollo at 25° Incidence: $P_{T2} = 1.0 \text{ Atm}$	
	a. Windward Side	45
	b. Leeward Side	46

LIST OF TABLES (continued)

Table		Page
10	Stagnation-Point Ablation Characteristics of Apollo Heat-Shield Material	
	a. Steady-State Ablation	54
	b. Simulated Transient Ablation (High Pyrolysis Gas Rates)	55
11	Stagnation-Point Heat- and Mass-Transfer Coefficients for Apollo Heat-Shield Material	
	a. Steady-State Ablation	57
	b. Simulated Transient Ablation (High Pyrolysis Gas Rates)	58
12	Nonsimilar Laminar Boundary Layer About Apollo at 25° Incidence: 20,000 Btu/Lb, 1.0 Atm	
	a. Leeward Side, Low Pyrolysis Gas Rates (Virgin Material Ablation), Uniform Wall Temperature	69
	b. Leeward Side, High Pyrolysis Gas Rates, Uniform Wall Temperature	70
	c. Windward Side, Moderate Pyrolysis Gas Rates, Uniform Wall Temperature	71
	d. Windward Side, Moderate Pyrolysis Gas Rates, Variable Wall Temperature	72
13	Nonsimilar Laminar/Turbulent Boundary Layer About Apollo at 25° Incidence: 20,000 Btu/Lb, 1.0 Atm	
	a. Leeward Side, Low Pyrolysis Gas Rates (Virgin Material Ablation), Uniform Wall Temperature	76
	b. Leeward Side, High Pyrolysis Gas Rates, Uniform Wall Temperature	77
14	Char and Pyrolysis Gas Elemental Mass Fractions in AVCOAT 5026-39/HC-GP (Prior to Coking)	100
15	Char Species Mass Fractions (Prior to Coking)	101
16	Virgin Plastic Thermal Properties	113
17	Char Thermal Properties	114
18	Summary of Driver Temperature Cases	117
19	Apollo Mission Summary	127
20	Summary of Apollo Flights and Body Points for which Flight Predictions were Made	129
21	Time-Dependent Boundary Conditions Used in CMA Flight Predictions	
	a. Case 1 - Flight AS 202, Body Point Z71,Y0 (705)	131
	b. Case 2 - Flight AS 502, Body Point 705	132
	c. Case 3 - Flight AS 501, Body Point 705	133
	d. Case 4 - Flight AS 202, Body Point Z0,Y33	134
	e. Case 5 - Flight AS 501, Body Point 710	135
	f. Case 6 - Flight AS 502, Body Point 707	136
	g. Case 7 - Flight AS 501, Body Point 707	137

LIST OF TABLES (concluded)

Table		Page
22	Summary of Factors Used in Flight Predictions	138
23	Summary of Errors in Predicted In-Depth Temperature Response	150

LIST OF FIGURES

Figure		Page
1	Apollo Command Module Sketch	5
2	Comparison of Theoretical and Experimental Pressure Distributions about Apollo at Zero Incidence	10
3	Stagnation-Point Velocity-Gradient Ratio for Apollo at Angle of Attack	16
4	Variation of Spreading Factor with Distance Around the Body for Apollo at Angle of Attack	
	a. Leeward Side	17
	b. Windward Side	17
5	Comparison of BLIMP Convective Heating Predictions with Wind Tunnel Test Results for Apollo at Zero Incidence	21
6	Comparison of BLIMP Convective Heating Predictions with Wind Tunnel Test Results for Apollo at 25° Incidence	28
7	Comparison of BLIMP Convective Heating Predictions with Wind Tunnel Test Results for Apollo at 33° Incidence	29
8	Comparison of BLIMP Predictions for Wind-Tunnel Test Conditions with NASA/MSFC Convective Heating Factors for Apollo at 25° Angle of Attack	31
9	Ratio of Apollo Convective Heating at Station $\bar{s}/R = 0.9875$ to Convective Heating at Axisymmetric Stagnation Point	32
10	Nonablating Heat-Transfer Coefficient to Axisymmetric Stagnation Point: $R_{eff} = 13.0$ Ft, $T_w = 2000^\circ R$	34
11	Predicted Laminar Nonablating Heat-Transfer Coefficient Around Apollo at 25° Angle of Attack	39
12	Ratio of Predicted Heat-Transfer Coefficients for Flight and Wind-Tunnel Conditions	40
13	Momentum Thickness Reynolds Numbers for Laminar Air Boundary Layer About Apollo at Incidence	
	a. Windward Side	42
	b. Leeward Side	43

LIST OF FIGURES (continued)

Figure		Page
14	Ratio of Turbulent to Laminar Nonablating Heat-Transfer Coefficients for Apollo at Incidence	
	a. Windward Side, Aft of Toroid	48
	b. Leeward Side, Aft Heat Shield and Toroid	49
15	Mass-Transfer Coefficient Correlation for Apollo Material Ablation	60
16	Mass-Transfer Coefficient Blowing Correction for the Apollo Material	61
17	Accuracy of Apollo Material Mass-Transfer Coefficient Correlation	62
18	Heat-Transfer Coefficient Correlation for Apollo Material Ablation	64
19	Heat-Transfer Coefficient Blowing Correction for the Apollo Material	65
20	Accuracy of Apollo Material Heat-Transfer Coefficient Correlation	66
21	Transfer Coefficients for Nonsimilar Laminar Boundary Layer about Apollo at 25° Incidence Normalized by Values Obtained from Axisymmetric Stagnation-Point Correlation	
	a. Mass-Transfer Coefficient	73
	b. Heat-Transfer Coefficient	74
22	Transfer Coefficients for Nonsimilar Laminar/Turbulent Boundary Layer about Apollo at 25° Incidence Normalized by Values Obtained from Axisymmetric Stagnation-Point Correlation	
	a. Mass-Transfer Coefficient	78
	b. Heat-Transfer Coefficient	78
23	Radiation Fluxes from Uniform Slabs, $\delta = 1$ cm	85
24	Radiation Fluxes from Uniform Slabs, $\delta = 10$ cm	86
25	Radiation and Flow Terms in the Shock Layer Energy Balance	89
26	Nonadiabatic Cooling Factors as Functions of the Slope Parameter	90
27	Effect of Pressure on the Nonadiabatic Cooling Factors, $\delta_{AD} = 10$ cm	91
28	Comparison with Nonadiabatic Cooling Factors Obtained in Other Investigations	92
29	Interpolation Function for the Slope Parameter for the Shock Layer Model	94

ORIGINAL PAGE IS
OF POOR QUALITY

LIST OF FIGURES (continued)

Figure		Page
30	The Slope Parameter and the Correction Factors to be Applied to Adiabatic Radiation Fluxes for Apollo 4	95
31	Predicted Radiation Fluxes for Apollo 4	96
32	Predicted and Measured Radiation Intensities for Apollo 4	97
33	Chemical and Visual Microscopic Observations of Flight-Tested Apollo Heat-Shield Material	103
34	Pyrolysis-Gas Carbon Mass Fraction for the Apollo Material Considering Coking	107
35	Pyrolysis Gas Enthalpy for the Apollo Material Considering Coking	108
36	Driver Temperature Calculations Using Envelope of AVCO Char Conductivity Data	
	a. Flight AS 502, Body Point 705	116
	b. Flight AS 502, Body Point 707	116
37	Driver Temperature Calculations for Flight AS 502, Body Point 705 Using Effective Char Thermal Conductivity Data	118
38	Driver Temperature Calculations for Flight AS 502, Body Point 707 Using Effective Char Thermal Conductivity Data	119
39	Driver Temperature Calculations for Flight AS 501, Body Point 705 Using Effective Char Thermal Conductivity Data	120
40	Surface Thermochemistry Map for Apollo Material Considering Coking (Reactive Pyrolysis Gas)	124
41	Comparison of Predicted Temperatures with Thermocouple Response for Flight AS 202, Body Point Z71,YO (705)	141
42	Comparison of Predicted Temperatures with Thermocouple Response for Flight AS 502, Body Point 705	142
43	Comparison of Predicted Temperatures with Thermocouple Response for Flight AS 501, Body Point 705	143
44	Comparison of Predicted Temperatures with Thermocouple Response for Flight AS 202, Body Point ZO,Y33	144
45	Comparison of Predicted Temperatures with Thermocouple Response for Flight AS 501, Body Point 710	145
46	Comparison of Predicted Temperatures with Thermocouple Response for Flight AS 502, Body Point 707	
	a. Laminar Flow	146
	b. Laminar/Turbulent Flow	147

LIST OF FIGURES (continued)

Figure		Page
47	Comparison of Predicted Temperatures with Thermocouple Response for Flight AS 501, Body Point 707	
	a. Laminar Flow	148
	b. Laminar/Turbulent Flow	149
48	Surface Recession and Char Penetration for Flight AS 202	
	a. Case 1 (Body Point Z71, YO (705))	152
	b. Case 4 (Body Point ZO, Y33)	152
49	Surface Recession and Char Penetration for Flight AS 501	
	a. Case 3 (Body Point 705)	153
	b. Case 5 (Body Point 710)	153
	c. Case 7 (Body Point 707)	153
50	Surface Recession and Char Penetration for Flight AS 502	
	a. Case 2 (Body Point 705)	154
	b. Case 6 (Body Point 707)	154
51	Predicted Blowing Rates and Surface Temperatures for Flight AS 501, Body Point 705	155
52	Predicted Density of Surface Material and Corresponding Temperatures for Flight AS 501, Body Point 705	157
53	In-Depth Temperature and Material Density Profiles for Flight AS 501, Body Point 705	158
	a. Temperature Profiles	158
	b. Material Density Profiles	158
54	Material Density Profiles for Flight AS 202	159
	a. Case 1 (Body Point Z71, YO (705))	159
	b. Case 4 (Body Point ZO, Y33)	159
55	Material Density Profiles for Flight AS 501	
	a. Case 3 (Body Point 705)	160
	b. Case 5 (Body Point 710)	160
	c. Case 7 (Body Point 707)	160
56	Material Density Profiles for Flight AS 502	
	a. Case 2 (Body Point 705)	161
	b. Case 6 (Body Point 707)	161
57	Carbon Density Profiles for Flight AS 202	
	a. Case 1 (Body Point Z71, YO (705))	163
	b. Case 4 (Body Point ZO, Y33)	163
58	Carbon Density Profiles for Flight AS 501	
	a. Case 3 (Body Point 705)	164
	b. Case 7 (Body Point 707)	164
59	Carbon Density Profiles for Flight AS 502	
	a. Case 2 (Body Point 705)	165
	b. Case 6 (Body Point 707)	165

LIST OF FIGURES (concluded)

Figure		Page
60	Heating Rate Predictions for Flight AS 501, Body Point 705	167
61	Blowing Reduction Histories Predicted for Flight AS 501, Body Point 705	167
62	Partition of Surface Heating Rates for Flight AS 501, Body Point 705	168
63	Partition of Integrated Surface Heating for Flight AS 501, Body Point 705	168
64	Partition of Interior Energy Terms for Flight AS 501, Body Point 705	169
65	Comparison of Predicted Heating Rates with Wafer Calorimeter Data for Body Point 705	
	a. Flight AS 502	171
	b. Flight AS 501	171
66	Comparison of Predicted Heating Rates with Wafer Calorimeter Data for Body Point 707	
	a. Flight AS 502	172
	b. Flight AS 501	173
67	Reynolds Number and Blowing Rate Time Histories for Flight AS 502, Body Point 707	175
68	Transition Correlation for Apollo Leeward Aft Heat Shield Applied to Flights AS 502 and AS 501, Body Point 707	176
69	Comparison of Predicted Heating Rates with Asymptotic Calorimeter Data for Flight AS 501, Body Point 710	178

LIST OF SYMBOLS

A	cross-section area
B	pre-exponential factor in Arrhenius type relation for plastic decomposition (see Eq. (47))
B'	thermodynamic blowing parameter defined by Eq. (25)
B'_0	blowing parameter defined by Eq. (24)
C_H	Stanton number defined implicitly by Eq. (21)
C'_H	Stanton number defined implicitly by Eq. (23)
C_M	overall Stanton number for mass transfer defined by Eq. (20)
C_{M_k}	Stanton number for mass transfer for element k defined by Eq. (16)
C_p	specific heat at constant pressure
D	Apollo reference dimension = $2R$
\bar{D}	reference binary diffusion coefficient introduced by the approximation for binary diffusion coefficients embodied in Eq. (19)
D_{ij}	binary diffusion coefficient for species i and j
E_a/R	activation energy in Arrhenius type relation for plastic decomposition (see Eq. (47))
F	radiative flux directed towards wall
F_i	diffusion factor for species i introduced by the approximation for binary diffusion coefficients embodied in Eq. (19)
F_1, F_2, F_3, F_4, F_5	correction factors to be applied to obtain the nonablating heat-transfer coefficient $\rho_e U_e C_{H_0}'$ (see Eq. (33))

G_1, G_2	correction factors to be applied to obtain the mass-transfer blowing correction (see Eq. (34))
h	static enthalpy
\bar{h}	enthalpy associated with a unit mass change in condensed phase in pyrolysis zone
h_1, h_2	metric coefficients defined implicitly by Eq. (1). h_2 is the spreading factor employed in the axisymmetric analogy
h_w	enthalpy of the gas mixture at the wall
H_r	recovery enthalpy
H_T	total enthalpy
H_1, H_2	correction factors to be applied to obtain the heat-transfer blowing correction (see Eq. (35))
i	stagnation-point velocity-gradient ratio defined by Eq. (12)
\tilde{j}_k	diffusional mass flux of element k per unit area
k	thermal conductivity
K	streamline curvature
K_i	mass fraction of species i
\tilde{K}_k	mass fraction of element k irrespective of molecular configuration
\tilde{K}_{C_g}	elemental mass fraction of carbon in the pyrolysis gas
Le	system Lewis number (see Reference 29)
\dot{m}	mass flow rate per unit area
M	Mach number
\mathcal{M}	molecular weight

p	pressure
p_T	local stagnation pressure
p_{T_2}	total pressure behind the shock
Pr	Prandtl number
q_r	net radiative heat flux directed toward the wall
q_w	convective heat flux to the wall (conduction plus diffusion)
r_o	local radius of body in a meridian plane for an axisymmetric shape at zero incidence
R	Apollo reference dimension (see Figure 1)
Re_D	Reynolds number based on D
Re_θ	Reynolds number based on momentum thickness
s	orthogonal coordinate parallel to body surface which reduces at the inviscid surface to the streamline distance measured from the flight stagnation point
\dot{s}	surface recession rate
\bar{s}	distance along streamline measured from geometric center of Apollo aft heat shield (see Figure 1)
\bar{s}_o	distance from geometric center of Apollo aft heat shield to flight stagnation point
s_T	distance from flight stagnation point to point where boundary layer transition initiates
S	slope parameter employed in the nonadiabatic radiation analysis defined by Eq. (42)
\bar{S}	normalized slope parameter employed in the nonadiabatic radiation analysis defined in Figure 29
T	temperature

u	velocity component in s direction
U_e	boundary-layer edge velocity
v	velocity component in y direction
V_∞	flight velocity
w	velocity component in z direction
y	orthogonal coordinate normal to body surface
z	coordinate parallel to body surface orthogonal to s and y
Z_i	a quantity for species i defined by Eq. (18)
Z_i^*	a quantity for species i defined by Eq. (17)
\tilde{Z}_k^*	a quantity for element k employed in the definition of $\rho_e U_e C_{M_k}$ (see Eq. (16)) defined by Eq. (17)

GREEK SYMBOLS

α	angle of attack
α^*	flux normalizing parameter (see Reference 9)
α_{ki}	mass fraction of element k in species i
β	conventional pressure gradient parameter (see Reference 9)
γ	velocity gradient; also, factor employed in the definition of Z_i^* (see Eq. (17))
Γ	nonadiabatic radiation cooling loss parameter defined in Figure 27
δ	shock standoff distance
δ_n	thickness of node in coking analysis
ϵ	surface emittance

θ	momentum thickness; also time
θ_B	angle local body normal makes with the free stream velocity vector
λ	meridional angle relative to geometric center of Apollo aft heat shield (see Figure 8)
λ_H	parameter used to correlate heat-transfer coefficient blowing correction data given by Eq. (31)
λ_M	parameter used to correlate mass-transfer coefficient blowing correction data given by Eq. (29)
μ	viscosity
ξ	transformed streamwise coordinate (see Reference 9)
ρ	density
ϕ	parameter used to correlate mass-transfer coefficient blowing correction data defined by Eq. (27)

SUPERSCRIPTS

*	signifies that quantity is normalized by α^*
---	---

SUBSCRIPTS

AD	refers to adiabatic shock layer calculation
b	refers to base state for dividing the energy flux into convective and diffusive terms
c	refers to char
e	refers to boundary-layer edge
g	refers to pyrolysis gas
i,j	refers to i^{th} or j^{th} molecular species, respectively
k	refers to k^{th} element

n refers to n^{th} nodal point
 o refers to zero mass addition value
 s refers to conditions just behind the bow shock in Section 4;
 refers to zero-incidence stagnation point elsewhere
 stag refers to actual (flight) stagnation point
 w refers to wall value
 α refers to angle-of-attack case
 ∞ refers to free-stream conditions ahead of the shock

SECTION 1

INTRODUCTION AND SUMMARY

A number of the earlier Apollo orbital and superorbital unmanned reentry flights were well instrumented with pressure sensors, radiometers, calorimeters, char sensors, and in-depth thermocouples.¹ In addition, rather extensive laboratory investigations have been conducted for representative samples (cores) of flight-tested heat-shield ablation material (e.g., Refs. 2 through 4). The purpose of the present investigation is to employ sophisticated analytical tools developed previously^{5,6} and attempt to rationalize these data in order to assess the adequacy of the analytical procedures, and to improve their reliability for use on future manned reentry studies. On the basis of these studies, a specific heat-shield design procedure is recommended.

The basic design tool is a one-dimensional in-depth heat conduction code (CMA) which permits surface ablation and in-depth depolymerization and coking events.⁷ Major inputs to this program include tables of normalized ablation rates obtained from a surface thermochemical ablation program (EST) based on the analysis presented in Reference 8, and correlations of chemically-reacting laminar and turbulent nonsimilar boundary layer solutions obtained with the BLIMP program.⁹ A brief summary of these three codes, including a summary of several minor modifications which were made during the present contract, is presented in Appendix A. Current user's manuals are contained in References 10 through 12, respectively.

Studies of the inviscid flow field about Apollo at angle of attack are presented in Reference 13 and summarized in Section 2. Nominal agreement with wind-tunnel pressure distribution data has been obtained for zero angle of attack using a time-asymptotic solution procedure¹⁴; however, it was found that further work is required to obtain useful solutions at angle of attack for body shapes of the Apollo class. While these modifications are straightforward and not extensive, they were well beyond the scope of the present effort. Therefore, it is still necessary to rely on wind-tunnel pressure distribution data. Procedures are also described in Section 2 for obtaining approximate streamline spreading information for use in three-dimensional boundary-layer solutions using the axisymmetric analogy.

The convective heating correlations are presented in Section 3. Agreement of boundary-layer solutions with wind-tunnel convective heating data is excellent. A correction for extending the results of wind-tunnel tests to flight conditions is presented which is usually small for laminar flow; an increase in convective heating by a factor of 3 to 5 is seen to be appropriate for turbulent flow. A comprehensive set of stagnation-point blowing corrections for heat- and mass-transfer coefficients (including chemical-reaction effects appropriate to the Apollo ablation material) is presented and shown to be represented quite accurately with simple analytical formulas. Corrections to these blowing corrections for positions around the body are presented which are small for turbulent as well as laminar flow except in the toroidal region.

Solutions are presented for radiation heating in the stagnation region which agree quite well with radiometer data and recent predictions by NASA/MSC personnel¹⁵. These results are described in Section 4.

The models employed for surface thermochemical ablation and in-depth pyrolysis and coking events are discussed in Section 5. The material response is divided into three regimes based on surface temperature. At low surface temperatures, pyrolysis takes place to form a carbonaceous char and a pyrolysis gas which is considered to be frozen (containing excess carbon); the surface is not permitted to recede. At intermediate temperatures the pyrolysis gas is permitted to coke in accordance with a simple relation that the pyrolysis gas carbon content is a function of temperature; surface recession is permitted consistent with coking and reactive pyrolysis gas effects. At high temperatures, the pyrolysis gas is considered to be in equilibrium with the char such that in-depth char erosion can take place; the corresponding surface recession model is tantamount to that of carbon ablation including pyrolysis gas effects. Material thermal properties are based on laboratory tests of post-flight material samples (e.g., Ref. 3). These data are validated by a series of driver-temperature calculations.

The Apollo flight predictions are presented in Section 6. Body locations considered include the stagnation region, a position on the leeward side of the aft heat shield* in the pitch plane (yields turbulent flow), a position around the toroid on the conical afterbody on the windward side (flow still attached, but barely), and a position on the leeward side of the aft heat shield substantially off the pitch plane. Flights AS 501 and AS 502 (superorbital) and AS 202 (orbital) were considered. Predictions of surface recession, char penetration,

* In accordance with Apollo terminology, the aft heat shield is the blunt front face of the vehicle.

in-depth temperatures, char densities and (to the extent available) heating rates were typically satisfactory indicating that heating rates (including the blowing corrections), pressure distributions, material properties, ablation model, and coking model are all adequate or at least compensating. It is significant that the reported solutions were all first attempts with the exception of two cases where transition to turbulent flow occurs. Here the solutions were purposefully run laminar and the results were examined in order to develop preliminary transition criteria including mass-transfer effects. The results here are also very encouraging.

The recommended design procedure is presented in Section 7. Recommendations for further analysis and program refinements are presented in Section 8.

SECTION 2

INVISCID FLOW FIELD STUDIES

In order to theoretically predict heating and ablation rates about Apollo and related configurations, it is necessary to account for the convective heat transfer resulting from a highly three-dimensional boundary layer. This, in turn, requires knowledge of certain characteristics of the three-dimensional inviscid flow field. As a minimum it is necessary to know the pressure distribution about the vehicle. It is also desirable to know at least the shock shape and surface streamlines if the full inviscid flow field cannot be obtained. Given only the pressure distribution (including the location of the stagnation point), a boundary-layer edge condition can be computed by an isentropic expansion and a boundary-layer solution can be generated using a planar or axisymmetric flow assumption. Given also the shock shape, a nonisentropic expansion can be considered by performing a simple balance between the mass passing through the shock and the mass entering the boundary layer. Given the surface streamline pattern, the boundary-layer solution can be improved to include three-dimensional streamline divergence effects through use of the axisymmetric analogy.*

The Apollo configuration consists of three basic components:

1. The aft heat shield, which is a segment of a sphere
2. The conical afterbody
3. The toroidal section which connects the aft heat shield with the afterbody.

A sketch of the Apollo command module with full-scale dimensions is presented in Figure 1.

*When boundary-layer crossflow effects are small (valid near the pitch plane away from the stagnation point), the three-dimensional boundary layer equations reduce to a form analogous to the axisymmetric case except that the metric coefficient for the streamline spreading replaces the axisymmetric radial coordinate. Thus, given the streamline divergence, the boundary layer solution along the pitch plane can be obtained by a straightforward axisymmetric boundary layer solution.

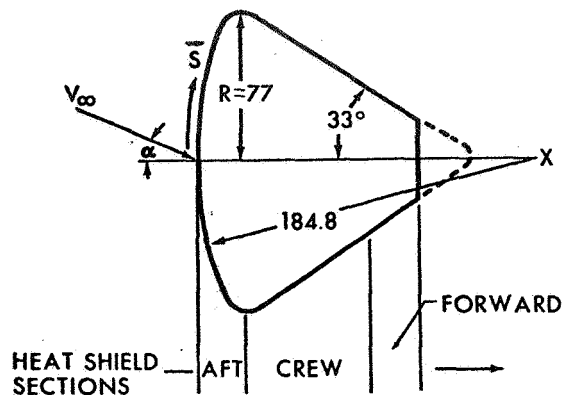
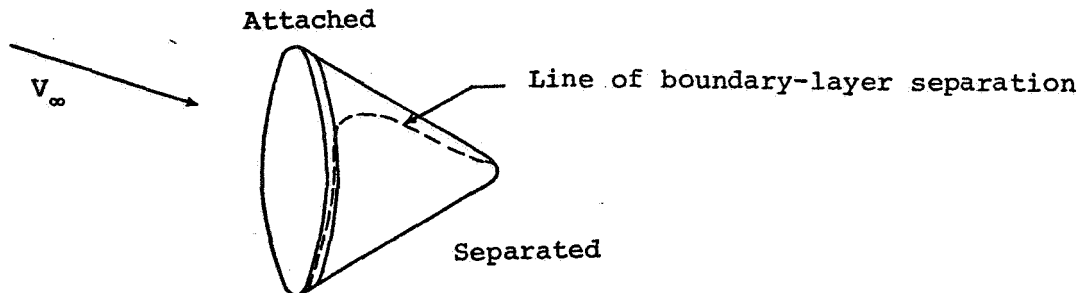


Figure 1. Apollo Command Module Sketch

On the aft heat shield the boundary layer is always attached. It stays attached over a portion of the windward side past the toroid and onto the conical afterbody for angles of attack greater than 20° or so. However, the flow is highly separated over the remainder of the conical afterbody (see sketch).



An accurate treatment of the flow field about Apollo would require a coupled viscous-inviscid fully three-dimensional analysis including separated flow considerations. Such a solution procedure is well beyond the current state of the art. It is still useful, however, to obtain flow field solutions over the aft heat shield, if possible, in order to provide accurate streamline information and entropy distributions. Furthermore, a three-dimensional inviscid flow field solution is necessary if a three-dimensional boundary layer solution is to be performed.

At the time that the Apollo program was initiated, there was no capability in the country to predict the flow field over the Apollo aft heat shield at angle of attack. Therefore, wind-tunnel pressure data were generated and applied directly to flight trajectories in the form of pressure ratio factors (see Ref. 16). As Apollo flight data became available, direct comparisons have been made between flight and wind-tunnel pressure data (e.g., Ref. 17). Agreement has been good.

over the aft heat shield. However, pressures measured in flight over the conical afterbody have generally been lower than predictions based on the wind-tunnel data. While this disagreement could be associated with experimental difficulties, it may also be the result of viscous interaction effects produced by the massive injection of pyrolysis gases and/or real gas effects, neither of which were experienced in the wind-tunnel tests.

During the past few years there has been substantial progress in the ability to predict three-dimensional inviscid flow fields about simple bodies at angle of attack. While the Apollo shape does present special difficulties, due principally to its extreme bluntness and its negative-incidence conical afterbody, there has been encouraging progress here as well. In particular, solutions have been reported for the spherical portion of the aft heat shield of Apollo at angle of attack using an inverse program,¹⁸ for the blunt-body portion of an Apollo-like body at angle of attack using a time-dependent solution procedure¹⁹, and for very blunt ellipsoidal noses at zero incidence²⁰ using a second time-dependent technique which has also been extended to angle of attack and coupled to a supersonic afterbody program¹⁴. Therefore, as part of the present study, a small effort was made to obtain inviscid flow-field solutions about Apollo at angle of attack in order to provide improved boundary-layer edge information for the aft heat shield calculation.

With regard to the prediction of pressure distributions over the conical afterbody, this, as mentioned previously, is not possible with present-day computational techniques. Therefore, an empirical approach must be used there. Fortunately, this is not serious because the heating rates are low over the conical afterbody. Also, the flight measurements, if they can be believed, indicate that the wind-tunnel pressure data are conservative. In fact, with the flight pressure data now available, one could correct the pressure distribution factors to agree with the flight data if desired.

Unfortunately, the inviscid flow field numerical studies could not be completed within the limited scope; however, the results of the study are most encouraging. These results are described in detail in Reference 13 and are summarized below in Section 2.1. At the present time, therefore, it is still necessary for Apollo shape vehicles to rely upon direct use of wind-tunnel pressure data (or flight data when available). Furthermore, in the absence of inviscid flow-field solutions, it is necessary to estimate streamline spreading by the use of approximate analytical procedures.* The approach which has been employed in the present study is described in Section 2.2.

* Oil flow experiments are unlikely to yield a sufficiently accurate description of the inviscid streamlines.

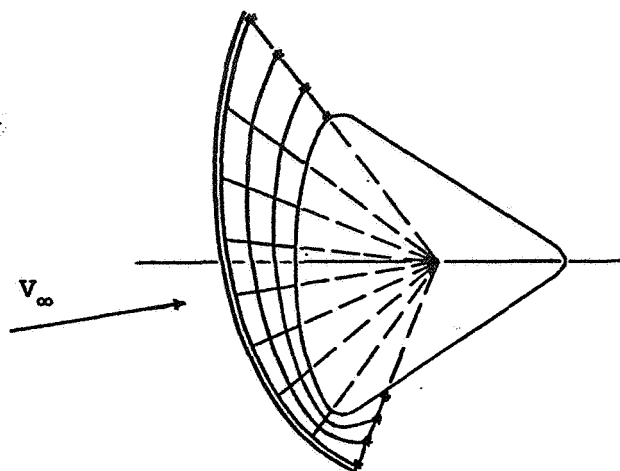
2.1 NUMERICAL STUDIES OF APOLLO INVISCID FLOW FIELD

A brief evaluation of existing three-dimensional blunt body computer codes was made, keeping in mind that no significant code development was included within the scope of this contract. The results of this study showed there are three candidate codes: an inverse solution procedure described in Reference 18, and two codes which obtain the solution to the steady flow field as the asymptotic limit of an unsteady flow^{14,19}. The characteristics of these three codes are summarized in more detail in Reference 13. Briefly, it was concluded that the code described in Reference 19 is too inaccurate (within present computer storage and speed restrictions) and that the inverse procedure of Reference 18 offers no possibility of obtaining satisfactory solutions around the toroid and, in addition, is operationally not suited for design studies. On the other hand, it was concluded that the code developed at GASL for Sandia¹⁴ has the potential for obtaining satisfactory solutions at acceptable cost for the flow about Apollo at incidence providing some minor code modifications successfully remove certain probable sources of numerical difficulties.

As mentioned, the GASL/Sandia code employs a time-dependent solution procedure in which the steady solution is obtained as the time asymptotic limit of an unsteady flow. For computational purposes, the flow field is divided into three regions: the bow shock, the body surface, and the interior of the flow. In the interior, the solution in time is obtained by an accurate, explicit, second-order finite difference procedure. The bow shock wave is treated numerically as a sharp discontinuity, in contradistinction to the more common (and less accurate) shock smearing procedures. At the body and shock, a method of characteristics procedure is used.

The computational problems which were anticipated are the result of:

1. Mesh size restrictions. Because of the high curvature on the toroidal section of the Apollo capsule, it was anticipated that a finite difference grid more dense than is typically used with the code would be required; hence, it was necessary to determine whether or not currently available core storage on a Univac 1108 would be sufficient and whether corresponding computational times would be acceptable.
2. Extrapolations of certain boundaries. In the solution procedure, in advancing the solution from one time step to another, the solution at certain "outer boundary" points is obtained by linear extrapolation from interior points (see sketch).



*Solutions at these points
obtained by linear extrapolation.

Apollo at incidence - Computational Grid in Pitch Plane

Since the extrapolation is done in the region near the toroid, it was expected that the large changes in flow variables there would probably result in some computational difficulty.

3. Shock and body points in the supersonic region. The solution procedure used at the shock and body points tends to become unstable when the flow is appreciably supersonic. With most geometries, this is not a problem because the part of the computational domain where the flow is supersonic can be restricted in size and in maximum Mach number. However, due to the concentrated expansion around the toroid, fairly large regions with Mach numbers appreciably greater than unity were expected to lead to some instabilities, thus requiring remedial action.

The results of the evaluation, which are fully reported in Reference 13, are:

1. Mesh size. A computational mesh about twice that normally sufficient for more moderately blunted configurations is required. This probably results in requiring a computer with core storage on the order of 100-130K words (e.g., CDC 6600 or the use of drum storage on Univac 1108). Corresponding computing times would be on the order of 1/2-1 hour on a CDC 6600 and at least twice as long on an 1108.
2. Extrapolations. As anticipated, extrapolations at the outer boundary did cause numerical trouble. However, it appears that these difficulties can be overcome with relatively simple code modifications.
3. Shock and body points. Here the problems are a little more serious but not insurmountable. The current solution procedure needs to be significantly modified by replacing one momentum equation and the

equation relating pressure and normal velocity component with two compatibility equations along bicharacteristics. While these changes are straightforward, they require major code modifications that were beyond the present scope.

One of the important results of the effort was to determine with confidence that the computational procedure is powerful enough to obtain accurate solutions for Apollo flow fields at acceptable cost. This conclusion was reached by examining solutions obtained at zero incidence, as shown, for example in Figure 2. There the excellent agreement between theory and experiment at Mach 10 shows that the basic computational procedure is certainly adequate for obtaining flow field solutions about Apollo. (The theoretical solution was obtained in about 1 minute on the Univac 1108 computer.) However, comparable results at high incidence cannot be obtained without the changes to the computer code mentioned above. Additional theoretical results at zero incidence and computer code modifications necessary to obtain comparable results at incidence are discussed in detail in Reference 13.

2.2 AXISYMMETRIC ANALOGY

2.2.1 Analysis

In 1955 Eichelbrenner and Oudart noted that when the boundary layer cross flow is small (velocities and crosswise gradients), the boundary layer equations reduce to a form analogous to the axisymmetric flow equations.^{21,22} In order to illustrate this, consider the three-dimensional boundary layer equations for steady compressible flow of a perfect gas with constant specific heats and constant Prandtl number (see, for example, Eqs. (1) through (5) of Reference 21). Let us consider curvilinear coordinates (s, z, y) where y is the surface normal direction and s and z are taken to be the projections of the external streamlines on to the surface and their orthogonal trajectories in the surface, respectively. These coordinates are assigned velocity components (u, w, v) and metric coefficients $(h_1, h_2, 1)$ where an element of length within the boundary layer $d\ell$ is given by

$$d\ell^2 = h_1^2 ds^2 + h_2^2 dz^2 + dy^2 \quad (1)$$

Neglecting those terms containing crossflow velocity or crosswise gradients, the three-dimensional boundary-layer equations reduce to

$$\rho \left(\frac{u}{h_1} \frac{\partial u}{\partial s} + v \frac{\partial u}{\partial y} \right) = \frac{\rho_e u_e}{h_1} \frac{\partial u_e}{\partial s} + \frac{\partial}{\partial y} \left(\mu \frac{\partial u}{\partial y} \right) \quad (2)$$

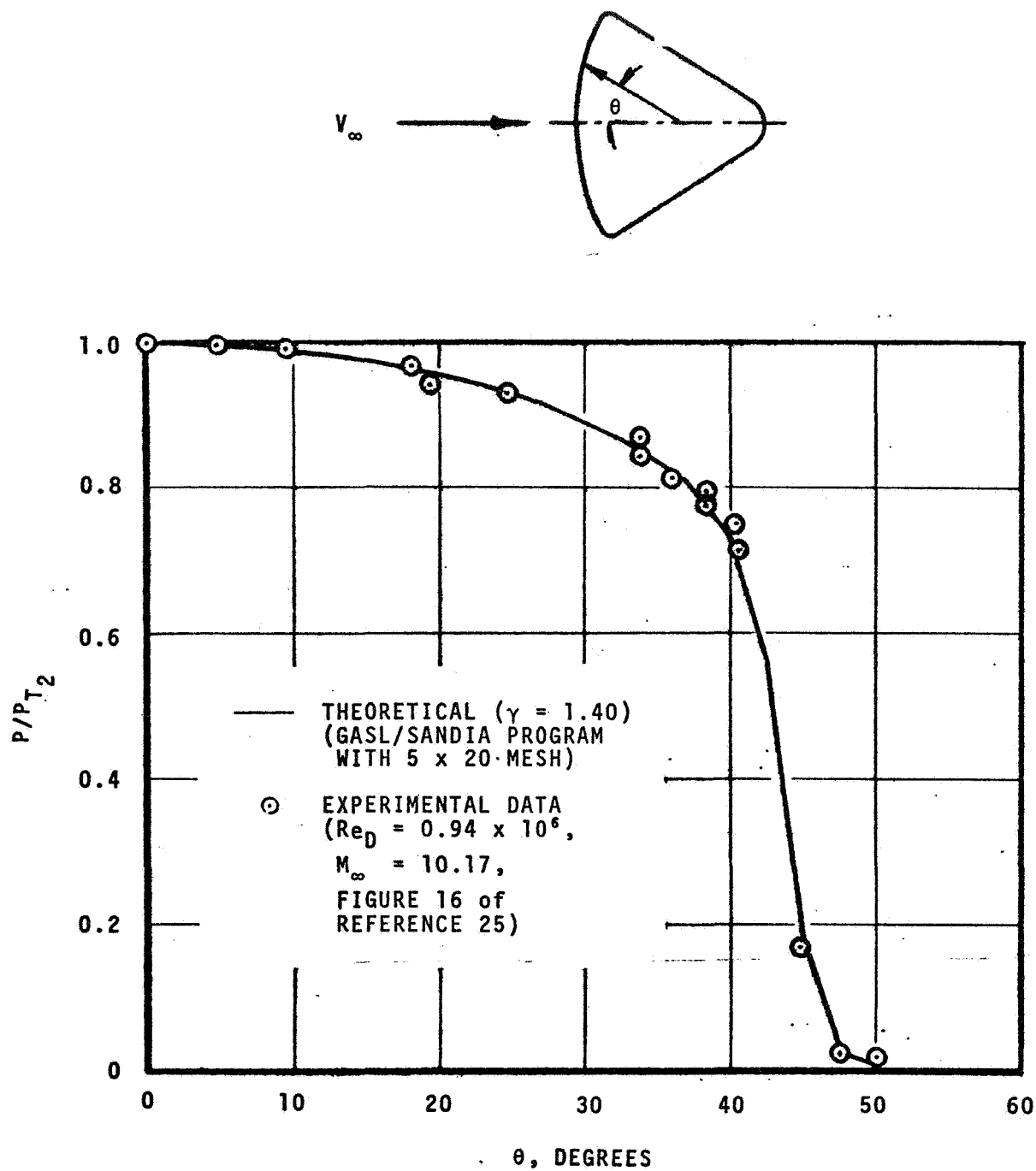


Figure 2. Comparison of Theoretical and Experimental Pressure Distributions about Apollo at Zero Incidence

ORIGINAL PAGE IS
OF POOR QUALITY

$$\rho \left(\frac{u}{h_1} \frac{\partial h}{\partial s} + v \frac{\partial h}{\partial y} \right) + \frac{\rho_e u u_e}{h_1} \frac{\partial u_e}{\partial s} = \frac{1}{Pr} \frac{\partial}{\partial y} \left(\mu \frac{\partial h}{\partial y} \right) + \mu \left(\frac{\partial u}{\partial y} \right)^2 \quad (3)$$

$$\frac{1}{h_1 h_2} \frac{\partial}{\partial s} (\rho h_2 u) + \frac{\partial}{\partial y} (\rho v) = 0 \quad (4)$$

where ρ is the density, μ is the viscosity, Pr is the Prandtl number, h is the enthalpy defined by

$$h = C_p T \quad (5)$$

where C_p is the specific heat at constant pressure and T is the temperature, and the subscript e refers to the boundary-layer edge.

Defining the length scale h_1 to be unity, it is apparent that the three-dimensional small crossflow boundary-layer equations (Eqs. (2)-(4)) are identical to the axisymmetric boundary-layer equations with h_2 replacing the local body radius r_0 of axisymmetric flow theory. This is not too surprising when it is recognized that for axisymmetric flow $(1/r_0)(\partial r_0/\partial s)$ is nothing more than a measure of the rate at which the inviscid edge streamlines diverge as is $(1/h_2)(\partial h_2/\partial s)$ for the more general case. Thus, when the small crossflow approximation holds, it is possible to obtain the solution of a three-dimensional problem by solving an analogous axisymmetric problem.

In order to solve these analogous equations, it is necessary to obtain the spreading factor h_2 from a solution of the inviscid flow field. The most appealing way to do this would be to solve the three-dimensional steady Euler equations exactly. However, as discussed in the previous section, it is presently not possible to obtain solutions satisfactory for this purpose. The best available computer codes for obtaining three-dimensional flow fields are only partially successful in obtaining pressure distributions on Apollo configurations, and it is much more difficult to obtain the local streamline divergence. In lieu of such a rigorous solution procedure, it was decided to limit detailed attention to the pitch plane - where the approximate method of Hearne et al²³ is applicable.* This approach employs thin-shock-layer and Newtonian-crossflow pressure-distribution approximations to obtain the pitch-plane streamline divergence. In the vicinity of the stagnation point, this approximation is certain

* It is judged that no reliable methods exist for estimating h_2 for positions off the pitch plane. Furthermore, the small crossflow approximation becomes less valid at positions off the pitch plane (crossflow is identically zero in the pitch plane). Therefore, detailed consideration of positions off the pitch plane are not practical without three-dimensional inviscid solutions and may not be satisfactory without three-dimensional boundary-layer solutions.

to be invalid, and a semi-empirical correlation approach is used to obtain the divergence. Briefly, with the thin-shock-layer and small-crossflow approximations, the Euler equations in orthogonal streamline coordinates are given by*

$$\frac{1}{h_2} \frac{\partial}{\partial s} (\rho h_2 u) + \frac{\partial}{\partial y} (\rho v) = 0 \quad (6)$$

$$u \frac{\partial u}{\partial s} + v \frac{\partial u}{\partial y} = - \frac{1}{\rho} \frac{\partial p}{\partial s} \quad (7)$$

$$u \frac{\partial v}{\partial s} + v \frac{\partial v}{\partial y} - Ku^2 = - \frac{1}{\rho} \frac{\partial p}{\partial y} \quad (8)$$

$$u \frac{\partial H}{\partial s} + v \frac{\partial H}{\partial y} = 0 \quad (9)$$

where H is the total enthalpy, p is the pressure, K is the curvature, and the other parameters are as defined previously. Assuming that the crossflow pressure is given by

$$\frac{p}{p_{z=0}} = \frac{\cos^2 \theta_B}{(\cos^2 \theta_B)_{z=0}} \quad (10)$$

where θ_B is the angle the local surface normal makes with the free stream velocity vector, and noting that $h_2 \sim z$ near the pitch plane, where z is the rectangular coordinate measured normal to the pitch plane, leads to a second order ordinary linear differential equation for the variable h_2

$$\frac{d^2 h_2}{ds^2} - \frac{1}{\rho u^2} \frac{\partial p}{\partial s} \frac{dh_2}{ds} + \frac{1}{R_c^2} \left[1 - 2 \frac{p_T}{\rho u^2} \cos^2 \theta_B \right] h_2 = 0 \quad (11)$$

where R_c is the surface radius of curvature and p_T is the total pressure. Using the empirically determined pitch-plane pressure distribution and stagnation point location and an initial condition to be discussed below, this equation can be integrated to obtain the variation of h_2 with the streamwise coordinate s .

In order to perform this integration it is necessary to know the behavior of h_2 as $s \rightarrow 0$ for use as an initial condition. In Reference 23 this is done by obtaining the solution of Equation (11) for small s , yielding

* See Reference 23 for details.

$$h_2 \sim s^i \quad i \equiv \gamma_{z_{stag}} / \gamma_{s_{stag}} \quad (12)$$

where $\gamma_{z_{stag}}$ and $\gamma_{s_{stag}}$ are the crosswise and pitch-plane stagnation-point velocity gradients. With this definition, it can be shown that the streamwise pressure gradient parameter at the stagnation point β_{stag} is given by

$$\beta_{stag} = \frac{1}{1+i} \quad (13)$$

Now $i = 0$ and $\beta_{stag} = 1.0$ for two-dimensional flow and $i = 1.0$ and $\beta_{stag} = 1/2$ for axisymmetric flow; hence, Equation (12) is correct in these two limiting cases. However, for values of $0 < i < 1$, Equation (12) is singular at the stagnation point due to the fact that the approximations employed in the development of Equation (11) break down there and that the small crossflow approximation itself fails at the stagnation point. Another problem with the direct use of Equation (12) at the stagnation point is that no standard approximate theories, including Newtonian, will yield accurate enough results for $\gamma_{z_{stag}}$ and $\gamma_{s_{stag}}$.

In order to obtain the appropriate value of i for use as an initial condition in a given problem and for calculating the value of the stagnation point β_{stag} , use can be made of the fact that the coefficients of Equation (11) involving ρu^2 , p , etc. contain implicit information about the velocity gradient ratio i . Thus a satisfactory value of i can be found by iterative solution of Equation (11) for the specified edge conditions until a solution $h_2(s)$ is found which is virtually independent of the value of s_0 where the integration is started. This approach would not be expected to yield accurate results at the stagnation point but should be valid in the vicinity of the stagnation point and at positions around the body.

2.2.2 Results

Solutions to Equation (11) are shown in Table 1 for the leeward pitch plane of a subscale Apollo at 33° angle-of-attack. The solutions are presented in the form of the spreading factor $h_2(s)$ normalized by the value at station number 10 ($m = 10$).^{*} Results are shown for i of 0.500, 0.400, and 0.345 for

^{*}The spreading factor can be normalized in any manner desired since it is the rate of change of the spreading factor, and not its scale, that is important in the boundary layer solution. For this same reason, the values of h_2 (or normalized h_2) obtained from the present subscale Apollo calculations are directly applicable for use in full-scale Apollo boundary-layer calculations for corresponding values of s/R . Selection of the $h_2(s)$ at $m = 10$ for the normalizing parameter was made arbitrarily and for convenience in comparing the results for different values of i and different initial stations.

TABLE 1
SPREADING FACTOR DISTRIBUTIONS ABOUT LEeward SIDE OF APOLLO
AT 33° INCIDENCE FOR VARIOUS VALUES OF THE
STAGNATION-POINT VELOCITY-GRADIENT RATIO

m	S* (feet)	Spreading Factor/Spreading Factor at Station m = 10							
		i = 0.500		i = 0.400		i = 0.345		m _O = 4	m _O = 4
		m _O = 2	m _O = 4	m _O = 2	m _O = 4	m _O = 2	m _O = 4		
2	.5000-02	.2280-00	.3652-00	.2475-00	.4048-00	.2636-00	.4297-00	.42998-00	
3	.1000-01	.3086-00	.4456-00	.3255-00	.4763-00	.3365-00	.4960-00	.49619-00	
4	.2000-01	.4110-00	.5094-00	.4223-00	.5348-00	.4297-00	.5510-00	.55120-00	
5	.3000-01	.4812-00	.6144-00	.4901-00	.6325-00	.4960-00	.6442-00	.64424-00	
6	.4000-01	.5388-00	.7039-00	.5462-00	.7170-00	.5510-00	.7254-00	.72542-00	
7	.6000-01	.6354-00	.8606-00	.6407-00	.8661-00	.6442-00	.8697-00	.86979-00	
8	.8000-01	.7190-00	.1000-01	.7228-00	.1000-01	.7254-00	.1000-01	.1000-01	
9	.1200-00	.8670-00	.1129-01	.8687-00	.1122-01	.8697-00	.1121-01	.11218-01	
10	.1600-00	.1000-01	.1281-01	.1000-01	.1271-01	.1000-01	.1265-01	.12654-01	
11	.2000-00	.1124-01	.1424-01	.1122-01	.1403-01	.1121-01	.1401-01	.14011-01	
12	.2500-00	.1270-01	.1552-01	.1267-01	.1541-01	.1265-01	.1529-01	.15292-01	
13	.3000-00	.1408-01	.1685-01	.1403-01	.1663-01	.1401-01	.1649-01	.16495-01	
14	.3500-00	.1531-01	.1803-01	.1532-01	.1777-01	.1529-01	.1761-01	.17614-01	
15	.4000-00	.1660-01	.1910-01	.1653-01	.1882-01	.1649-01	.1864-01	.18640-01	
16	.4500-00	.1773-01	.1921-01	.1766-01	.1892-01	.1649-01	.1873-01	.18737-01	
17	.5000-00	.1877-01	.1931-01	.1879-01	.1902-01	.1649-01	.1883-01	.18833-01	
18	.5500-00	.1897-01	.1941-01	.1889-01	.1911-01	.1649-01	.1893-01	.18930-01	
19	.5100-00	.1907-01	.1950-01	.1898-01	.1917-01	.1649-01	.1902-01	.19021-01	
20	.5150-00	.1916-01	.1960-01	.1907-01	.1921-01	.1649-01	.1911-01	.19111-01	
21	.5200-00	.1925-01	.1969-01	.1917-01	.1930-01	.1649-01	.1919-01	.19198-01	
22	.5250-00	.1934-01	.1977-01	.1925-01	.1939-01	.1649-01	.1927-01	.19277-01	
23	.5300-00	.1942-01	.1985-01	.1933-01	.1947-01	.1649-01	.1934-01	.19347-01	
24	.5350-00	.1949-01	.1991-01	.1940-01	.1954-01	.1649-01	.1940-01	.19407-01	
25	.5400-00	.1957-01	.1996-01	.1946-01	.1960-01	.1649-01	.1945-01	.19456-01	
26	.5450-00	.1955-01	.1996-01	.1946-01	.1960-01	.1649-01	.1945-01	.19456-01	
27	.5500-00	.1960-01	.2001-01	.1951-01	.1965-01	.1649-01	.1949-01	.19497-01	
28	.5550-00	.1964-01	.1985-01	.1958-01	.1969-01	.1649-01	.1949-01	.19497-01	
29	.5600-00	.1949-01	.1985-01	.1940-01	.1954-01	.1649-01	.1949-01	.19497-01	

* R = 0.288 feet, see Figure 1 (0.045 scale). These results are directly applicable to full scale Apollo for the same s/R.

solutions starting at stations m_0 of 2 and 4. The value of $i = 0.345$ is selected as best since the spreading factors $h_2(s)$ are almost identical for m_0 of 2 and 4. What this really means is that $h_2 \sim s^{0.345}$ between 0.005 feet ($m = 2$) and 0.020 feet ($m = 4$). The adequacy of this approach is established in Section 3.1 where predictions of heat-transfer distributions using these results are shown to compare very well with wind-tunnel data.

Solutions were obtained for the windward and leeward sides of subscale Apollo at angles of attack of 25 and 33°. The values of i obtained by the above process are presented in Figure 3. Curves have been faired through these solutions extrapolating to the zero angle-of-attack case where $i = 1.0$ (axisymmetric flow). It can be seen that the flow in the vicinity of the stagnation point is more nearly axisymmetric on the leeward side than on the windward side (i.e., the i is closer to unity). The resulting values of the spreading factor for these four cases are shown as functions of distance from the stagnation point in Figure 4. It should be noted that the spreading factor approaches a constant on the windward side (i.e., planar flow) as the toroid is approached.

2.3 SUMMARY OF INVISCID FLOW FIELD STUDIES

A survey of existing three-dimensional flow field computer codes was made and the GASL/Sandia code¹⁴ was selected as being the only one suitable for extension to Apollo application. Solutions were obtained for zero angle of attack, but it was determined that program modifications beyond the scope of the present effort would be required to obtain satisfactory solutions at large angles of attack. In the absence of a reliable exact inviscid solution, the pressure factor curves developed by NASA/MSFC on the basis of wind tunnel and flight data were judged to yield the best data for predicting heat shield pressure distributions on the Apollo at incidence.

In addition, a method is described by which approximate three-dimensional boundary-layer solutions can be obtained in the vicinity of the pitch plane using the BLIMP nonsimilar axisymmetric boundary-layer code through the use of the axisymmetric analogy. This requires a measure of the local streamline spreading. An approximate method developed by Hearne et al²³ is employed for obtaining this information in the vicinity of the pitch plane. Briefly, in the vicinity of the pitch plane, the pressure gradient normal to the pitch plane is assumed given by Newtonian theory. Then a linear ordinary second order differential equation with variable coefficients is obtained for the streamline spreading. Boundary-layer solutions have been obtained, using this procedure, which agree well with wind-tunnel convective heating data for Apollo at incidence. These results will be described in Section 3.1. The relatively minor changes required in the BLIMP program to permit use of the axisymmetric analogy are summarized in Appendix A.

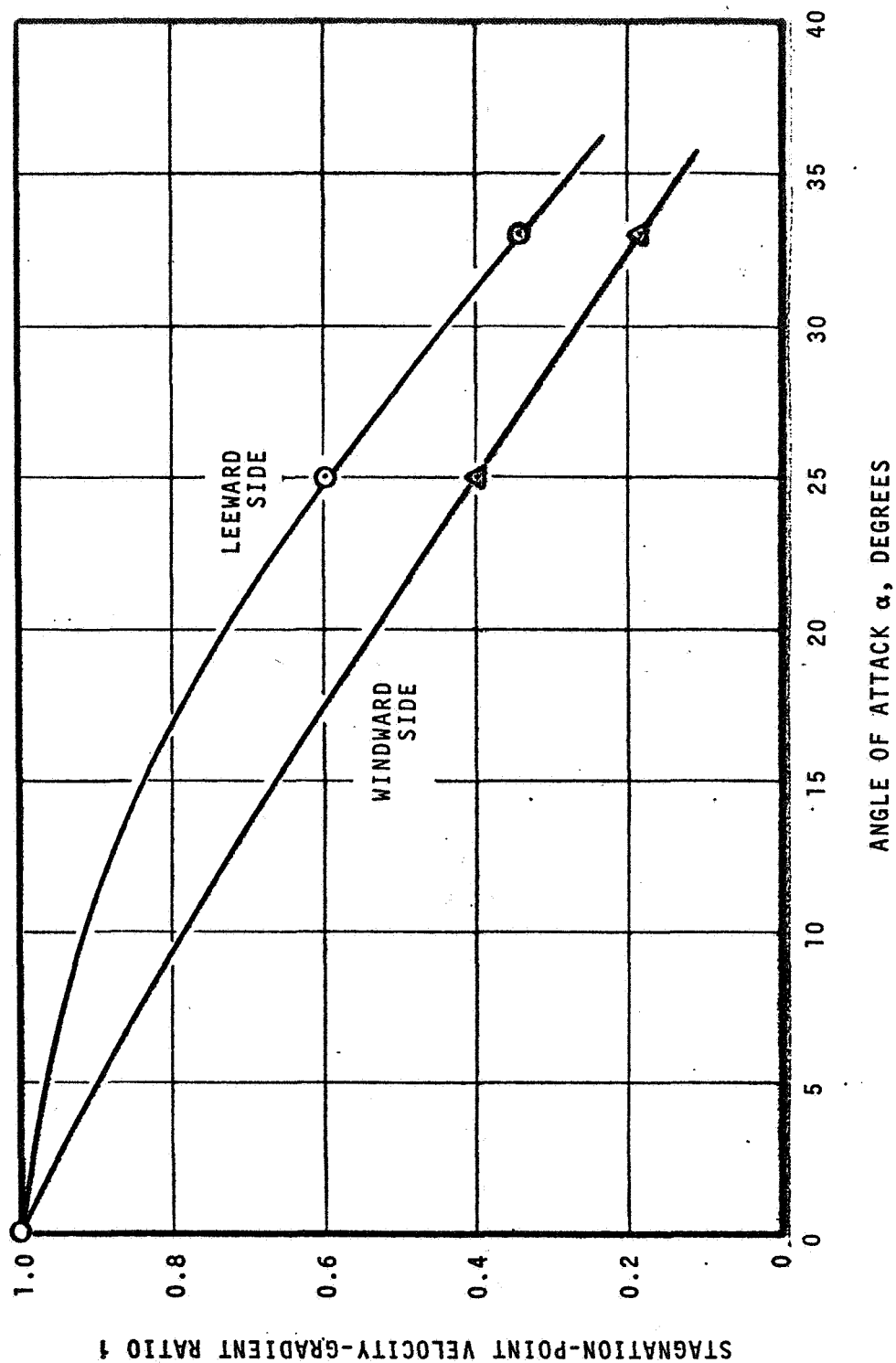


Figure 3. Stagnation-Point Velocity-Gradient Ratio for Apollo at Angle of Attack

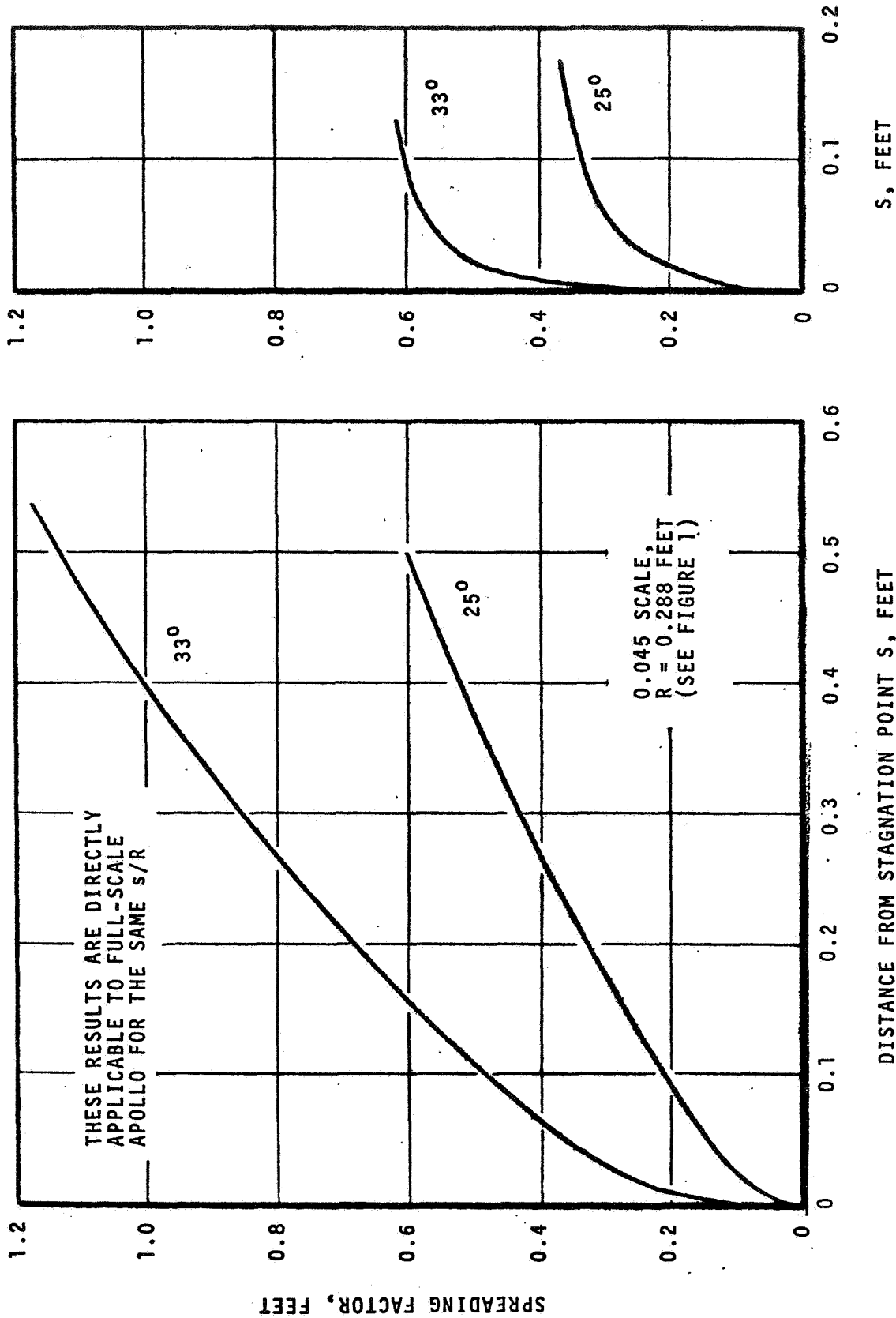


Figure 4. Variation of Spreading Factor with Distance Around the Body for Apollo at Angle of Attack

SECTION 3

CONVECTIVE HEATING STUDIES

There are three basic procedures for representing convective heating rates to a reentry vehicle.

1. Use of simple integral or self-similar procedures or correlations obtained therefrom
2. Use of correlations of chemically-reacting, nonsimilar boundary-layer solutions
3. Use of a computer code which couples the chemically-reacting, non-similar boundary layer to the charring ablation response.

The first approach is the one which has been typically used in the past. A coupled procedure (the third approach) has been developed^{6,24} but is too costly for incorporation into a heat-shield design procedure. The second procedure has the simplicity and economy of the first method, but approaches the accuracy of the third method. It is this approach which is employed in the present effort.

The calculation of heat- and mass-transfer rates is conveniently divided into three steps.

1. Nonablating stagnation-point boundary-layer solutions
2. Nonablating nonsimilar laminar and turbulent boundary-layer solutions about the vehicle normalized by the stagnation-point values
3. Ablating stagnation-point and nonsimilar laminar and turbulent boundary-layer solutions about the vehicle normalized by the local nonablating values.

Solutions have been generated with the BLIMP code described in References 9 and 12 and summarized in Appendix A. Unequal diffusion coefficients were considered in all of these calculations. The BLIMP program was modified to accommodate the axisymmetric analogy discussed in Section 2.2. The modifications to the program are also presented in Appendix A. The nonablation and ablation solutions are presented and correlated in Sections 3.2 and 3.3, respectively. A summary of the recommended procedure for utilizing these correlations in heat-shield design studies is presented in Section 3.4. First, however, BLIMP

solutions for convective heat-transfer rates are compared to wind-tunnel data in Section 3.1.

3.1 WIND-TUNNEL CORRELATIONS

A series of boundary-layer solutions was generated using the BLIMP program for representative wind-tunnel test conditions in order to validate the ability of BLIMP to predict convective heating rates about Apollo at angle of attack. The wind-tunnel tests and solutions were performed for a 0.045 scale model of Apollo (see Figure 1). Solutions were generated for zero incidence and for 25° and 33° angles of attack. The solutions are based on wind-tunnel pressure distributions; the remaining boundary-layer edge properties were obtained by an isentropic expansion. A curve fit of pressure data (to obtain the pressure gradient parameter β) and the isentropic expansion calculation are performed as a part of the BLIMP calculation.

3.1.1 Results for Zero Incidence

The case of zero incidence provides a good base to verify the ability of the BLIMP code to predict convective heating about Apollo-like configurations. In this case, the flow is axisymmetric and the dependence of the radial coordinate r with distance, s , from the stagnation point is known precisely. However, this is not to say that one can expect perfect agreement. In the first place, there is a rather significant scatter in pressure distribution data as shown in Figure 2. The heat transfer depends not only on the pressure level, but also on the derivative of pressure through the pressure gradient parameter, β . The situation is particularly acute in the toroidal region where curvature is high and expansion is rapid. Secondly, one cannot expect good agreement between theory and experiment in the vicinity of and beyond the point of maximum radius due to separation ($S/R = 1.08$, $S = 0.312$ feet for 0.045 scale - see Figure 1).

The wind-tunnel test chosen for correlation was conducted in the JPL 21-inch HWT at nominal Mach 9 and high Reynolds number and was reported in Reference 25. The stations considered and the corresponding values of pressure ratio and spreading factor (for this problem, the local body radius) are presented in Table 2. The resulting values of β and heat-transfer rates calculated by BLIMP are also presented in Table 2. It can be seen that the values of β in the vicinity of $S = 0.30$ feet are somewhat irregular. This is due to a combination of inaccuracies in pressure itself and in the curve-fitting process. The predicted and experimental heat-transfer rates are compared in Figure 5. Predictions reported in Reference 25 based on Lees analyses are also presented in Figure 5. Considering the experimental scatter of the pressure and heat-

TABLE 2

INPUT CONDITIONS TO BLIMP PROGRAM AND PREDICTED HEATING
 RATES FOR APOLLO AT ZERO INCIDENCE:
 JPL 21-INCH HWT AT NOMINAL MACH 9
 AND HIGH REYNOLDS NUMBER

S*	r_o feet	P/P_{T_2}	β	q_w Btu/sec ft ²	q_w/q_{ws}
.0000	.0000	1.0000	.500	36.00	1.000
.0288	.0288	.9976	.501	35.96	.999
.0576	.0576	.9904	.502	35.81	.995
.1120	.1118	.9637	.502	35.18	.977
.1610	.1598	.9250	.540	34.40	.956
.2120	.2080	.8590	.678	34.37	.955
.2450	.2390	.7850	.924	34.92	.970
.2535	.2470	.7550	1.409	36.03	1.001
.2605	.2540	.7140	1.568	36.66	1.018
.2648	.2580	.6880	1.745	36.83	1.023
.2707	.2628	.6360	2.301	37.29	1.036
.2780	.2700	.5510	2.622	36.39	1.011
.2838	.2746	.4660	3.397	34.52	.959
.2880	.2780	.3800	5.364	32.39	.900
.2921	.2810	.2600	8.577	26.76	.743
.2952	.2830	.1680	9.332	19.58	.544
.3000	.2854	.0950	7.251	11.88	.330
.3050	.2875	.0600	5.829	7.77	.216
.3100	.2880	.0430	5.768	5.75	.160
.3200	.2860	.0200	10.343	3.20	.089
.3310	.2800	.0085	6.723	1.45	.040
.3400	.2760	.0090	-4.568		

* R = 0.288 feet, see Figure 1 (0.045 scale)

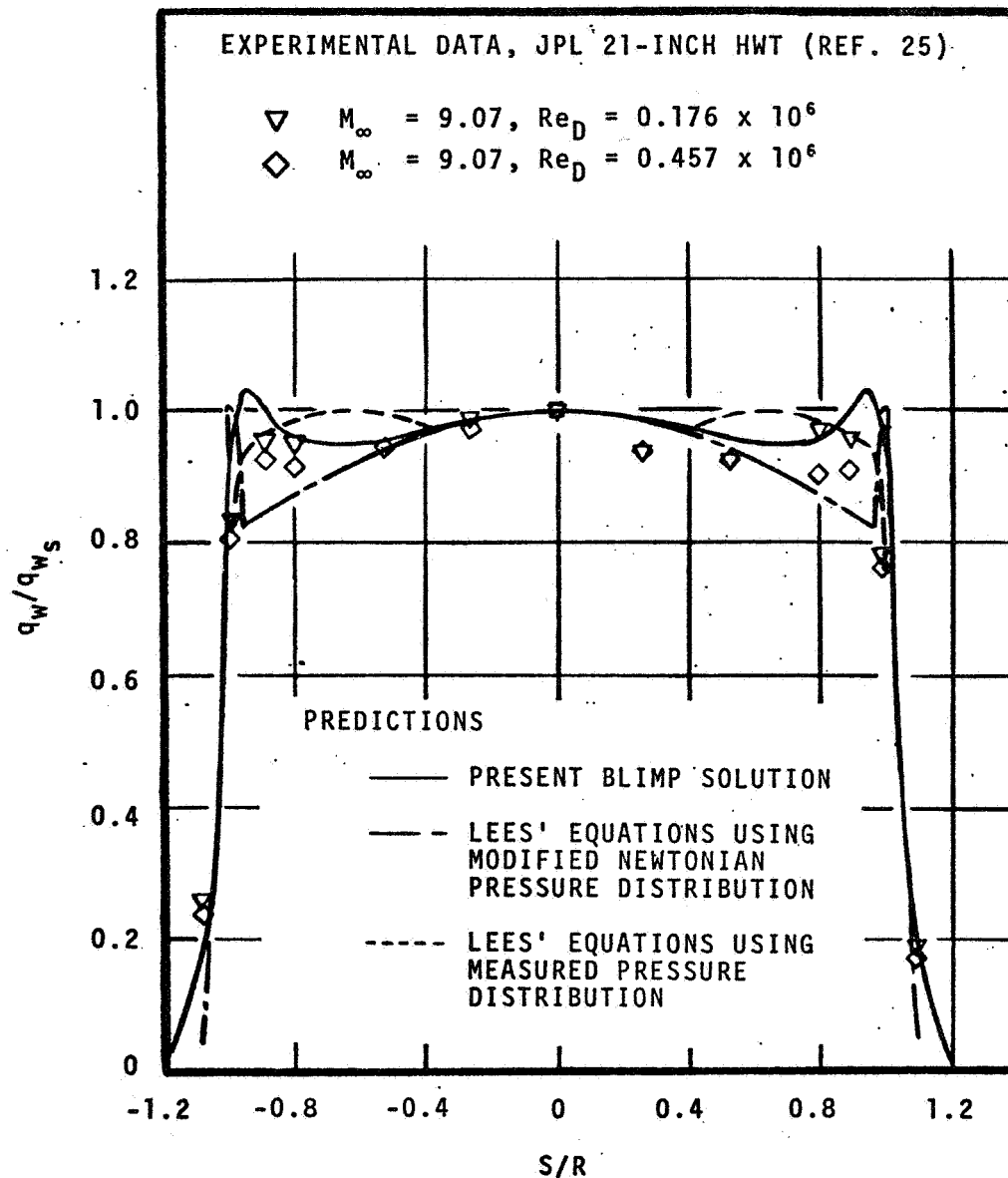


Figure 5. Comparison of BLIMP Convective Heating Predictions with Wind Tunnel Test Results for Apollo at Zero Incidence

transfer data, the agreement between the BLIMP solution and experiment is considered satisfactory.

3.1.2 Results for Angle of Attack

Boundary-layer solutions were also generated with the BLIMP program for the pitch-plane ray of Apollo at angles of attack of 25° and 33° for comparison with AEDC wind-tunnel convective heating data^{25,26}. Solutions were generated for assumed planar flow, for assumed axisymmetric flow and for approximate three-dimensional flow using the axisymmetric analogy discussed in Section 2.2. The streamwise stations that were employed in the calculations together with pressure distributions and spreading factors are presented in Tables 3 and 4 for the 25° and 33° cases, respectively. The spreading factors are unity for planar flow (i.e., no spreading), are taken as the distance to the surface from a line intersecting the flight stagnation point and normal to the surface at the flight stagnation point for axisymmetric flow, and are taken directly from the results presented in Section 2.2.2 for three-dimensional flow.*

The pressure gradient parameter β for the windward side 25° angle of attack case is shown in Table 5. The values of β are seen to scale roughly with the stagnation point values, namely $\beta_{\text{stag}} = 1.000$ for planar flow, 0.500 for axisymmetric flow and 0.714 for 3-D flow (see Eq. (13)). The smoothness of the $\beta(s)$ curve is typical of that obtained for all four cases, the irregularities again being the result of inaccuracies in the pressure derivative obtained by curve fitting experimental pressure data.

The predicted and experimental convective heating rates are compared in Figures 6 and 7 for the 25° and 33° angle-of-attack cases, respectively. The boundary-layer solutions were initiated at the stagnation point, of course, and proceeded in the leeward and windward directions independently. It can be seen that the stagnation-point solutions obtained from the windward and leeward solutions do not agree. Furthermore, there is erratic behavior in the near vicinity of the stagnation point. This would be expected for anything short of a full three-dimensional theory since the axisymmetric analogy breaks down there. A smooth curve connecting the windward and leeward solutions has been drawn through the stagnation region for the axisymmetric analogy case.

The axisymmetric theory overpredicts and the two-dimensional theory underpredicts the local heating rates.** The deviation between the two solutions is typically 35 percent over the "aft heat shield" and in the vicinity of the toroid,

*As mentioned previously, the boundary-layer solution is independent of the scale of the spreading factor.

**This was also observed in References 25 and 26.

TABLE 3
PRESSURE DISTRIBUTION AND SPREADING FACTORS
ABOUT APOLLO AT 25° INCIDENCE

(a) Windward Side

S* feet	P/P _{T2}	Spreading Factors		
		Axisymmetric	3-D Analogy	Planar
.000	1.0000	.0000	.0000	1.0000
.005	.9997	.0050	.1201	1.0000
.010	.9987	.0100	.1587	1.0000
.015	.9970	.0150	.1866	1.0000
.020	.9944	.0200	.2087	1.0000
.025	.9905	.0249	.2271	1.0000
.030	.9850	.0297	.2426	1.0000
.035	.9770	.0347	.2558	1.0000
.040	.9680	.0396	.2674	1.0000
.045	.9580	.0445	.2776	1.0000
.050	.9410	.0495	.2867	1.0000
.055	.9160	.0544	.2946	1.0000
.060	.8820	.0593	.3013	1.0000
.065	.8260	.0640	.3070	1.0000
.070	.7560	.0687	.3121	1.0000
.075	.6680	.0730	.3168	1.0000
.080	.5840	.0770	.3209	1.0000
.085	.4840	.0806	.3247	1.0000
.090	.3740	.0838	.3281	1.0000
.095	.2510	.0864	.3312	1.0000
.100	.1280	.0884	.3339	1.0000
.105	.0850	.0896	.3364	1.0000
.110	.0640	.0898	.3388	1.0000
.115	.0490	.0898	.3413	1.0000
.120	.0410	.0898	.3438	1.0000
.125	.0360	.0898	.3465	1.0000
.130	.0330	.0898	.3493	1.0000
.135	.0310	.0898	.3524	1.0000
.140	.0300	.0898	.3556	1.0000
.150	.0295	.0898	.3627	1.0000
.160	.0290	.0898	.3708	1.0000
.170	.0290	.0898	.3798	1.0000

* R = 0.288 feet, see Figure 1 (0.045 scale)

TABLE 3 (CONCLUDED)

(b) Leeward Side

S* feet	P/P _{T2}	Spreading Factors		
		Axisymmetric	3-D Analogy	Planar
.000	1.0000	.0000	.0000	1.0000
.004	.9999	.0040	.0364	1.0000
.008	.9996	.0080	.0552	1.0000
.012	.9991	.0120	.0704	1.0000
.016	.9983	.0160	.0832	1.0000
.020	.9970	.0200	.0940	1.0000
.025	.9943	.0250	.1053	1.0000
.030	.9914	.0300	.1149	1.0000
.035	.9883	.0350	.1236	1.0000
.040	.9851	.0399	.1317	1.0000
.060	.9720	.0595	.1607	1.0000
.080	.9560	.0793	.1869	1.0000
.120	.9260	.1182	.2357	1.0000
.160	.8890	.1575	.2823	1.0000
.200	.8470	.1963	.3272	1.0000
.240	.7970	.2350	.3703	1.0000
.280	.7390	.2733	.4114	1.0000
.320	.6800	.3100	.4505	1.0000
.360	.6190	.3460	.4877	1.0000
.400	.5550	.3806	.5229	1.0000
.420	.5230	.3975	.5397	1.0000
.430	.5110	.4050	.5480	1.0000
.440	.4880	.4130	.5561	1.0000
.450	.4720	.4210	.5640	1.0000
.455	.4620	.4250	.5679	1.0000
.460	.4490	.4286	.5718	1.0000
.465	.4390	.4323	.5756	1.0000
.470	.4260	.4362	.5794	1.0000
.475	.4120	.4400	.5831	1.0000
.480	.3940	.4435	.5868	1.0000
.485	.3730	.4460	.5903	1.0000
.490	.3360	.4483	.5938	1.0000

* R = 0.288 feet, see Figure 1 (0.045 scale)

TABLE 4
PRESSURE DISTRIBUTION AND SPREADING FACTORS
ABOUT APOLLO AT 33° INCIDENCE

(a) Windward Side

S* feet	P/P _{T2}	Spreading Factors		
		Axisymmetric	3-D Analogy	Planar
.000	1.0000	.0000	.0000	1.0000
.005	.9986	.0049	.3752	1.0000
.010	.9945	.0095	.4277	1.0000
.015	.9876	.0142	.4613	1.0000
.020	.9780	.0188	.4864	1.0000
.025	.9600	.0231	.5063	1.0000
.030	.9250	.0274	.5226	1.0000
.035	.8330	.0314	.5356	1.0000
.040	.7290	.0351	.5459	1.0000
.045	.6180	.0384	.5545	1.0000
.050	.4950	.0409	.5620	1.0000
.055	.3620	.0424	.5684	1.0000
.060	.2550	.0427	.5741	1.0000
.065	.1780	.0427	.5792	1.0000
.070	.1200	.0427	.5838	1.0000
.075	.0800	.0427	.5881	1.0000
.080	.0535	.0427	.5921	1.0000
.085	.0405	.0427	.5949	1.0000
.090	.0390	.0427	.5949	1.0000
.095	.0450	.0427	.5949	1.0000
.100	.0540	.0427	.5949	1.0000
.105	.0595	.0427	.5949	1.0000
.110	.0610	.0427	.5949	1.0000
.115	.0595	.0427	.5949	1.0000
.120	.0560	.0427	.5949	1.0000
.130	.0540	.0427	.5949	1.0000
.140	.0535	.0427	.5949	1.0000
.210	.0500	.0427	.5949	1.0000
.310	.0400	.0427	.5949	1.0000
.410	.0300	.0427	.5949	1.0000
.510	.0200	.0427	.5949	1.0000

* R = 0.288 feet, see Figure 1 (0.045 scale)

TABLE 4 (CONCLUDED)

(b) Leeward Side

S* feet	P/P _{T2}	Spreading Factors		
		Axisymmetric	3-D Analogy	Planar
.000	1.0000	.0000	.0000	1.0000
.005	.9997	.0050	.1608	1.0000
.010	.9987	.0100	.2052	1.0000
.020	.9950	.0200	.2620	1.0000
.030	.9887	.0300	.3024	1.0000
.040	.9800	.0400	.3360	1.0000
.060	.9610	.0600	.3927	1.0000
.080	.9400	.0800	.4423	1.0000
.120	.8900	.1180	.5303	1.0000
.160	.8340	.1560	.6097	1.0000
.200	.7790	.1940	.6840	1.0000
.250	.7080	.2410	.7716	1.0000
.300	.6360	.2870	.8543	1.0000
.350	.5660	.3380	.9325	1.0000
.400	.4940	.3760	1.0058	1.0000
.450	.4220	.4200	1.0740	1.0000
.500	.3500	.4610	1.1366	1.0000
.505	.3420	.4650	1.1425	1.0000
.510	.3300	.4690	1.1484	1.0000
.515	.3240	.4770	1.1542	1.0000
.520	.3050	.4800	1.1598	1.0000
.525	.2800	.4840	1.1654	1.0000
.530	.2430	.4880	1.1706	1.0000
.535	.1930	.4910	1.1755	1.0000
.540	.1250	.4940	1.1798	1.0000
.545	.0670	.4970	1.1834	1.0000
.550	.0370	.5000	1.1864	1.0000
.555	.0200	.5020	1.1889	1.0000
.560	.0090	.5050	1.1909	1.0000

* R = 0.288 feet, see Figure 1 (0.045 scale)

TABLE 5

STREAMWISE PRESSURE GRADIENT PARAMETER DISTRIBUTION
ABOUT WINDWARD SIDE OF APOLLO AT 25° INCIDENCE

Streamwise Distance, s ft*	Streamwise Pressure Gradient Parameter, β		
	Axisymmetric	3-D Analogy	Planar
.000	.500	.714	1.000
.005	.500	.715	1.001
.010	.510	.724	1.013
.015	.513	.735	1.027
.020	.561	.803	1.117
.025	.595	.848	1.169
.030	.656	.933	1.270
.035	.632	.908	1.222
.040	.535	.771	1.026
.045	.660	.957	1.263
.050	.845	1.237	1.619
.055	.905	1.328	1.719
.060	.931	1.372	1.751
.065	1.096	1.613	2.030
.070	1.152	1.696	2.109
.075	1.071	1.570	1.932
.080	1.083	1.582	1.933
.085	1.302	1.897	2.307
.090	1.645	2.391	2.903
.095	2.696	3.906	4.745
.100	3.064	4.436	5.411
.105	1.505	2.163	2.657
.110	1.217	1.708	2.115
.115	1.452	1.989	2.487
.120	1.094	1.465	1.851
.125	.841	1.102	1.409
.130	.615	.788	1.020
.135	.411	.516	.677
.140	.172	.211	.281
.150	.052	.060	.083
.160	.064	.072	.102
.170	-.044	-.047	-.069

* R = 0.288 feet, see Figure 1 (0.045 scale)

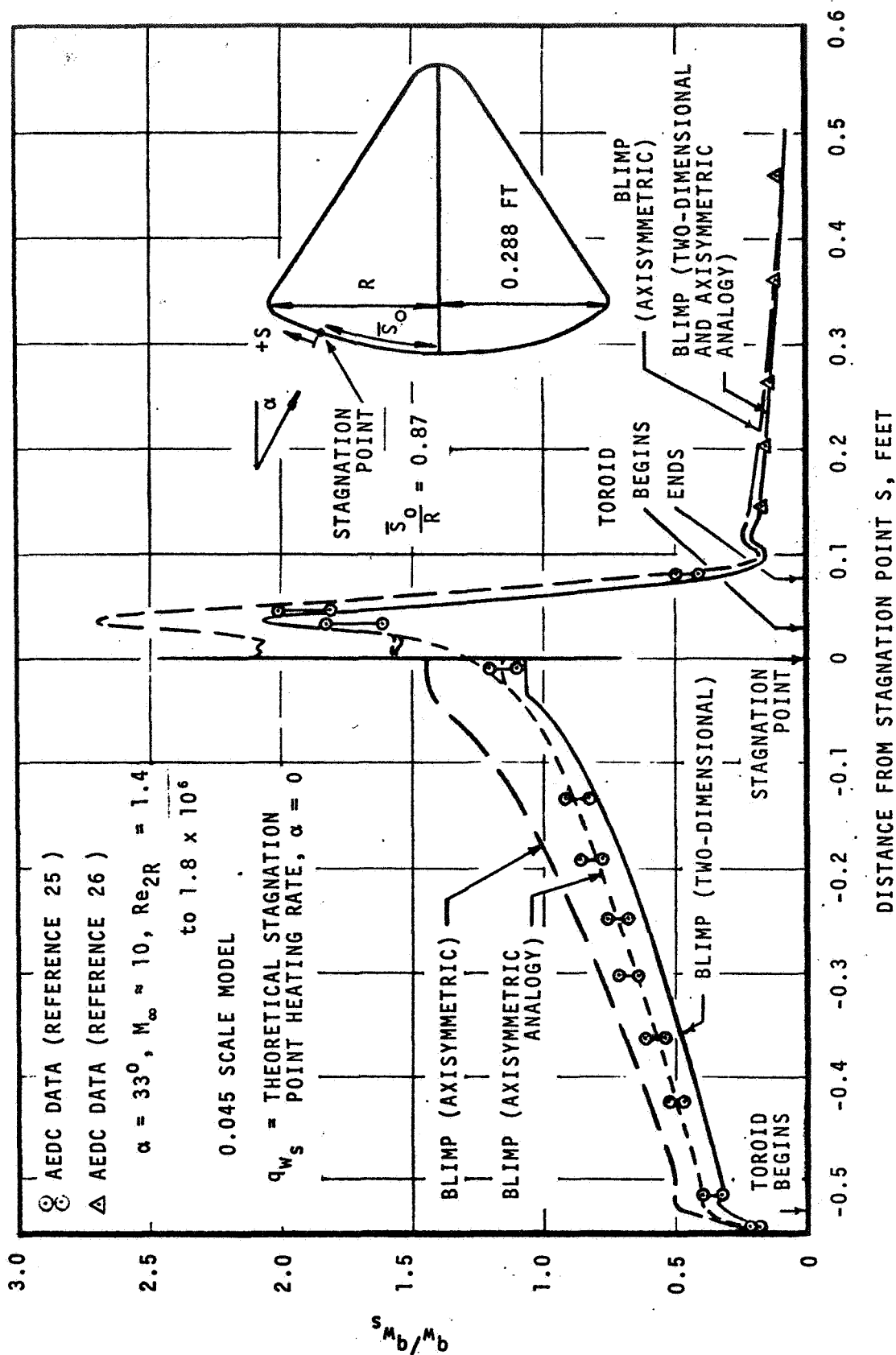


Figure 7. Comparison of BLIMP Convective Heating Predictions with Wind Tunnel Test Results for Apollo at 33° Incidence

but tends to vanish on the conical afterbody. The axisymmetric analogy solutions show remarkably good agreement except for a couple of data points in the vicinity of the toroid for the 25° angle-of-attack case. It should be noted here that while the results are presented in normalized form, the same normalizing parameter is used for predictions and data; thus, the agreement shown in Figures 6 and 7 is for absolute values of heating rates, not just heating-rate distributions.

NASA/MSC has employed "convective heating factors" to obtain convective heating rates at various positions on the Apollo heat shield²⁷. These factors based on wind-tunnel heating data, are normalized by the convective heating at a position $\bar{S}/R = 0.9875$. The NASA/MSC convective heating factors for 25° angle of attack are presented in Figure 8. The curves $\lambda = 90^\circ$ and $\lambda = 270^\circ$ refer to the windward and leeward sides of the heat shield, respectively. The intermediate values of λ refer to off-the-pitch plane rays. The BLIMP pitch plane predictions for 25° angle of attack are also shown in Figure 8. These were corrected for the different normalizing parameter by use of Figure 9 which was taken directly from the NASA/MSC convective heating factors for several angles of attack²⁷.

The NASA/MSC convective heating factors are based on a composite of all available wind-tunnel data. Thus, if the wind tunnel data considered in Figure 6 are representative, one would expect the agreement of theory and experiment to be the same for the NASA/MSC convective heating factors as it was for the specific tests considered in Figure 6. For the most part this is the case. The agreement is excellent over most of the body, and the BLIMP prediction is a few percent high in the windward toroidal region (in the vicinity of peak heating) and low at the beginning of the conical afterbody on the windward side. The only discrepancy seems to be back on the conical afterbody on the windward side ($\bar{S}/R = 1.4$) where the BLIMP prediction is high in the present comparison while it agreed very well when compared directly with data (Fig. 6). The BLIMP solution and wind-tunnel data both asymptote to a convective heating factor of 0.070, while the NASA/MSC curve approaches 0.045. Perhaps the NASA/MSC factors have been modified to account for the lower pressures measured in flight on the conical afterbody (see Section 2.0).

In conclusion, the comparison between BLIMP predictions and wind-tunnel pitch-plane convective-heating data is for the most part excellent. This can be interpreted two ways. First, it represents an independent validation of the quality of the wind-tunnel test results and thus the NASA/MSC convective heating factors, which are based on wind-tunnel data. Secondly, it shows that the BLIMP program, which has full chemistry capabilities, can be used as a tool to calculate pitch plane distributions for Apollo at flight conditions. These BLIMP

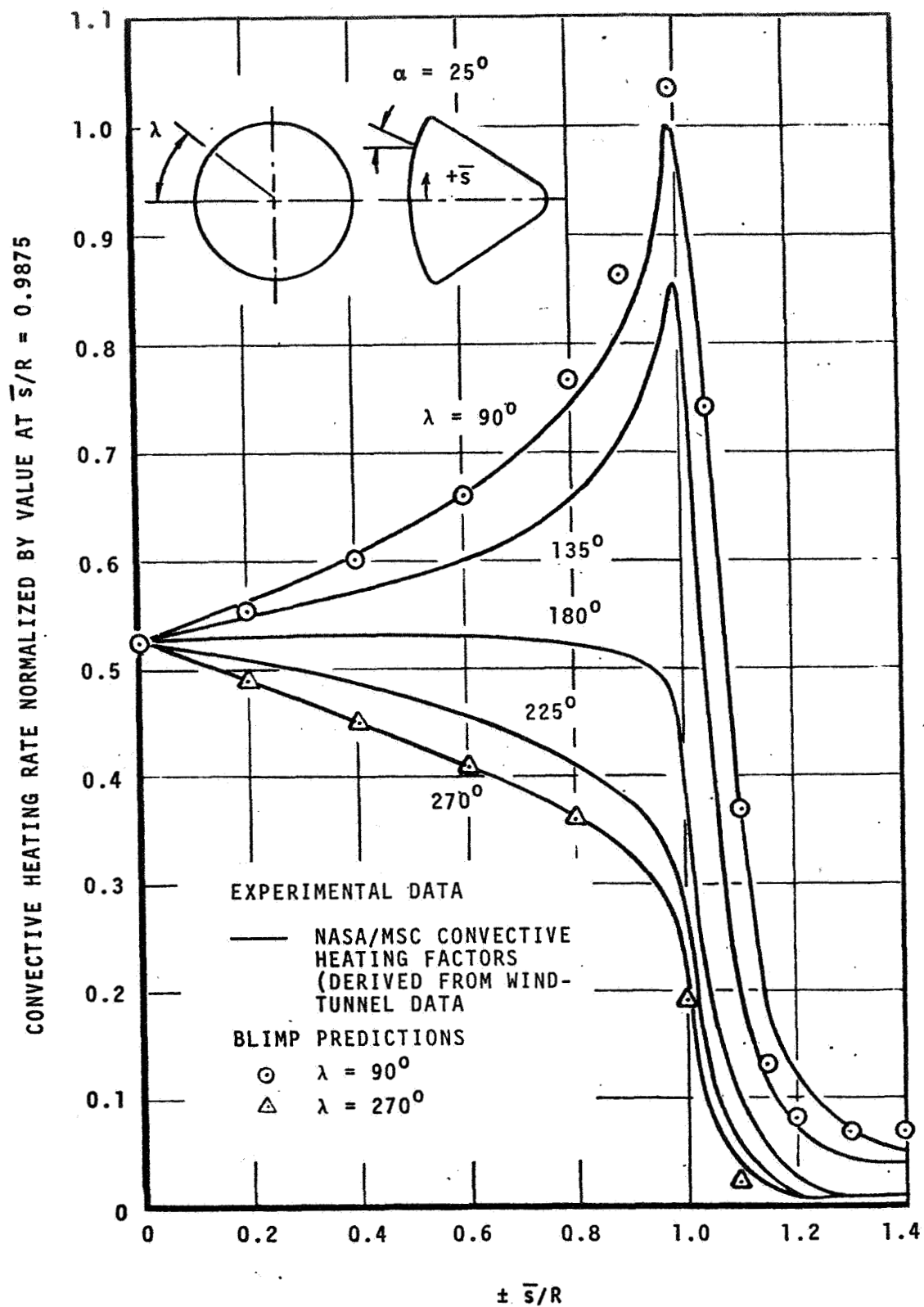


Figure 8. Comparison of BLIMP Predictions for Wind-Tunnel Test Conditions with NASA/MSFC Convective Heating Factors for Apollo at 25° Angle of Attack

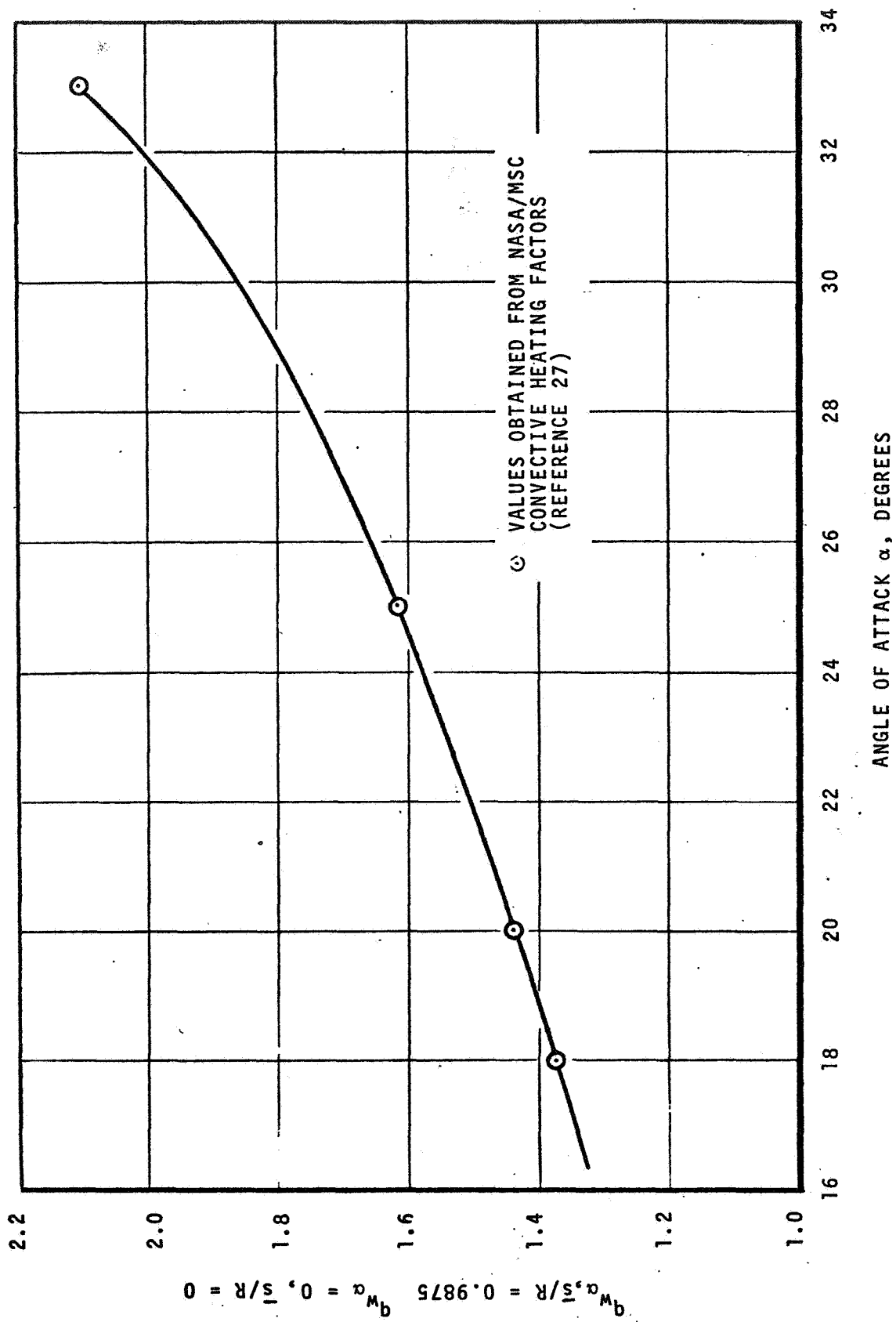


Figure 9. Ratio of Apollo Convective Heating at Station $\bar{s}/R = 0.9875$ to Convective Heating at Axisymmetric Stagnation Point

solutions can then be used to correct the convective heating factors for flight conditions - directly for the pitch plane and by interpolation for positions off the pitch plane. This study has been performed and is discussed in Section 3.2.

3.2 CONVECTIVE HEATING FLIGHT PREDICTIONS

Nonablating convective heat-transfer solutions considering unequal diffusion effects have been generated with the BLIMP chemically-reacting nonsimilar boundary-layer program (see Appendix A) and correlated for use in the Apollo flight predictions of Section 6.2. It has proven convenient to correlate the solutions in the following manner.

1. Stagnation-point solutions
2. Nonsimilar laminar boundary-layer solutions normalized by stagnation-point values
3. Nonsimilar turbulent boundary-layer solutions normalized by local laminar values.

The solutions and correlations are described in Sections 3.2.1 through 3.2.3, respectively.

3.2.1 Stagnation Point Boundary Layer

A matrix of air boundary-layer solutions was generated to encompass the range of flight conditions typically encountered in orbital or superorbital manned reentry (stagnation pressures P_{T_2} of 0.0001 to 1.0 atmosphere and total enthalpies H_{T_2} from 26,000 to 1500 Btu/lb). The results for a wall temperature T_w of 2000°R are presented in Figure 10 in the form of $\rho_e U_e C'_{H_O} / P_{T_2}^{1/2}$ where $\rho_e U_e C'_{H_O}$ is defined by

$$\rho_e U_e C'_{H_O} = q_{w_o} / (H_{T_e} - h_w) \quad (14)$$

with the subscripts o and s referring to the nonablation case and the stagnation point, respectively. An effective nose radius of 13.0 feet was used in these calculations. The variation of $\rho_e U_e C'_{H_O} / P_{T_2}^{1/2}$ with P_{T_2} and H_{T_2} is primarily due to chemistry effects. In order to illustrate this, curves of percent dissociation and ionization are also shown in Figure 10.

Solutions were also generated for wall temperatures of 500, 4000 and 6000°R. The values of $\rho_e U_e C'_{H_O}$ ratioed to the 2000°R values are presented in Table 6. A curve fit of these results, heavily weighted toward the higher pressures (which are needed to achieve high temperatures) takes the form

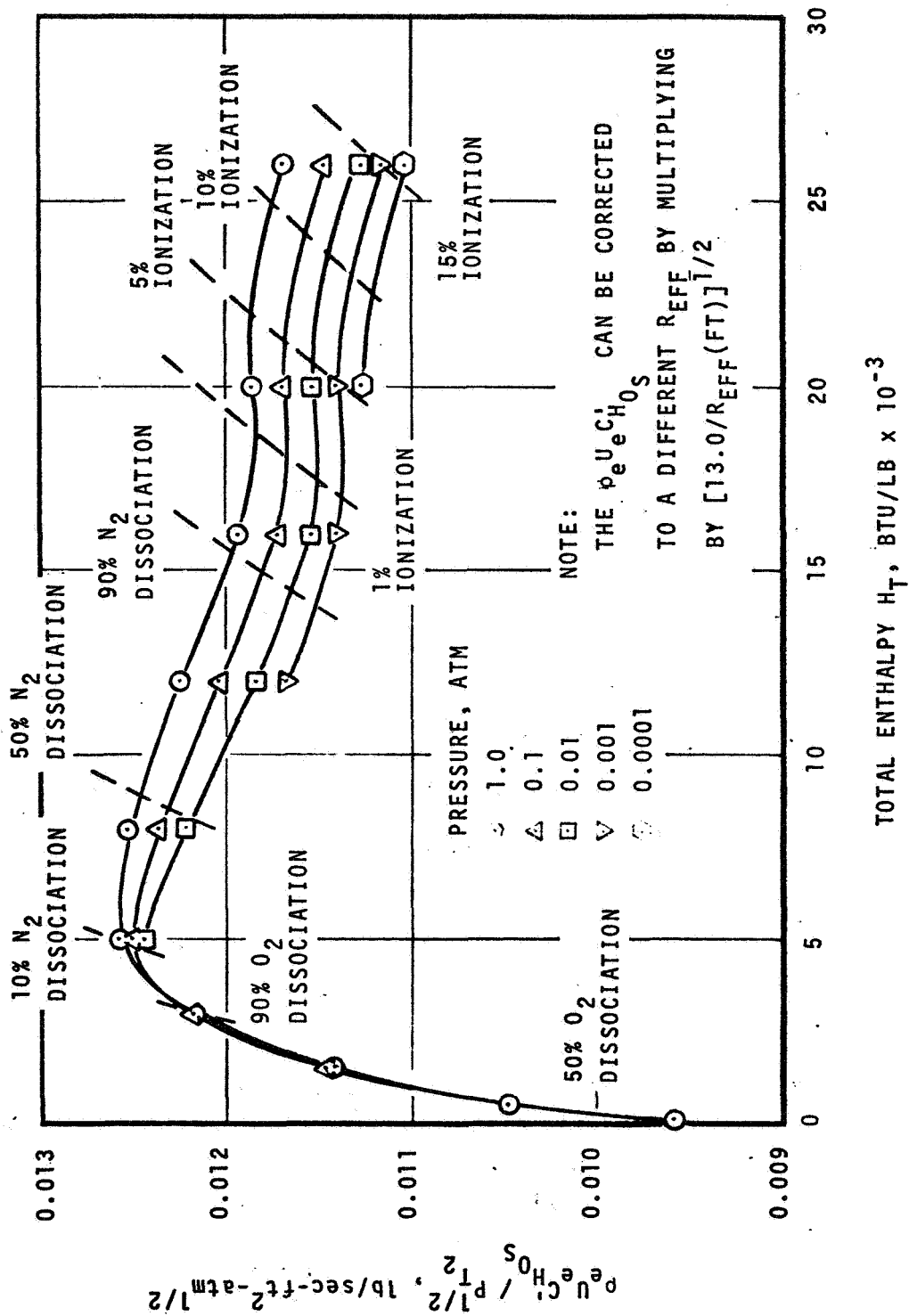


Figure 10. Nonablating Heat-Transfer Coefficient to Axisymmetric Stagnation Point: $R_{eff} = 13.0 \text{ Ft}$, $T_w = 2000^\circ\text{R}$

TABLE 6

WALL TEMPERATURE CORRECTION FOR NONABLATING
STAGNATION-POINT HEAT-TRANSFER COEFFICIENT

Total Enthalpy, Btu/lb	$\rho_e U_e C_{H_0}' / \rho_e U_e C_{H_0}'$ for T_w ($^{\circ}\text{R}$) of			
	500	2000	4000	6000
$P_{T_2} = 1.0 \text{ ATM}$				
26,000	--	1.000	0.989	0.965
20,000	--	↓	0.986	0.960
16,000	--	↓	0.989	0.965
12,000	1.006	↓	0.989	0.962
8,000	1.006	↓	0.994	0.967
5,000	1.004	↓	1.001	0.977
3,000	1.001	↓	1.011	1.003
1,500	--	↓	1.013	1.042
$P_{T_2} = 0.1 \text{ ATM}$				
26,000	--	1.000	0.989	0.959
20,000	--	↓	0.985	0.947
16,000	--	↓	0.985	0.945
12,000	1.005	↓	0.989	0.942
8,000	1.006	↓	0.994	0.941
5,000	1.003	↓	1.001	0.940
3,000	1.001	↓	1.016	0.956
1,500	--	↓	1.030	1.016
$P_{T_2} = 0.01 \text{ ATM}$				
26,000	--	1.000	0.989	0.954
20,000	--	↓	0.984	0.937
16,000	--	↓	0.984	0.933
12,000	1.004	↓	0.989	0.932
8,000	1.006	↓	0.993	0.928
5,000	1.001	↓	0.999	0.914
$P_{T_2} = 0.001 \text{ ATM}$				
26,000	--	1.000	0.985	0.951
20,000	--	↓	0.983	0.934
16,000	--	↓	0.982	0.926
12,000	--	↓	0.983	0.929
$P_{T_2} = 0.0001 \text{ ATM}$				
26,000	--	1.000	0.982	0.947
20,000	--	↓	0.970	0.931

ORIGINAL PAGE IS
OF POOR QUALITY

$$\frac{C'_{H_{O_S}}}{C'_{H_{O_S}} @ 2000^{\circ}R} = \begin{cases} 1.007 - 0.0035 \left(\frac{T_W}{1000} \right) & T_W \leq 2000^{\circ}R \\ 1.001 + 0.0025 \left(\frac{T_W}{1000} \right) - 0.0015 \left(\frac{T_W}{1000} \right)^2 & T_W \geq 2000^{\circ}R \end{cases} \quad (15)$$

This yields the following results

$T_W (^{\circ}R)$	$C'_{H_{O_S}} / C'_{H_{O_S}} @ 2000^{\circ}R$
500	1.005
1,000	1.003
2,000	1.000
3,000	0.995
4,000	0.987
5,000	0.976
6,000	0.962

3.2.2 Laminar Nonsimilar Boundary Layer

Laminar nonsimilar air boundary-layer solutions were generated for several representative flight conditions using the BLIMP program with the axisymmetric analogy. Solutions were generated for the leeward and windward pitch plane rays about Apollo at 25° angle of attack with a uniform wall temperature of 2000°R. The resulting convective heat-transfer coefficients $\rho_e U_e C'_{H_{O_S}}$ normalized by the zero-incidence stagnation-point values $\rho_e U_e C'_{H_{O_S}}$ are tabulated in Table 7 and presented graphically in Figure 11. Results obtained for typical wind-tunnel test conditions are also shown in Table 7 and Figure 11 for comparison. It can be seen that the solutions at flight conditions are nearly indistinguishable from each other but tend to be somewhat higher than the wind-tunnel results at positions far removed from the stagnation point. The ratio of flight to wind-tunnel heat-transfer coefficients is presented in Figure 12 for the 25° solutions and a 33° solution. It can be seen that the correction is less than about 5 percent on the aft heat shield but becomes 20 percent on the conical afterbody and 25 to 40 percent on the toroid.

Recalling from Section 3.1 that the wind-tunnel BLIMP predictions agree well with experimental wind-tunnel data and, hence, the NASA/MSC convective

TABLE 7
NONABLATING LAMINAR HEAT-TRANSFER COEFFICIENT DISTRIBUTIONS
ABOUT APOLLO AT 25° INCIDENCE

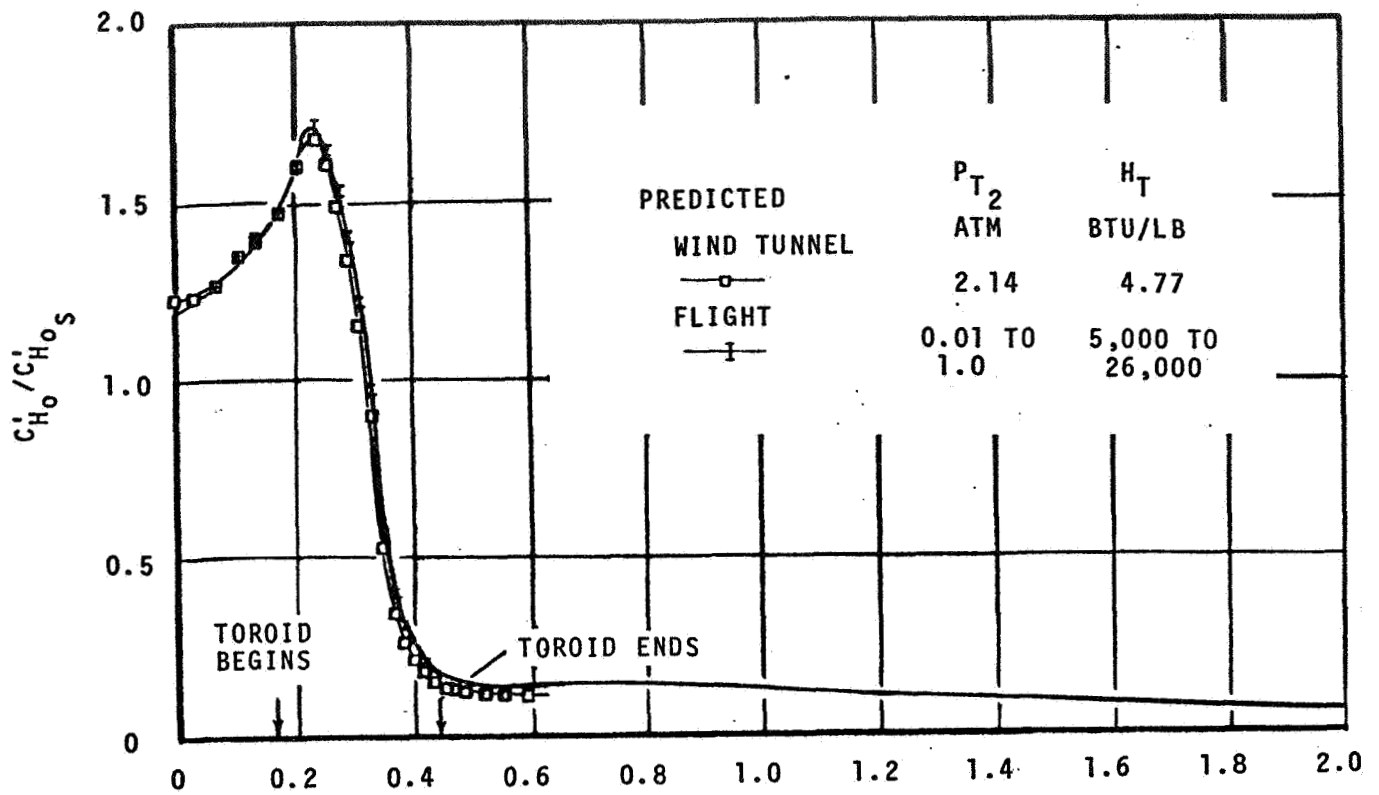
(a) Windward Side

S/R	Heat-Transfer Coefficient $\rho_e U_e^2 CH_o'$ Normalized by Zero-Incidence Stagnation Point Value				
	Wind Tunnel	Flight Conditions			
	477 Btu/lb. 2.14 Atm	20,000 Btu/lb 1.0 Atm	26,000 Btu/lb 0.01 Atm	20,000 Btu/lb 0.01 Atm	12,000 Btu/lb 0.01 Atm
.000	1.225	1.212	1.211	1.212	1.217
.035	1.238	1.242	1.240	1.241	1.246
.069	1.270	1.265	1.262	1.263	1.271
.104	1.354	1.351	1.347	1.348	1.359
.139	1.390	1.404	1.400	1.401	1.412
.173	1.476	1.462	1.458	1.459	1.473
.208	1.599	1.608	1.600	1.605	1.626
.242	1.678	1.710	1.696	1.702	1.730
.260	1.604	1.642	1.632	1.641	1.662
.277	1.483	1.531	1.522	1.531	1.549
.294	1.335	1.397	1.388	1.398	1.412
.312	1.147	1.213	1.204	1.217	1.229
.329	.901	.972	.965	.974	.983
.346	.536	.598	.598	.603	.600
.364	.352	.411	.412	.414	.409
.381	.266	.315	.317	.319	.315
.398	.211	.251	.253	.254	.251
.416	.176	.212	.214	.215	.212
.433	.153	.186	.189	.189	.187
.450	.139	.170	.172	.172	.171
.468	.126	.159	.161	.161	.161
.485	.121	.151	.152	.152	.152
.519	.117	.142	.144	.144	.144
.554	.114	.140	.142	.141	.142
.589	.113	.140	.142	.141	.142
.623		.142	.144	.142	.143
.686		.146	.148	.147	.146
.757		.146	.149	.147	.146
.976		.134	.136	.135	.132
1.194		.116	.118	.117	.114
1.621		.091	.093	.091	.090
1.989		.064	.065	.064	.064

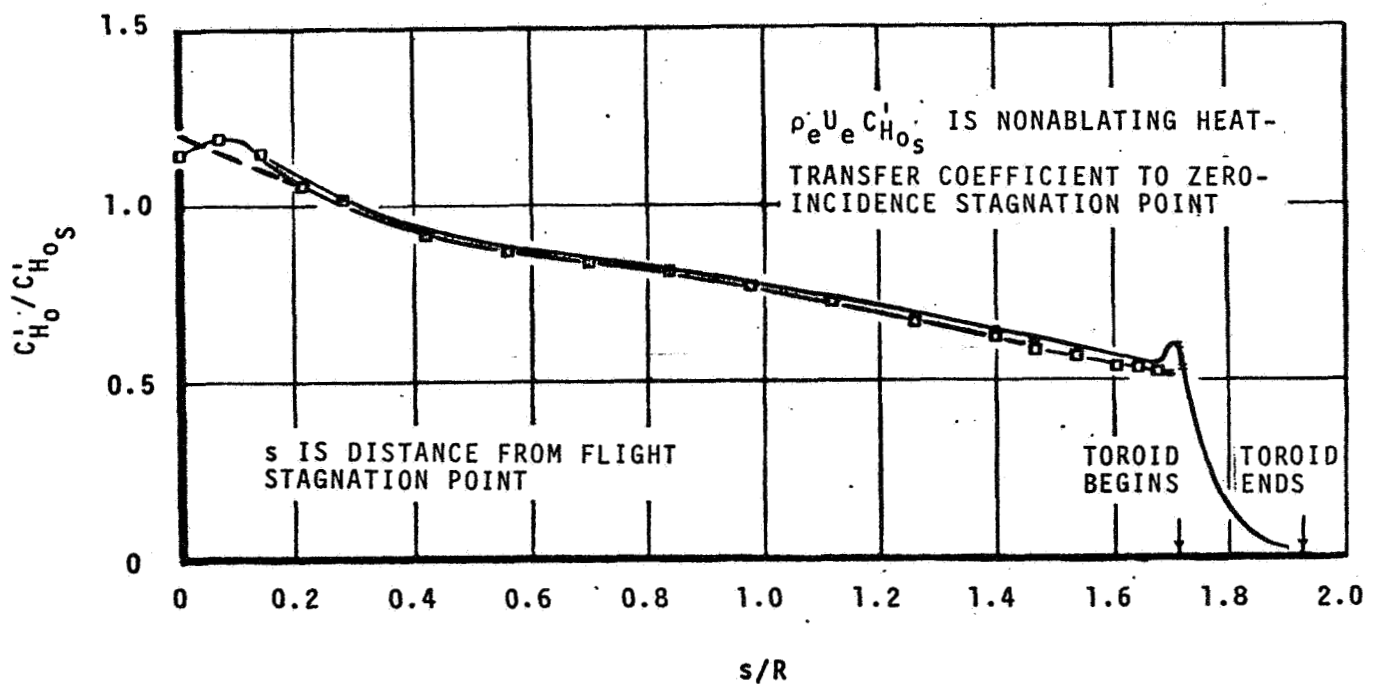
TABLE 7 (CONCLUDED)

(b) Leeward Side

S/R	Heat-Transfer Coefficient h_{e, CH_4} Normalized by Zero-Incidence Stagnation Point Value				
	Wind Tunnel	Flight Conditions			
	477 Btu/lb 2.14 Atm	20,000 Btu/lb 1.0 Atm	26,000 Btu/lb 0.01 Atm	20,000 Btu/lb 0.01 Atm	12,000 Btu/lb 0.01 Atm
.000	1.140	1.081	1.080	1.080	1.082
.069	1.191	1.184	1.182	1.181	1.189
.138	1.152	1.156	1.155	1.155	1.159
.208	1.059	1.078	1.078	1.078	1.076
.277	1.016	1.031	1.030	1.029	1.029
.415	.917	.927	.926	.926	.925
.554	.877	.888	.887	.887	.887
.692	.841	.851	.850	.851	.852
.830	.812	.821	.819	.821	.823
.969	.770	.785	.783	.785	.788
1.107	.722	.740	.738	.740	.741
1.246	.674	.693	.690	.694	.695
1.384	.623	.644	.641	.645	.647
1.453	.587	.618	.615	.621	.622
1.522	.574	.594	.592	.596	.598
1.591	.548	.569	.566	.570	.573
1.626	.536	.559	.556	.560	.564
1.661	.525	.546	.543	.548	.555
1.678	.525	.505	.503	.506	.507
1.695	.526	.598	.601	.598	.615
1.703		.538	.546	.537	.555
1.727		.372	.379	.371	.381
1.744		.274	.279	.275	.279
1.775		.168	.170	.170	.169
1.805		.092	.098	.098	.096
1.814		.062	.064	.064	.062
1.842		.037	.038	.038	.036
1.873		.027	.029	.028	.027



a. Windward Side



b. Leeward Side

Figure 11. Predicted Laminar Nonablating Heat-Transfer Coefficient Around Apollo at 25° Angle of Attack

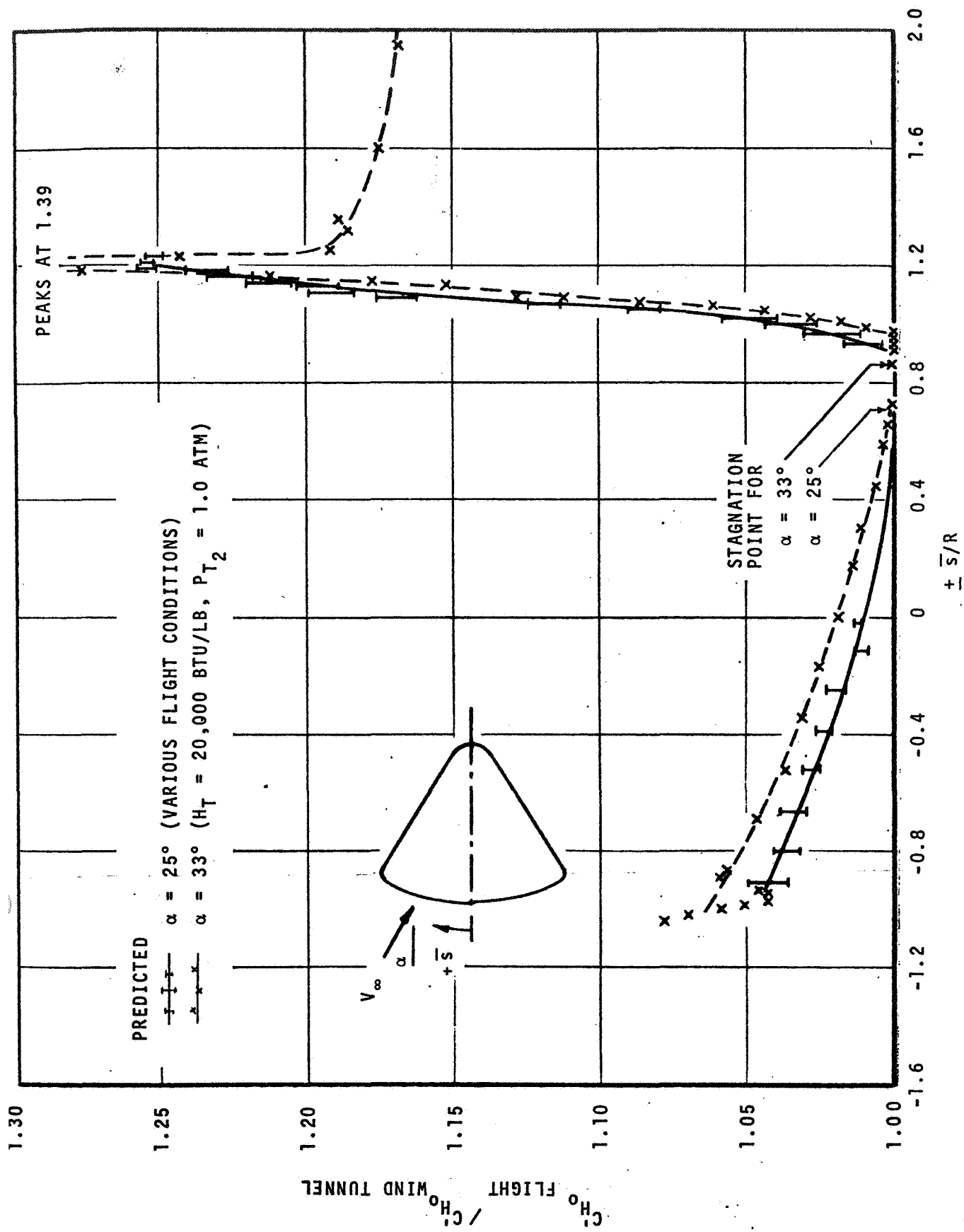


Figure 12. Ratio of Predicted Heat-Transfer Coefficients for Flight and Wind-Tunnel Conditions

heating factors, it can be concluded that these factors can be applied to flight provided they are corrected using Figure 12.

The laminar boundary-layer solutions also yield values for momentum thickness Reynolds numbers, Re_{θ_0} , which are useful for establishing boundary-layer transition criteria. The Re_{θ_0} are presented in Figure 13 normalized by $\sqrt{P_{T_2}}$ for 25° and 33° angles of attack, total enthalpies of 5,000 to 26,000 Btu/lb, and stagnation pressures of 0.01 and 1.0 atm. The results are seen to fall into a reasonably narrow band on the windward and leeward sides. Note that the Re_{θ_0} continues to increase in going around the toroid on the windward side even though the boundary layer is rapidly accelerating. The reason for this is that the momentum thickness θ increases faster than the unit Reynolds number decreases. This is demonstrated in Table 8 for the windward ray, 25°, 20,000 Btu/lb, 1.0 atm case.

3.2.3 Turbulent Nonsimilar Boundary Layer

Solutions were also generated for the air laminar/turbulent boundary layer around the windward and leeward pitch plane rays of Apollo at 25° incidence with a uniform wall temperature of 2000°R. Transition to turbulent flow was assumed to occur at an Re_{θ_0} of 200. Solutions were generated for a stagnation pressure of 1.0 atm with stagnation enthalpies of 20,000, 12,000, and 5,000 Btu/lb. The turbulent model which is employed in the BLIMP program is described in Reference 24 and summarized briefly in Appendix A. It is basically an eddy viscosity approach with the mixing length obtained from the solution of an ordinary differential equation between the wall and the local position in the boundary layer. Transition to turbulent flow is considered to be instantaneous to the extent that the fully turbulent transport properties are employed when the critical Re_{θ_0} is exceeded; however, there is a brief transitional period due to the nonsimilar effect of the upstream laminar boundary layer.

Convective heat-transfer coefficients $\rho_e U_e C_{H_0}$ are presented in Table 9 ratioed by the laminar stagnation point values $\rho_e U_e C_{H_{0s}}$. For these flight conditions and assumed critical Re_{θ_0} , transition is seen to occur in the toroidal region on the windward side and shortly before the geometric center of the aft heat shield on the leeward side. Of course, transition would be delayed for reduced pressures and higher critical Re_{θ_0} and vice versa.

The normalized turbulent heat-transfer coefficients tend to be fairly independent of flight conditions by two or three stations after transition. Since the laminar heat-transfer coefficients were also seen to be independent of flight conditions (see Table 7), it would seem appropriate to correlate the turbulent heating results in terms of local laminar values and the distance

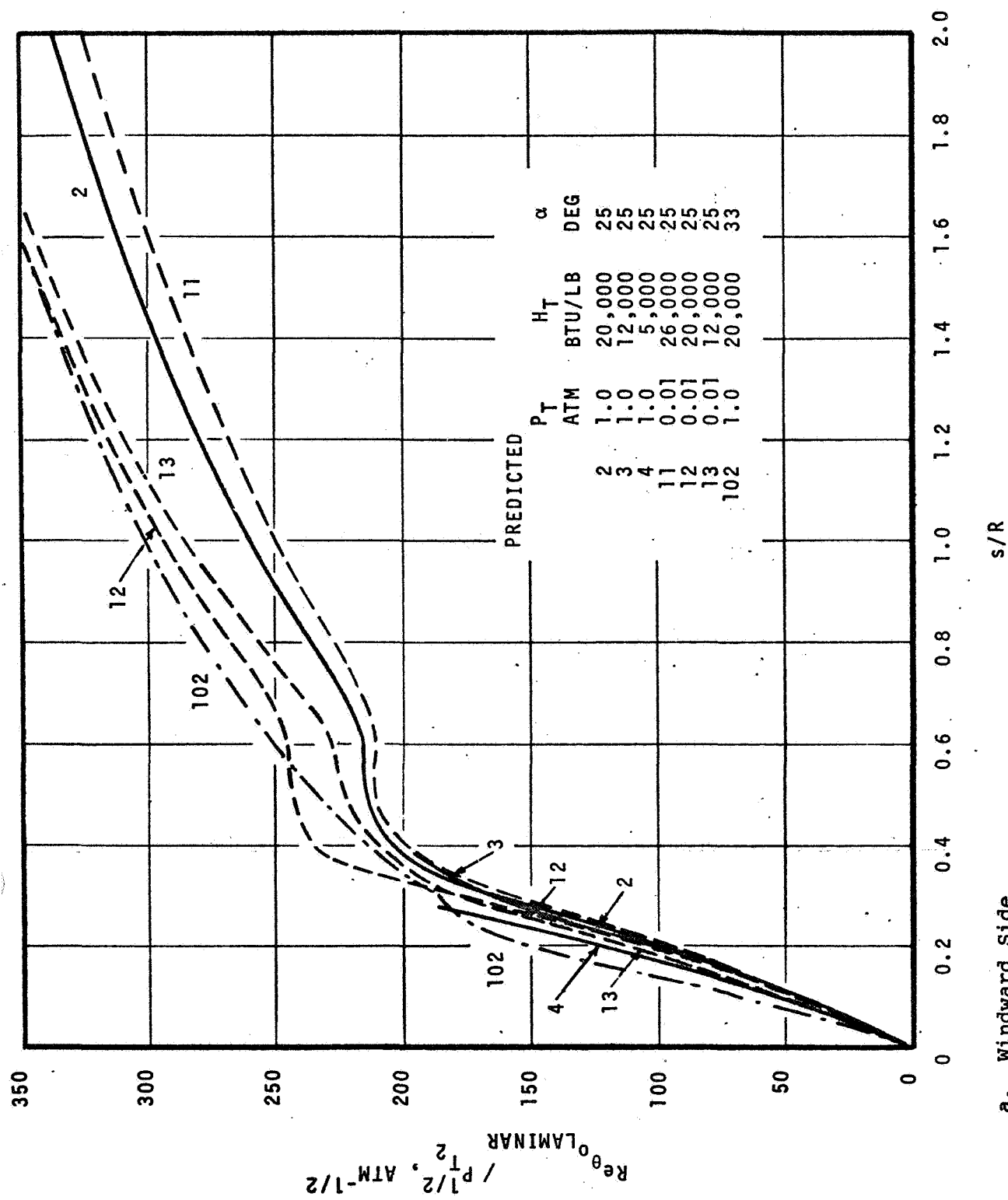
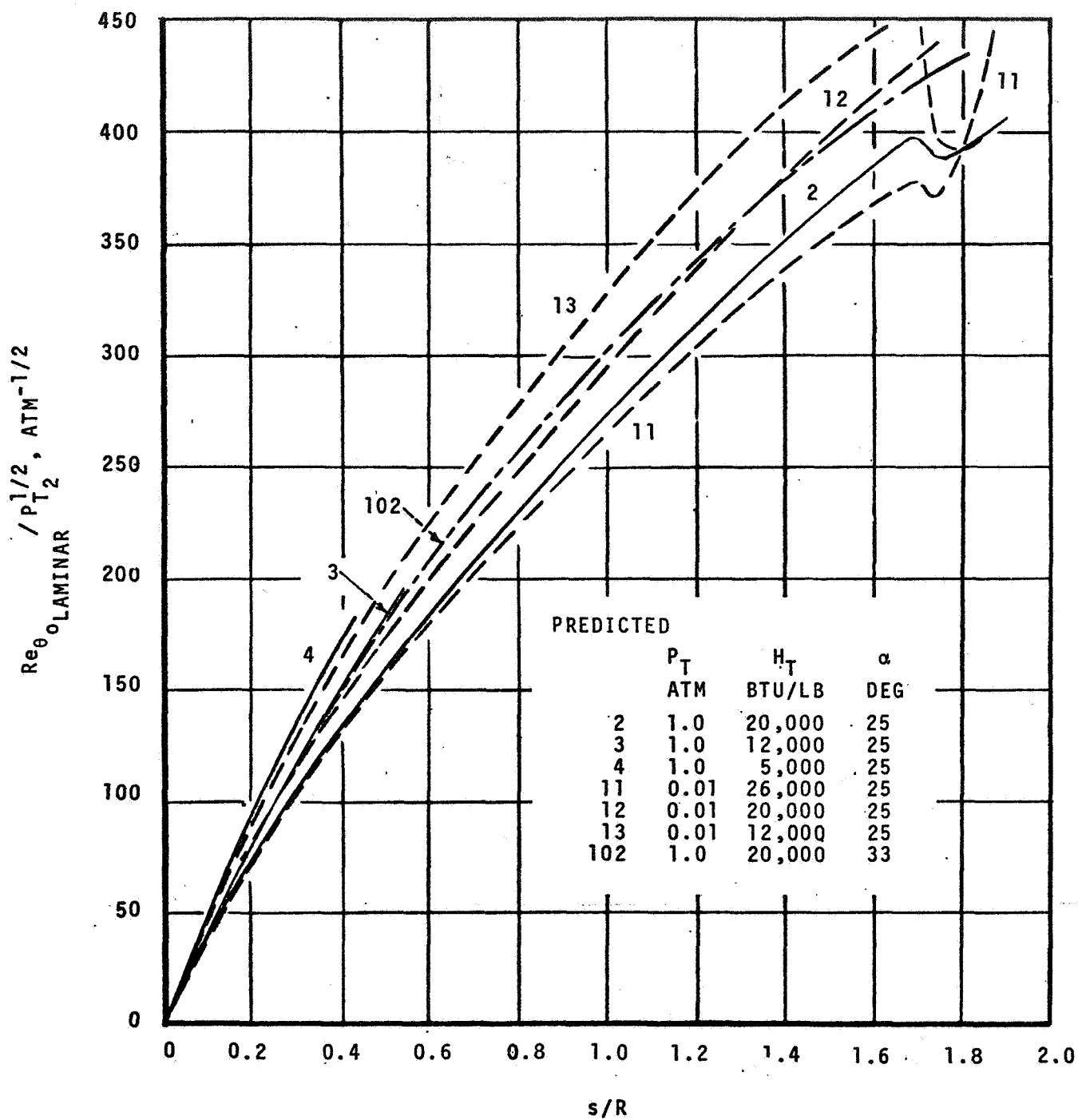


Figure 13. Momentum Thickness Reynolds Numbers for Laminar Air Boundary Layer About Apollo at Incidence



b. Leeward Side

Figure 13. Concluded

TABLE 8

PARAMETERS ASSOCIATED WITH THE MOMENTUM THICKNESS REYNOLDS NUMBER
ABOUT THE WINDWARD SIDE OF APOLLO AT 25° INCIDENCE:
 $H_T = 20,000 \text{ BTU/LB}$, $P_{T_2} = 1.0 \text{ ATM}$

S/R	Local Boundary-Layer Edge Properties					Momentum Thickness $\theta_o \times 10^2$	Re_{θ_o}
	Mach Number	Density $\times 10^4$	Velocity $\times 10^{-4}$	Viscosity $\times 10^4$	Re per $\text{foot}^{-1/4}$ $\times 10^{-4}$		
.000	.000	10.990	.000	1.164	.000	.396	.0
.035	.046	10.980	.040	1.164	.379	.387	14.7
.069	.095	10.940	.083	1.164	.781	.381	29.8
.104	.157	10.860	.137	1.162	1.277	.357	45.6
.139	.230	10.710	.200	1.160	1.850	.342	63.3
.173	.314	10.460	.274	1.157	2.476	.330	81.7
.208	.453	9.930	.392	1.149	3.390	.299	101.4
.242	.679	8.770	.581	1.129	4.513	.276	124.6
.260	.820	7.940	.693	1.114	4.948	.279	138.0
.277	.952	7.140	.795	1.097	5.176	.291	150.6
.294	1.117	6.140	.915	1.073	5.239	.311	162.9
.312	1.322	5.000	1.052	1.043	5.042	.345	173.9
.329	1.613	3.620	1.224	1.002	4.418	.413	182.5
.346	2.052	2.060	1.449	.948	3.150	.606	190.9
.364	2.293	1.452	1.561	.922	2.458	.803	197.4
.381	2.451	1.137	1.631	.907	2.045	.989	202.3
.398	2.595	.901	1.691	.893	1.707	1.204	205.5
.416	2.688	.771	1.729	.884	1.508	1.379	208.0
.433	2.755	.688	1.756	.878	1.376	1.525	209.8
.450	2.799	.638	1.774	.874	1.294	1.635	211.6
.468	2.831	.604	1.786	.872	1.237	1.720	212.8
.485	2.856	.578	1.796	.870	1.194	1.791	213.8
.519	2.873	.561	1.802	.868	1.164	1.849	215.2
.554	2.873	.561	1.802	.868	1.164	1.855	215.9
.589	2.865	.569	1.799	.869	1.179	1.834	216.2
.623	2.848	.587	1.792	.870	1.208	1.806	218.2
.686	2.815	.621	1.780	.873	1.265	1.771	224.0
.757	2.799	.638	1.774	.874	1.294	1.793	232.0
.976	2.806	.631	1.776	.874	1.282	2.022	259.2
1.194	2.853	.581	1.794	.870	1.199	2.350	281.8
1.621	2.949	.491	1.831	.862	1.043	3.019	314.9
1.989	3.150	.340	1.904	.845	.767	4.315	331.0

TABLE 9

NONABLATING LAMINAR/TURBULENT HEAT-TRANSFER COEFFICIENT
DISTRIBUTIONS ABOUT APOLLO AT 25° INCIDENCE: $P_{T_2} = 1.0$ ATM

(a) Windward Side

S/R*	Heat-Transfer Coefficient $\rho U C_{H_0}'$ Normalized by Zero-Incidence Stagnation Point Value*		
	20,000 Btu/lb	12,000 Btu/lb	5,000 Btu/lb
.000	1.212	1.207	1.208
.035	1.242	1.236	1.237
.069	1.265	1.261	1.262
.104	1.351	1.347	1.347
.139	1.404	1.400	1.399
.173	1.462	1.460	1.459
.208	1.608	1.610	1.604
.242	1.710	1.710	1.697
.260	1.642	1.645	1.626
.277	1.531	1.532	1.510
.294	1.397	1.396	3.955
.312	1.213	1.212	3.845
.329	.972	.967	3.111
.346	.598	.593	1.910
.364	.411	.406	1.347
.381	.782	.313	1.053
.398	.744	.650	.839
.416	.680	.645	.715
.433	.625	.611	.635
.450	.585	.579	.586
.468	.557	.553	.552
.485	.534	.531	.527
.519	.518	.515	.508
.554	.517	.513	.506
.589	.523	.519	.512
.623	.534	.531	.525
.686	.555	.552	.548
.757	.560	.558	.558
.976	.533	.531	.536
1.194	.478	.477	.482
1.621	.390	.391	.396
1.989	.272	.273	.275

*Transition indicated by horizontal line.

TABLE 9 (CONCLUDED)

(b) Leeward Side

S/R*	Heat-Transfer Coefficient $\rho_e U_e C_{H_0}$ Normalized by Zero-Incidence Stagnation Point Value*		
	20,000 Btu/lb	12,000 Btu/lb	5,000 Btu/lb
.000	1.081	1.075	1.076
.069	1.184	1.180	1.180
.138	1.156	1.149	1.150
.208	1.078	1.069	1.071
.277	1.031	1.021	1.022
.415	.927	.918	.919
.554	.888	.881	2.812
.692	2.841	2.791	3.073
.830	3.059	3.003	3.224
.969	3.164	3.093	3.304
1.107	3.165	3.100	3.320
1.246	3.111	3.059	3.293
1.384	3.014	2.970	3.217
1.453	2.951	2.911	3.161
1.522	2.875	2.839	3.089
1.591	2.781	2.749	2.994
1.626	2.727	2.699	2.936
1.661	2.646	2.624	2.849
1.678	2.540	2.518	2.738
1.695	2.635	2.616	2.808
1.703	2.285	2.272	2.409
1.727	1.602	1.605	1.667
1.744	1.180	1.184	1.219
1.775	.729	.732	
1.805	.406	.387	
1.814	.263		

* Transition indicated by horizontal line.

from the point of transition. This is done in Figure 14. The results are seen to collapse quite accurately into two curves, one for the leeward side with transition on the aft heat shield and one for the windward side with transition in the toroidal region. While these results are encouraging, further solutions are needed to obtain wide applicability. Furthermore, the turbulent model employed in the BLIMP code had not been validated for hypersonic boundary layers prior to the present study (some degree of validation is established in the flight predictions presented in Section 6.2).

3.3 MASS-TRANSFER CORRELATIONS

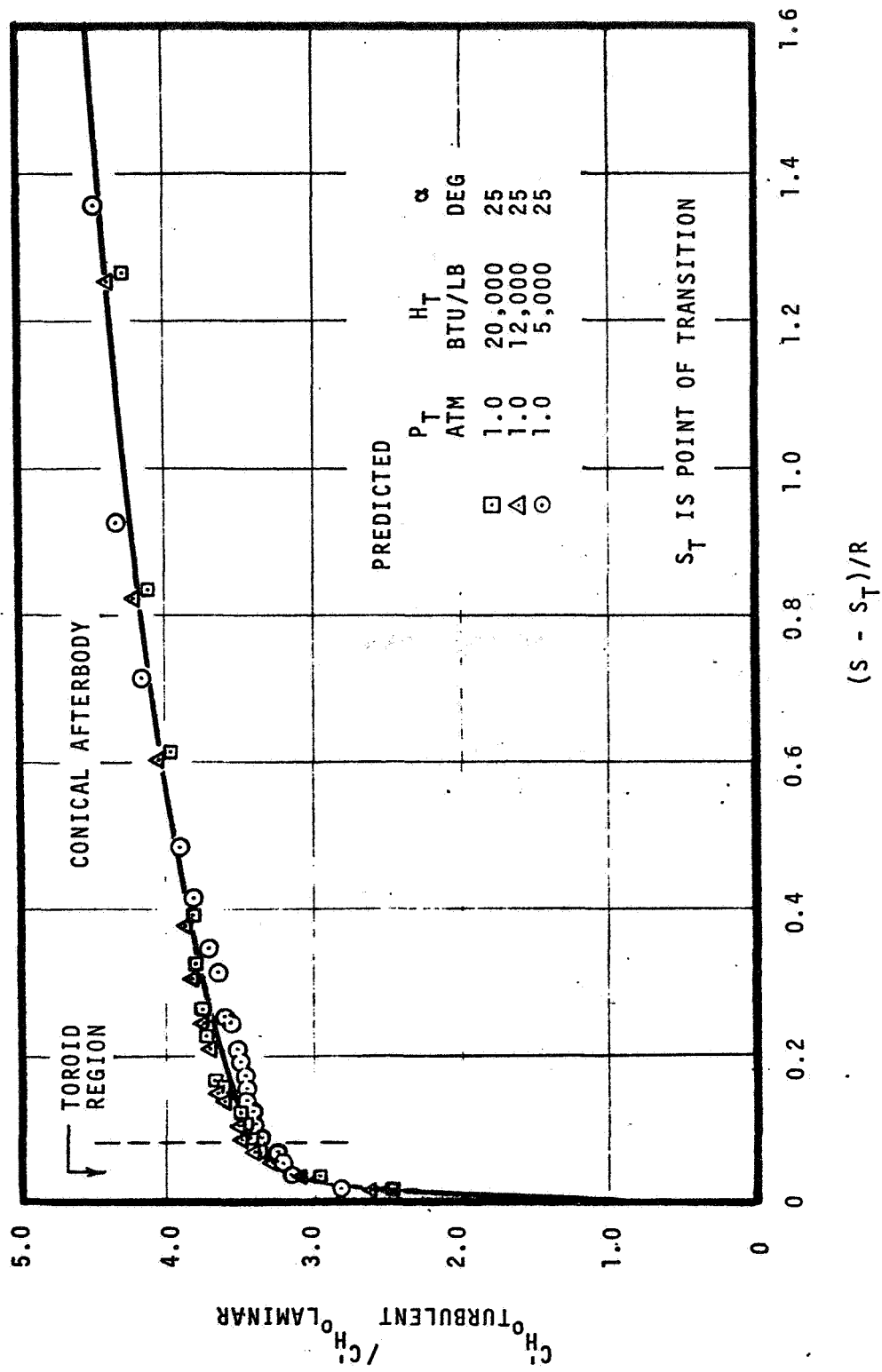
A study has been conducted to obtain correlations of unequal diffusion ~~coefficients~~ ^{boundary layer solutions} including effects of mass addition of chemically-active gases appropriate to Apollo heat-shield material ablation. The approach which has been taken is to correlate stagnation point blowing corrections for a wide range of flight conditions, and then to obtain corrections to these blowing corrections for positions away from the stagnation point for laminar and turbulent flow. The stagnation-point correlations are presented in Section 3.3.1. The laminar and turbulent corrections are then presented in Sections 3.3.2 and 3.3.3, respectively.

3.3.1 Stagnation Point

a. Background

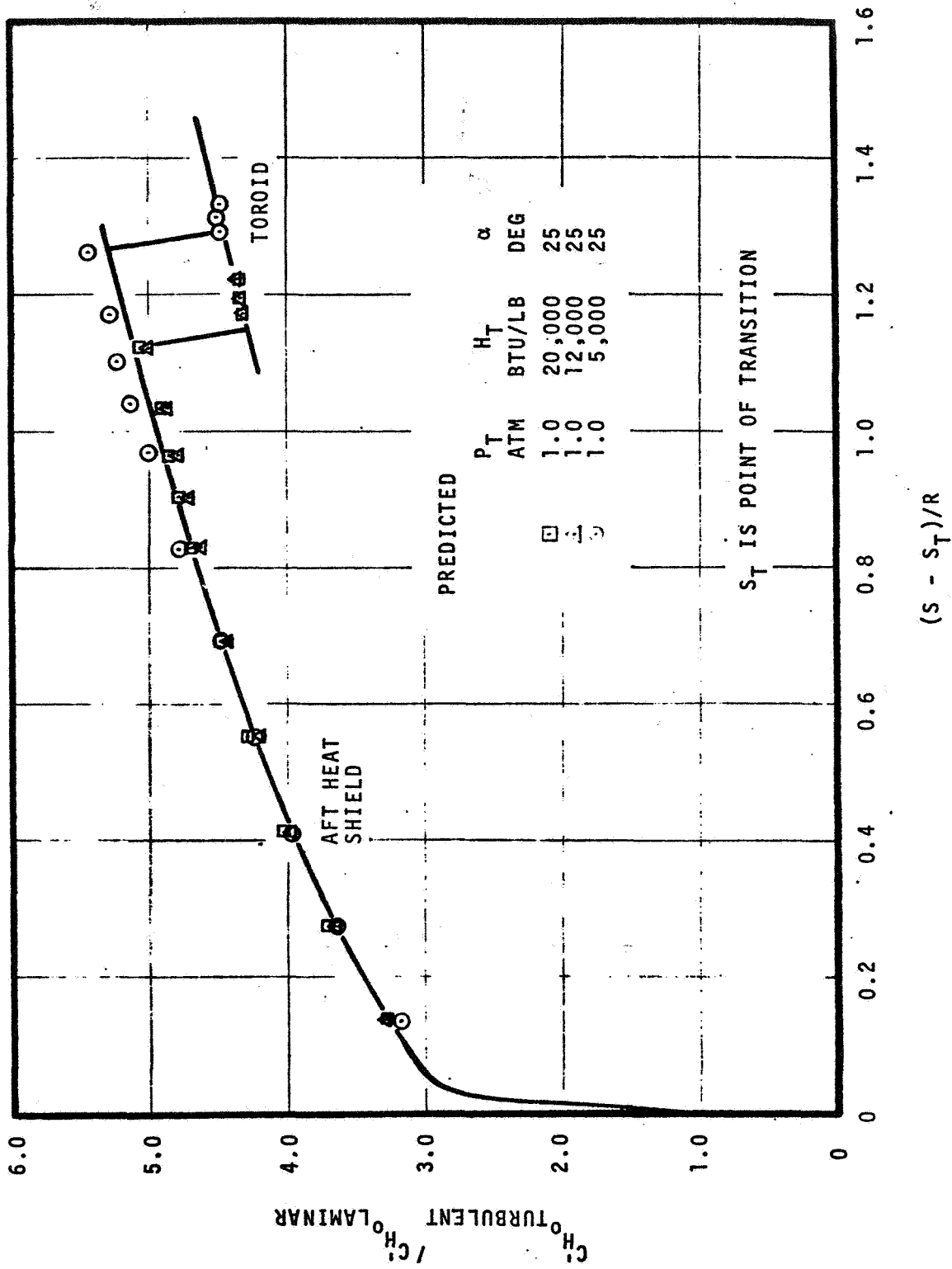
Heat- and mass-transfer coefficient approaches have proven to be very useful for correlating theoretical as well as experimental heat- and mass-transfer results for nonreacting boundary-layer flows. They also have been used with success to correlate the results of chemically-reacting air boundary-layer calculations. Techniques which have worked well for these simplified flows have been applied extensively to flow situations involving chemically-reacting boundary layers over ablating bodies. This approach was bred of necessity since it has only been recently that boundary-layer solution procedures with general-chemistry and ablating-surface-boundary-condition capabilities such as BLIMP have become available. The recent advent of such codes might make further use of transfer-coefficient approaches seem unnecessary. However, they are still extremely useful as a basis for correlating boundary-layer solution data to avoid the necessity for coupling the boundary-layer procedure to a transient in-depth conduction procedure.

A transfer-coefficient approach for chemically active boundary layers over ablating surfaces including unequal diffusion effects was postulated in



a. Windward Side, Aft of Toroid

Figure 14. Ratio of Turbulent to Laminar Nonablating Heat Transfer Coefficients for Apollo at Incidence



b. Leeward Side, Aft Heat Shield and Toroid

Figure 14. Concluded

Reference 28. This procedure was recently evaluated on the basis of solutions generated with the BLIMP chemically-reacting boundary-layer procedure^{29,30}.

There were two aspects of the transfer-coefficient approach which were of primary concern. The first, not fundamentally required but an integral part of the Reference 28 approach, has to do with the ability of the procedure to assimilate unequal-diffusion effects within the framework of a single mass-transfer coefficient without introducing unacceptably large errors. The second was with regard to the simplicity and generality with which the resulting heat- and mass-transfer coefficients can be correlated in terms of such parameters as non-ablating heat-transfer coefficients, Lewis number, and blowing corrections.

Boundary-layer solutions were considered for steady-state ablation of graphite and a typical reinforced plastic under ballistic reentry conditions. In these calculations, the boundary layer was fully coupled with the ablative material response; the wall boundary condition satisfying the elemental mass balances, a steady-state energy balance, and surface equilibrium. Thus, the solutions were representative of a class of reentry problems that one might want to solve using the unequal-diffusion film-transport formulation. In addition, boundary-layer solutions were considered for a variety of assigned injection rate problems over a wide range of injectant molecular weight.

It was demonstrated in References 29 and 30 that the use of a single mass-transfer coefficient is quite accurate for predicting such quantities as ablation rates and surface temperatures using transfer coefficients obtained directly from boundary-layer solution data. With regard to the ability to correlate the resulting transfer coefficients, the results were highly encouraging. A tentative approach was recommended which was believed to be a substantial improvement over previous practices, but it was recognized that a greater body of boundary-layer solution data would have to be considered before any final conclusions could be drawn. In the present study solutions have been generated and correlated for Apollo material ablation over a wide range of flight conditions representative of orbital and superorbital reentry.

The approach introduced in Reference 28 and investigated in Reference 29 correlates diffusive mass fluxes, \tilde{j}_{k_w} , in the following form

$$\tilde{j}_{k_w} = \rho_e U_e C_{M_k} (\tilde{z}_{k_w}^* - \tilde{z}_{k_e}^*) \quad (16)$$

where $\rho_e U_e C_{M_k}$ is an elemental mass-transfer coefficient, \tilde{z}_k^* is defined as

$$\tilde{z}_k^* = \sum_i \alpha_{ki} \tilde{z}_i^* \quad \tilde{z}_i^* = \frac{z_i^Y \cdot K_i^{1-Y}}{\sum_j z_j^Y \cdot K_j^{1-Y}} \quad (17)$$

the subscripts w and e refer to the wall and boundary layer edge, α_{ki} is the mass fraction of element k in species i, K_i is the mass fraction of species i, Z_i is defined by

$$Z_i = \frac{K_i/F_i}{\sum_j K_j/F_j} \quad (18)$$

F_i is the "diffusion factor" for species i obtained from a correlation of binary diffusion coefficients, \mathcal{D}_{ij} , in accordance with the relation*

$$\mathcal{D}_{ij} \approx \bar{D}/F_i F_j \quad (19)$$

\bar{D} is a reference diffusion coefficient, and γ is a weighting parameter which can be selected arbitrarily.

A primary purpose for introducing the \tilde{Z}_k^* potential was to attempt to reduce the $\rho_e U_e C_{M_k}$ to a single $\rho_e U_e C_M$ in unequal-diffusion similar** boundary-layer problems through appropriate choice of the γ weighting parameter. A γ of 0 corresponds to $\tilde{Z}_k^* = \tilde{K}_k$ and would be expected to be appropriate for problems where convection dominates, while a value of $\gamma = 1$ corresponds to $\tilde{Z}_k^* = \tilde{Z}_k$ and would be expected to be appropriate when diffusive processes dominate (e.g., Couette flow). Based on analogy with the relative magnitudes of conductive and convective terms in the energy equation, a value of γ of 2/3 was recommended in Reference 28 for boundary layer flows. It was demonstrated in References 29 and 30 that a γ of 2/3 while not precise was indeed appropriate and that the errors in such quantities as ablation rates and surface temperatures are negligible if the individual $\rho_e U_e C_{M_k}$ are averaged on the basis of the absolute values of the sums of the \tilde{j}_{k_w} divided by the absolute values of the sums of the \tilde{Z}_k^* driving potentials

*The accuracy of this correlation in representing the individual \mathcal{D}_{ij} was investigated in Reference 28 where it was shown to be satisfactory as long as elastic collisions dominate the transport processes.

**In nonsimilar boundary-layer problems, the $\rho_e U_e C_{M_k}$ will differ in general even for assumed equal diffusion coefficients if there are more than two effective components, namely if the elemental composition of the edge gas or injected material varies with streamwise position.

$$\rho_e U_e C_M = \frac{\sum_k |\rho_e U_e C_{M_k} (\tilde{z}_{k_w}^* - \tilde{z}_{k_e}^*)|}{\sum_k |\tilde{z}_{k_w}^* - \tilde{z}_{k_e}^*|} = \frac{\sum_k |\tilde{j}_{k_w}|}{\sum_k |\tilde{z}_{k_w}^* - \tilde{z}_{k_e}^*|} \quad (20)$$

A relation for expressing the surface convective heat flux q_w in terms of $\rho_e U_e C_M$, a heat-transfer coefficient $\rho_e U_e C_H$, and appropriate driving potentials was also introduced in Reference 28 and evaluated in Reference 29.* In particular, it was shown that if chemical reactions are confined to the wall the q_w could logically be expressed as

$$q_w = \rho_e U_e C_H \left[(H_r - h_b)_{fe} + \sum_i K_{i_w} \int_{T_w}^{T_b} C_{p_i} dT \right] + \rho_e U_e C_M \sum_i (z_{i_e}^* - z_{i_w}^*) h_{i_b} \quad (21)$$

where H_r is the recovery enthalpy, h_b is the gas enthalpy evaluated at a base temperature T_b which divides the energy flux into convective and diffusive terms, the subscript fe refers to a frozen edge state, and C_{p_i} and h_i are the specific heat and enthalpy of species i . The degree of success of this correlation is dependent upon whether simple and accurate correlations for $\rho_e U_e C_H$ can be found. For example, when Equation (21) was originally introduced, it was suggested for lack of anything better that $\rho_e U_e C_H$ might be related to $\rho_e U_e C_M$ through a Chilton-Colburn type relation

$$C_M/C_H = (Le)^{2/3} \quad (22)$$

for chemically-reacting as well as frozen boundary layers, where Le is a system Lewis number defined in Reference 29. It was seen in Reference 29 that Equation (21) is inaccurate for large mass-injection rates, especially when chemical reactions take place between injected species and boundary-layer edge species. One can, therefore, either devise more elaborate correlation expressions than Equation (22) or seek an alternative expression to Equation (21) for correlating surface heat fluxes. For example, it was shown in Reference 29 that it might be

*The q_w as defined in this report includes conduction and diffusion effects and does not include convection associated with mass addition into the boundary layer - it is the same as the q_a of Reference 9. Furthermore, it includes solid and gas phase combustion effects; hence no "heat of combustion" correction is needed.

appropriate to define a heat-transfer coefficient (identified as $\rho_e U_e C_H'$ to distinguish it from the $\rho_e U_e C_H$ of Equation (21)) on the basis of an equilibrium enthalpy potential*

$$q_w = \rho_e U_e C_H' (H_e - h_w) \quad (23)$$

where H_e is the total enthalpy at the edge of the boundary layer and h_w is the enthalpy of the gas mixture adjacent to the wall. Note that Equation (23) is a direct generalization of Equation (14) to include mass-transfer effects. The Apollo material studies conducted in the present effort indeed suggest that Equation (23) is superior to Equation (21) for the present purpose. This will be demonstrated in Section 3.3.1d below.

b. Boundary Layer Solutions

A matrix of unequal diffusion BLIMP solutions was generated over a wide range of flight conditions for the stagnation-point (zero incidence) boundary layer over ablating Apollo heat-shield material while satisfying surface equilibrium and a steady-state surface energy balance. Surface ablation rate and surface temperature as well as convective heating rate are calculated during the course of the solution with this approach. Flight conditions considered cover the range of H_T of 26,000 to 5,000 Btu/lb and P_{T_2} of 1.0 to 0.0001 atm. Various incident radiation heating rates were assigned in these problems: these fluxes were considered to pass unattenuated through the boundary layer but to enter into the surface energy balance. Solutions were also generated for several flight conditions for assigned surface temperatures and assigned pyrolysis gas rates. Both moderate and high pyrolysis gas rates were considered. The composition of the pyrolysis gas was considered to be a function of surface temperature consistent with the coking model to be discussed in Section 5.1. Although energy balances were not satisfied in these latter solutions, a surface equilibrium requirement was retained; hence, char recession rates and convective heating rates were calculated during the course of these solutions as well. In all, a total of 72 boundary-layer solutions was generated, and all of these have been considered in the heat- and mass-transfer correlations presented in the sections which follow.

The basic boundary-layer solution results are presented in Tables 10a and 10b for the steady-state and high pyrolysis gas injection rate cases, respectively. Included in this tabulation, in addition to the flight conditions of stagnation pressure, stagnation enthalpy, and incident radiation flux, are the surface temperature, the diffusive heat flux to the wall q_w , the char

*The use of an equilibrium potential for chemically-reacting boundary layers was suggested by Spaulding in Reference 31.

TABLE 10
STAGNATION-POINT ABLATION CHARACTERISTICS OF APOLLO HEAT-SHIELD MATERIAL
(a) Steady-State Ablation

H_T Btu/lb	P Atm	q_r Btu/ sec ft ²	T_w °R	q_w Btu/ sec ft ²	$\dot{m}_c \times 10^3$ lb/ sec ft ²	$\dot{m}_g \times 10^3$ lb/ sec ft ²	h_w Btu/lb	m_w	m_w/m_e	$Le_w^{2/3}$
26000.	1.0000	0.	5217.	236.20	1.8569	2.0891	1167.0	24.73	1.902	.8394
26000.	1.0000	250.	5992.	175.50	3.2400	3.6450	3266.0	23.13	1.779	.7949
26000.	.1000	0.	3988.	79.53	.5096	.5734	405.4	25.28	1.984	.8539
26000.	.1000	90.	4782.	74.52	.5355	.6025	916.9	24.83	1.949	.8397
26000.	.0100	0.	3009.	25.63	.1561	.1757	35.5	25.19	2.010	.8522
26000.	.0100	22.	3499.	24.96	.1555	.1749	216.5	25.30	2.019	.8550
26000.	.0010	0.	2263.	8.18	.0491	.0553	-210.6	25.12	2.034	.8526
26000.	.0001	0.	1696.	2.57	.0154	.0174	-391.4	25.18	2.064	.8589
20000.	1.0000	0.	4947.	190.80	1.7939	2.0181	934.8	24.76	1.745	.8386
20000.	1.0000	250.	5894.	144.20	2.8616	3.2194	2784.0	23.28	1.641	.7993
20000.	1.0000	300.	5994.	128.60	3.4108	3.8372	3452.0	22.69	1.599	.7840
20000.	1.0000.	350.	6055.	107.70	4.2456	4.7764	4157.0	21.92	1.545	.7665
20000.	1.0000	400.	6125.	94.15	5.1059	5.7441	4990.0	21.34	1.504	.7540
20000.	1.0000	450.	6134.	71.37	6.4659	7.2741	5736.0	20.13	1.419	.7323
20000.	.1000	0.	3774.	63.75	.5148	.5792	318.8	25.03	1.787	.8450
20000.	.1000	35.	4197.	62.67	.5224	.5876	531.1	24.80	1.770	.8371
20000.	.0100	0.	2844.	20.45	.1584	.1782	-18.8	25.01	1.806	.8465
20000.	.0100	15.	3257.	20.26	.1592	.1791	126.5	24.99	1.804	.8446
20000.	.0010	0.	2137.	6.50	.0495	.0557	-249.2	25.05	1.827	.8509
20000.	.0001	0.	1603.	2.05	.0155	.0174	-415.6	25.12	1.850	.8578
16000.	1.0000	0.	4718.	157.90	1.7544	1.9736	786.2	24.61	1.604	.8326
16000.	1.0000	65.	5103.	151.40	1.8513	2.0827	1095.0	24.39	1.590	.8274
16000.	.1000	0.	3582.	51.71	.5148	.5792	232.9	24.94	1.660	.8421
16000.	.1000	20.	3874.	50.89	.5186	.5834	353.8	24.97	1.662	.8430
16000.	.0100	0.	2698.	16.54	.1592	.1791	-78.8	24.94	1.689	.8446
16000.	.0100	4.	2843.	16.43	.1588	.1786	-28.9	24.96	1.690	.8448
16000.	.0010	0.	2025.	5.22	.0496	.0559	-296.4	25.05	1.717	.8517
12000.	1.0000	0.	4450.	124.90	1.7515	1.9705	614.0	24.62	1.409	.8321
12000.	.1000	0.	3379.	40.91	.5224	.5876	150.0	24.76	1.448	.8365
12000.	.0100	0.	2548.	13.13	.1619	.1821	-136.1	24.77	1.474	.8396
12000.	.0010	0.	1915.	4.17	.0506	.0570	-340.2	24.86	1.499	.8462
8000.	1.0000	0.	4080.	88.15	1.7440	1.9620	411.2	24.70	1.209	.8339
8000.	.1000	0.	3107.	29.18	.5308	.5972	38.6	24.61	1.229	.8324
8000.	.0100	0.	2350.	9.45	.1662	.1870	-219.1	24.63	1.249	.8361
5000.	1.0000	0.	3648.	56.20	1.6885	1.8995	227.8	24.76	1.068	.8363
5000.	.1000	0.	2792.	18.91	.5256	.5914	-78.2	24.71	1.082	.8368
5000.	.0100	0.	2122.	6.23	.1658	.1865	-302.3	24.76	1.099	.8417

TABLE 10 (CONCLUDED)
(b) Simulated Transient Ablation (High Pyrolysis Gas Rates)

H_T Btu/lb	P Atm	q_r Btu/ sec ft ²	T_w °R	q_w Btu/ sec ft ²	$\dot{m}_c \times 10^3$ lb/ sec ft ²	$\dot{m}_g \times 10^3$ lb/ sec ft ²	h_w Btu/lb	m_w	m_w/m_e	$Le_w^{2/3}$
20000.	1.0000	0.	4500.	197.90	1.7115	1.9255	644.4	24.95	1.758	.8432
20000.	1.0000	0.	4500.	178.00	1.3548	5.1612	774.5	20.59	1.451	.7293
20000.	1.0000	0.	4500.	123.70	.6212	11.6088	1114.0	14.85	1.047	.6574
20000.	1.0000	0.	4500.	110.60	.3718	14.4182	1314.0	13.13	.925	.6497
20000.	1.0000	0.	4500.	99.42	.2165	16.2435	1453.0	12.29	.866	.6485
20000.	1.0000	0.	4500.	85.41	.1176	18.1324	1554.0	11.75	.828	.6486
20000.	1.0000	0.	5400.	180.20	1.9722	2.2188	1438.0	24.26	1.710	.8257
20000.	1.0000	0.	5400.	158.30	1.3718	5.7342	1982.0	20.27	1.428	.7282
20000.	1.0000	0.	5400.	129.90	.7802	9.2598	2440.0	17.38	1.225	.6832
20000.	1.0000	0.	6134.	66.15	6.8235	7.6765	5886.0	19.86	1.400	.7280
20000.	1.0000	0.	6134.	59.93	7.2941	8.2059	6066.0	19.55	1.378	.7231
20000.	1.0000	0.	6134.	54.48	7.7647	8.7353	6230.0	19.26	1.357	.7187
20000.	1.0000	0.	6134.	49.95	8.2353	9.2647	6381.0	18.98	1.338	.7147
20000.	1.0000	0.	6134.	46.42	8.7059	9.7941	6523.0	18.71	1.319	.7108
20000.	1.0000	0.	6134.	43.81	9.1765	10.3235	6653.0	18.44	1.300	.7072
20000.	1.0000	0.	6134.	40.64	9.8824	11.1176	6822.0	18.08	1.274	.7025
20000.	1.0000	0.	6134.	36.37	10.5882	11.9118	6947.0	17.78	1.253	.6985
20000.	.0100	0.	2702.	20.51	.1583	.1780	-66.7	25.02	1.806	.8473
20000.	.0100	0.	2700.	19.77	.0729	.4184	-112.5	22.47	1.622	.7738
20000.	.0100	0.	2700.	15.19	.0000	1.0090	40.7	17.90	1.292	.7136
20000.	.0100	0.	3600.	20.05	.1605	.1806	263.6	24.96	1.802	.8427
20000.	.0100	0.	3600.	17.90	.1275	.4846	264.4	20.91	1.510	.7350
20000.	.0100	0.	3600.	12.48	.0654	1.0966	381.7	15.18	1.096	.6601
12000.	1.0000	0.	4499.	124.40	1.7595	1.9795	640.0	24.63	1.410	.8324
12000.	1.0000	0.	4500.	113.90	1.3520	5.2600	786.7	20.11	1.151	.7206
12000.	1.0000	0.	4500.	79.60	.5788	11.8712	1153.0	14.43	.826	.6549
12000.	1.0000	0.	5400.	110.80	2.0541	2.3109	1496.0	23.78	1.361	.8109
12000.	1.0000	0.	5400.	99.20	1.3845	5.9215	2083.0	19.62	1.123	.7164
12000.	1.0000	0.	5400.	82.03	.7492	9.5708	2550.0	16.80	.962	.6763
5000.	1.0000	0.	2702.	58.95	1.6715	1.8805	-110.4	24.82	1.071	.8406
5000.	1.0000	0.	2700.	57.17	.7374	4.3816	-161.7	22.18	.957	.7671
5000.	1.0000	0.	2700.	42.97	.0000	10.6600	278.9	17.32	.747	.7213
5000.	1.0000	0.	3604.	56.34	1.6861	1.8969	211.1	24.76	1.068	.8363
5000.	1.0000	0.	3600.	52.53	1.2965	5.0415	203.3	20.39	.880	.7262
5000.	1.0000	0.	3600.	37.34	.6165	11.4435	337.8	14.59	.629	.6584

removal rate \dot{m}_c , the pyrolysis gas rate \dot{m}_g (equal to $1.125 \dot{m}_c$ for steady-state ablation)*, the wall gas enthalpy, the molecular weight of the gas at the wall M_w , the ratio of wall to edge-gas molecular weight M_w/M_e , and the Lewis number of the gas at the wall Le_w raised to the $2/3$ power.

The transfer-coefficient results are presented in Tables 11a and 11b for the steady-state and high pyrolysis gas injection rate cases, respectively. Included in this tabulation are:

- The nonablating heat-transfer coefficient $\rho_e U_e C'_{H_0}$, defined by Equation (14) and obtained from interpolation of the results presented in Section 3.2.1.
- The mass-transfer coefficient $\rho_e U_e C_M$, defined implicitly by Equation (16) with $\gamma = 2/3$ and with the individual $\rho_e U_e C_{Mk}$ averaged using Equation (20)
- The heat-transfer coefficient $\rho_e U_e C'_H$, defined by Equation (23)
- The heat-transfer coefficient $\rho_e U_e C_H$, defined implicitly by Equation (21) with wall temperature selected to be the base temperature T_b
- The blowing parameter B'_0 , defined by

$$B'_0 \equiv \dot{m} / \rho_e U_e C'_{H_0} \quad (24)$$

where \dot{m} is the total mass flux injected into the boundary layer $\dot{m}_g + \dot{m}_c$

- The thermodynamic blowing parameter B' defined by

$$B' \equiv \dot{m} / \rho_e U_e C_M \quad (25)$$

- A mass-transfer coefficient blowing correction $\rho_e U_e C_M / \rho_e U_e C'_{H_0}$
- A heat-transfer coefficient blowing correction $\rho_e U_e C'_H / \rho_e U_e C'_{H_0}$
- A heat-transfer coefficient Lewis number correlation, $\rho_e U_e C_M / \rho_e U_e C_H (Le_w)^{2/3}$

These mass- and heat-transfer coefficient results are discussed and correlated in the following two sections.

* In steady-state ablation 18 lb/sec ft² of pyrolysis gas are generated for every 16 lb/sec ft² of char recession consistent with the pyrolysis decomposition model that 34 lb of virgin material decomposes into 18 lb of pyrolysis gas and 16 lb of char (see Section 5.1).

TABLE 11
STAGNATION-POINT HEAT- AND MASS-TRANSFER COEFFICIENTS FOR APOLLO HEAT-SHIELD MATERIAL
(a) Steady-State Ablation

H_T Btu/lb	P Atm	$\rho_e U_e C_{H_2O}$ $\times 10^3$ lb/ sec ft ²	$\rho_e U_e C_M$ $\times 10^3$ lb/ sec ft ²	$\rho_e U_e C_{H_2O}^1$ $\times 10^3$ lb/ sec ft ²	$\rho_e U_e C_H$ $\times 10^3$ lb/ sec ft ²	B'_O	B'	$\frac{C_M}{C_{H_2O}}$	$\frac{C_H^1}{C_{H_2O}}$	$\frac{C_M/C_H}{Le_w^{2/3}}$
26000.	1.0000	11.4000	8.5550	9.5140	12.4800	.346	.461	.750	.835	.817
26000.	1.0000	11.2800	6.1190	7.7200	12.6200	.610	1.125	.542	.684	.610
26000.	.1000	3.5860	2.8170	3.1070	4.0200	.302	.384	.786	.866	.821
26000.	.1000	3.5700	2.7550	2.9710	3.8360	.319	.413	.772	.832	.855
26000.	.0100	1.1220	.8876	.9872	1.3230	.296	.374	.791	.880	.787
26000.	.0100	1.1190	.8884	.9680	1.2530	.295	.372	.794	.865	.829
26000.	.0010	.3518	.2787	.3122	.4354	.297	.375	.792	.887	.751
26000.	.0001	.1107	.0877	.0975	.1370	.296	.374	.792	.881	.745
20000.	1.0000	11.5500	8.6580	10.0100	14.4500	.330	.440	.750	.867	.714
20000.	1.0000	11.4100	6.7250	8.3730	14.4800	.533	.904	.589	.734	.581
20000.	1.0000	11.3900	5.8230	7.7720	14.5600	.636	1.245	.511	.682	.510
20000.	1.0000	11.3800	5.0830	6.7970	12.8700	.793	1.775	.447	.597	.515
20000.	1.0000	11.3700	3.8200	6.2730	13.5000	.954	2.840	.336	.552	.375
20000.	1.0000	11.3700	2.6140	5.0030	11.4100	1.208	5.256	.230	.440	.313
20000.	.1000	3.6550	2.8190	3.2390	4.6110	.299	.388	.771	.886	.724
20000.	.1000	3.6400	2.7800	3.2190	4.7400	.305	.399	.764	.884	.701
20000.	.0100	1.1470	.8939	1.0220	1.4560	.293	.377	.779	.891	.725
20000.	.0100	1.1440	.8886	1.0190	1.4820	.296	.381	.777	.891	.710
20000.	.0010	.3599	.2833	.3208	.4561	.292	.371	.787	.891	.730
20000.	.0001	.1134	.0899	.1005	.1413	.291	.367	.793	.886	.742
16000.	1.0000	11.7000	8.6650	10.3800	16.2600	.319	.430	.741	.887	.640
16000.	1.0000	11.6500	8.4750	10.1600	16.4600	.338	.464	.727	.872	.622
16000.	.1000	3.6700	2.7740	3.2800	5.1700	.298	.394	.756	.894	.637
16000.	.1000	3.6560	2.7710	3.2530	5.1320	.301	.398	.758	.890	.641
16000.	.0100	1.1500	.8722	1.0290	1.6690	.294	.388	.758	.895	.619
16000.	.0100	1.1480	.8733	1.0250	1.6550	.294	.386	.761	.893	.625
16000.	.0010	.3610	.2764	.3204	.5135	.292	.382	.766	.888	.632
12000.	1.0000	12.0400	8.7460	10.9700	16.5700	.309	.426	.726	.911	.634
12000.	.1000	3.7800	2.8000	3.4520	5.2330	.294	.396	.741	.913	.640
12000.	.0100	1.1810	.8619	1.0820	1.6790	.291	.390	.747	.916	.626
12000.	.0010	.3689	.2787	.3381	.5310	.292	.386	.755	.917	.620
8000.	1.0000	12.4400	8.7600	11.6200	16.2500	.298	.423	.704	.934	.646
8000.	.1000	3.9020	2.7650	3.6650	5.2530	.289	.408	.709	.939	.632
8000.	.0100	1.2210	.8716	1.1500	1.6800	.289	.405	.714	.942	.621
5000.	1.0000	12.5900	8.6740	11.7800	15.1800	.285	.414	.689	.936	.683
5000.	.1000	3.9660	2.7380	3.7240	4.8340	.282	.408	.690	.939	.677
5000.	.0100	1.2470	.8660	1.1760	1.5380	.283	.407	.694	.943	.669

TABLE 11 (CONCLUDED)

(b) Simulated Transient Ablation (High Pyrolysis Gas Rates)

H_T Btu/lb	P Atm	$\rho_e U_e \dot{C}_H$ $\times 10^3$ lb/ sec ft ²	$\rho_e U_e \dot{C}_M$ $\times 10^3$ lb/ sec ft ²	$\rho_e U_e \dot{C}_H'$ $\times 10^3$ lb/ sec ft ²	$\rho_e U_e \dot{C}_H$ $\times 10^3$ lb/ sec ft ²	B'_O	B'	$\frac{C_M}{C_H} \frac{CH_O}{CH_O}$	$\frac{C_M}{C_H} \frac{1}{le_w^{2/3}}$
20000.	1.0000	11.6300	8.8530	10.2300	14.4300	.313	.411	.761	.728
20000.	1.0000	11.6300	6.5410	9.2580	17.3000	.560	.989	.567	.522
20000.	1.0000	11.6300	2.9220	6.5470	16.9000	1.052	4.185	.251	.263
20000.	1.0000	11.6300	1.5980	5.9170	17.6600	1.272	9.255	.137	.139
20000.	1.0000	11.6300	1.0270	5.3600	16.8700	1.415	16.027	.088	.094
20000.	1.0000	11.6300	.6456	4.6300	15.0500	1.569	28.268	.056	.066
20000.	1.0000	11.4800	8.2660	9.7080	14.8600	.365	.507	.720	.674
20000.	1.0000	11.4800	6.2040	8.7870	17.4200	.619	1.145	.540	.489
20000.	1.0000	11.4800	4.1710	7.3990	17.4200	.875	2.407	.363	.350
20000.	1.0000	11.3700	2.3600	4.6870	10.7900	1.275	6.144	.208	.300
20000.	1.0000	11.3700	2.0500	4.3010	10.0400	1.363	7.561	.180	.282
20000.	1.0000	11.3700	1.7650	3.9570	9.3690	1.451	9.348	.155	.262
20000.	1.0000	11.3700	1.5010	3.6680	8.8310	1.539	11.659	.132	.238
20000.	1.0000	11.3700	1.2530	3.4440	8.4570	1.627	14.765	.110	.208
20000.	1.0000	11.3700	1.0160	3.2830	8.2420	1.715	19.193	.089	.174
20000.	1.0000	11.3700	.6899	3.0840	7.9920	1.847	30.439	.061	.123
20000.	1.0000	11.3700	.4401	2.7860	7.3780	1.979	51.125	.039	.085
20000.	.0100	1.1480	.8957	1.0220	1.4460	.293	.375	.780	.731
20000.	.0100	1.1480	.7760	.9828	1.6750	.428	.633	.676	.599
20000.	.0100	1.1480	.4164	.7753	1.9060	.879	2.423	.363	.306
20000.	.0100	1.1460	.8834	1.0160	1.5040	.299	.386	.775	.697
20000.	.0100	1.1400	.6843	.9072	1.7310	.537	.894	.600	.538
20000.	.0100	1.1400	.3196	.6360	1.7660	1.019	3.636	.280	.274
12000.	1.0000	12.0400	8.7360	10.9500	16.5900	.311	.428	.726	.633
12000.	1.0000	12.0400	6.2560	10.1600	21.5700	.549	1.057	.520	.402
12000.	1.0000	12.0400	2.5860	7.3390	21.0600	1.034	4.814	.215	.187
12000.	1.0000	11.9000	7.9780	10.5500	18.8500	.367	.547	.670	.522
12000.	1.0000	11.9000	5.7810	10.0000	23.7200	.614	1.264	.486	.340
12000.	1.0000	11.9000	3.7170	8.6800	23.7200	.867	2.776	.312	.232
5000.	1.0000	12.5800	8.8080	11.5300	13.8900	.282	.403	.700	.754
5000.	1.0000	12.5800	7.5060	11.0800	15.0900	.407	.682	.597	.648
5000.	1.0000	12.5800	3.5530	9.1020	15.1700	.847	3.000	.282	.325
5000.	1.0000	12.5900	8.6810	11.7600	15.1100	.285	.413	.690	.687
5000.	1.0000	12.5900	6.3910	10.9500	17.5400	.503	.992	.508	.502
5000.	1.0000	12.5900	2.6430	8.0110	16.0400	.958	4.563	.210	.250

c. Mass-Transfer Coefficient Correlations

Blowing correction curves are often expressed analytically in the form

$$C_M/C_{M_0} = \phi / (e^\phi - 1) \quad (26)$$

where

$$\phi \equiv 2\lambda_M B'_O C_M/C_{M_0} = 2\lambda_M \dot{m} / \rho_e U_e C_{M_0} \quad (27)$$

$\rho_e U_e C_{M_0}$ is a nonablating mass-transfer coefficient, and λ_M is a blowing reduction parameter determined from experiments or boundary-layer solution data. It was demonstrated in Reference 29 that convenient and satisfactory results can be obtained with this relation with the further simplification

$$\rho_e U_e C_{M_0} = \rho_e U_e C_{H_0}^i \quad (28)$$

The parameter λ_M for perfect correlation for the present boundary-layer solutions is presented in Figure 15 in terms of η_w/η_e . A single curve is drawn through the data points which has the form

$$\lambda_M = 0.141 \left(\frac{\eta_w}{\eta_e} \right)^2 - 0.820 \left(\frac{\eta_w}{\eta_e} \right) + 1.861 \quad (29)$$

Application of this correlation yields the variation of $C_M/C_{H_0}^i$ versus $B'_O = \dot{m} / \rho_e U_e C_{H_0}^i$ shown in Figure 16. Note the effect that decreased molecular weight ratio η_w/η_e has on increasing the blowing reduction for mass transfer.

The accuracy of the mass-transfer coefficient correlation of Equations (26) through (29) is demonstrated in Figure 17 which compares the values of $C_M/C_{H_0}^i$ obtained from the correlation to those obtained from the boundary-layer solutions. Errors in $C_M/C_{H_0}^i$ are seen to be typically less than two percent and usually less than one percent. Of course, the errors in $\rho_e U_e C_M$ become substantially larger as $C_M/C_{H_0}^i$ approaches zero, but this is not serious since $\rho_e U_e C_M$ itself is becoming small (relative to $\rho_e U_e C_{H_0}^i$). While additional parameters such as B'_O , \dot{m}_g/\dot{m}_c , H_T and T_w could probably be employed to improve this curve fit, the above correlation is sufficiently accurate that it has been adopted for the present application.

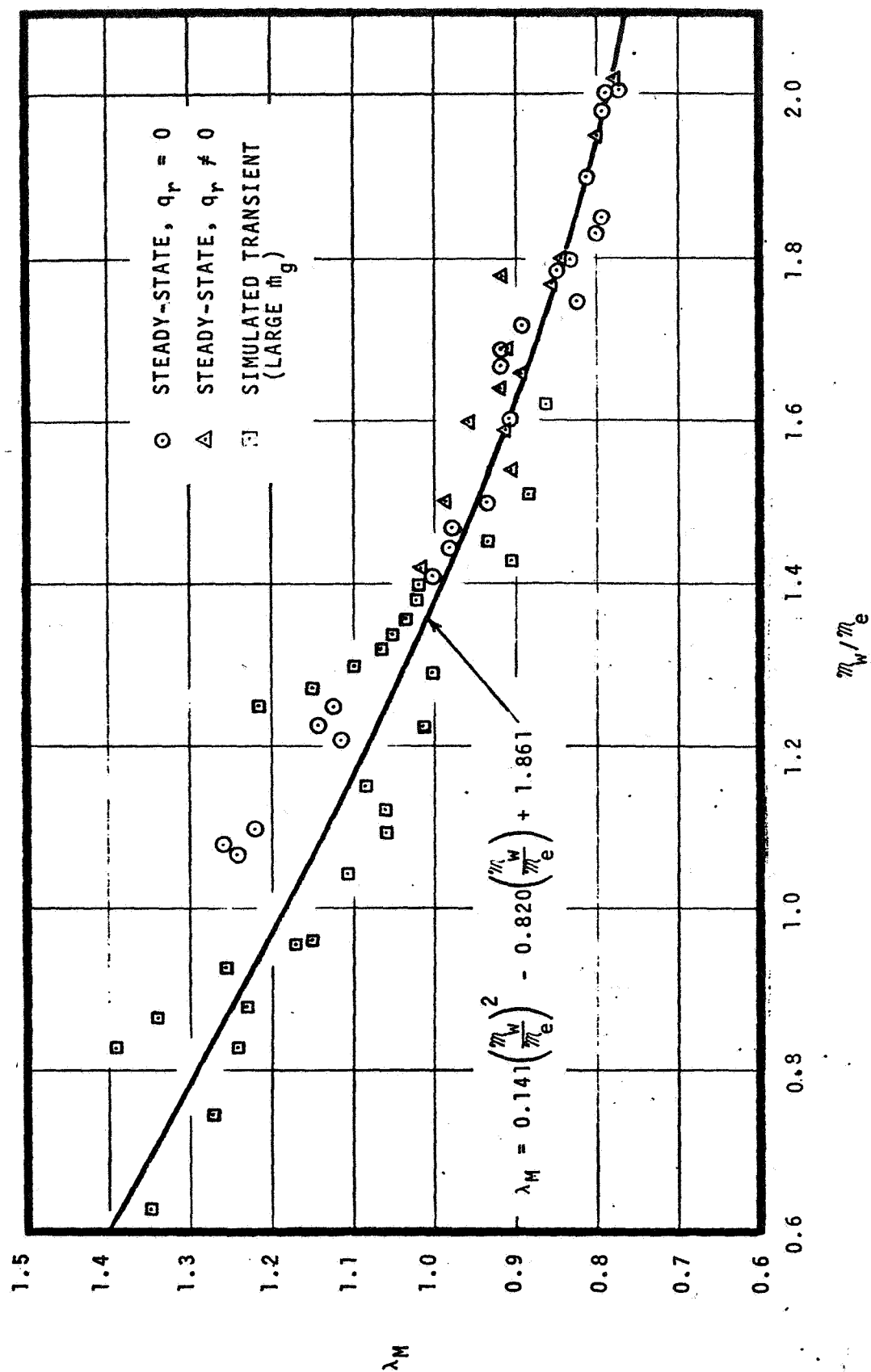


Figure 15. Mass-Transfer Coefficient Correlation for Apollo Material Ablation

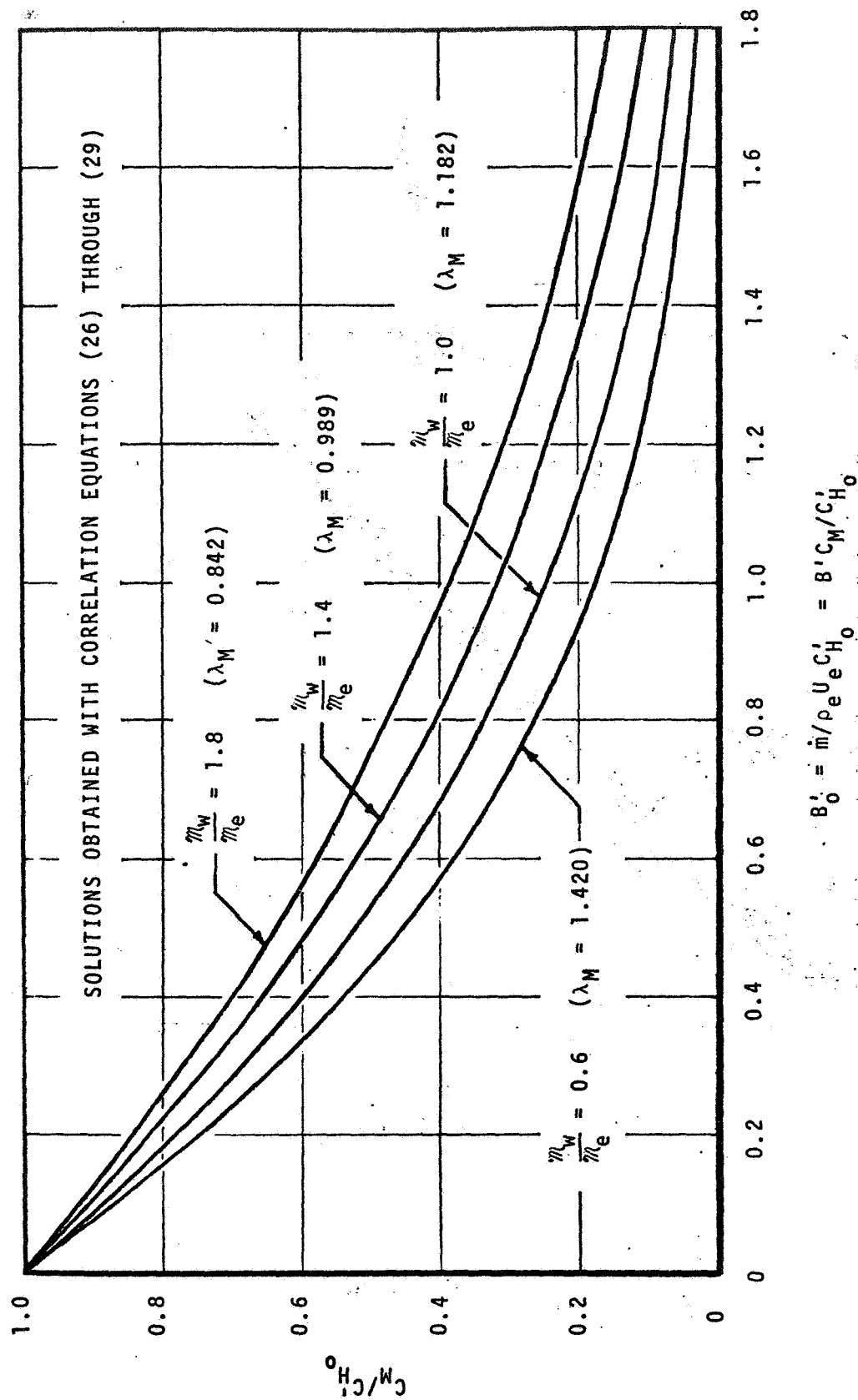


Figure 16. Mass-Transfer Coefficient Blowing Correction for the Apollo Material

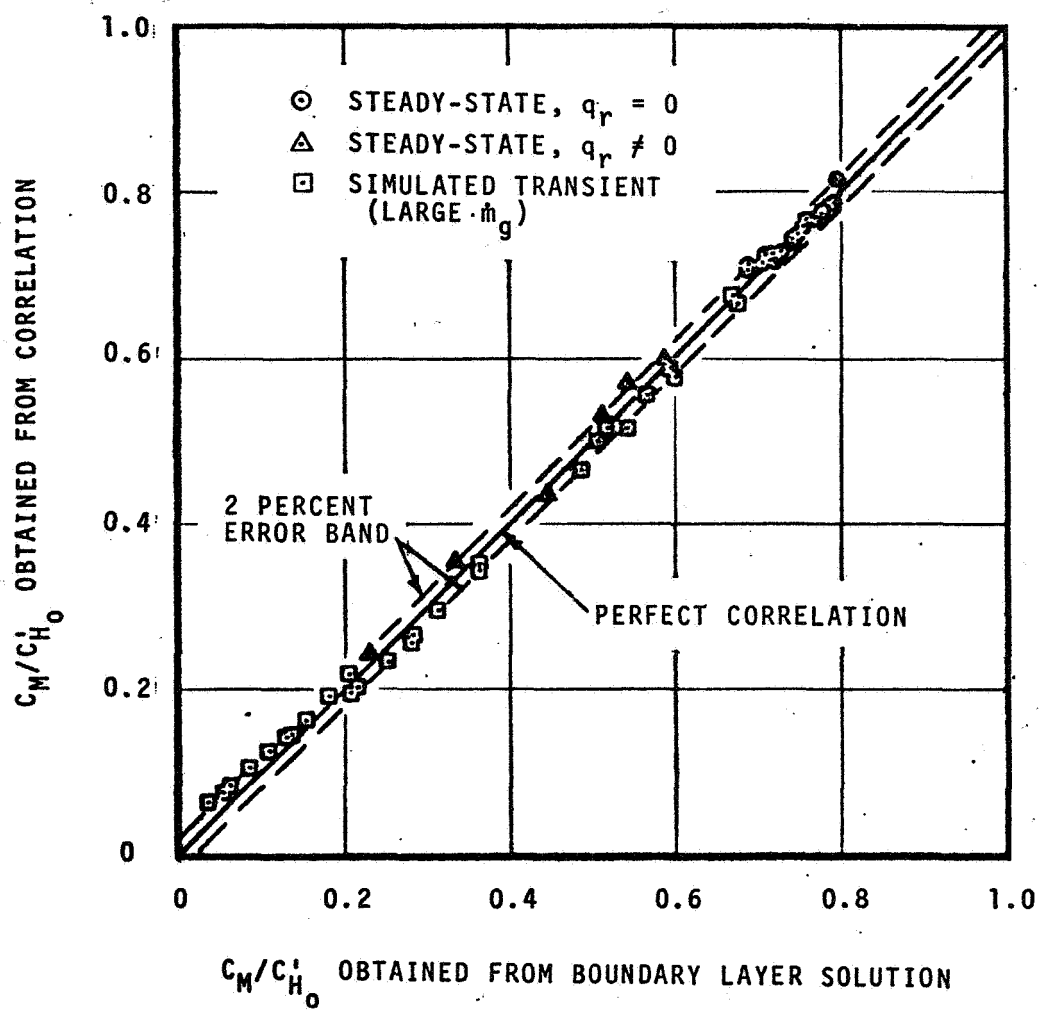


Figure 17. Accuracy of Apollo Material Mass-Transfer Coefficient Correlation

d. Heat-Transfer Coefficient Correlations

As mentioned in Section 3.3.1a, there are a number of ways for representing the surface convective heat flux q_w . Two approaches have been considered in the present effort, through the $\rho_e U_e C_H$ of Equation (21) and the $\rho_e U_e C_H'$ of Equation (23).

In order to test the accuracy of the Equation (22) Lewis number correlation, $C_M/C_H Le_w^{2/3}$ has been presented in Table 11. It can be seen that this parameter deviates considerably from unity at the higher blowing rates. Attempts to develop more accurate correlations of $\rho_e U_e C_H$ through C_M/C_H and C_H/C_{H_0}' met with only fair success.* Hence, the use of $\rho_e U_e C_H$ was abandoned in favor of $\rho_e U_e C_H'$.

The $\rho_e U_e C_H'$ data were also correlated in a number of ways. The simplest and most accurate correlation of those considered is given by

$$\frac{C_H'}{C_{H_0}'} = \max \left\{ \left[1.0 - \max \left\{ \lambda_H \left(\frac{\dot{m}}{\rho_e U_e C_{H_0}'} - 0.125 \right), 0 \right\} \right], 0.27 \right\} \quad (30)$$

where λ_H is a correlation parameter. The parameter λ_H for perfect correlation is presented in Figure 18 in terms of $\mathcal{M}_w/\mathcal{M}_e$. The data points are seen to fall into a fairly narrow band which is represented well by the curve

$$\lambda_H = \begin{cases} 0.417 & \text{for } \frac{\mathcal{M}_w}{\mathcal{M}_e} < 1.0 \\ 0.224 \left(\frac{\mathcal{M}_w}{\mathcal{M}_e} - 1 \right)^2 + 0.134 \left(\frac{\mathcal{M}_w}{\mathcal{M}_e} - 1 \right) + 0.417 & \text{for } \frac{\mathcal{M}_w}{\mathcal{M}_e} > 1.0 \end{cases} \quad (31)$$

The variation of C_H'/C_{H_0}' with $B_0' = \dot{m}/\rho_e U_e C_{H_0}'$ obtained using this correlation is presented in Figure 19. Note here that the effect of molecular weight ratio is in a direction opposite to that for C_M/C_{H_0}' (see Figure 16), an increase in $\mathcal{M}_w/\mathcal{M}_e$ increasing the blowing reduction for heat transfer.

The accuracy of the heat-transfer coefficient correlation of Equations (30) and (31) is demonstrated in Figure 20 which compares the values of C_H'/C_{H_0}'

*Note from Table 11 that $\rho_e U_e C_H$ is typically greater than $\rho_e U_e C_H'$. It is shown in Reference 29 that this behavior is due to chemical reactions between the injected gases and the edge gas.

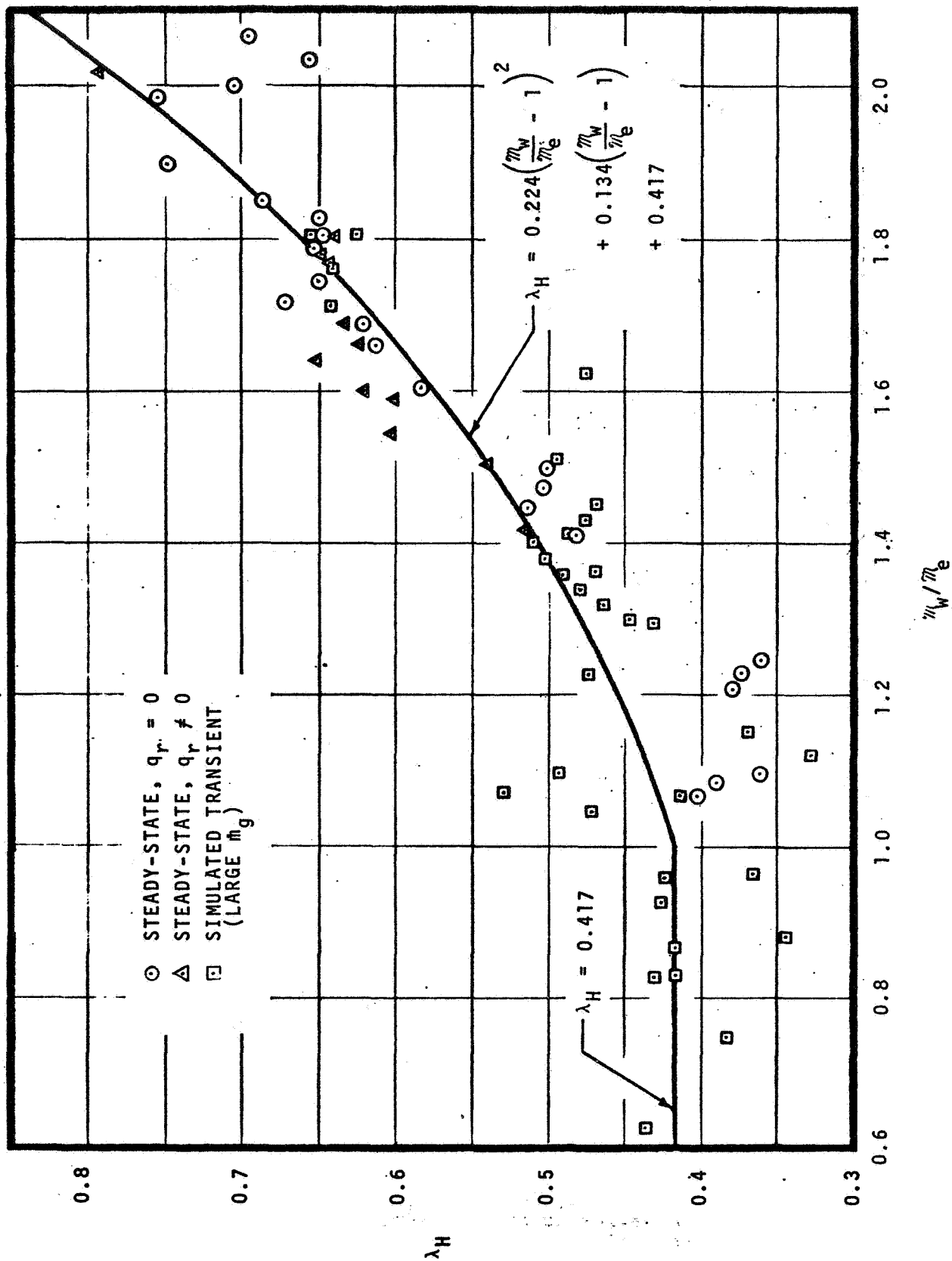


Figure 18. Heat-Transfer Coefficient Correlation for Apollo Material Ablation

ORIGINAL PAGE IS
OF POOR QUALITY

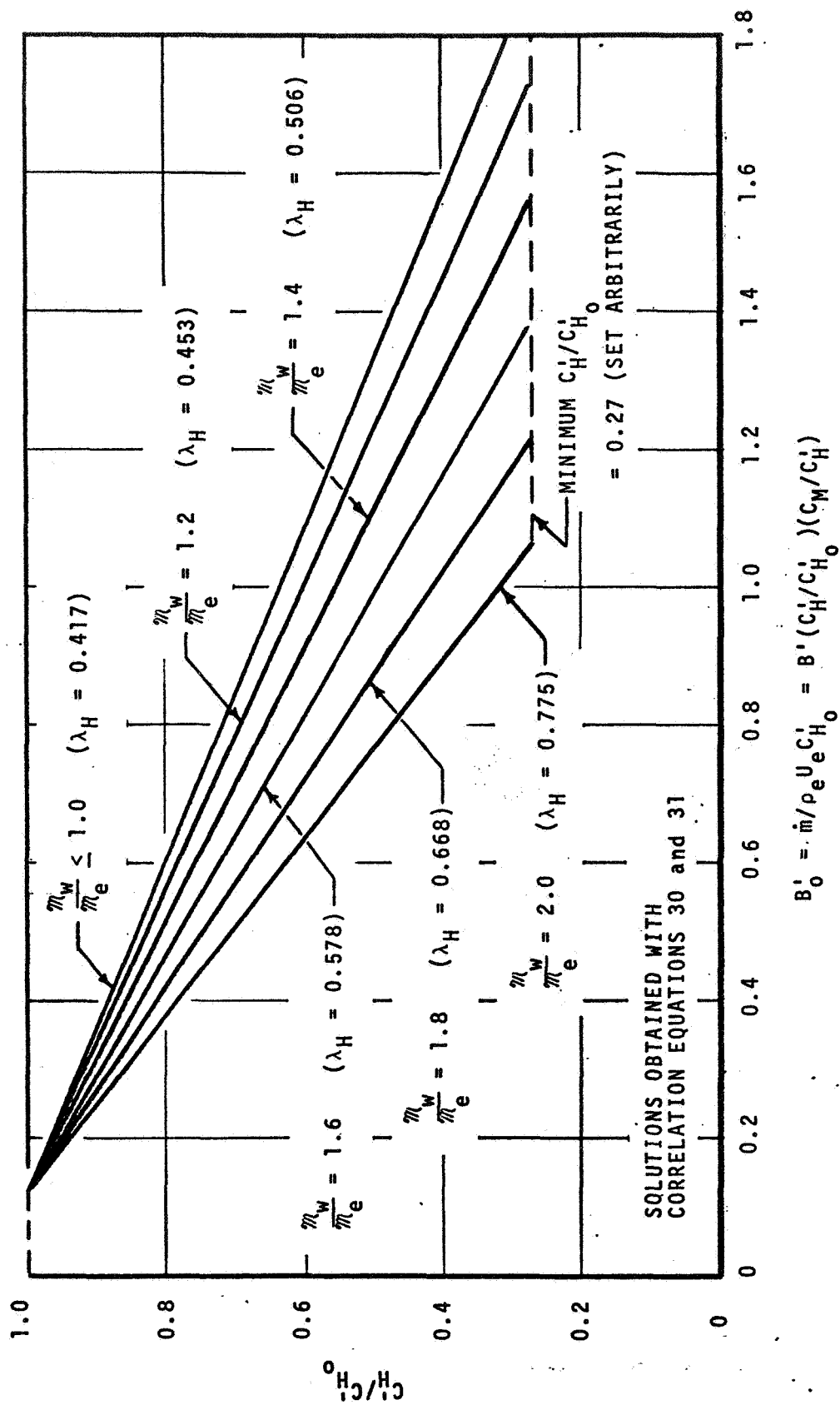


Figure 19. Heat-Transfer Coefficient Blowing Correction for the Apollo Material

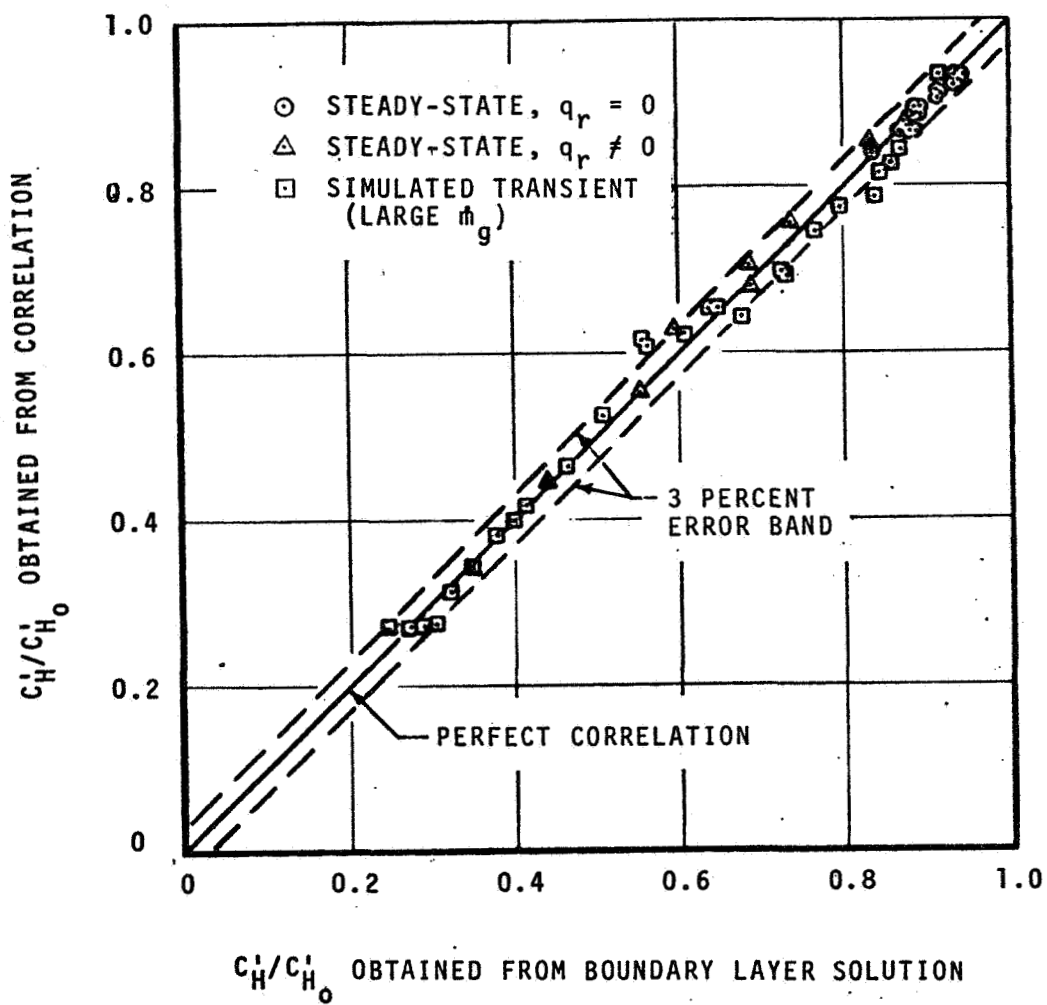


Figure 20. Accuracy of Apollo Material Heat-Transfer Coefficient Correlation

obtained from the correlation to those obtained from the boundary-layer solutions. Errors in $C_H^i/C_{H_0}^i$ are seen to be less than three percent except for three of the 72 solutions which exhibit nominally five percent error. Again, as in the case of $\rho_e U_e C_M$, it would probably be possible to improve upon this correlation by permitting λ_H to be a function of such parameters as \dot{m}_g/\dot{m}_c , etc. but the correlation of Equations (30) and (31) is judged to be adequate and consistent with the present data.

It should be noted that the two "max" functions in Equation (30) which limit the $C_H^i/C_{H_0}^i$ to values not in excess of 1.0 at very low blowing rates and not less than 0.27 at very high blowing rates have been introduced arbitrarily: there are no boundary-layer solutions to substantiate the former limit and only three to substantiate the latter.* This is of no consequence, however, since the former occurs only during a very brief and unimportant portion of a typical reentry trajectory and the latter corresponds to blowing rates higher than those experienced in any of the Apollo flight predictions presented in Section 6.

It is also significant to note that the blowing reduction for heat transfer is considerably less than that for mass transfer at large injection rates, the $C_M/C_{H_0}^i$ becoming as much as an order of magnitude smaller than $C_H^i/C_{H_0}^i$.

3.3.2 Laminar Nonsimilar Boundary Layer

Solutions were generated for laminar nonsimilar boundary layers around the windward and leeward pitch plane rays of Apollo at 25° angle of attack including Apollo material ablation. Four problems were considered as shown in the following tabulation.

Case	Location	Temperature Distribution	Char Removal Rates	Pyrolysis Gas Rates
1	Leeward	4000° R	Determined from surface equilibrium condition	Low*
2	Leeward	4000° R		High
3	Windward	4000° R		Moderate
4	Windward	5400-2000° R		Moderate

* Steady-State Pyrolysis-Gas Rates

All four cases considered surface equilibrium so that char recession rate was obtained as part of the solution. The first three cases considered a constant wall temperature of 4000° R while the fourth case considered a temperature distribution representative of peak heating during a lunar return trajectory. In

* The 0.27 lower limit was introduced to limit errors in $C_H^i/C_{H_0}^i$ for these three high-blowing solutions to 3 percent.

Case 1, steady-state pyrolysis gas rates were calculated as part of the solution (i.e., $\dot{m}_g = 1.125 \dot{m}_c$ - see footnote in Section 3.3.1b). In Cases 3 and 4, a moderately high pyrolysis gas rate is superimposed upon the steady-state rate in the form of a constant normalized pyrolysis gas rate \dot{m}_g^* of 0.40, where \dot{m}_g^* is defined by

$$\dot{m}_g^* = \dot{m}_g / \alpha^* \quad (32)$$

where the normalizing parameter α^* is defined in the nomenclature (see Ref. 9). In Case 2, a high value of \dot{m}_g^* of 1.00 is superimposed upon the steady-state pyrolysis gas rate. Pertinent results from these solutions are presented in Tables 12a through 12d for Cases 1 through 4, respectively.

It is of interest to compare the blowing corrections for mass and heat transfer to blowing corrections calculated for the local value of m_w/m_e and $B'_0 = \dot{m} / \rho_e U_e C_{H_0}'$ using the correlations developed in Section 3.3.1 for the axisymmetric (zero incidence) stagnation point (Eqs. (26) through (31)). For this purpose the blowing corrections for C_M/C_{H_0}' and C_H/C_{H_0}' normalized by their respective axisymmetric-stagnation-point blowing corrections (as described above) are presented in Figures 21a and 21b, respectively. The results for the leeward side with low pyrolysis gas rates (Case 1) agree very well with the stagnation point blowing corrections. The agreement for the leeward side with high pyrolysis gas rates (Case 2) is not as good, with errors in $\rho_e U_e C_M$ and $\rho_e U_e C_H'$ as high as 15 percent. However, relative to $\rho_e U_e C_{H_0}'$ these errors are quite acceptable considering that C_M/C_{H_0}' is about 0.12 and C_H/C_{H_0}' is about 0.45 (see Table 12b) with the consequence that errors in C_M/C_{H_0}' are less than 2 percent and errors in C_H/C_{H_0}' are less than 7 percent. Case 3, which considers the windward side with moderately high \dot{m}_g , yields a maximum error in $\rho_e U_e C_M$ of 42 percent, in C_M/C_{H_0}' of 22 percent, in $\rho_e U_e C_H'$ of 10 percent, and in C_H/C_{H_0}' of 7 percent. However, these errors occur on the conical afterbody where the heating rates are reduced an order of magnitude from those on the aft heat shield (see Table 12c) so again they are not serious. Furthermore, the injection rates in this case are much higher than those typically experienced over the conical afterbody.

Case 4 considers a variable wall temperature representative of peak heating during a typical lunar return flight. This represents the most severe test for the transfer-coefficient approach because the surface temperature in the stagnation region is sufficiently high that carbon is introduced into the boundary layer in excess of that needed for surface equilibrium at downstream stations. Consequently, mass-transfer rates (and thus the $\rho_e U_e C_M$) are reduced over a portion of the body (near the toroid) to levels well below the stagnation-point

TABLE 12

NONSIMILAR LAMINAR BOUNDARY LAYER ABOUT APOLLO AT 25° INCIDENCE:
20,000 BTU/LB, 1.0 ATM

(a) Leeward Side, Low Pyrolysis Gas Rates (Virgin Material Ablation),
Uniform Wall Temperature

S/R	T_w °R	q_w Btu/ sec ft ²	\dot{m}_C $\times 10^3$ lb/ sec ft ²	\dot{m}_g $\times 10^3$ lb/ sec ft ²	θ $\times 10^3$ ft	m_w/m_e	B'_O	$\frac{C_M}{C_{H_2O}}$	$\frac{C'_H}{C_{H_2O}}$
.000	4000.	219.80	1.7802	2.0028	4.858	1.759	.295	.764	.876
.069	4000.	240.90	1.9506	2.1944	4.448	1.758	.295	.764	.877
.138	4000.	234.90	1.9040	2.1420	4.530	1.759	.295	.764	.876
.208	4000.	218.60	1.7736	1.9954	4.826	1.758	.295	.764	.874
.277	4000.	209.10	1.6965	1.9085	5.040	1.757	.295	.764	.874
.415	4000.	188.00	1.5271	1.7179	5.570	1.755	.296	.765	.874
.554	4000.	180.30	1.4654	1.6486	5.789	1.754	.296	.765	.875
.692	4000.	172.90	1.4071	1.5829	5.995	1.751	.296	.766	.875
.830	4000.	166.90	1.3605	1.5305	6.162	1.747	.297	.768	.875
.969	4000.	159.40	1.3031	1.4659	6.359	1.744	.298	.769	.875
1.107	4000.	150.00	1.2296	1.3834	6.641	1.740	.298	.771	.874
1.246	4000.	140.60	1.1558	1.3002	6.972	1.735	.299	.773	.874
1.384	4000.	130.50	1.0767	1.2113	7.363	1.729	.300	.775	.874
1.453	4000.	125.50	1.0376	1.1674	7.585	1.727	.301	.776	.874
1.522	4000.	120.70	.9991	1.1239	7.825	1.723	.301	.778	.875
1.591	4000.	115.70	.9600	1.0800	8.100	1.718	.302	.780	.876
1.626	4000.	113.90	.9459	1.0641	8.252	1.714	.303	.783	.877
1.661	4000.	111.70	.9299	1.0461	8.453	1.709	.305	.786	.880
1.678	4000.	101.20	.8442	.9498	8.702	1.709	.300	.775	.863
1.695	4000.	124.30	1.0405	1.1705	8.756	1.697	.312	.804	.896
1.703	4000.	110.80	.9784	1.1006	9.671	1.684	.326	.842	.888
1.727	4000.	74.82	.6555	.7375	12.220	1.646	.316	.814	.868
1.744	4000.	53.28	.4885	.5495	15.500	1.622	.320	.825	.839
1.775	4000.	30.75	.2992	.3366	22.980	1.586	.319	.825	.788
1.805	4000.	15.09	.1832	.2062	39.510	1.545	.357	.932	.707
1.814	4000.	8.50	.1199	.1349	58.240	1.515	.348	.911	.594
1.842	4000.	5.32	.0634	.0713	80.540	1.485	.309	.000	.626

TABLE 12 (CONTINUED)

(b) Leeward Side, High Pyrolysis Gas Rates,
Uniform Wall Temperature

S/R	T _w °R	q _w Btu/ sec ft ²	$\dot{m}_C \times 10^3$ lb/ sec ft ²	$\dot{m}_g \times 10^3$ lb sec ft ²	$\theta \times 10^3$ ft	m_w/m_e	B' _O	$\frac{C_M}{C_{H_2O}}$	$\frac{C_H}{C_{H_2O}}$
.000	4000.	106.20	.3718	16.2582	6.246	.918	1.298	.130	.432
.069	4000.	130.50	.3718	17.6382	4.793	.796	1.284	.111	.492
.138	4000.	125.50	.3906	17.3794	5.767	.885	1.297	.112	.478
.208	4000.	111.20	.3435	16.3365	6.217	.893	1.306	.113	.454
.277	4000.	104.00	.3247	15.6353	6.525	.896	1.307	.113	.444
.415	4000.	91.18	.2871	14.0829	7.248	.898	1.309	.114	.433
.554	4000.	87.68	.2871	13.4529	7.527	.901	1.306	.117	.434
.692	4000.	84.56	.2824	12.8876	7.772	.902	1.305	.119	.437
.830	4000.	82.83	.2824	12.4076	7.956	.903	1.304	.123	.443
.969	4000.	79.82	.2729	11.8771	8.179	.903	1.306	.125	.447
1.107	4000.	75.69	.2541	11.2259	8.519	.901	1.310	.125	.450
1.246	4000.	72.01	.2447	10.5353	8.918	.898	1.313	.126	.457
1.384	4000.	67.75	.2301	9.7999	9.390	.896	1.315	.128	.463
1.453	4000.	65.80	.2231	9.4159	9.656	.895	1.314	.129	.467
1.522	4000.	64.19	.2202	9.0138	9.940	.895	1.311	.131	.475
1.591	4000.	62.67	.2198	8.5732	10.260	.896	1.304	.134	.484
1.626	4000.	63.02	.2259	8.3261	10.420	.897	1.291	.137	.495
1.661	4000.	63.39	.2353	7.9977	10.640	.899	1.270	.140	.509
1.678	4000.	52.45	.1859	7.7161	10.950	.892	1.320	.138	.456
1.695	4000.	74.99	.3153	7.4577	10.960	.902	1.096	.133	.551
1.703	4000.	65.61	.3327	6.3893	12.000	.902	1.054	.141	.536
1.727	4000.	39.18	.2480	4.5570	14.870	.894	1.091	.000	.463

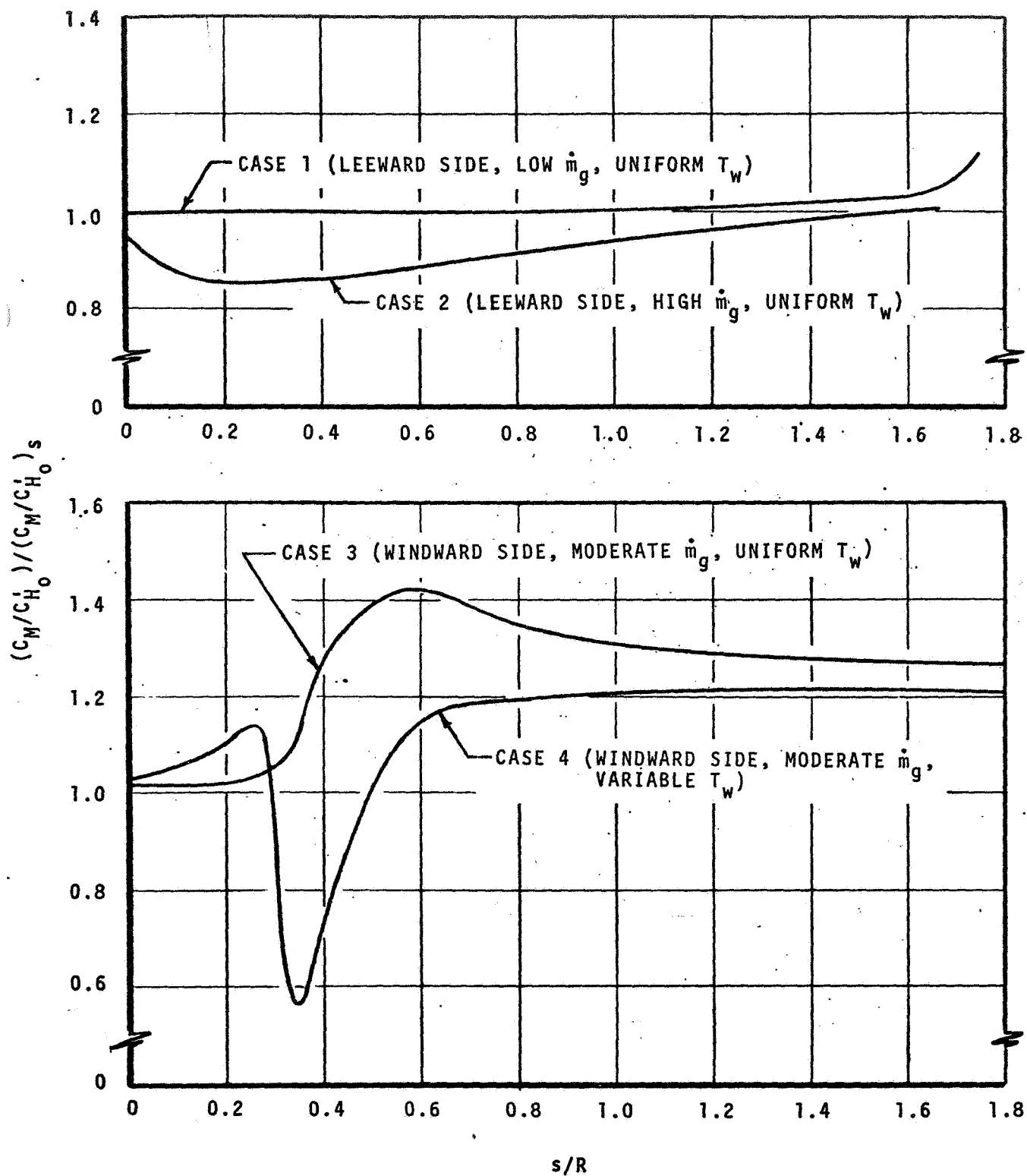
TABLE 12 (CONTINUED)
(c) Windward Side, Moderate Pyrolysis Gas Rates,
Uniform Wall Temperature

S/R	T _w °R	q _w Btu/ sec ft ²	\dot{m}_C x 10 ³ lb/ sec ft ²	\dot{m}_G x 10 ³ lb/ sec ft ²	θ x 10 ³ ft	$\eta_w \eta_e$	B' _O	$\frac{C_M}{C_{H_2O}}$	$\frac{C'_H}{C'_{H_2O}}$
.000	4000.	192.00	1.3144	8.5496	4.562	1.321	.686	.465	.683
.035	4000.	196.30	1.3426	8.7574	4.456	1.320	.686	.465	.683
.069	4000.	201.30	1.3788	8.8812	4.373	1.321	.684	.467	.687
.104	4000.	215.60	1.4767	9.4533	4.092	1.321	.683	.468	.690
.139	4000.	224.20	1.5369	9.8431	3.921	1.320	.684	.468	.690
.173	4000.	235.10	1.6141	10.1659	3.769	1.322	.680	.469	.695
.208	4000.	261.00	1.7972	11.0628	3.414	1.320	.675	.471	.701
.242	4000.	280.10	1.9351	11.6749	3.151	1.315	.673	.474	.709
.260	4000.	269.80	1.8593	11.3607	3.179	1.309	.679	.476	.710
.277	4000.	252.60	1.7365	10.6535	3.325	1.302	.683	.477	.713
.294	4000.	232.20	1.6024	9.6976	3.553	1.293	.682	.477	.719
.312	4000.	203.70	1.4160	8.3870	3.942	1.282	.681	.478	.726
.329	4000.	165.70	1.1694	6.5816	4.713	1.266	.673	.480	.738
.346	4000.	101.40	.7336	4.1004	6.901	1.232	.682	.491	.734
.364	4000.	66.47	.4913	2.9367	9.125	1.208	.705	.503	.702
.381	4000.	50.10	.3736	2.3184	11.220	1.190	.720	.509	.689
.398	4000.	39.85	.3002	1.8658	13.640	1.174	.729	.514	.690
.416	4000.	33.04	.2522	1.6038	15.600	1.164	.739	.518	.676
.433	4000.	28.48	.2193	1.4317	17.250	1.155	.747	.520	.663
.450	4000.	25.56	.1972	1.3258	18.480	1.148	.755	.522	.653
.468	4000.	23.74	.1826	1.2544	19.430	1.144	.762	.522	.648
.485	4000.	22.30	.1708	1.2002	20.220	1.139	.768	.522	.644
.519	4000.	20.77	.1566	1.1604	20.860	1.133	.782	.520	.635
.554	4000.	20.42	.1507	1.1603	20.930	1.128	.792	.516	.635
.589	4000.	20.46	.1473	1.1797	20.690	1.123	.799	.510	.635
.623	4000.	20.62	.1454	1.2056	20.380	1.119	.805	.503	.633
.686	4000.	21.49	.1478	1.2492	20.000	1.115	.809	.490	.641
.757	4000.	22.02	.1496	1.2514	20.290	1.111	.807	.480	.654
.976	4000.	20.74	.1396	1.1324	23.010	1.102	.801	.464	.673
1.194	4000.	18.08	.1225	.9755	26.890	1.095	.798	.457	.678
1.621	4000.	14.25	.0988	.7514	34.760	1.085	.789	.453	.682
1.989	4000.	10.11	.0740	.5084	49.720	1.073	.768	.459	.689

TABLE 12 (CONCLUDED)

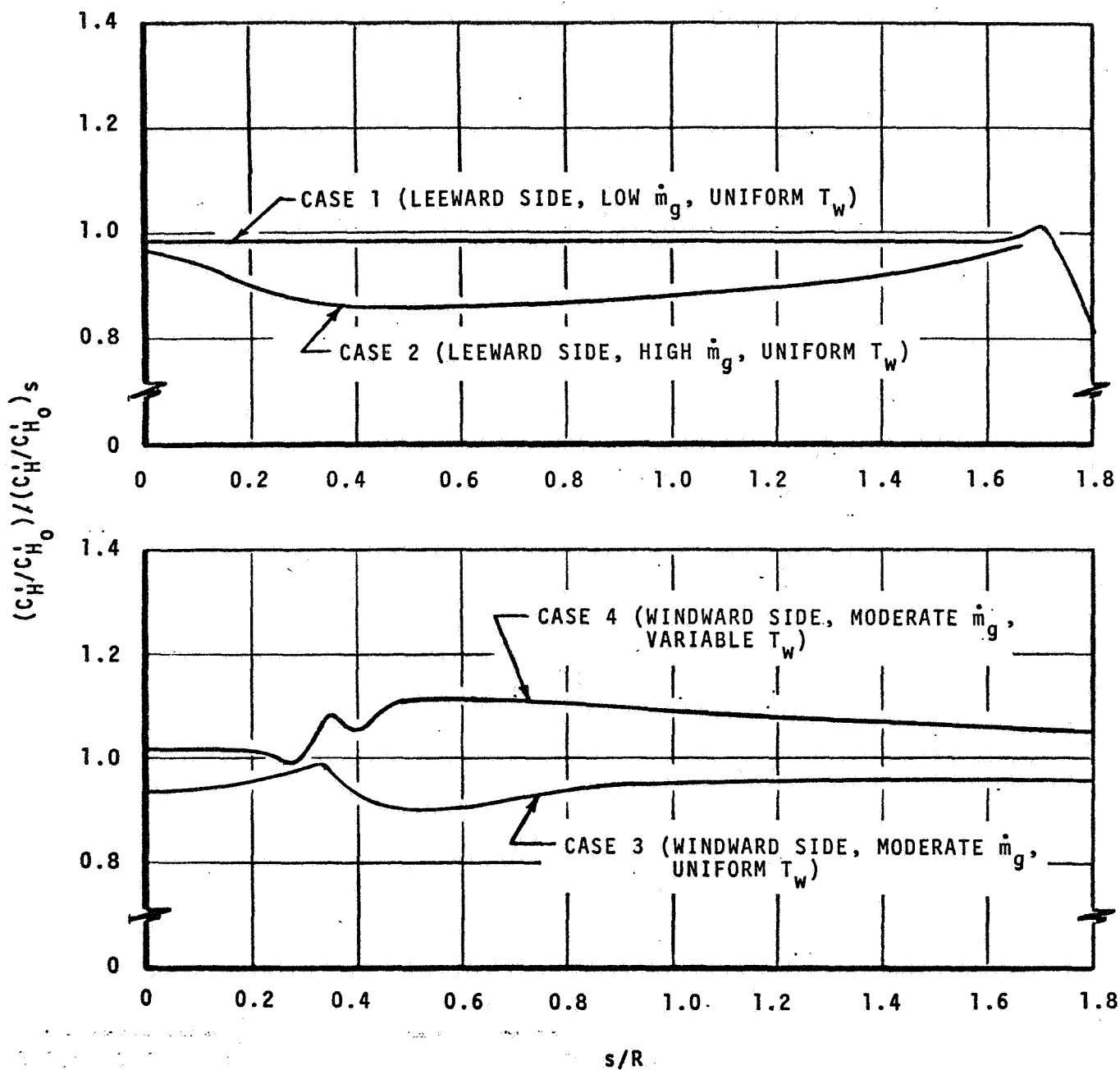
(d) Windward Side, Moderate Pyrolysis Gas Rates,
Variable Wall Temperature

S/R	T _w °R	q _w Btu/ sec ft ²	$\dot{m}_C \times 10^3$ lb/ sec ft ²	$\dot{m}_G \times 10^3$ lb/ sec ft ²	$\theta \times 10^3$ ft	m_w/m_e	B' _O	$\frac{C_M}{C_H} \frac{CH_O}{CH_O}$	$\frac{C_H}{C_H} \frac{CH_O}{CH_O}$
.000	5200.	161.80	2.0372	9.3628	4.516	1.271	.804	.399	.627
.035	5220.	163.70	2.1191	9.6309	4.411	1.269	.809	.395	.622
.069	5240.	167.60	2.2212	9.8288	4.327	1.268	.814	.396	.626
.104	5255.	196.20	2.3708	10.4592	4.053	1.242	.812	.397	.691
.139	5270.	202.10	2.5064	10.9336	3.894	1.236	.820	.399	.688
.173	5280.	210.20	2.6635	11.3465	3.750	1.235	.820	.401	.688
.208	5290.	230.50	3.0207	12.4393	3.398	1.233	.825	.406	.689
.242	5300.	240.50	3.3421	13.2579	3.133	1.226	.834	.410	.680
.260	5290.	228.20	3.1581	12.8219	3.157	1.219	.835	.409	.672
.277	5270.	213.00	2.8376	11.8924	3.296	1.212	.827	.407	.673
.294	5200.	206.30	2.1341	10.2959	3.502	1.207	.764	.393	.710
.312	5000.	206.10	.9318	7.8422	3.843	1.213	.620	.352	.796
.329	4700.	182.30	.3064	5.6106	4.531	1.223	.521	.329	.855
.346	4300.	122.10	.0202	3.2978	6.571	1.209	.475	.322	.910
.364	3900.	84.11	-.0000	2.3840	8.660	1.196	.497	.345	.898
.381	3600.	63.10	.0127	1.9123	10.630	1.188	.522	.366	.867
.398	3350.	50.10	.0301	1.5619	12.920	1.178	.541	.382	.858
.416	3100.	42.56	.0381	1.3629	14.780	1.169	.563	.398	.855
.433	2850.	38.30	.0438	1.2342	16.340	1.162	.584	.412	.870
.450	2700.	34.96	.0489	1.1591	17.500	1.155	.605	.425	.867
.468	2600.	32.65	.0532	1.1088	18.410	1.150	.621	.434	.864
.485	2520.	30.84	.0560	1.0710	19.170	1.146	.637	.442	.860
.519	2440.	28.62	.0601	1.0519	19.790	1.140	.665	.455	.843
.554	2380.	27.97	.0655	1.0645	19.860	1.135	.688	.463	.839
.589	2340.	27.82	.0701	1.0929	19.660	1.132	.705	.467	.829
.623	2320.	27.82	.0744	1.1256	19.380	1.128	.719	.469	.820
.686	2310.	28.25	.0828	1.1762	19.060	1.125	.733	.468	.808
.757	2300.	28.21	.0913	1.1857	19.370	1.122	.739	.464	.802
.976	2250.	25.49	.0982	1.0858	22.120	1.120	.749	.461	.791
1.194	2200.	21.83	.0924	.9416	25.980	1.109	.755	.461	.781
1.621	2100.	16.91	.0790	.7291	33.880	1.102	.754	.462	.771
1.989	2000.	11.84	.0600	.4927	48.820	1.093	.733	.466	.766



a. Mass-Transfer Coefficient

Figure 21. Transfer Coefficients for Nonsimilar Laminar Boundary Layer about Apollo at 25° Incidence Normalized by Values Obtained from Axisymmetric Stagnation-Point Correlation



b. Heat-Transfer Coefficient

Figure 21. Concluded

correlations.* It is of interest to compare Cases 3 and 4 since they differ only in the wall temperature distributions (and hence char removal rates). They both show satisfactory agreement on the aft heat shield, although the agreement is quite a bit better for Case 3. As the toroid is approached, the $\rho_e U_e C_M$ decreases sharply below the correlation values for Case 4 while they begin to increase for Case 3. On the conical afterbody, the agreement with the stagnation-point correlation is actually better for Case 4 than for Case 3. It can be seen from Figure 21b that the error in $\rho_e U_e C_H'$ for Case 4 is about the same as for Case 3 except that the $\rho_e U_e C_H'$ is higher than the stagnation-point correlation for Case 4 whereas it is lower for Case 3.

From this discussion, it would appear that the stagnation-point blowing corrections can be applied to positions around the body with satisfactory engineering accuracy with the exception of the sharp decrease in $\rho_e U_e C_M$ in the vicinity of the toroid in Case 4. Fortunately, this behavior is limited to a relatively short portion of the trajectory (when T_w in the stagnation region exceeds about 4500°R), to a small portion of the body (in the vicinity of the toroid), and leads to conservative predictions when it does occur. Therefore this effect also can probably be neglected for engineering design calculations. In conclusion, while non-negligible effects have been observed, they are not serious; furthermore, the number and type of solutions which have been considered are not sufficiently general to develop meaningful corrections to the zero-incidence stagnation-point correlations. Therefore, it is recommended that "stagnation-point" blowing corrections (based on local $\dot{m}/\rho_e U_e C_{H_0}'$ and $\mathcal{M}_w/\mathcal{M}_e$) be employed for all positions around the body as long as the flow is laminar. Turbulent flow is considered in the next section.

3.3.3 Turbulent Nonsimilar Boundary Layer

Two solutions were generated for nonsimilar laminar/turbulent boundary layers around the leeward pitch plane ray of Apollo at 25° incidence including Apollo material ablation. In both cases, the surface was considered to be in equilibrium with the adjacent gas and the wall temperature was considered to be 4000 R; they differed in that Case 1 considered "low" pyrolysis gas injection rates while Case 2 considered "high" pyrolysis gas rates (as defined in Section 3.3.2). Transition was presumed to occur at the same streamwise station where it had occurred in the nonsimilar air boundary layer solutions of Section 3.2.3. Pertinent results from these solutions are presented in Tables 13a and 13b.

The C_M/C_{H_0}' and C_H'/C_{H_0}' blowing corrections normalized by their respective zero-incidence "stagnation-point" values are presented in Figures 22a and 22b. The normalizing parameter here is based on the correlations of Equations (26)

* This effect was observed previously in graphite ablation solutions³².

TABLE 13

NONSIMILAR LAMINAR/TURBULENT BOUNDARY LAYER ABOUT APOLLO AT 25° INCIDENCE:
20,000 BTU/LB, 1.0 ATM

(a) Leeward Side, Low Pyrolysis Gas Rates (Virgin Material Ablation),
Uniform Wall Temperature

S/R*	T _w °R	q _w Btu/ sec ft ²	$\dot{m}_c \times 10^3$ lb/ sec ft ²	$\dot{m}_g \times 10^3$ lb/ sec ft ²	$\theta \times 10^3$ ft	m _w /m _e	B' _O	$\frac{C_M}{C_H} \frac{CH_O}{CH_O}$	$\frac{C_H}{C_H} \frac{CH_O}{CH_O}$
.000	4000.	219.80	1.7802	2.0028	4.858	1.759	.295	.764	.876
.069	4000.	240.90	1.9506	2.1944	4.448	1.758	.295	.764	.877
.138	4000.	234.90	1.9040	2.1420	4.530	1.759	.295	.764	.876
.208	4000.	218.60	1.7736	1.9954	4.826	1.758	.295	.764	.874
.277	4000.	209.10	1.6965	1.9085	5.040	1.757	.295	.764	.874
.415	4000.	188.00	1.5271	1.7179	5.570	1.755	.296	.765	.874
.554	4000.	180.30	1.4654	1.6486	5.789	1.754	.296	.765	.875
.692	4000.	618.90	4.6588	5.2412	10.520	1.674	.294	.722	.940
.830	4000.	650.50	4.9929	5.6171	13.480	1.654	.292	.715	.919
.969	4000.	673.00	5.1200	5.7600	16.050	1.636	.290	.704	.920
1.107	4000.	675.40	5.1106	5.7494	18.550	1.621	.289	.697	.923
1.246	4000.	659.60	5.0165	5.6435	21.030	1.610	.289	.694	.917
1.384	4000.	629.50	4.8471	5.4529	23.580	1.602	.288	.691	.904
1.453	4000.	611.20	4.7388	5.3312	24.920	1.600	.288	.691	.897
1.522	4000.	591.10	4.6118	5.1882	26.300	1.597	.287	.691	.890
1.591	4000.	568.50	4.4569	5.0141	27.790	1.593	.287	.691	.885
1.626	4000.	556.10	4.3699	4.9161	28.580	1.588	.287	.691	.883
1.661	4000.	538.70	4.2452	4.7758	29.540	1.584	.287	.692	.881
1.678	4000.	517.90	4.0753	4.5847	30.420	1.581	.288	.692	.883
1.695	4000.	530.50	4.2485	4.7795	30.490	1.574	.289	.000	.872

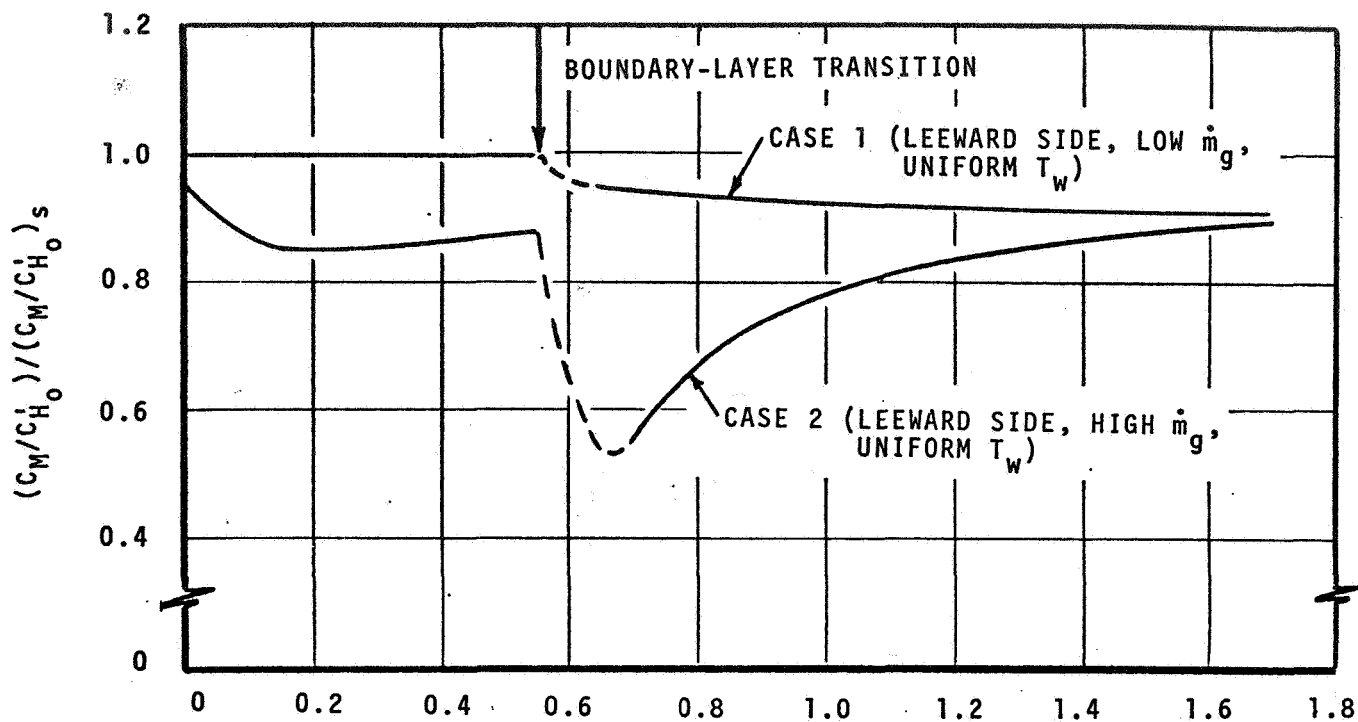
* Transition considered to occur at S/R = 0.554.

TABLE 13 (CONCLUDED)

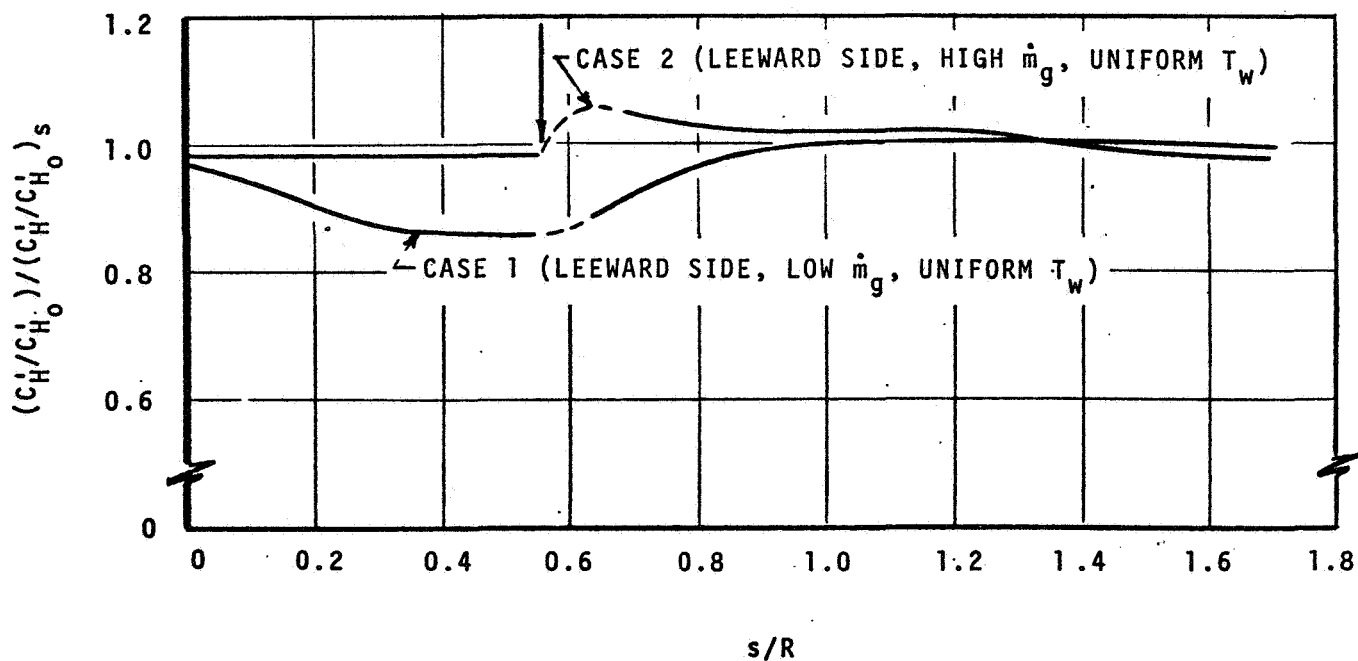
(b) Leeward Side, High Pyrolysis Gas Rates,
Uniform Wall Temperature

S/R*	T _w °R	q _w Btu/ sec ft ²	$\dot{m}_C \times 10^3$ lb/ sec ft ²	$\dot{m}_g \times 10^3$ lb/ sec ft ²	$\theta \times 10^3$ ft	η_w/η_e	B' B ₀	$\frac{C_M}{C_H} \frac{CH_4}{CH_2O}$	$\frac{C'_H}{C'_H} \frac{CH_4}{CH_2O}$
.000	4000.	106.20	.3718	16.2582	6.246	.918	1.298	.130	.432
.069	4000.	130.50	.3718	17.6382	4.793	.796	1.284	.111	.492
.138	4000.	125.50	.3906	17.3794	5.767	.885	1.297	.112	.478
.208	4000.	111.20	.3435	16.3365	6.217	.893	1.306	.113	.454
.277	4000.	104.00	.3247	15.6353	6.525	.896	1.307	.113	.444
.415	4000.	91.18	.2871	14.0829	7.248	.898	1.309	.114	.433
.554	4000.	87.68	.2871	13.4529	7.527	.901	1.306	.117	.434
.692	4000.	485.80	2.8565	15.7835	11.990	1.087	.553	.272	.748
.830	4000.	554.10	3.6047	16.1453	14.610	1.155	.544	.359	.791
.969	4000.	587.70	3.8776	15.9324	17.000	1.192	.528	.411	.811
1.107	4000.	595.70	3.9671	15.4029	19.430	1.214	.516	.445	.822
1.246	4000.	590.00	3.9624	14.7176	21.890	1.228	.506	.469	.828
1.384	4000.	573.00	3.8866	13.9134	24.460	1.239	.498	.486	.830
1.453	4000.	561.20	3.8235	13.4665	25.810	1.243	.494	.494	.830
1.522	4000.	546.80	3.7478	12.9822	27.200	1.246	.491	.501	.830
1.591	4000.	528.80	3.6489	12.4311	28.680	1.247	.488	.508	.830
1.626	4000.	518.10	3.5896	12.1104	29.450	1.247	.485	.511	.829
1.661	4000.	502.30	3.5045	11.6755	30.350	1.247	.484	.516	.829
1.678	4000.	483.60	3.3661	11.2939	31.270	1.246	.487	.519	.831
1.695	4000.	491.00	3.5374	11.0826	30.980	1.246	.468	.515	.814
1.703	4000.	420.20	3.0941	9.4959	34.010	1.236	.465	.000	.803

* Transition considered to occur at S/R = 0.554.



a. Mass-Transfer Coefficient



b. Heat-Transfer Coefficient

Figure 22. Transfer Coefficients for Nonsimilar Laminar/Turbulent Boundary Layer about Apollo at 25° Incidence Normalized by Values Obtained from Axisymmetric Stagnation-Point Correlation

through (31) using local values of $\dot{m}/\rho_e U_e C_{H_O}'$ and \dot{m}_w/\dot{m}_e with the turbulent $\rho_e U_e C_{H_O}'$. The C_M/C_{H_O}' lie several percent below the "stagnation-point" blowing corrections, while the C_H'/C_{H_O}' agree very well with the stagnation-point correlation. While the error in $\rho_e U_e C_M$ immediately after transition is quite large for Case 2, the error in C_M/C_{H_O}' does not exceed 13 percent (see Table 13b).

Comparing the blowing corrections for laminar and turbulent flow at a given station, the $\rho_e U_e C_{H_O}'$ for turbulent flow is much larger, the $\dot{m}/\rho_e U_e C_{H_O}'$ is smaller (even though \dot{m} is larger), and the blowing corrections ($1 - C_M/C_{H_O}'$ and $1 - C_H'/C_{H_O}'$) are thus smaller. Hence, the ablation rate is larger and the blowing correction is smaller for turbulent flow even though the blowing correction curves are roughly the same.

In conclusion, the blowing corrections developed for zero-incidence stagnation point (laminar) flow are seen to apply to turbulent flow about Apollo at incidence with good accuracy for C_H'/C_{H_O}' and with reasonable engineering accuracy for C_M/C_{H_O}' as long as the local turbulent flow value of $\rho_e U_e C_{H_O}'$ is brought into the normalizing parameters. The two turbulent-flow solutions which were generated would thus suggest that the stagnation point blowing correction relations for C_M/C_{H_O}' and C_H'/C_{H_O}' be applied directly to turbulent flow without correction.

3.4 SUMMARY OF CONVECTIVE HEATING STUDIES

It has been demonstrated that the BLIMP program predicts wind-tunnel convective heating data very well, and that the wind-tunnel predictions differ from flight predictions by a consistent (and typically small) correction. Thus, the NASA/MSC convective heating factors (which are based on wind-tunnel data) can be used together with this small correction to predict nonablating convective heat-transfer distributions at various angles of attack and for all positions on the heat shield surface, at least where the boundary layer is attached.

Simple blowing reduction relationships for heat and mass transfer are then developed for the Apollo heat-shield material which are reasonably accurate (usually within two percent) for a wide range of flight conditions and considering large pyrolysis-gas injection situations as well as steady-state ablation. These relations are then shown to be adequate for use (typically within 10 percent) for positions around the body, including nonsimilar effects, for turbulent as well as laminar flow, as long as the surface temperature in the stagnation region does not exceed about 4500°R.

In summary, the following procedure is recommended for the calculation of the $\rho_e U_e C_M$ and $\rho_e U_e C_H'$ required for transient CMA calculations and has been employed in the flight predictions of Section 6.2.

Step 1: Calculate Nonablating Heat-Transfer Coefficient $\rho_e U_e C'_{H_o}$

$$\rho_e U_e C'_{H_o} = \rho_e U_e C'_{H_o_s} F_1 F_2 F_3 F_4 F_5 \quad (33)$$

where

- $\rho_e U_e C'_{H_o_s}$ is the heat-transfer coefficient for the axisymmetric stagnation point for $T_w = 2000^\circ R$ (Fig. 10)
- F_1 is the NASA/MSC convective heating factor for laminar flow at the location and angle of attack of interest (e.g., Fig. 8)
- F_2 is a correction to change the normalizing parameter from the $\bar{S}/R = 0.9875$ used in the NASA/MSC convective heating factors to the axisymmetric (zero incidence) stagnation point (Fig. 9)
- F_3 is a correction to the NASA/MSC convective heating factors reflecting the significance of flight conditions on heating distributions (Fig. 12)
- F_4 is a correction for turbulent flow (Fig. 14) to be used when a critical Re_{θ_o} is exceeded, where Re_{θ_o} is given by Figure 13
- F_5 is a wall-temperature correction to $\rho_e U_e C'_{H_o_s}$ (neglected - see Eq. (15))

Step 2: Calculate Blowing Corrections C_M/C'_{H_o} and C'_H/C'_{H_o}

$$\frac{C_M}{C'_{H_o}} = \frac{C_M}{C'_{H_o}} \bigg|_s G_1 G_2 \quad (34)$$

$$\frac{C'_H}{C'_{H_o}} = \frac{C'_H}{C'_{H_o}} \bigg|_s H_1 H_2 \quad (35)$$

where

$C_M/C'_{H_o} \big|_s$ and $C'_H/C'_{H_o} \big|_s$ are the axisymmetric (zero-incidence) stagnation-point blowing corrections (Eqs. (26) through (31))

G_1 and H_1 are corrections to the stagnation-point blowing corrections for positions away from the stagnation point due to nonsimilar effects (neglected - see Section 3.3.2)

G_2 and H_2 are corrections to the laminar nonsimilar blowing corrections for turbulent flow when applicable (neglected - see Section 3.3.3).

Step 3: Calculate Local Heat- and Mass-Transfer Coefficients

$$\rho_e U_e C_M = \rho_e U_e C_{H_o}' \left(\frac{C_M}{C_{H_o}'} \right) \quad (36)$$

$$\rho_e U_e C_H' = \rho_e U_e C_{H_o}' \left(\frac{C_H'}{C_{H_o}'} \right) \quad (37)$$

The changes in the CMA and EST programs necessary to employ these procedures are described in Appendix A.

SECTION 4

INCIDENT RADIATION STUDIES

The purpose here is to obtain an independent evaluation of radiation flux levels. The approach taken is to (1) review the prediction procedures presently employed at NASA-MSC, (2) identify areas of particular importance, (3) identify areas of low confidence levels, (4) establish priorities from (2) and (3), (5) perform selected calculations and (6) make recommendations for improving the procedure based on the results of (5). The results of these studies are presented in the following subsections.

4.1 REVIEW OF NASA/MSC PROCEDURES

The following radiation flow field model is used to predict equilibrium* radiation fluxes at NASA/MSC:

- a. The shock shape in the pitch plane is taken from wind tunnel experiments for given angles of attack. It is normalized against the normal shock standoff distance. The resulting shape is assumed to be invariant with flight conditions.
- b. The shock shape is assumed to have a sinusoidal variation about the vehicle axis for two planes (45° and 90°) other than the pitch plane. Thus, these two assumptions reduce the problem of determining the shock shape about the body to that of determining the normal standoff distance.
- c. The normal standoff distance is scaled from wind tunnel data using a calculation procedure applicable to spheres. This procedure includes real gas effects in the air region of the shock layer but does not include nonadiabatic effects or effects caused by blowing.

The flight conditions enter the spherical scaling law only through the density ratio across the bow shock. Thus, the specification of

*Nonequilibrium effects were immediately placed at the bottom of the list of priorities, because they are not very important relative to equilibrium radiation (let alone convection) and the state-of-the-art is such that predictions from first principles are essentially impossible.

the shock shape about the body has been reduced to the calculation of the jump conditions across the bow shock at the shock normal position.

- d. The fluxes about the body are assumed to be fully characterized by the flux at a reference condition. Thus, the flux distribution (considering different planes and angles-of-attack) were calculated at a particular flight condition, normalized to the reference condition and fixed for all other flight conditions.
- e. The reference fluxes are obtained from the plane-parallel, adiabatic layer fluxes by applying a correction factor of .84 to account for geometric effects and the correction factors of Chin (Ref. 33) to account for nonadiabatic effects. The first correction is accurate for optically thin layers, the second for a two-band radiation model. Interactions with the boundary layer are assumed to be negligible.
- f. The plane-parallel, adiabatic layer fluxes are obtained from the radiation properties model of Page et al (Ref. 34) which is a three-step-plus-one-line model, valid for air at uniform conditions.

In assessing the importance of these steps, one must consider where the heating is most intense and where flight data is available to evaluate candidate changes in the prediction procedure. On both counts, the region near the shock normal condition is the most important. Indeed, adequate data does not appear to be available to evaluate the flux distributions. Steps (c), (e) and (f) above are important in the shock normal region; consequently, they will receive major attention.

One must also consider the confidence levels associated with each step. Steps (a), (b) and (d) are clearly very approximate. It is fortunate that they are also of relatively less importance. Of the important steps, (c) should be quite satisfactory as the shock standoff distance is not a sensitive function of the flow field method employed (within limits), and the radiation flux levels are not particularly sensitive to the standoff distance. Step (f) should be moderately satisfactory because the radiation model employed (Ref. 34) is thought to be accurate. Finally, step (e) is important and should have appreciably larger uncertainties associated with it than steps (c) and (f).

Based on these considerations, the priorities established were to verify step (f), and to consider improvements to step (e), in that order. Logically, the flux distribution would be considered next, but this is beyond the scope of the effort.

4.2 VERIFICATION OF REFERENCE RADIATION CONDITIONS

4.2.1 Plane-Parallel Adiabatic Layer Fluxes

In the NASA/MSC procedure, the plane-parallel, adiabatic layer fluxes are obtained from the model of Page et al (Ref. 34) which is a three-step-plus-one-line model applicable to air at uniform conditions. Solutions have been obtained for comparison with the predictions of the Aerotherm RAD program and its variants (Refs. 35 to 38) which employs a detailed model of the important contributions from the molecular band systems (within the bandless model approximation), the photodissociation, photoionization and free-free transitions, and each of 118 low lying atomic lines.

The predictions from the two methods are compared in Figures 23 and 24. The RAD code predictions for a 1 cm thick slab (Figure 23) are about 10 percent higher at 9000°K and in excellent agreement at the higher temperatures. For a 10 cm thick slab at 1 atm pressure (Figure 24), the RAD code predictions are about 10 percent higher at 9000°K, in excellent agreement at 10,000°K and about 10 percent lower at 11,000°K. For a 10 cm thick slab at .1 atm, the RAD code predictions are in excellent agreement at 9000°K, about 10 percent lower at 10,000°K, and about 20 percent lower at 11,000°K. Thus, step (f) of the NASA/MSC procedure yields fluxes within about 10 percent of those obtained at Aerotherm for conditions encountered during Apollo reentry (also shown on Figure 24). This should be viewed as good agreement.*

4.2.2 Nonadiabatic Effects

In the NASA/MSC procedure the nonadiabatic factors are obtained from Chin's (Ref. 33) coupled flowfield/two band radiation model. These factors could be obtained by using the Aerotherm RABLE (Radiating Boundary Layer Environment) operating in its shock layer mode (see Ref. 6). However, this procedure was not employed because of the limited scope of the present effort. Instead, a correlation of inviscid flow field solutions presented by Page et al (Ref. 34) was combined with the RAD code. The resulting prediction procedure employed the detailed RAD code radiation model fully coupled to an approximate, inviscid shock layer model.

Page et al (Ref. 34) modeled the stagnation region of the coupled radiating shock layer problem as

* One possible contributor to the 10 percent differences observed is the N^- photo-detachment transition which is normally not included in the RAD code properties model. To assess its effect, the data of Morris et al (Ref. 39) were incorporated into the RAD code and predictions were made at 10,000°K and are also presented in Figure 24. The agreement is seen to be slightly better at .1 atm and slightly worse at 1 atm, indicating that N^- does not account for the differences observed.

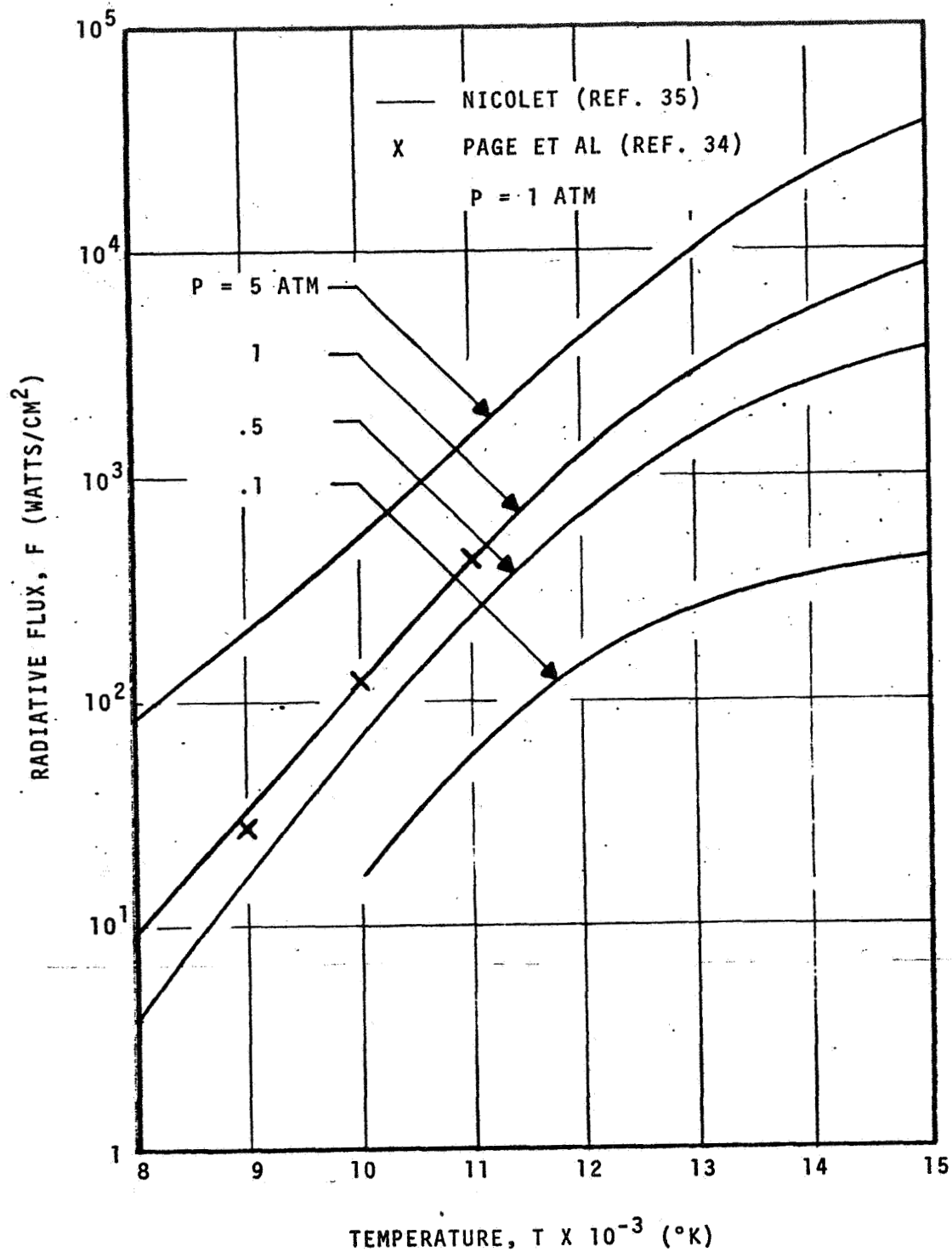


Figure 23. Radiation Fluxes from Uniform Slabs, $\delta = 1$ cm

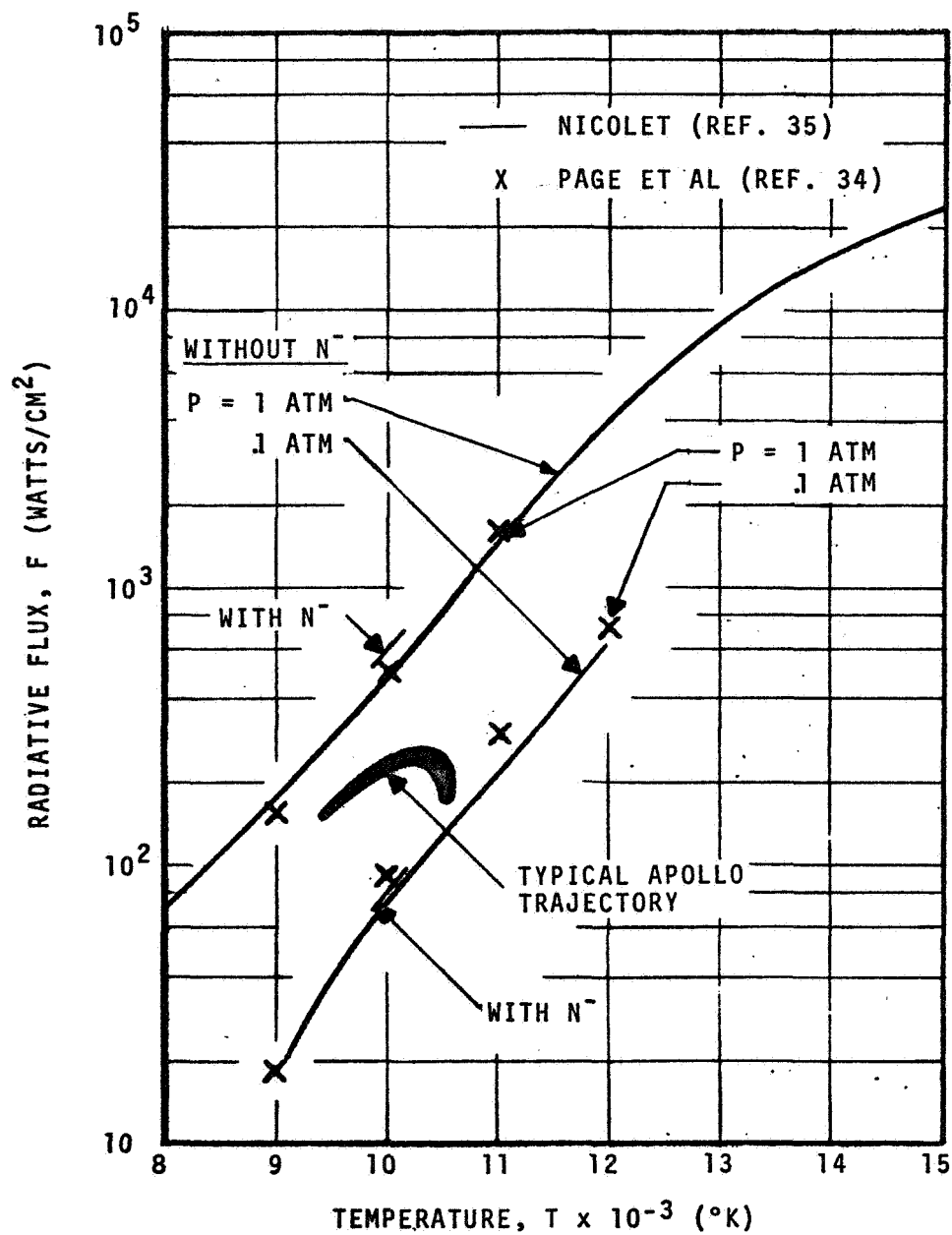


Figure 24. Radiation Fluxes from Uniform Slabs, $\delta = 10$ cm

$$\delta/\delta_{AD} = \int_0^1 h/h_s d(y/\delta) \quad (38)$$

$$P = \text{const.} \quad (39)$$

$$\rho v \frac{dh}{dy} = \frac{dq_r}{dy} \quad (40)$$

$$\frac{\rho v}{\rho_s v_s} = .5 (y/\delta)^2 - 1.5 (y/\delta) + 1 \quad (41)$$

where y is the distance normal to the surface, δ is the standoff distance, δ_{AD} is the adiabatic standoff distance, the subscript s refers to conditions just behind the bow shock and the other quantities have their usual meanings. Equations (38) to (41) were selected for the present study because of their simplicity and their ability to accept an arbitrarily complex radiation transport model.

In the present approach, an enthalpy profile of the form

$$h = h_s [1 - S \cdot (1 - y/\delta)] \quad (42)$$

was assumed, where S is an unknown parameter to be obtained during the solution. Also, the flow was assumed to be hypersonic in front of the shockwave and very subsonic behind it allowing the approximations

$$h \approx H_T \quad (43)$$

$$P \approx P_T \text{ (behind the shock)} \quad (44)$$

to be introduced. Equations (41) to (44) were substituted into Equations (38) and (40), and the results integrated over y/δ . This yielded

$$\frac{\delta}{\delta_{AD}} = 1 - \frac{S}{2} \quad (45)$$

$$q_{r_w} - q_{r_s} = \text{const} \cdot S \cdot H_T \rho_\infty V_\infty \quad (46)$$

which is a one parameter set and can be solved by employing the RAD code to evaluate the net radiative heat loss ($q_{r_w} - q_{r_s}$) as a function of S .

Solutions are obtained to Equations (45) and (46) through a two-step procedure. Initially, the mass flow rate, $\rho_\infty V_\infty$, and adiabatic shock standoff distance are calculated for the flight conditions and body size of interest. These are used to evaluate the right side of Equation (46) as a function of $\rho_\infty V_\infty$, H_T and S . The RAD code, the adiabatic standoff distance and Equation (45) are used to evaluate the left side of Equation (46) as functions of P_T (total pressure), H_T , δ_{AD} and S . The intercepts of the two families of curves are selected to eliminate the parameter S and yield the desired solutions.

The terms in Equations (45) and (46) have been presented in Figures 25 and 26 for $P_T = 1$ atm, and $\delta_{AD} = 10$ cm as an example of the procedure. The intercepts of the solid lines and the curves with alternating dots and dashes yield the solutions (unique values of S). The nonadiabatic wall fluxes follow immediately from the dotted curves. These have been normalized against their adiabatic values ($S = 0$) and are presented in Figure 26.

Using this procedure, nonadiabatic cooling factors, q_r/q_{AD} , have been calculated for the range of conditions of interest for Apollo reentry. These are presented in Figures 27 and 28 as a function of the radiation loss parameter, Γ . Presentation of the data in this fashion typically eliminates the pressure and path length dependence and - as indicated by some studies - the total enthalpy dependence as well. However, the results of the present study indicate that total enthalpy must be retained as a parameter but allow the elimination of pressure and path length with very slight penalties in accuracy (see Figure 27, for example).

The cooling factors are compared with those of other studies in Figure 28. For the conditions of primary interest ($q_r/q_{AD} > 0.5$), the present results are a few percent higher than those obtained using the NASA/MSC procedure, a few percent higher than the correlations of Olstad (Ref. 40) as reported by Bartlett et al (Ref. 41), significantly higher than the correlation of Page et al (Ref. 34) and significantly lower than the results of several early calculations.* Some of the differences can be attributed to the radiation models - the early calculations considered only optically thin radiation, while the NASA/MSC procedure does not consider lines. Others (Olstad) are within the expected accuracy of the correlation. The results of Page et al (Ref. 34) appear low for reasons which are not clear.

*The dashed curve shown in Figure 28 was taken from Reference 34, where the early studies are referenced.

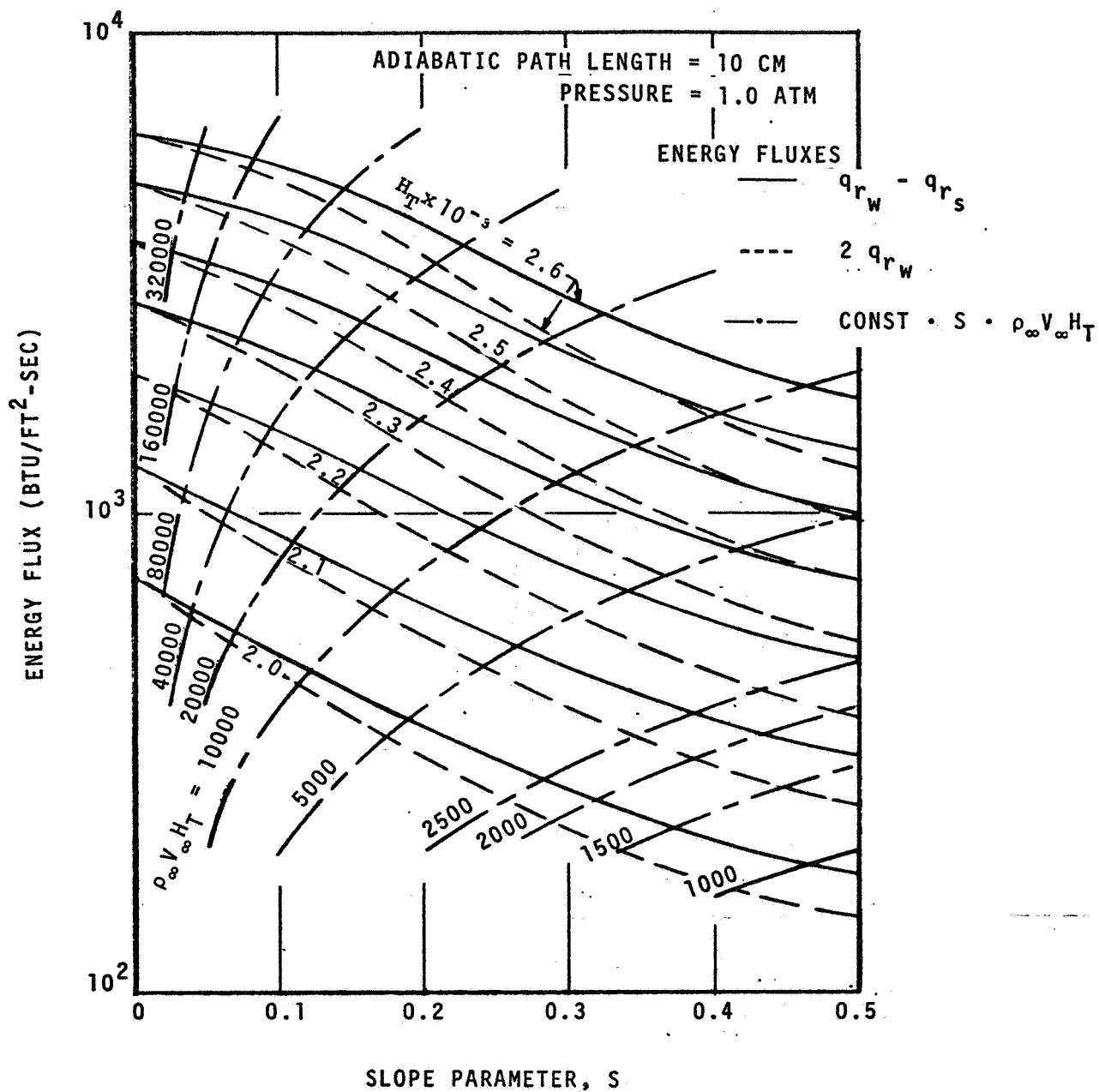


Figure 25. Radiation and Flow Terms in the Shock Layer Energy Balance

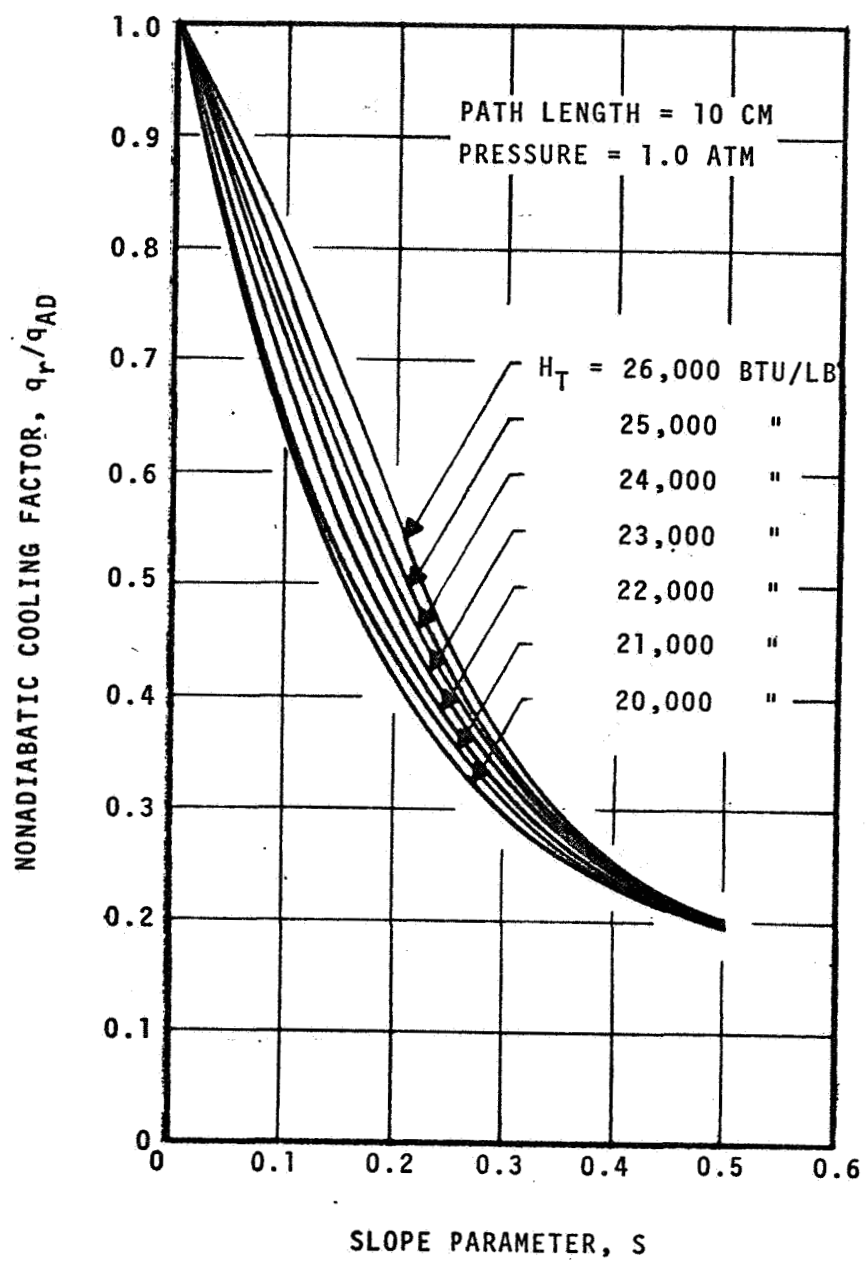


Figure 26. Nonadiabatic Cooling Factors as Functions of the Slope Parameter

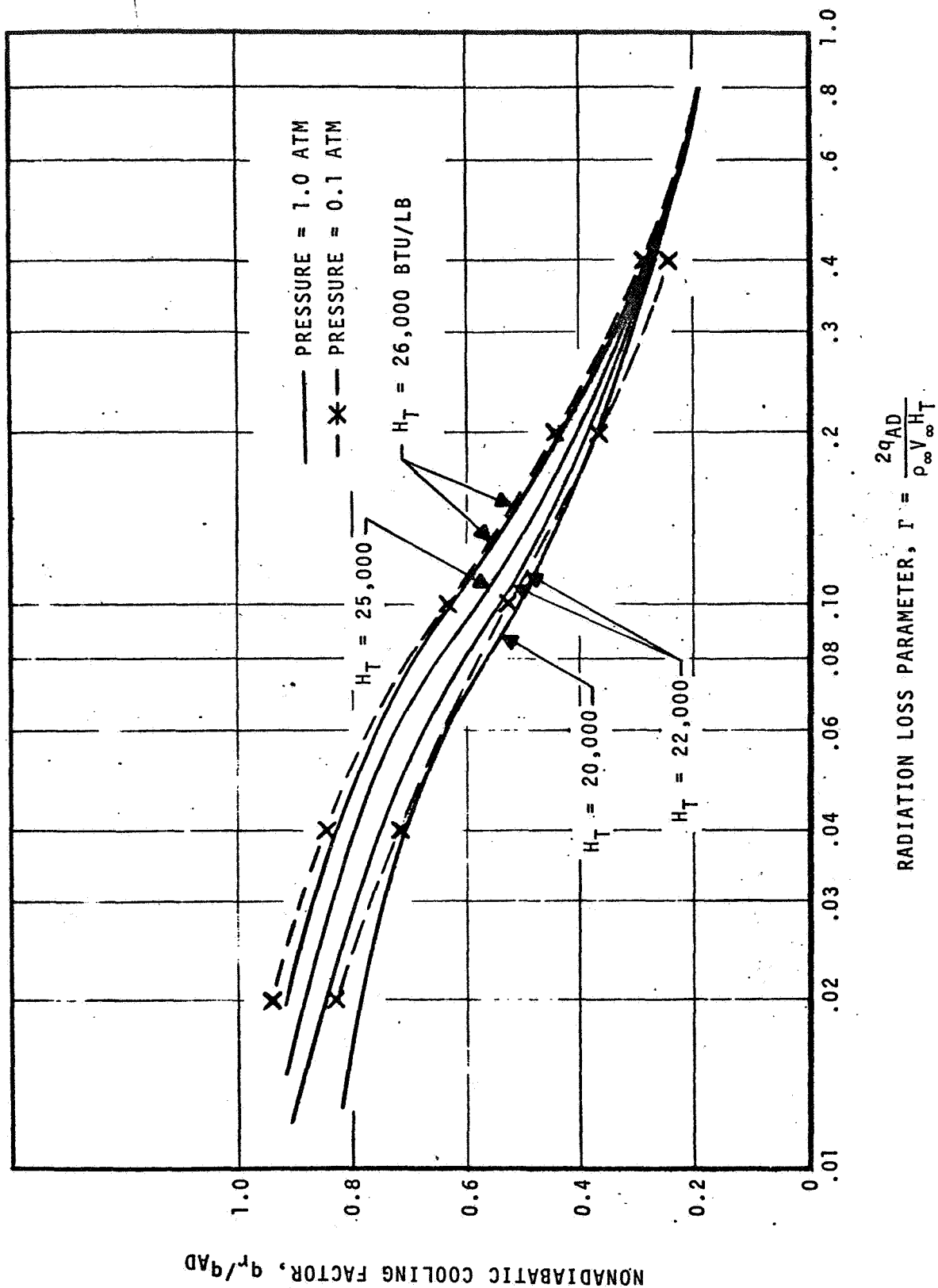


Figure 27. Effect of pressure on the Nonadiabatic Cooling Factors, $\delta_{AD} = 10$ cm

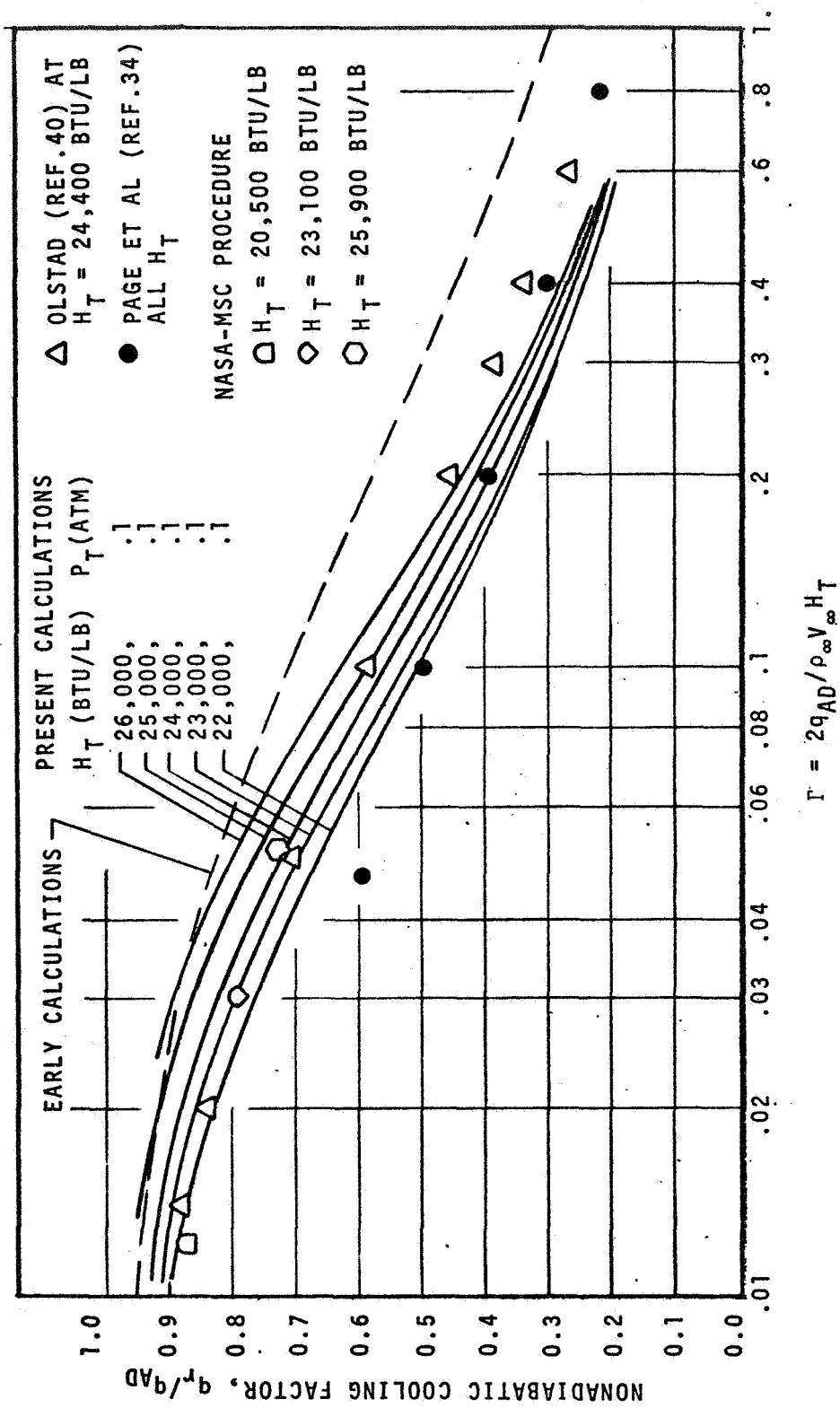


Figure 28. Comparison with Nonadiabatic Cooling Factors Obtained in Other Investigations

4.2.3 Spectral Effects

It is often necessary to have spectral fluxes or intensities at the surface. This can be conveniently accomplished through the interpolation function* presented in Figure 29. The procedure is to (1) obtain the nonadiabatic factor q_r/q_{AD} from Figure 27 or 28, (2) obtain the normalized slope parameter, \bar{S} , from Figure 29, (3) obtain the slope parameter, S , from \bar{S} (see Figure 29), and (4) employ the RAD code or a similar radiation transport procedure to calculate the desired fluxes and/or intensities at the surface.

4.3 FLIGHT PREDICTIONS AND COMPARISON WITH NASA/MSC PREDICTION AND FLIGHT DATA

A prediction of radiative heating was made for Flight 501 (Apollo 4), Body Point 703 (near the stagnation point) and compared to the NASA/MSC predictions and flight data. The procedure employed in the prediction was that described in the previous subsection plus a three-dimensional correction factor of 0.84 (after the NASA/MSC procedure). The flow field conditions are from the post flight report (Ref. 51), and the shock standoff distance (taken constant at 14 cm) is from Reference 15. The intermediate parameters (q_r/q_{AD} , S and the total correction factor) are presented in Figure 30. The fluxes and intensities are presented in Figures 31 and 32, respectively.

In comparing the prediction procedures with each other and with the measurements, the following observations are pertinent:

- o The present procedure yields a slightly wider and flatter pulse. This is true for both the total and visible fluxes and for the visible intensities incident upon the radiometer.
- o In comparing with the measurements, the present procedure is in slightly better agreement at peak heating conditions, and in slightly worse agreement at both early and late times.

4.4 DISCUSSION AND CONCLUSIONS

4.4.1 Confidence Levels in the Predictions

In both the NASA/MSC procedure and the present study, the interaction between the incident flux and the boundary layer is not included. This is probably the most important single factor limiting the accuracy of the predictions. The justifications usually given for this approach are (1) the radiation absorbed by the boundary layer is approximately equal to the radiation emitted by the boundary layer, and/or (2) the net radiation absorbed by the boundary layer tends to be compensated for by an increase in convective heating (over

*The interpolation function was obtained by correlating the limited amount of data generated in the present study. It should not be used for conditions significantly different from those encountered during Apollo reentry.

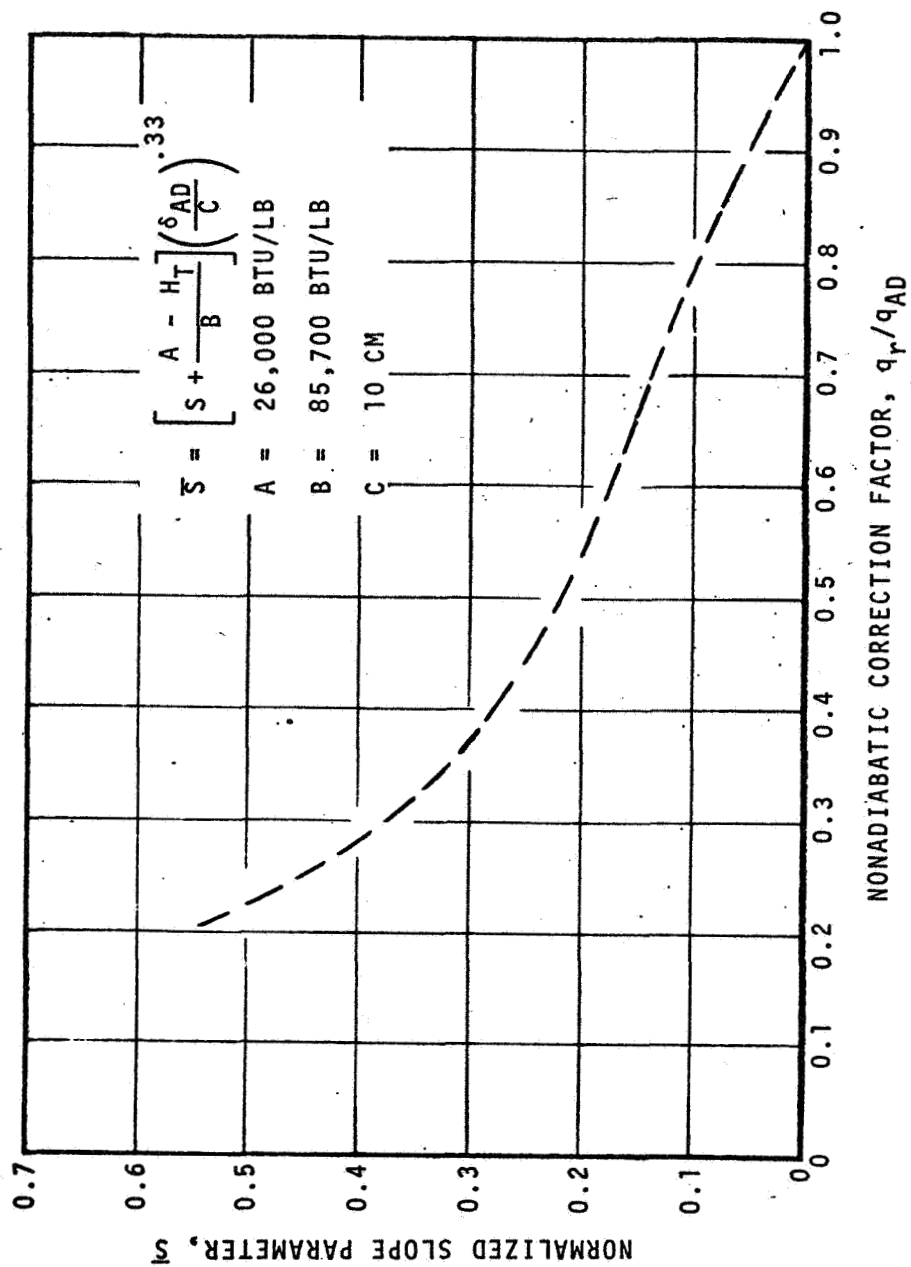


Figure 29. Interpolation Function for the Slope Parameter for the Shock Layer Model

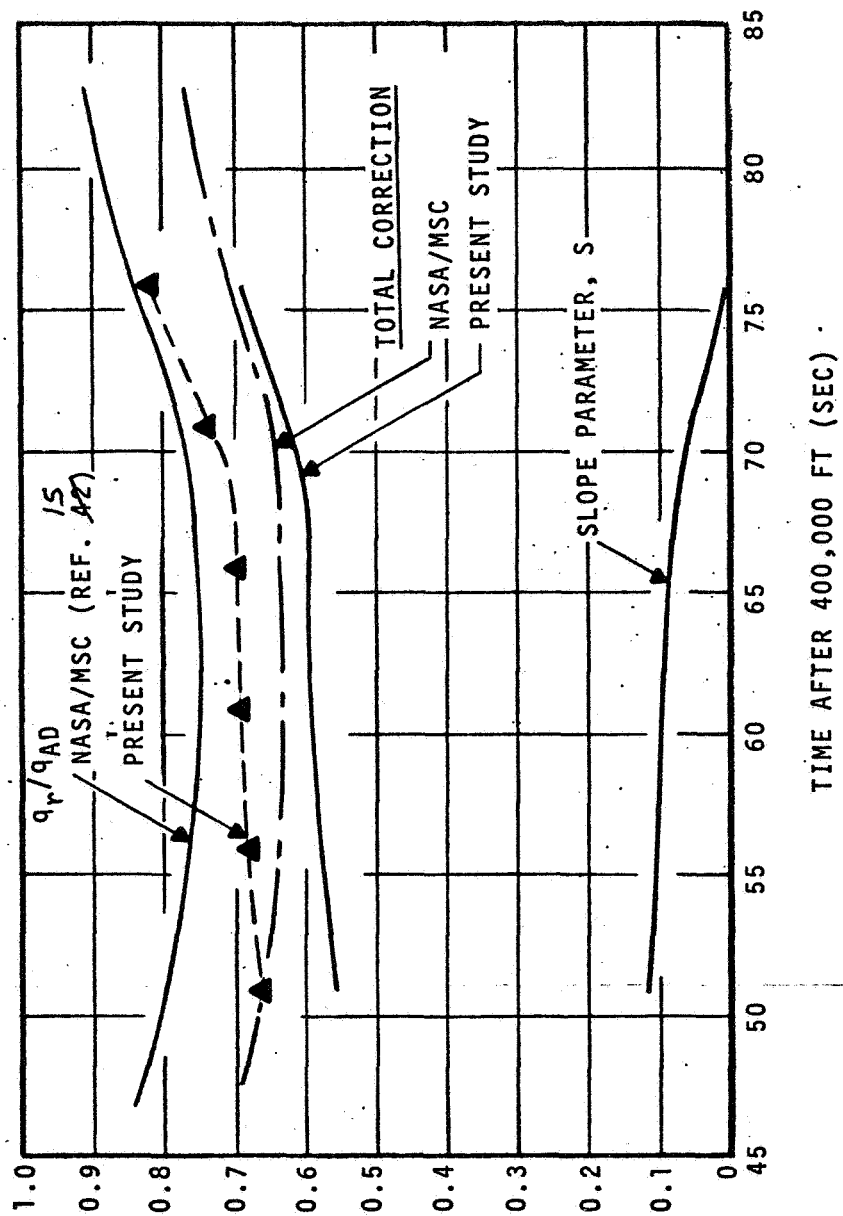


Figure 30. The Slope Parameter and the Correction Factors to be Applied to Adiabatic Radiation Fluxes for Apollo 4

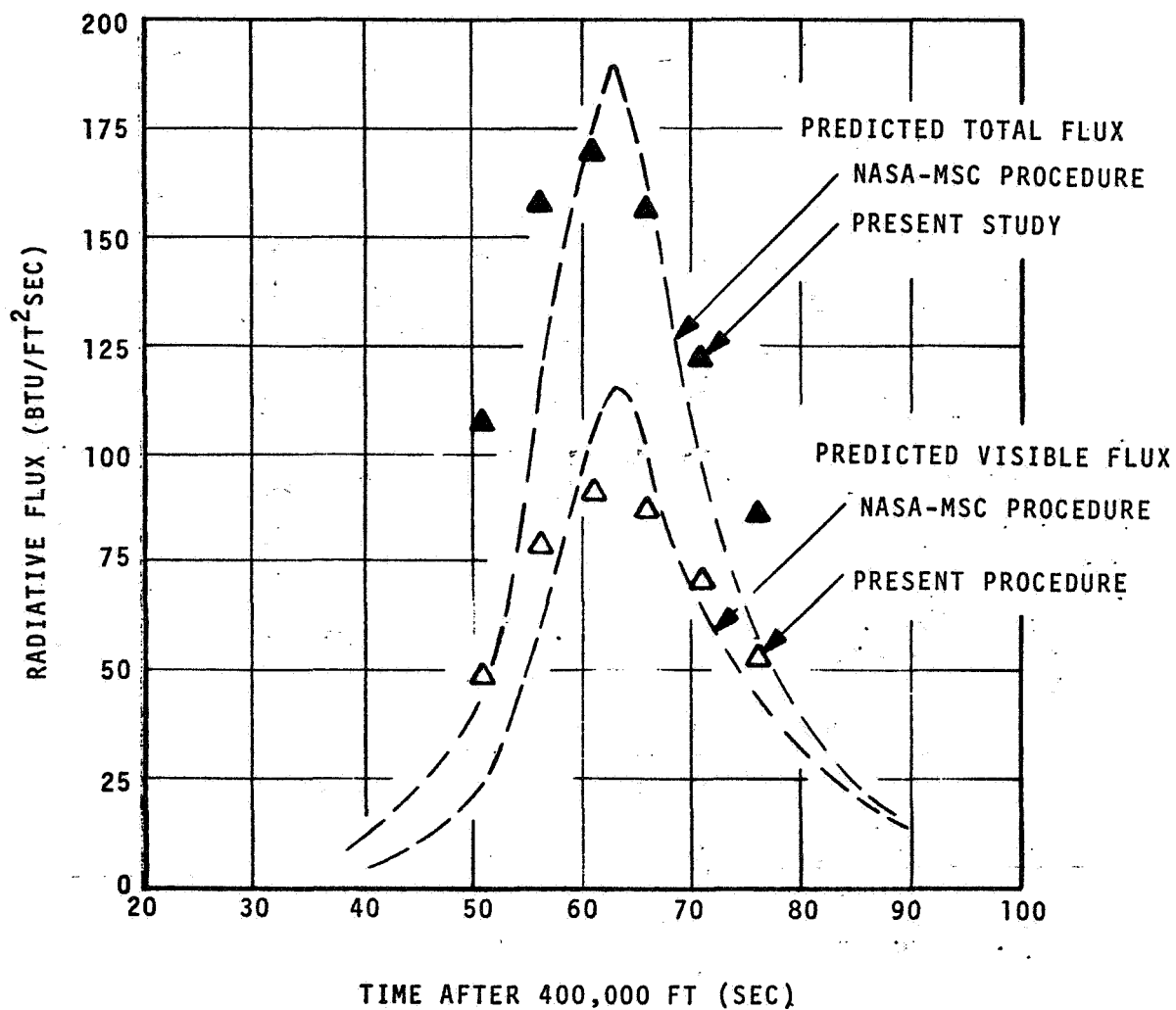


Figure 31. Predicted Radiation Fluxes for Apollo 4

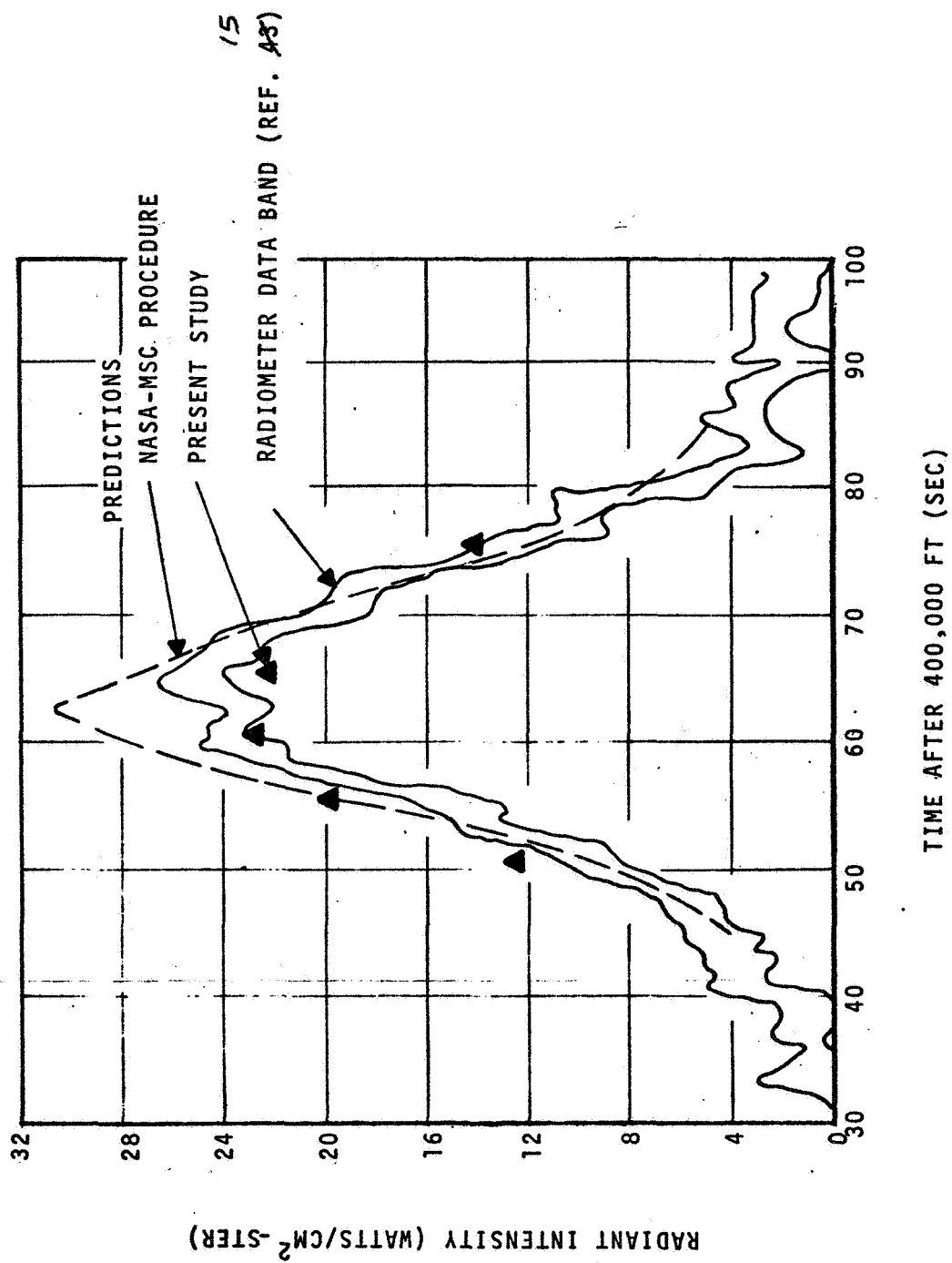


Figure 32. Predicted and Measured Radiation Intensities for Apollo 4

the predicted values without radiation coupling). These have been demonstrated to be roughly valid in various studies (Refs. 6, 42 and 43) and tend to justify the approach in obtaining the total flux (radiation plus convection) which reaches the wall.*

4.4.2 Conclusions

The transport quantities predicted in the present study differ in some details from those obtained using the NASA/MSC procedure, which predict intensities slightly higher than the measured data. However, the differences were within the uncertainty range one might expect in making such predictions (± 10 -15 percent, generally). Moreover, the differences between prediction procedures are inconsequential relative to the total (radiative plus convective) heating flux. Thus, the results of the present study tend to support the NASA/MSC procedures for that portion of the body and trajectory where radiation heating is a significant contribution to the total heating.

* The spectral distributions of the incident flux cannot be so readily justified, as carbon containing boundary layers tend to absorb in the ultraviolet and emit in the visible. Thus, one would expect the boundary layer to cause an increase in the visible flux.

SECTION 5

MATERIAL RESPONSE MECHANISM STUDIES

The Apollo heat shield consists of a low density ablation material bonded to a primary structure. The low density ablation material is Avcoat 5026-39/HC-GP, an epoxy novalac resin with phenolic microballoons and silica fiber reinforcement in a fiberglass honeycomb matrix. Although the epoxy-honeycomb combination maintains its cellular appearance after fabrication, the virgin material is treated theoretically as a continuum with uniform thermal and mechanical properties.

Upon being subjected to sufficiently high heating, the Avcoat material decomposes chemically forming a pyrolysis gas and a char residue. The fully-developed char is principally carbon and silica but does contain other ash impurities, while the primary pyrolysis gas is in a highly nonequilibrium state, containing substantial excess carbon. There is considerable experimental evidence that under certain conditions the pyrolysis gas cokes out carbon which then deposits on the char. Also, chemical reactions between the carbon and silica in the char can take place. There are several competing mechanisms which interact to control the surface ablation response. These include carbon oxidation, redeposition of silica on the surface due to reaction of silica-carbon reaction products with oxygen in the boundary layer, and liquid-layer runoff of silica. The situation is further complicated by the chemical state of the pyrolysis gas which can be oxidizing, reducing, or inert relative to the char material in the vicinity of the surface.

In a previous study of Apollo material response mechanisms^{44,45} the virgin material was permitted to decompose into a char and pyrolysis gas, but coking and silica-carbon reactions in-depth were not allowed. Several alternative surface thermochemical ablation models were considered, and it was seen that best agreement with ground and flight data could be achieved by an empirical B'_C-T_w relation coupled with a "fissure" model where the pyrolysis gas is considered to escape without contributing to surface chemistry events or to a blowing reduction for heat and mass transfer. An alternative approach was employed in Reference 46 which reports substantial agreement with flight data considering coking and an empirical $s-T_w$ relation limited by diffusion-controlled carbon ablation. However, neither of these studies had the benefit of the convective heating correlations generated under the present study. Therefore,

while the development of an improved in-depth and surface material response model was not a major objective of the present study, some attention was directed to this problem in order to provide an improved baseline for the evaluation of flight convective heating data.

The basic material decomposition model is the same as that employed previously in References 44 and 45. It is summarized in Section 5.1. After careful consideration of various improvements that could be made in the analysis of char layer mechanisms, a simple coking model was selected as being consistent with the available data, with the level of effort of the present study, and with practical computational considerations. This model is described in Section 5.2. The thermal properties model is described in Section 5.3. The validity of the in-depth theoretical approach and thermal properties model is assessed in Section 5.4 by a series of driver temperature calculations. A surface thermochemical ablation model consistent with the in-depth coking model is presented in Section 5.5. The results of the material response studies are summarized in Section 5.6.

5.1 MATERIAL DECOMPOSITION MODEL

The material decomposition model utilized in the present study is the same as that considered in previous studies^{44,45}. On the basis of chemical and thermogravimetric analysis data supplied by NASA/MSFC, the elemental composition of the primary pyrolysis gas and char is taken to be as indicated in Table 14.

TABLE 14
CHAR AND PYROLYSIS GAS ELEMENTAL MASS FRACTIONS IN
AVCOAT 5026-39/HC-GP (PRIOR TO COKING)

Element	Pyrolysis Gas	Char
H	0.0930	--
B	--	0.0079
C	0.5470	0.4880
N	0.0190	--
O	0.3410	0.2605
Al	--	0.0212
Si	--	0.1852
Ca	--	0.0366

These compositions are based on a virgin material density of 34.0 lb/ft³ and a primary char density of 16.0 lb/ft³, where the char is composed of the compounds listed in Table 15. At elevated temperatures, coking is permitted to occur and

TABLE 5
CHAR SPECIES MASS FRACTIONS (PRIOR TO COKING)

Species	Mass Fraction
C*	0.4880
SiO ₂ *	0.3971
Al ₂ O ₃ *	0.0384
CaO*	0.0510
B ₂ O ₃ *	0.0255

the composition of the pyrolysis gas and char differ from the values presented in Tables 14 and 15. Furthermore, for the purposes of the in-depth analysis, the char is treated as carbon and a second material with the properties of silica. These considerations will be discussed further in Section 5.2.

The model for plastic decomposition which is used by the CMA program is of the form

$$\frac{\partial \rho}{\partial \theta} = B e^{-E_a/RT} \rho_o \left(\frac{\rho - \rho_r}{\rho_r} \right)^{\psi} \quad (47)$$

where

ρ = instantaneous density

ρ_r = residual or char density

ρ_o = original or virgin density

θ = time

T = temperature

The numerical values used for the Apollo heat-shield material in the present studies are:

$$\rho_o = 34.0 \text{ lb/ft}^3$$

$$\rho_r = 16.0 \text{ lb/ft}^3$$

$$B = 1.06 \times 10^6 \text{ sec}^{-1}$$

$$\psi = 2.5$$

$$E_a/R = 24,530^\circ\text{R}$$

Further details regarding the CMA decomposition model are presented in References 7 and 10.

5.2 CHAR LAYER MODEL INCLUDING COKING

5.2.1. General

Extensive tests of heat-shield samples (cores) taken from recovered Apollo vehicles and from laboratory tests have been conducted by AVCO Corporation²⁻⁴. A summary of their chemical and visual microscopic observations of these cores is presented in Figure 33 which was taken from Reference 3. It can be seen that many complex phenomena take place in the char layer at least to some extent. The two physical events of most concern are the following:

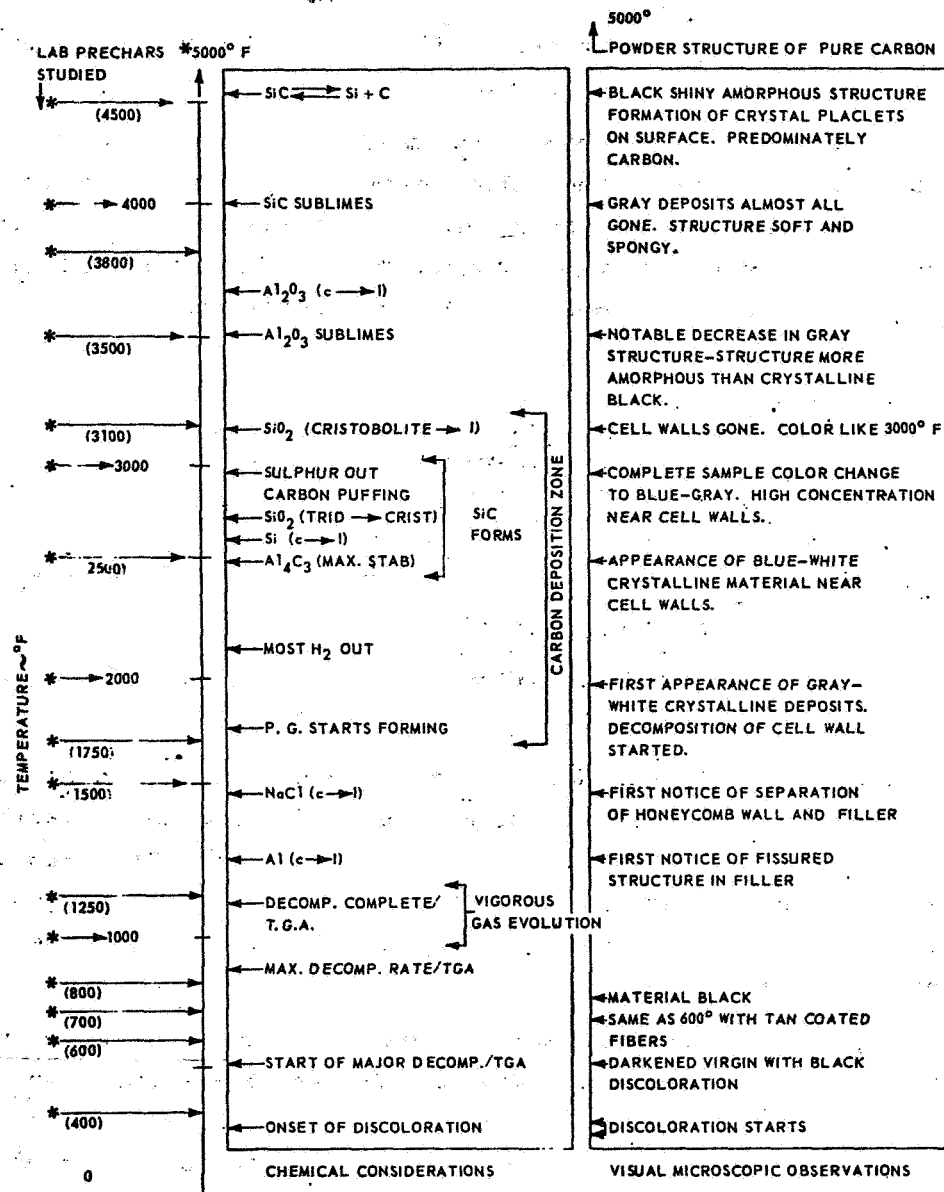
1. Carbon deposition onto the char matrix ("coking") from the initial pyrolysis gases as they pass through the char as evidenced by the formation of pyrolytic graphite (referred to as P.G. in Fig. 33).
2. Reactions between carbon residue and silica reinforcement in the char as evidenced by the formation of SiC*.

Both of these effects, if they take place to any great extent, could appreciably affect the material response. There is little question but that the amount of coking is extensive; substantial increases in char density and carbon content have consistently been observed in the AVCO studies within a temperature range identified in Figure 33. The degree to which silica-carbon reactions actually take place is more difficult to assess; the AVCO studies show only a trace of SiC* and show actually an increase in ash content in the char layer*; furthermore the reaction of silica is obscured by the fact that silica can reform at the surface in the presence of oxygen and silica melting and liquid flow can occur.

Further complicating the selection of an in-depth model is the interaction between in-depth phenomena and surface thermochemistry phenomena. Both silica-carbon reactions and coking change the chemical compositions of the char and the gases injected into the boundary layer, and thus add to the number of parameters which must be considered in the surface thermochemistry solution for the CMA code.

A description of the CMA code and its coupling to the surface thermochemical ablation problem through a transfer-coefficient approach is presented in Appendix A. In brief, surface thermochemistry information is generated with the EST program (or an equivalent code) and assembled in tables which are used as input to the CMA program. In the standard CMA program, these tables are based on the following three independent variables:

*The ash content was obtained in the AVCO core analyses by chemical removal of the carbon and hydrogen from the char²⁻⁴. Thus the ash would be expected to be principally silica plus the other impurities listed in Table 15. However, it is speculated in Reference 3 that the ash may contain substantial unburned carbon.



Source: Reference 3

Figure 33. Chemical and Visual Microscopic Observations of Flight-Tested Apollo Heat-Shield Material

1. Pressure
2. Dimensionless pyrolysis gas rate B'_g
3. Dimensionless char erosion rate B'_c

Note that the chemical compositions of the char and pyrolysis gas do not appear in the list of variables since they are assumed to be fixed.

As observed above, silica-carbon reactions and coking, if considered in the ablation calculations, change these previously fixed chemical compositions of char and pyrolysis gas. In addition, the silica-carbon reaction introduces a new "product gas" which must be accounted for. These considerations yield the following list of parameters for a transfer-coefficient approach to the surface ablation calculation:

1. Pressure
2. Dimensionless pyrolysis gas rate B'_g
3. Pyrolysis gas composition as influenced by coking
4. Silica-carbon reaction gas products injection rate B'_{g_2}
5. Dimensionless char rate B'_c
6. Char structure composition as influenced by both coking and silica-carbon reactions.

This number of independent variables would result in an enormous table of the enthalpy and temperature information needed for the ablation calculations, far too large for a design-oriented computer code. To obtain an appropriately simple ablation code required the careful consideration of a number of alternative simplifications in the surface state solution. Some of the more attractive simplifications examined were

1. Ignore silica-carbon reactions. This removes parameter 4 and also greatly simplifies the chemical nature of the surface state solution. As mentioned above, core-data from References 2 through 4 do not actually substantiate the occurrence of extensive silica-carbon reactions, so this simplification seems justifiable.

2. Invoke either the fissure model or the inert injectant gas model of References 44 and 45. This suppresses chemical interactions with the injected pyrolysis and reaction gases and thus effectively deletes parameters 2, 3 and 4. There is much experimental support for the belief that injected gases are effectively inert in the surface state solution^{44,45}; however, one does not have to assume a frozen pyrolysis gas, necessarily, to achieve this result. This was illustrated in References 44 and 45 and will be demonstrated further in

Section 5.4 of this report. There is no question that numerous fissures occur in the Apollo heat-shield material as demonstrated by the AVCO core studies³. However, it is unlikely that the effect of these fissures is such as to prohibit completely any mixing between the pyrolysis gas and boundary layer species.

3. Simplify the thermochemical model of char erosion to account for carbon erosion only, treating the silica as chemically inert. This eliminates parameter 6. This simplification has frequently been used in the past for carbon-rich silica-reinforced chars and has never really been shown to be inappropriate. Indeed, the core analyses of the Apollo material support this model³. A study of several core results reported in Reference 3 showed that the increase in ash density below the heated surface mentioned previously often corresponds approximately to the amount of silica originally located in the eroded portion of the heat shield.

4. Drastically simplify the coking model, perhaps by empirically adjusting the char density, or by allowing condensed phase carbon to appear in the pyrolysis gas but not to be deposited on the char.

The best balance between the simplicity required of a design code and the detail required to model the most important physics of the Apollo material response appears to justify the adoption of simplifications 1 and 3 from the list above. These simplifications eliminate the chemical influence of silica on both surface and in-depth ablation mechanisms and reduce the surface ablation problem to one of carbon erosion in the presence of reactive pyrolysis gases.

Elimination of silica-carbon reactions in depth and consideration of a carbonaceous surface leaves four parameters if coking kinetics are to be treated precisely (parameters 1, 2, 3 and 5 listed above). However, since reaction rates are not known anyway, it was decided to employ a more global approach which has the decided advantage that it reduces the number of parameters to three. This is accomplished by assuming the composition of the pyrolysis gas \tilde{K}_C to be a function of temperature and pressure only.* In particular, the pyrolysis gas is assumed to be frozen below a temperature T_L and to be in equilibrium above a temperature T_H . At intermediate temperatures, the amount of carbon in the pyrolysis gas is assumed to vary linearly from the frozen composition at T_L to the equilibrium composition at T_H . With \tilde{K}_C a function of temperature and pressure only, the composition of the pyrolysis gas is known if P and T_w are known. Thus, as far as the surface chemistry tables are concerned, the only parameters which are required are P , B'_g and T_w . Note that for this purpose T_w is substituted in place of the previously employed B'_c .

This approach has a powerful computational advantage in addition to the surface thermochemistry simplification noted above. Obviously, the assumption

*The pressure is taken to be the boundary-layer pressure which varies with time; pressure is not permitted to vary in-depth in the present approach.

of the composition function $\tilde{K}_{C_g}(T,p)$ eliminates any detailed considerations of coking kinetics. "Coking" is computed merely by reference to the $\tilde{K}_{C_g}(T,p)$ chart, as will be discussed in detail below.

While this model is certainly very desirable from a computational point of view, it has merit only if it represents the known physics adequately. A rather extensive study of the Flight AS 501 core evaluation performed by AVCO³ was made which suggested that coking typically starts at 2250°R and is completed by 3600°R. Note that this temperature range is in substantial agreement with the core summary chart prepared by AVCO (Fig. 33).

In order to complete the model, it is necessary to allow for the disposition of silica as the surface recedes. While there seems on the basis of the AVCO ash profile data to be some evidence for the buildup of silica within the char layer, this data is somewhat questionable as mentioned previously and thus does not warrant the development of such a model. Therefore, it was decided to let the silica be removed mechanically (with no net energy absorption) as surface carbon is eroded.

The appropriate values of pyrolysis gas carbon fraction \tilde{K}_{C_g} and enthalpy h_g in the equilibrium regime ($T > 3600^\circ\text{R}$) were determined with the EST program operated in a conventional closed-system mode (see Appendix A). Calculations were performed for a gas mixture with the chemical composition of the frozen pyrolysis gas (see Table 14); any carbon present in excess of that required for equilibrium precipitates out, and the residual gas composition is that which is in equilibrium with carbon at the pressure and temperature considered. The resulting equilibrium values of \tilde{K}_{C_g} and h_g are presented in Figures 34 and 35, respectively. Also shown in Figure 34 is the frozen value of \tilde{K}_{C_g} applicable at temperatures below 1250°K (2250°R) and the assumed linear decrease in carbon content in the coking region from the frozen condition at 1250°K to the equilibrium condition at 2000°K (3600°R). The h_g in the frozen pyrolysis-gas region was taken to be the same as that employed in previous studies⁴⁴.

Analysis and programming developments to implement this in-depth (sub-surface) model used the existing CMA code as a basis. The restriction of coking events to 2250°R and above made it feasible to consider coking as occurring only in the "mature char" portions of the material, thus separating the pyrolysis-events computation from the coking calculations and simplifying the coding still further. Coking mass-balance operations are simplified, as noted above, by the use of the $\tilde{K}_{C_g}(T,p)$ function; this allows coking rates to be determined by simple reference to the \tilde{K}_{C_g} table appropriate to each node, with due reference to the local rates of gas flow. Energy events associated with coking, although more complex, are treated in the same general manner. The nodal energy balance

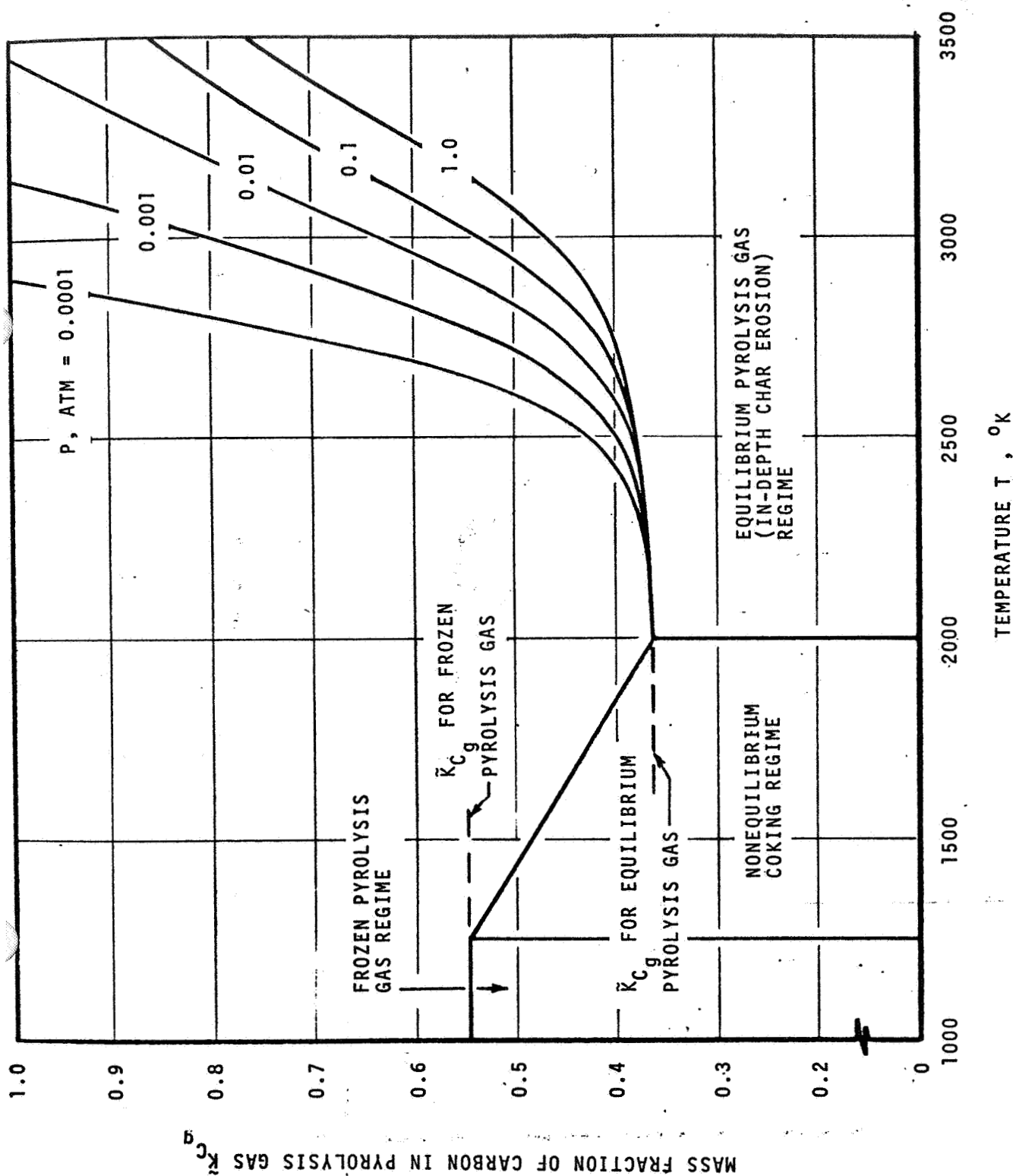


Figure 34. Pyrolysis-Gas Carbon Mass Fraction for the Apollo Material Considering Coking

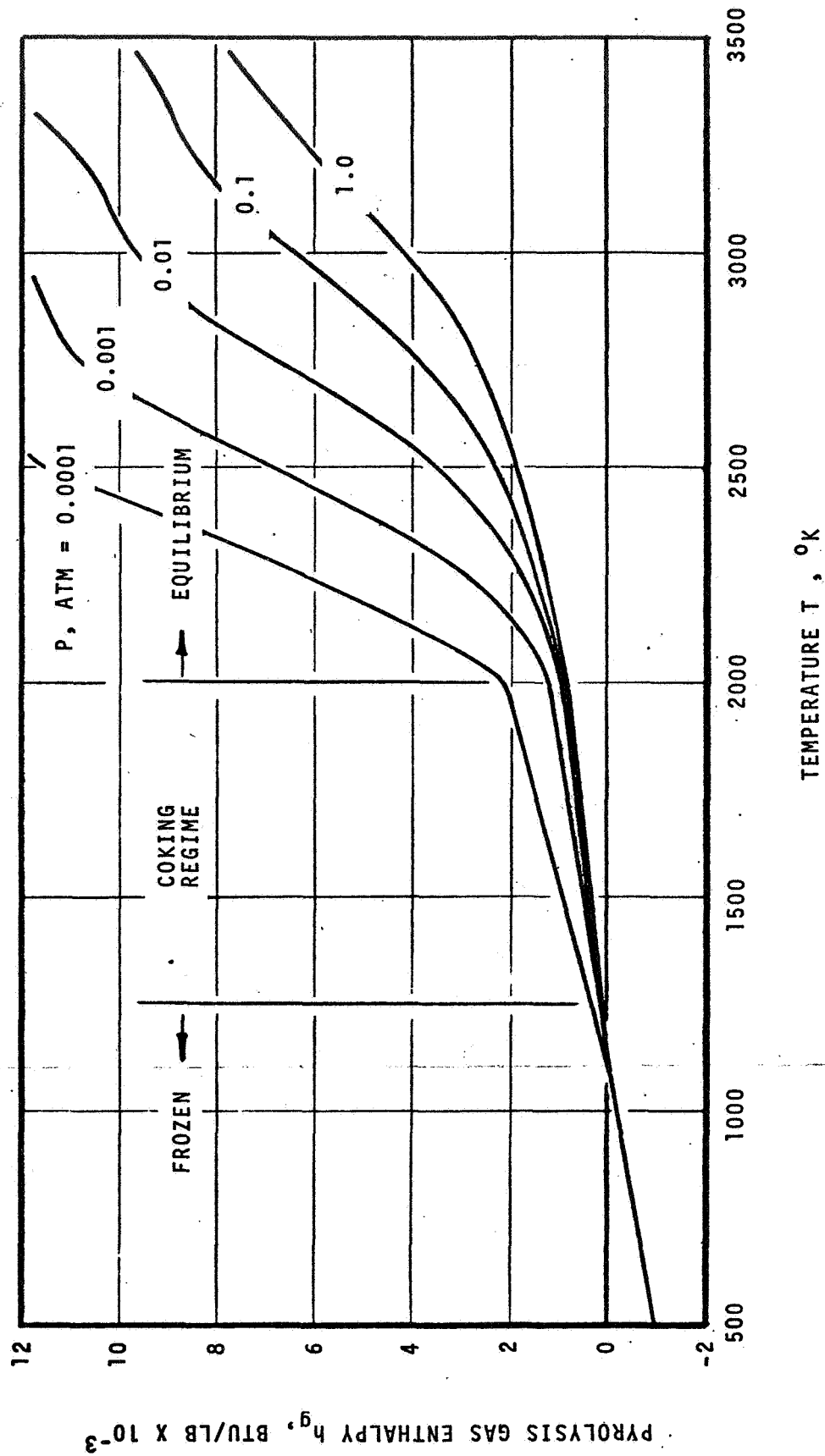


Figure 35. Pyrolysis Gas Enthalpy for the Apollo Material Considering Coking

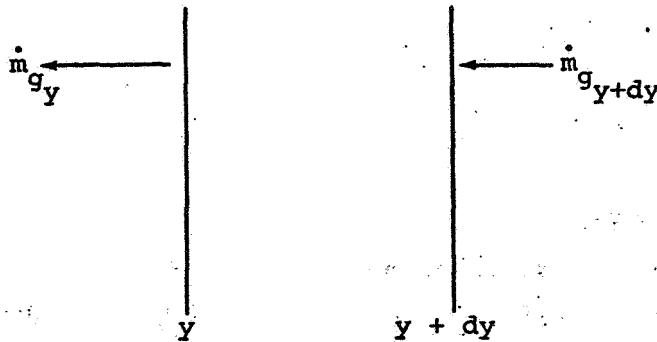
operations when coking occurs are quite similar to those in the existing CMA program, and only minor coding changes were required to allow coking to be considered. The analysis is discussed in Section 5.2.2 which follows. The details of the coding changes to permit coking are presented in Appendix A.

5.2.2 Details of Analysis Modifications

a. Mass Balance Operations

Differential Equation

The differential equation for mass conservation during coking derives from the physical situation illustrated in the sketch:



Here \dot{m}_g describes the total gas flow (lb/sec) at a point y .

Since carbon is the material being transferred or "coked", it is desired to write a "conservation of carbon" law. The rate of carbon flow in and out of the carbon volume is given by

$$\text{Carbon in} = \tilde{K}_{Cg_{y+dy}} \dot{m}_{g_{y+dy}} = \left(\tilde{K}_{Cg} + \frac{\partial \tilde{K}_{Cg}}{\partial y} dy \right) \left(\dot{m}_{g_y} + \frac{\partial \dot{m}_g}{\partial y} dy \right) \quad (48)$$

$$\text{Carbon out} = \tilde{K}_{Cg_y} \dot{m}_{g_y} \quad (49)$$

Also the rate of change of local char density is given by

$$\left(\frac{\partial \rho}{\partial \theta} \right)_y = \frac{\text{carbon in} - \text{carbon out}}{\text{volume}} \bigg|_y = \frac{\tilde{K}_{Cg_y} \frac{\partial \dot{m}_g}{\partial y} + \dot{m}_{g_y} \frac{\partial \tilde{K}_{Cg}}{\partial y}}{A} \quad (50)$$

where A is the local cross-section area. The conservation of mass gives

$$\left(\frac{\partial \dot{m}_g}{\partial y} \right)_\theta = \frac{\partial}{\partial \theta} (\rho A)_Y = A \left(\frac{\partial \rho}{\partial \theta} \right)_Y + \rho \left(\frac{\partial A}{\partial \theta} \right)_Y \quad (51)$$

Substitution of Equation (51) into Equation (50) gives

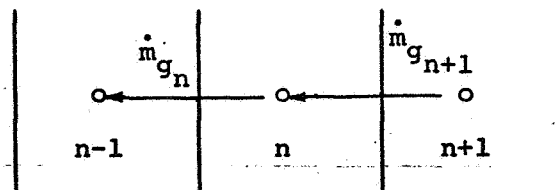
$$\left(\frac{\partial \rho}{\partial \theta} \right)_Y = \tilde{K}_{C_{g_Y}} \left(\frac{\partial \rho}{\partial \theta} \right)_Y + \frac{\dot{m}_{g_Y}}{A} \frac{\partial \tilde{K}_{C_g}}{\partial y} \quad (52)$$

which simplifies to the desired relation

$$\left(\frac{\partial \rho}{\partial \theta} \right)_Y = \frac{\frac{\dot{m}_g}{A} \frac{\partial \tilde{K}_{C_g}}{\partial y}}{(1 - \tilde{K}_{C_{g_Y}})} \quad (53)$$

Difference Equation

An appropriate difference version of Equation (53) for use in the CMA code may be obtained either from a differencing of Equation (53) or from an independent derivation analogous to that leading to Equation (53). The second procedure is generally safer. Consider the finite difference node n and surrounding nodes $n-1$ and $n+1$ as illustrated in the sketch:



The rate of carbon flow in and out of the node is given by

$$\text{carbon in} = \dot{m}_{g_{n+1}} \tilde{K}_{C_{g_{n+1}}} \quad (54)$$

$$\text{carbon out} = \dot{m}_{g_n} \tilde{K}_{C_{g_n}} \quad (55)$$

ORIGINAL PAGE IS
OF POOR QUALITY

Hence

$$\dot{m}_{\text{coke}} = \text{carbon in} - \text{carbon out} = \dot{m}_{g_{n+1}} \tilde{K}_{C_{g_{n+1}}} - \dot{m}_{g_n} \tilde{K}_{C_{g_n}} \quad (56)$$

The conservation of mass gives

$$\dot{m}_{\text{coke}} = \dot{m}_{g_{n+1}} - \dot{m}_{g_n} \quad (57)$$

or

$$\dot{m}_{g_n} = \dot{m}_{g_{n+1}} - \dot{m}_{\text{coke}} \quad (58)$$

Substitution of Equation (58) into Equation (56) yields

$$\dot{m}_{\text{coke}} = \dot{m}_{g_{n+1}} \tilde{K}_{C_{g_{n+1}}} - (\dot{m}_{g_{n+1}} - \dot{m}_{\text{coke}}) \tilde{K}_{C_{g_n}} \quad (59)$$

which gives, after rearrangement

$$\dot{m}_{\text{coke}} = \frac{\dot{m}_{g_{n+1}} (\tilde{K}_{C_{g_{n+1}}} - \tilde{K}_{C_{g_n}})}{(1 - \tilde{K}_{C_{g_n}})} \quad (60)$$

The density change rate for node n of thickness δ_n is

$$\left. \frac{\partial \rho}{\partial \theta} \right)_y = \frac{\dot{m}_{\text{coke}}}{A \delta_n} = \frac{\dot{m}_{g_{n+1}}}{A} \frac{(\tilde{K}_{C_{g_{n+1}}} - \tilde{K}_{C_{g_n}})}{\delta_n} \frac{1}{(1 - \tilde{K}_{C_{g_n}})} \quad (61)$$

which is the difference analog of Equation (53).

b. Energy Equation

The energy equation does not change from the quite general energy equation built into the CMA code as reported in Reference 7 except in one minor detail. This equation, repeated for convenience,*

$$\rho C_p \frac{\partial T}{\partial \theta} \bigg|_x = \frac{1}{A} \frac{\partial}{\partial x} \left(kA \frac{\partial T}{\partial x} \right)_{\theta} + (h_g - \bar{h}) \frac{\partial \rho}{\partial \theta} \bigg|_y + \dot{s} \rho C_p \frac{\partial T}{\partial x} \bigg|_{\theta} + \frac{\dot{m}_g}{A} \frac{\partial h_g}{\partial x} \bigg|_{\theta} \quad (62)$$

may be viewed as a "conservation of sensible energy" equation at constant x , and thus has a close relation with the usual form of energy equations in applications including chemical changes. The second term on the right hand side represents the "creation of sensible energy" due to pyrolysis.

The one change required to change this equation from a "pyrolysis equation" to a "coking" equation merely changes \bar{h} to h_{C*} where h_{C*} (the enthalpy of carbon) is the enthalpy associated with a unit mass of coking.

The difference form of the energy equation, also reported in Reference 7, naturally has the same form in the coking zone.

c. Coked Zone Properties

The analysis changes described above to add coking events to the CMA code logically required some extension to the treatment of property values in the code so as to include the coked zone properties in a realistic manner. The coking zone specific heat may realistically be treated as a straightforward mass-weighted average of the specific heats for silica and carbon. No such simple rule may be suggested for the thermal conductivity of the coked material. In the absence of a reliable theoretical model for the thermal conductivity of a heterogeneous composite, the user is allowed to specify the conductivity of "coked char" as a function of density and temperature.

5.3 MATERIAL THERMAL PROPERTIES MODEL

The thermal properties used in the present study for the Apollo heat shield virgin material and char are presented in Tables 16 and 17, respectively,

*The symbols x and y both refer to the coordinate normal to the ablating surface; x is fixed to the receding surface and y is fixed in space relative to the back wall. The symbol \bar{h} is the enthalpy associated with a unit mass change in condensed phase in the pyrolysis zone.

as functions of temperature. With the exception of char thermal conductivity at high temperature (above 2660°R), these data are identical to those considered in a previous study⁴⁴.

TABLE 16
VIRGIN PLASTIC THERMAL PROPERTIES

T °R	C _p Btu/lb°R	k Btu/ft sec°R	ε
460	0.350	1.33 x 10 ⁻⁵	0.65
560	0.350	1.61 x 10 ⁻⁵	0.65
660	0.356	1.83 x 10 ⁻⁵	0.65
760	0.360	1.97 x 10 ⁻⁵	0.65
860	0.370	2.00 x 10 ⁻⁵	0.65
960	0.420	1.94 x 10 ⁻⁵	0.65
1,060	0.440	1.86 x 10 ⁻⁵	0.65
1,160	0.440	1.83 x 10 ⁻⁵	0.65
1,260	0.440	1.83 x 10 ⁻⁵	0.65
1,360	0.440	1.89 x 10 ⁻⁵	0.65
1,460	0.440	2.03 x 10 ⁻⁵	0.65
5,000	0.440	2.03 x 10 ⁻⁵	0.65

Virgin plastic and char specific heat data are the same as those used as of March 1968 in the NASA/MSC STAB II code for the Apollo material⁴⁷. Virgin and char emissivities are held constant at 0.65 consistent with the data of References 48 and 49.* The thermal conductivity of the virgin plastic is based on AVCO laboratory test data presented in Reference 2. The char thermal conductivity is also based on these data, interpreted in the light of a series of driver-temperature flight predictions presented in Section 5.4.

The AVCO tests demonstrate that the char conductivity is strongly dependent upon the highest temperature which the char has previously experienced, the so-called pre-char temperature. For example, the conductivity at a temperature of 3000°R is substantially reduced if the char has previously experienced a temperature of 4500°R or above. The envelope of the AVCO conductivity charts

* Emissivity data for the Apollo material presented in Reference 3 would suggest a somewhat lower value at temperatures above 2000°R.

TABLE 17
CHAR THERMAL PROPERTIES

T °R	C _p Btu/lb °R	k Btu/ft sec °R	ε
460	0.35	1.33 x 10 ⁻⁵	0.65
860	0.35	2.00 x 10 ⁻⁵	↓
1,060	0.35	1.86 x 10 ⁻⁵	
1,360	0.37	1.94 x 10 ⁻⁵	
1,460	0.40	2.03 x 10 ⁻⁵	
1,710	0.45	2.89 x 10 ⁻⁵	
1,860	0.50	4.03 x 10 ⁻⁵	
2,060	0.50	6.81 x 10 ⁻⁵	
2,260	↓	1.00 x 10 ⁻⁴	
2,460		1.16 x 10 ⁻⁴	
2,660		1.38 x 10 ⁻⁴	
2,860		1.27 x 10 ⁻⁴	
3,060		1.11 x 10 ⁻⁴	
3,260		9.00 x 10 ⁻⁵	
3,460		1.93 x 10 ⁻⁵	
3,660		2.08 x 10 ⁻⁵	
3,860		2.18 x 10 ⁻⁵	
4,060		2.22 x 10 ⁻⁵	
4,260		2.20 x 10 ⁻⁵	
4,460		2.08 x 10 ⁻⁵	
4,660		1.94 x 10 ⁻⁵	
4,860		1.82 x 10 ⁻⁵	
5,060		8.5 x 10 ⁻⁶	
5,260		7.4 x 10 ⁻⁶	
5,660		4.0 x 10 ⁻⁶	
5,860		2.1 x 10 ⁻⁶	
6,060	↓	1.5 x 10 ⁻⁶	↓
6,460	0.50	7.0 x 10 ⁻⁷	

(i.e., when the pre-char temperature is equal to the char temperature) is appropriate to use prior to the first peak heating in a typical Apollo reentry trajectory, but as demonstrated in Section 5.4 leads to substantial errors later in the trajectory when char-layer temperatures drop substantially. The driver temperature calculations indicated that reasonable accuracy can be obtained while considering only temperature (and not pre-char temperature) as a parameter by considering the envelope values at temperatures below 2660°R and "averaged" values at higher temperatures. It is these latter values which are presented in Table 17.

The pyrolysis gas enthalpy was presented previously in Figure 35 as a function of temperature and pressure. The values at temperatures below 2250°R are representative of the frozen pyrolysis gas, the values at temperatures above 3600°R are based on equilibrium for a gas with the composition of Table 14 except for the carbon content which is obtained from Figure 34. The pyrolysis gas enthalpies at intermediate temperatures are obtained by interpolation between these two extremes.

Heats of formation of the virgin plastic, char, and pyrolysis gas for a datum of 536°R are

$$\Delta H_{f_{vp}} = -2,390 \text{ Btu/lb}$$

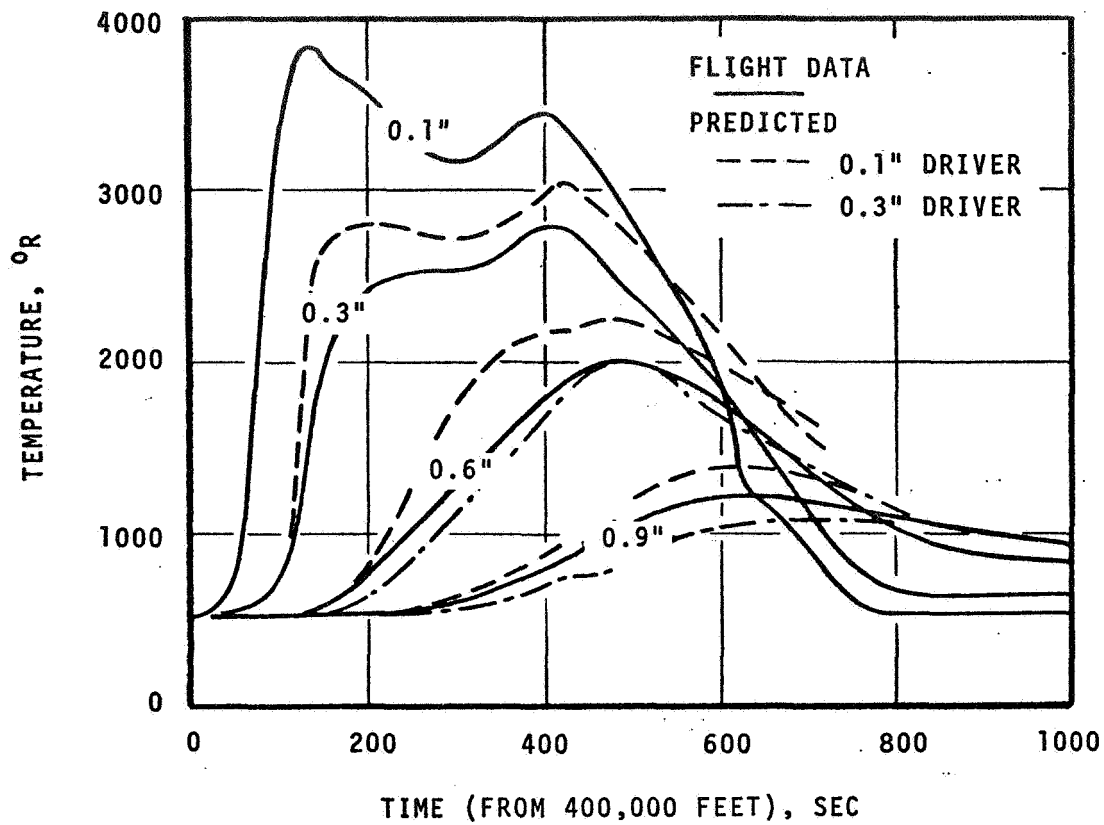
$$\Delta H_{f_c} = -3,310 \text{ Btu/lb}$$

$$\Delta H_{f_{pg}} = 0$$

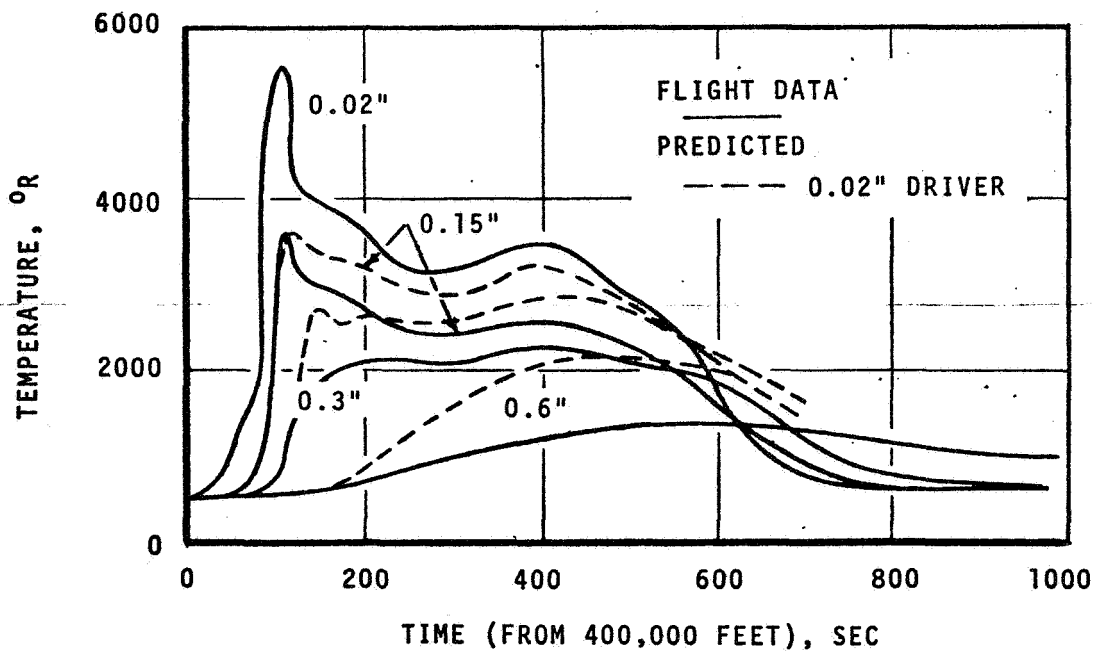
5.4 DRIVER TEMPERATURE CALCULATIONS

An evaluation of the in-depth thermal response model of the Apollo material presented in Sections 5.1 through 5.3 was carried out utilizing the "driver temperature" option of the Charring Material Ablation (CMA) program (see Appendix A). Driver temperature calculations were performed for several thermocouples from Apollo flights AS 501 and AS 502. The specific cases considered are identified in Table 18.

Initially Cases 1 through 3 were considered using the "envelope" values for char thermal conductivity. The results are presented in Figures 36a and 36b for Body Points 705 and 707, respectively. It can be seen that the predicted in-depth temperatures agree quite well with the flight data prior to peak heating for all cases and agree reasonably well (within 200°F) throughout the flight for Case 2. The agreement is not as good for the other two thermocouples which, being nearer the surface, were subjected to higher temperatures.



a. Flight AS 502, Body Point 705



b. Flight AS 502, Body Point 707

Figure 36. Driver Temperature Calculations Using Envelope of AVCO Char Conductivity Data

TABLE 18

SUMMARY OF DRIVER TEMPERATURE CASES

Case	Flight	Body Point	Driver Thermocouple (Depth from Surface, in)
1	AS 502	705	0.10
2	AS 502	705	0.30
3	AS 502	707	0.02
4	AS 502	707	0.15
5	AS 501	705	0.10
6	AS 501	705	0.30

In particular, the in-depth temperatures are substantially overpredicted after the first peak heating. Although it is impossible to isolate and identify all the factors which contribute to the disagreement, it is reasonable to expect on the basis of the AVCO conductivity charts that the unrealistically high thermal conductivities in the outer (previously hot) parts of the ablator are a major contributor to the overprediction of in-depth temperatures.

Modification of the CMA program to permit "pre-char" temperature as a parameter would be rather extensive and was considered to be beyond the scope and intention of the present study. Therefore, a simpler, although cruder, method was adopted where an effective temperature-dependent char conductivity was sought by trial-and-error which would yield acceptably small errors. Guided by the AVCO charts, the char conductivity was reduced at temperatures above 2660°R from the envelope values to the values presented in Table 17.

Predicted in-depth temperatures using these effective char conductivities are shown in Figure 37 for Cases 1 and 2, Figure 38 for Cases 3 and 4, and Figure 39 for Cases 5 and 6. Substantial improvement was obtained for Case 1 where the maximum driver temperature is 3800°R. The results for Case 2 are virtually unchanged, and thus remain satisfactory, since the maximum temperature is only 2800°R. The results for Cases 4, 5, and 6, with maximum temperatures of 3500, 4200, and 3300°R, respectively, are also quite satisfactory. The agreement in Case 3, with a "measured" peak temperature of 5500°R, is still not good. However, there is evidence that this thermocouple (originally 0.02" from the surface) broke through the surface fairly early in the flight and may be

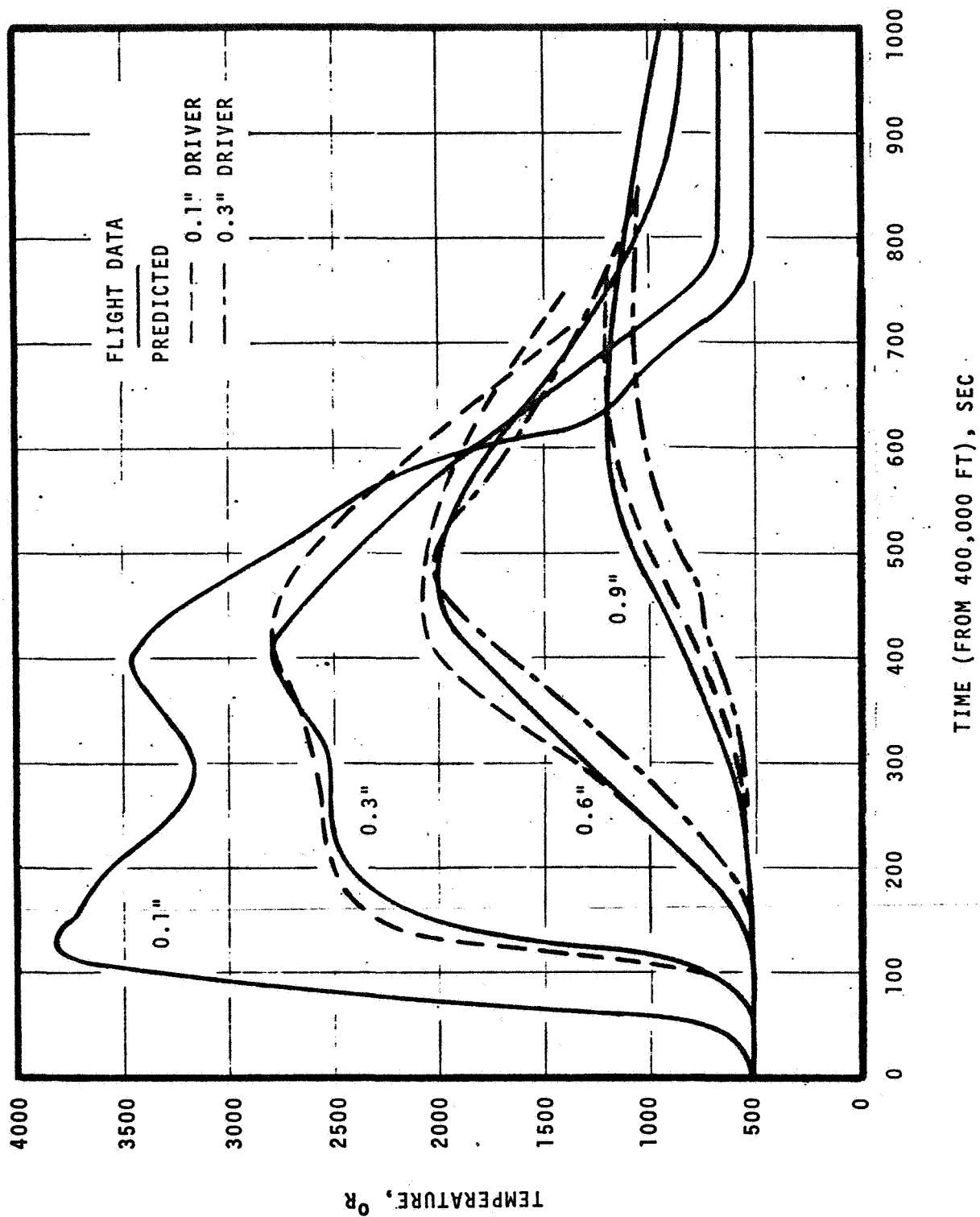


Figure 37. Driver Temperature Calculations for Flight AS 502, Body Point 705 Using Effective Char Thermal Conductivity Data

ORIGINAL PAGE IS
OF POOR QUALITY

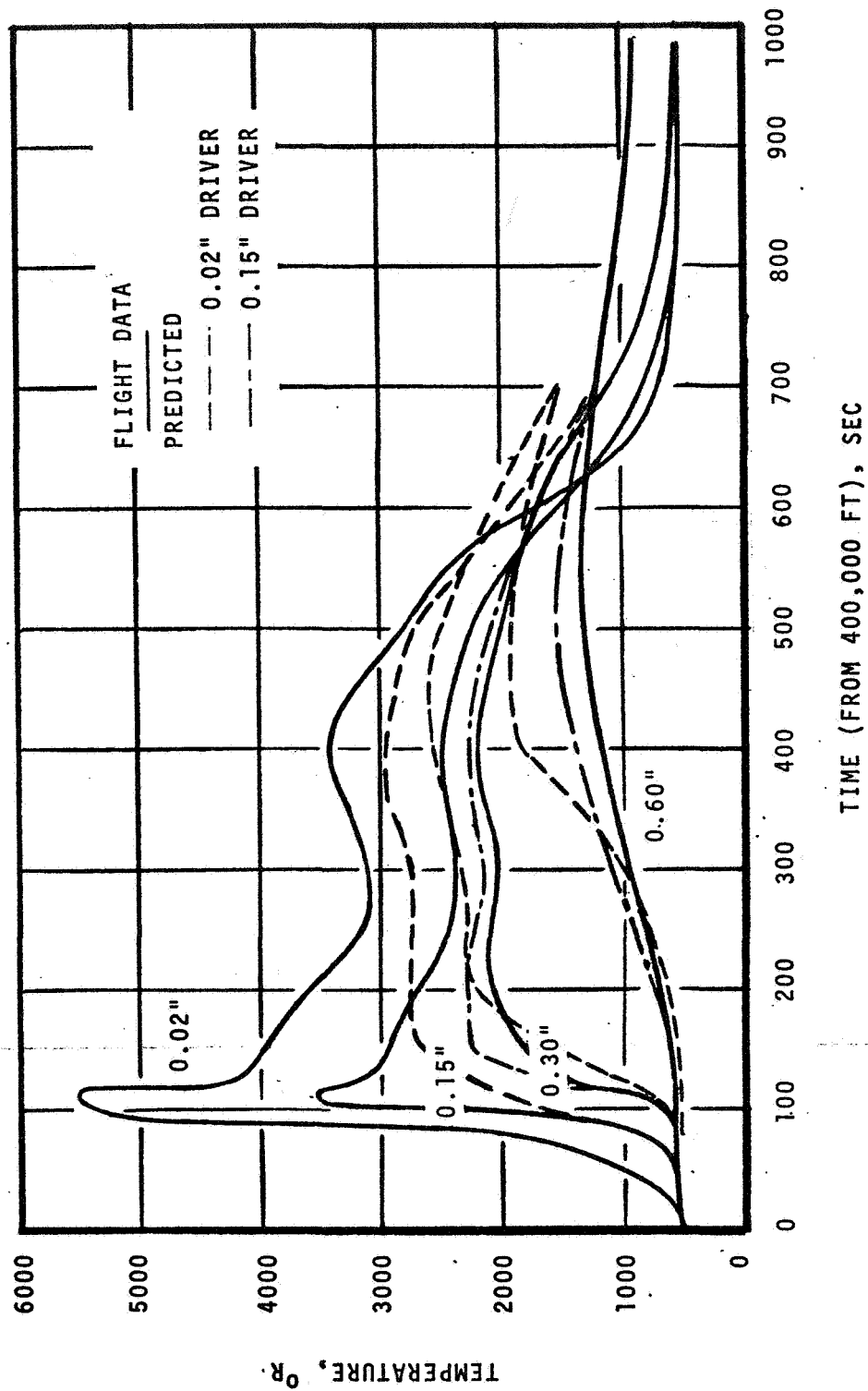


Figure 38. Driver Temperature Calculations for Flight AS 502, Body Point 707 Using Effective Char Thermal Conductivity Data

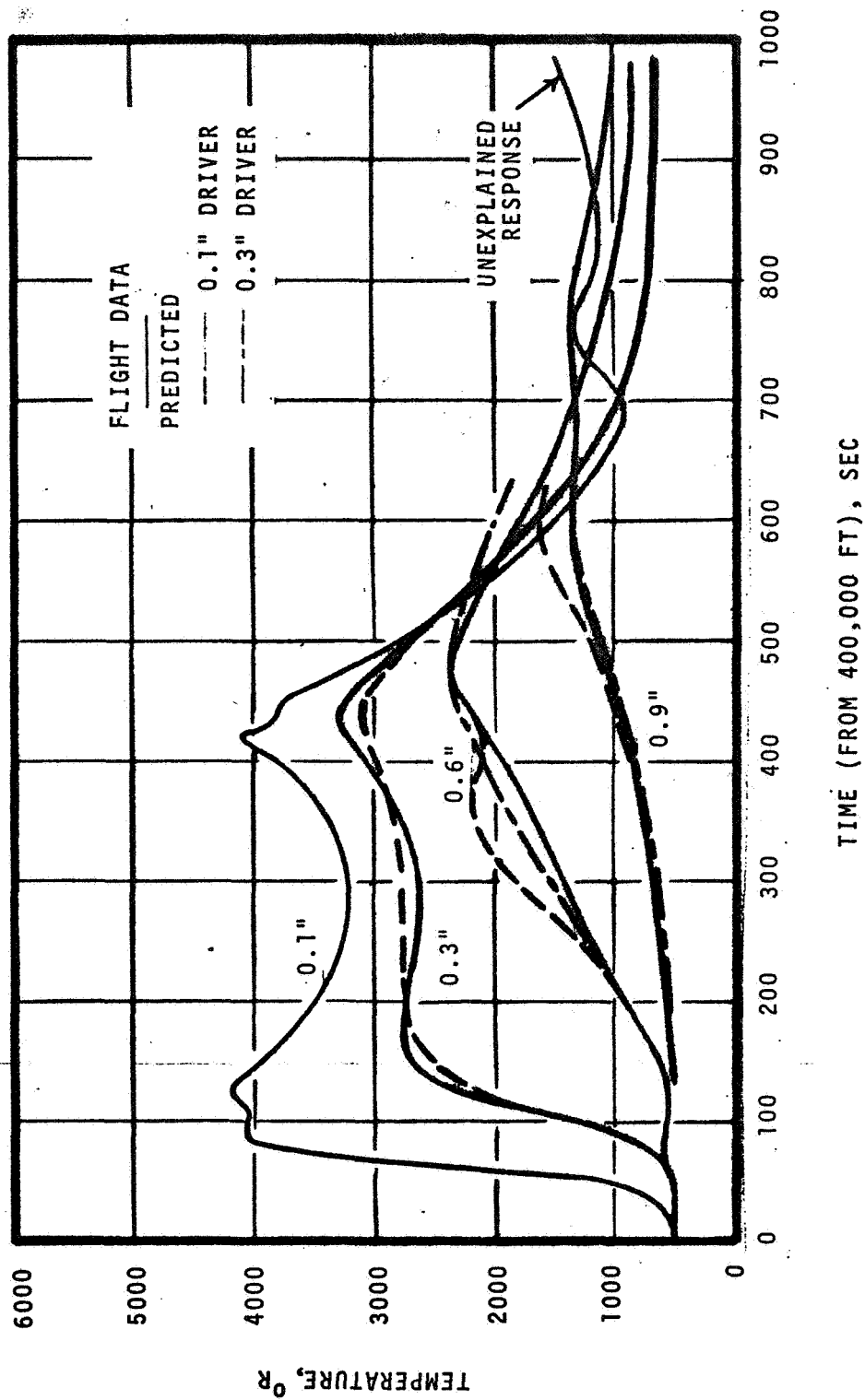


Figure 39. Driver Temperature Calculations for Flight AS 501, Body Point 705 Using Effective Char Thermal Conductivity Data

registering an inaccurate (if not meaningless) temperature response thereafter.* The present disagreement was therefore disregarded in judging the merits of the thermal properties model.

In conclusion, the thermal properties model described in Section 5.3 is judged adequate for the present purposes. While some finer tuning, probably with the inclusion of pre-char temperature as a parameter for char conductivity and specific heat, might be in order for an actual design study, the present accuracies (nominally 200°R or better) are satisfactory to provide an estimate for in-depth thermal analysis for the present purposes.

5.5 SURFACE THERMOCHEMICAL ABLATION MODEL

A comprehensive study of Apollo material ablation mechanisms was presented in Reference 44. Several surface thermochemical ablation models were postulated and compared to available ground and flight test data. Some of the more important parameters considered in the ablation analysis included various degrees of pyrolysis-gas reactivity, in-depth coking, mechanical removal of silica and/or silicon carbide), loss of pyrolysis gas through fissures which develop in the chars, and rate-controlled as well as diffusion-controlled surface chemical reactions. The model which appeared to correlate the flight data best also provided the best correlation for the ground test data. This model had the following major features. First, it assumed that the pyrolysis gases escape for the most part out of the boundary layer without contributing to a blowing reduction to the convective heat transfer. At low surface temperatures, an empirical Arrhenius-type law was employed. This was not included as a chemical kinetic law, but rather as a law for the mechanical removal of silica. At higher surface temperatures, the surface recession was limited by the availability of oxygen (diffusion-controlled carbon ablation regime). The oxygen supplied by the boundary-layer edge gas was supplemented by oxygen in the silica. Finally, at very high temperatures, carbon reactions with nitrogen and carbon sublimation became important.

There were a number of interrelated factors that contributed to the selection of this surface thermochemical ablation model. Briefly, it was seen that the correlation of ground and flight test data required the following considerations:

* No ablator core measurements were available in the Apollo 6 Mission report, but estimates of the ablator recession and char thickness at various body points were made. The estimated total recession was 0.05 inch for Body Point 707. The calculations performed in the present study predict breakthrough of the 0.02 inch thermocouple at 90 seconds, with a total surface recession of 0.079 inch (see Section 6.2).

1. It was necessary to choose a model where the pyrolysis gas did not play a major role in reducing the surface ablation rate at temperatures above 3600°R or so. This required consideration of equilibrium coking (so that the pyrolysis gas is in equilibrium with the char when it reaches the surface), a frozen pyrolysis gas, or a pyrolysis gas which does not mix with the boundary-layer gases (achieved through the "fissure" model mentioned above).

2. It was necessary to consider some form of an empirical ablation law at T_w below 3600°R or so to reduce ablation rates below those which would be predicted for diffusion-controlled carbon oxidation as a consequence of the competing mechanisms of mechanical removal of silica, silica-carbon reactions, and nonequilibrium pyrolysis gas effects.

3. It was necessary to consider a model where the pyrolysis gas did not contribute to a large reduction in convective heating rate.

In the Reference 44 studies the third factor could be realized only through adoption of the "fissure" model. While fissures are known to occur in Apollo material chars³, it seems unlikely that they would prohibit entirely any mixing of the pyrolysis gas and boundary-layer gas as presumed in the fissure model. Therefore, with the improved convective heat- and mass-transfer coefficient correlations presented in Section 3.3.1 (which were surprisingly different from the values used in the Reference 44 studies) and with the inclusion of coking, it seemed appropriate to consider first the other extreme case where the fissures are assumed to have negligible effect on the pyrolysis gas flow (i.e., a coking nonfissure model in the terminology of Reference 44). A partial-fissure model could then be developed if deemed appropriate on the basis of flight predictions. This approach was adopted and, as will be shown in Section 6, the coking nonfissure model has proven to be satisfactory without further modification.

With regard to the second factor listed above, utilization of the in-depth coking model described in Section 4.2 has made it possible to eliminate the use of any special rate law such as the silica mechanical-removal rate law of Reference 44. It has been seen that the equivalent of a rate law arises naturally as a consequence of reactive pyrolysis-gas effects. In particular, study of surface thermochemistry ablation tables generated with the EST program for the coking nonfissure model (presented later in this section) indicated the following:

1. At wall temperatures below 2250°R , the surface recession is predicted to be zero for normalized pyrolysis gas rates B'_g of 0.6 or greater. This is a consequence of the fact that the pyrolysis gas is considered to be frozen in depth (see Figure 34) but to achieve equilibrium in the boundary-layer, the

excess carbon in the pyrolysis gas thus exhausting the oxygen which diffuses across the boundary layer. This happens to be consistent with the surface temperature at which Apollo material ablation has been observed to begin to occur. For example, ablation is limited to temperatures greater than 2235°R in Reference 46.

2. Plateau behavior for B'_C versus T_w is predicted to occur for T_w above 3600°R. This results because the pyrolysis gas is considered to achieve equilibrium with the char in depth (see Figure 34). As mentioned previously, this is consistent with the T_w above which plateau behavior has been observed in ground tests (see, e.g., Figure 61 and remarks on page 110 of Ref. 2).

3. At wall temperatures between 2250°R and 3600°R, the B'_C are predicted to rise from zero to the plateau value as the amount of excess carbon in the pyrolysis gas drops from the frozen pyrolysis gas value to zero (see Figure 34). It may not be fortuitous that this rise is in substantial agreement with ground test data for values of B'_C of 0.6 to 1.0, the values typically experienced in ground tests⁴⁴.

On the basis of these observations it seemed appropriate to employ the diffusion-controlled coking surface thermochemistry map with no further development of an empirical rate law. As mentioned previously, comparison of predictions with flight data presented later in this report are sufficiently good to suggest that this approach also is satisfactory.

Surface thermochemical ablation tables were obtained with the EST program modified to include an assigned temperature open-system (surface ablation) calculation. The requisite modifications are discussed in Appendix A. The pyrolysis gas was considered to be reactive and the pyrolysis gas carbon fraction was considered to be a function of temperature as obtained from the closed-system pyrolysis-gas calculations (Figure 34). Unequal diffusion coefficients were considered in these calculations.

The resulting values for normalized char recession rates are shown as a function of wall temperature for several pressures and normalized pyrolysis gas rates B'_g in Figure 40. As mentioned previously, the solutions above 2000°K (3600°R) correspond to equilibrium coking; the solutions below 1250°K (2250°R) correspond to a pyrolysis gas which is frozen in depth but which achieves equilibrium at the surface with the char and boundary-layer gases; and the solutions between 1250 and 2000°K correspond to nonequilibrium coking in depth with the achievement of equilibrium at the surface.

In order to better understand these results, it is best to look first at the $B'_g = 0$ result which corresponds to the case where there is no pyrolysis

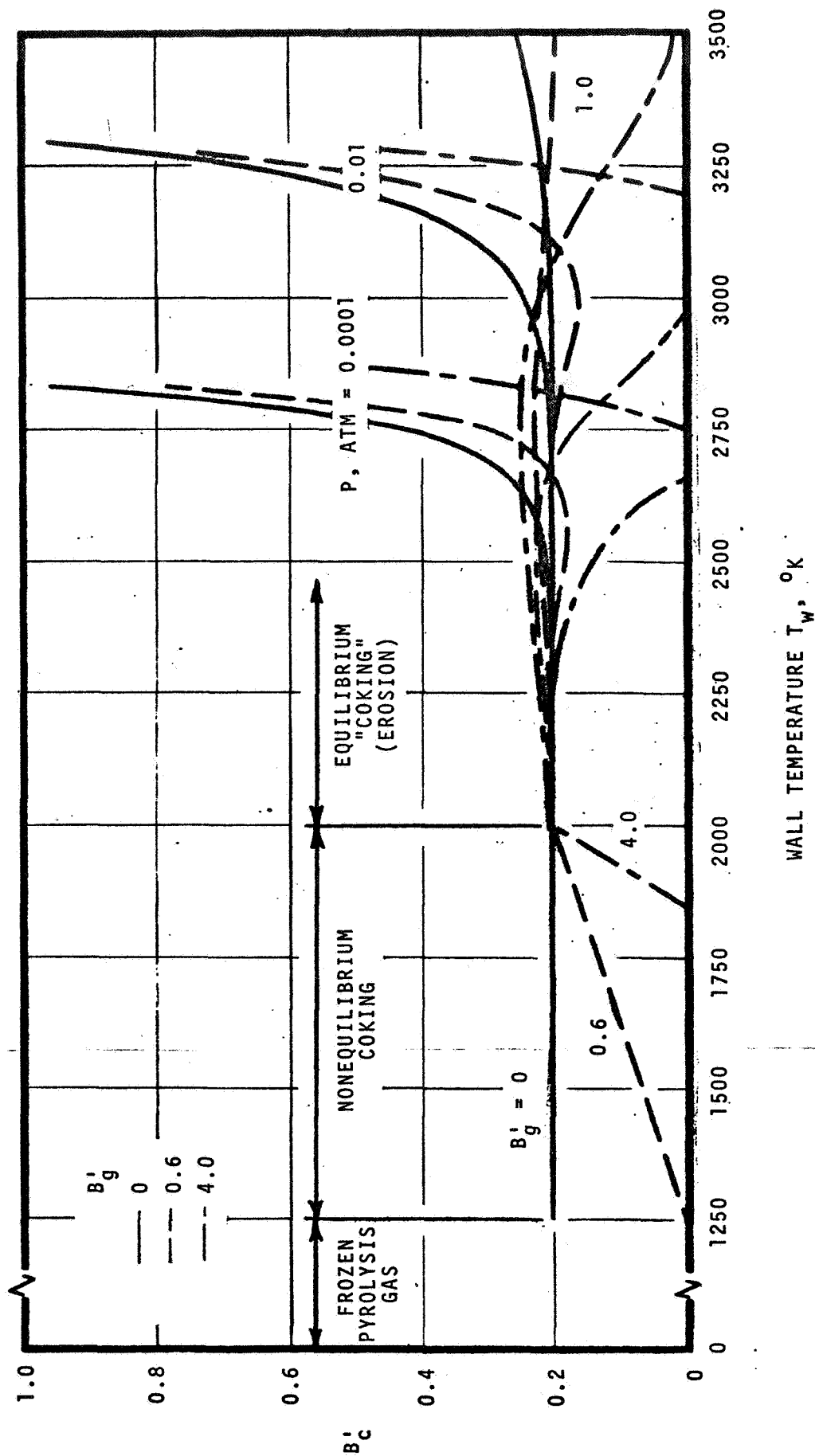


Figure 40. Surface Thermochemistry Map for Apollo Material Considering Coking (Reactive Pyrolysis Gas)

gas. It can be seen that the typical carbon plateau behavior* persists to high temperatures where sublimation becomes important. As B'_g is increased, the B'_c is seen to be first increased in the equilibrium coking region and then decreased at very high temperatures, and to decrease in the nonequilibrium coking and frozen pyrolysis gas regions. The reason for the increase in B'_c at moderately high temperatures can be attributed primarily to reactions of carbon with hydrogen and nitrogen. The decrease at low temperatures can be attributed to the fact that the pyrolysis gas contains carbon in excess of that required to achieve equilibrium with the carbonaceous char. The decrease in B'_c at very high temperatures and large values of B'_g is the result of preferential diffusion of hydrogen away from the surface leaving an excess of carbon from the pyrolysis gas in the vicinity of the wall (the calculations performed to obtain the carbon content of the coked pyrolysis gas as it approaches the surface consider equal diffusion). This latter phenomenon is predicted to occur at surface temperatures higher than those experienced during the Apollo flight predictions; hence, it will not be discussed further here.

5.6 SUMMARY OF MATERIAL RESPONSE MECHANISM STUDIES

As can be seen from the discussion in the preceding subsections, the selection of Apollo material in-depth and surface ablation models is still not straightforward in spite of the large number of ground tests, the relatively large amount of recovered flight data, excellent and detailed laboratory analyses of flight and laboratory-produced chars, and careful and comprehensive theoretical analyses. In brief, there are a number of interrelated and complex phenomena which take place in the char layer and at the surface which are not amenable to detailed analytical treatment using available data.

While it was not a primary objective of the present study to improve the material response model, it was felt that some effort should be expended in this direction in order to provide a better baseline for the evaluation of flight data. In particular, calorimeter data from the Apollo flights were typically not very useful; hence, the test of the aerothermal environment procedures developed in previous sections ultimately rests on the ability to predict in-depth temperatures and total surface recession.

On the basis of a thorough evaluation of all available flight data, laboratory data, and previous analytical efforts, it was decided to include an in-depth coking model, to ignore the effects of silica in both the in-depth and

* This is the contribution of carbon to the B'_c ; thus \dot{s} is determined using the density of carbon in the surface node.

surface ablation phenomena, to neglect the effects of fissures in the char on the flow of the pyrolysis gas through the char and into the boundary layer, and to consider a surface thermochemical boundary condition including reactive pyrolysis gas effects. This model has a major distinguishing characteristic that the carbon content of the pyrolysis gas is considered to be a function of temperature and pressure; as the pyrolysis gas percolates through the char it is considered to be frozen at temperatures below 2250°R , to be in equilibrium with carbon at temperatures above 3600°R , and to undergo nonequilibrium coking at intermediate temperatures. In all cases, the pyrolysis gas is considered to equilibrate with the char and boundary-layer gases at the surface. As a result, the excess carbon in the pyrolysis gas in the frozen and nonequilibrium pyrolysis gas regimes reduces ablation rates from carbon plateau values in the equilibrium regime to zero in the frozen pyrolysis gas regime; this behavior is seen to be in substantial agreement with ground test ablation results. Whether or not reactive pyrolysis gas effects are indeed the primary physical cause for the observed decrease in ablation rates at surface temperatures below 3600°R is not known; it seems just as likely that the decrease could be the result of inhibition of carbon ablation due to the presence of condensed-phase silica. For this reason, the reactive pyrolysis gas surface thermochemical ablation model is presently looked upon as a convenient empirical relation in the low surface temperature regime. With this one possible exception, the present model is believed to represent well the most important physical phenomena.

Driver temperature calculations performed for several flight thermocouple traces yielded satisfactory results. Flight predictions presented in Section 6 yield satisfactory predictions for surface recession and in-depth carbon profiles as well as in-depth temperature profiles. Hence, the present in-depth and surface ablation models are judged to be adequate.

SECTION 6

FLIGHT PREDICTIONS

The various computational procedures and techniques described in the previous sections were applied to a series of orbital and superorbital velocity unmanned Apollo flights. The approach which was taken is described in Section 6.1. The results are presented in Section 6.2, and the conclusions are summarized in Section 6.3.

6.1 APPROACH EMPLOYED FOR FLIGHT PREDICTIONS

A total of seven flight predictions were performed for various body points in the unmanned Flights AS 202, AS 501, and AS 502. The basic characteristics of these flights are summarized in Table 19 together with those for the first manned orbital flight (AS 205 - Apollo 7) and the first manned lunar flight (AS 503 - Apollo 8). The q and Q values shown are the peak heating rate

TABLE 19
APOLLO MISSION SUMMARY

Mission	Apollo Designation	Spacecraft Designation	Entry Velocity, (inertial) fps	Entry Angle, (inertial) deg	Lift/ Drag Ratio	Range, n. mi.	Entry Time, sec	Reference q Btu/ft ² -sec	Reference Q Btu/ft ²
AS-202	---	CSM 011	28,512	-3.53	0.275	2,295	1,234	83	20,862
AS-501	Apollo 4	CSM 017	36,545	-6.945	0.365	1,951	1,060	425	37,522
AS-502	Apollo 6	CSM 020	32,830	-5.85	0.350	1,935	1,140	197	27,824
AS-205	Apollo 7	CSM 101	25,846	-2.072	0.305	1,584	935	59	11,281
AS-503	Apollo 8	CSM 103	36,221	-6.48	0.300	1,350	868	296	26,140

and the integrated total heating at the NASA/MSR reference station $\bar{s}/R = 0.9875$. It can be seen that Flight AS 202 is an orbital mission somewhat more severe than the Apollo 7 flight, and that AS 501 and AS 502 are simulated lunar return missions which are, respectively, more and less severe than the manned Apollo 8 lunar return flight. Further information regarding these flights can be found in the Apollo Mission Reports⁵⁰⁻⁵².

The specific body points which were considered are identified in Table 20, together with a brief summary of the basic heating environment, the instrumentation which provided useful information, and the primary purpose for the selection of the body point. The selection of the seven cases listed in Table 20 was based on these criteria:

1. To provide a systematic and sequential assessment of various aspects of the theory used in making the predictions
2. To provide tests of the theory over a wide diversity of flight conditions and body locations
3. To concentrate on those flights and body locations where the flight conditions are accurately known and good quality data were obtained.

With regard to the instrumentation employed, the following items are worthy of note:

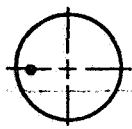
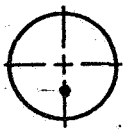

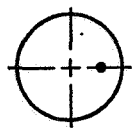
1. The thermocouples employed near the surface were designed such that they are expected to provide a reasonable assessment of the surface temperature once the char has ablated to the thermocouple depth. These "consumable" thermocouples are described in Reference 53.
2. The char sensors provided an indication of the char layer thickness throughout the flight.
3. The wafer calorimeters consisted of several graphite wafers stacked to allow removal of single wafers by aerodynamic forces when the surrounding heat shield material has receded. These calorimeters provided useful information only during the early portion of the trajectory - prior to significant ablation.
4. The asymptotic calorimeters, tailored in design to measure low heating rates, performed well where employed.
5. The core analyses consisted of profiles of density, elemental composition including ash content, weight loss, thermal properties, and postulated maximum temperatures as well as core surface recession, char layer thickness, and decomposition layer thickness.

Further information regarding the instrumentation can be found in the Apollo Mission Reports⁵⁰⁻⁵² and in Reference 54.

The generation of a CMA flight prediction requires the following information:

1. The reaction kinetic constants for virgin material decomposition - values presented in Section 5.1 were employed.

TABLE 20
SUMMARY OF APOLLO FLIGHTS AND BODY POINTS
FOR WHICH FLIGHT PREDICTIONS WERE MADE

Case	Flight	Body Point	Location	Description of Thermal Environment	Instrumentation Yielding Good Data	Purpose of Calculation
1	202	705 (Z71,Y0)		Relatively nonsevere convective heating - negligible radiation heating - little recession	6 thermocouples Char sensor Core analysis performed	Test of stagnation-point convective heating model
2	502	705		Severe convective heating - little radiation heating - moderate recession	4 thermocouples Char sensor Wafer calorimeter Core analysis performed	Test of surface ablation as well as convective heating models
3	501	705		Severe convective and radiation heating - relatively high recession	4 thermocouples Char sensor Wafer calorimeter Core analysis performed	Test of radiation heating as well as surface ablation and convective heating models
4	202	Z0,Y33		Relatively nonsevere convective heating - negligible radiation heating - no recession	3 thermocouples Core analysis performed	Test of convective heating model for position off the pitch plane
5	501	710		Mild convective heating - negligible radiation heating - no recession	3 thermocouples Asymptotic calorimeter	Test of convective heating model for position on conical afterbody
6	502	707		Severe convective heating - mild radiation heating - moderate recession	4 thermocouples Char sensor Wafer calorimeter Core analysis performed	Test of transition and turbulent heating model as well as surface ablation
7	501	707		Severe convective heating - mild radiation heating - moderate recession	4 thermocouples Char sensor Wafer calorimeter Core analysis performed	Second test of transition and turbulent heating model

2. Material thermal properties - values presented in Section 5.3 were employed.
 3. Pyrolysis gas sensible enthalpy and carbon fraction - values presented in Figures 35 and 34 were employed.
 4. Time-dependent boundary conditions
 - a. Recovery enthalpy - taken as total enthalpy, consistent with correlation Equation (23)
 - b. Radiation heat rate - taken from NASA/MSC radiation heating factors and reference heating conditions (see Section 4)
 - c. Heat-transfer coefficient - obtained from convective-heating correlations presented in Section 3.2 and summarized in Section 3.4:
 - i - Stagnation-point value - obtained from Figure 10 for appropriate total enthalpy and pressure
 - ii - Correction for body point location for laminar flow F_1 - obtained from the NASA/MSC convective heating factors (e.g., Figure 8), corrected for the change in reference condition F_2 (Figure 9), and corrected for flight conditions F_3 (Figure 12).
 - iii - Correction for turbulent flow (when appropriate) F_4 - obtained from Figure 14. (The subject of transition and turbulent flow will be discussed later in Section 6.2.4b.
 - iv - Correction for wall temperature F_5 - neglected
 - d. Pressure - obtained from NASA/MSC pressure factors (see Section 2.0) and current stagnation pressure.
 - e. Edge molecular weight - obtained from EST calculations.
- The time-dependent boundary conditions actually used in the CMA calculations are presented in Tables 21a through 21g for the seven cases. The various convective heating factors, radiation heating factors, and pressure ratio factors employed in setting up these tables are summarized in Table 22.
5. Blowing reduction parameters - taken from Equations (29) and (31) for λ_M and λ_H , respectively.
 6. Surface thermochemistry tables - obtained from EST calculations reported in Section 5.5 - see Figure 40.

TABLE 21

TIME-DEPENDENT BOUNDARY CONDITIONS USED
IN CMA FLIGHT PREDICTIONS

(a) Case 1 - Flight AS 202, Body Point Z71,YO (705)

TIME (SEC)	PROB OPTN	RECOVERY ENTHALPY (BTU/LB)	RADIATION HEAT RATE (BTU/SQ FT- SECOND)	HEAT COEFF (LB/SQ FT- SECOND)	PRESSURE (ATM)	EDGE MOLECULAR WEIGHT
.00	1	14900.00	-0.00	.000048	.000008	14.87
11.50	1	14900.00	-0.00	.000076	.000016	14.98
21.50	1	14900.00	-0.00	.000114	.000041	14.96
31.50	1	14900.00	-0.00	.000169	.000090	15.04
51.50	1	14900.00	-0.00	.000367	.000450	15.13
61.50	1	14900.00	.81	.000534	.000970	15.19
71.50	1	14900.00	1.60	.000795	.002120	15.26
81.50	1	14900.00	2.70	.001140	.004280	15.33
91.50	1	14900.00	4.00	.001580	.008160	15.40
101.50	1	14900.00	4.90	.002080	.014100	15.48
121.50	1	14650.00	5.30	.003180	.032800	15.70
151.50	1	13590.00	5.50	.004700	.069300	16.34
181.50	1	12090.00	4.70	.005020	.076900	17.24
201.50	1	11200.00	3.60	.004570	.063500	17.79
221.50	1	10520.00	2.40	.003920	.046000	18.21
251.50	1	9900.00	1.40	.002750	.026200	18.59
301.50	1	9420.00	1.20	.001950	.011600	18.84
341.50	1	9220.00	1.60	.001750	.008460	19.03
401.50	1	8930.00	1.70	.002190	.014600	19.25
451.50	1	8370.00	1.50	.003620	.038200	19.84
491.50	1	7230.00	.70	.005220	.078400	20.95
551.50	1	4484.00	-0.00	.006250	.111000	23.62
611.50	1	2406.00	-0.00	.005520	.094000	26.34
671.50	1	1057.00	-0.00	.005160	.105000	29.01
731.50	1	285.00	-0.00	.004320	.080200	29.08
791.50	1	119.00	-0.00	.002910	.041000	29.08
851.50	1	100.00	-0.00	.006410	.243000	29.08
913.50	1	100.00	-0.00	.010100	.602000	29.08
1000.00	1	100.00	-0.00	.012600	.930000	29.08
1100.00	1	100.00	-0.00	.013000	1.000000	29.08

TABLE 21 (CONTINUED)

(b) Case 2 - Flight AS 502, Body Point 705

TIME (SEC)	PROB OPTN	RECOVERY ENTHALPY (BTU/LB)	RADIATION HEAT RATE (BTU/SQ FT- SECOND)	HEAT COEFF (LB/SQ FT- SECOND)	PRESSURE (ATM)	EDGE MOLECULAR WEIGHT
.00	1	19900.00	-0.00	.0001	.00001	13.810
6.50	1	19900.00	-0.00	.0001	.00003	13.780
14.50	1	19900.00	-0.00	.0002	.00010	13.790
26.50	1	20000.00	-0.00	.0005	.00066	13.910
36.50	1	20000.00	-0.00	.0011	.00338	14.000
46.50	1	20000.00	4.70	.0023	.01350	14.100
56.50	1	19800.00	7.40	.0040	.04050	14.200
66.50	1	19500.00	11.70	.0061	.09300	14.340
76.50	1	18700.00	14.00	.0082	.17200	14.530
86.50	1	17500.00	12.00	.0100	.25000	14.840
96.50	1	16000.00	9.70	.0108	.28600	15.390
106.50	1	14500.00	5.80	.0103	.28600	16.080
116.50	1	13300.00	4.70	.0091	.20000	16.680
136.50	1	11700.00	-0.00	.0075	.13100	17.560
166.50	1	10200.00	-0.00	.0063	.09200	18.520
196.50	1	9190.00	-0.00	.0055	.07100	19.260
226.50	1	8450.00	-0.00	.0048	.05360	19.820
266.50	1	7760.00	-0.00	.0043	.04190	20.380
296.50	1	7310.00	-0.00	.0044	.04350	20.780
326.50	1	6810.00	-0.00	.0049	.05440	21.280
366.50	1	5920.00	-0.00	.0061	.08310	22.200
426.50	1	4160.00	-0.00	.0073	.11600	23.900
506.50	1	2050.00	-0.00	.0068	.11400	27.210
566.50	1	947.00	-0.00	.0066	.12350	29.050
606.50	1	453.00	-0.00	.0058	.11100	29.080
646.50	1	210.00	-0.00	.0051	.09000	28.900
686.50	1	130.00	-0.00	.0046	.08060	28.900
710.00	1	100.00	-0.00	.0021	.06250	28.900
800.00	1	100.00	-0.00	.0030	.35000	28.900
850.00	1	100.00	-0.00	.0012	.47000	28.900

TABLE 21 (CONTINUED)

(c) Case 3 - Flight AS 501, Body Point 705

TIME (SEC)	PROB OPTN	RECOVERY ENTHALPY (BTU/LB)	RADIATION HEAT RATE (BTU/SQ FT- SECOND)	HEAT COEFF (LB/SQ FT- SECOND)	PRESSURE (ATM)	EDGE MOLECULAR WEIGHT
.00	1	24780.00	-0.00	.000077	.000020	12.44
2.80	1	24795.00	-0.00	.000095	.000030	12.53
6.80	1	24816.00	-0.00	.000140	.000050	12.59
20.80	1	24878.00	-0.00	.000580	.000910	12.78
30.00	1	24800.00	-0.00	.001500	.005000	12.90
40.00	1	24800.00	9.00	.004000	.020000	13.10
50.80	1	24344.00	35.00	.006890	.118000	13.32
62.00	1	22000.00	114.00	.009500	.190000	13.80
65.00	1	21300.00	96.00	.010000	.205000	13.92
70.00	1	20000.00	60.00	.011000	.233000	14.17
80.80	1	17966.00	20.00	.012300	.378000	14.76
90.00	1	16000.00	8.00	.010000	.230000	15.30
100.80	1	14430.00	5.00	.008910	.193000	16.05
140.80	1	11323.00	-0.00	.006560	.102000	17.77
200.80	1	9742.00	-0.00	.003600	.030600	18.72
240.80	1	9324.00	-0.00	.003020	.020800	18.98
280.80	1	8999.00	-0.00	.002900	.018900	19.23
340.80	1	8473.00	-0.00	.003660	.030200	19.72
400.80	1	7271.00	-0.00	.006600	.096400	20.94
440.80	1	5154.00	-0.00	.009550	.201000	23.08
460.80	1	3850.00	-0.00	.010100	.229000	24.22
500.80	1	1771.00	-0.00	.008200	.172000	27.92
540.80	1	826.00	-0.00	.006500	.126000	29.07
600.80	1	180.00	-0.00	.005300	.114000	29.07
640.80	1	100.00	-0.00	.003770	.053000	29.08
700.80	1	100.00	-0.00	.008600	.274000	29.08
700.80	1	100.00	-0.00	.012400	.673000	29.08
820.80	1	100.00	-0.00	.013100	.642000	29.08
900.80	1	100.00	-0.00	.013800	.708000	29.08
1046.80	1	100.00	-0.00	.015000	1.000000	29.08

TABLE 21 (CONTINUED)

(d) Case 4 - Flight AS 202, Body Point Z0,Y33

TIME (SEC)	PROB OPTN	RECOVERY ENTHALPY (BTU/LB)	RADIATION HEAT RATE (BTU/SQ FT- SECOND)	HEAT COEFF (LB/SQ FT- SECOND)	PRESSURE (ATM)	EDGE MOLECULAR WEIGHT
.00	1	14900.00	-.00	.000035	.000009	14.85
11.50	1	14900.00	-.00	.000055	.000018	14.96
21.50	1	14900.00	-.00	.000088	.000044	14.95
31.50	1	14900.00	-.00	.000122	.000097	15.02
51.50	1	14900.00	-.00	.000266	.000480	15.11
61.50	1	14900.00	.81	.000385	.001050	15.16
71.50	1	14900.00	1.60	.000575	.002290	15.23
81.50	1	14900.00	2.70	.000822	.004630	15.30
91.50	1	14900.00	4.00	.001140	.008820	15.38
101.50	1	14900.00	4.90	.001500	.015100	15.46
121.50	1	14650.00	5.30	.002300	.035400	15.67
151.50	1	13590.00	5.50	.003400	.074700	16.31
181.50	1	12090.00	4.70	.003620	.083000	17.21
201.50	1	11200.00	3.60	.003300	.068600	17.76
221.50	1	10520.00	2.40	.002830	.049700	18.18
251.50	1	9900.00	1.40	.002130	.028300	18.56
301.50	1	9420.00	1.20	.001400	.012600	18.81
341.50	1	9220.00	1.60	.001270	.009130	19.00
401.50	1	8930.00	1.70	.001580	.015700	19.22
451.50	1	8370.00	1.50	.002610	.041100	19.81
491.50	1	7230.00	.70	.003770	.084500	20.92
551.50	1	4484.00	-.00	.004500	.119000	23.60
611.50	1	2406.00	-.00	.003990	.101000	26.31
671.50	1	1057.00	-.00	.003730	.113000	29.00
731.50	1	285.00	-.00	.003120	.086300	29.08
791.50	1	119.00	-.00	.002100	.044300	29.08
851.50	1	100.00	-.00	.004640	.243000	29.08
913.50	1	100.00	-.00	.007310	.602000	29.08
1000.00	1	100.00	-.00	.009090	.930000	29.08
1100.00	1	100.00	-.00	.009430	1.000000	29.08

TABLE 21 (CONTINUED)

(e) Case 5 - Flight AS 501, Body Point 710

TIME (SEC)	PROB OPTN	RECOVERY ENTHALPY (BTU/LB)	RADIATION HEAT RATE (BTU/SQ FT- SECOND)	HEAT COEFF (LB/SQ FT- SECOND)	PRESSURE (ATM)	EDGE MOLECULAR WEIGHT
.00	1	24780.00	-0.00	.000004	.000001	13.76
2.80	1	24795.00	-0.00	.000006	.000001	13.85
6.80	1	24816.00	-0.00	.000008	.000002	13.92
20.80	1	24878.00	-0.00	.000032	.000033	14.19
50.80	1	24344.00	-0.00	.0000376	.004360	14.68
80.80	1	17966.00	-0.00	.000675	.013900	16.70
100.80	1	14430.00	-0.00	.000487	.007130	18.26
140.80	1	11323.00	-0.00	.000359	.003760	20.06
200.80	1	9742.00	-0.00	.000197	.001130	20.97
240.80	1	9324.00	-0.00	.000165	.000760	21.21
280.80	1	8999.00	-0.00	.000158	.000700	21.46
340.80	1	8473.00	-0.00	.000200	.001110	21.97
400.80	1	7277.00	-0.00	.000361	.003560	23.16
440.80	1	5154.00	-0.00	.000522	.007400	24.59
460.80	1	3856.00	-0.00	.000553	.008450	26.31
500.80	1	1771.00	-0.00	.000449	.006350	29.07
540.80	1	826.00	-0.00	.000354	.004650	29.08
600.80	1	180.00	-0.00	.000289	.003530	29.08
640.80	1	100.00	-0.00	.000206	.001950	29.08
700.80	1	100.00	-0.00	.000469	.010100	29.08
760.80	1	100.00	-0.00	.000678	.021200	29.08
820.80	1	100.00	-0.00	.000719	.023700	29.08
900.80	1	100.00	-0.00	.000751	.026200	29.08
1046.80	1	100.00	-0.00	.000820	.031000	29.08

TABLE 21 (CONTINUED)

(f) Case 6 - Flight AS 502, Body Point 707

TIME (SEC)	PROB OPTN	RECOVERY ENTHALPY (BTU/LB)	RADIATION HEAT RATE (BTU/SQ FT- SECOND)	HEAT COEFF (LB/SQ FT- SECOND)	PRESSURE (ATM)	EDGE MOLECULAR WEIGHT
.00	1	19900.00	-.00	.000023	.000005	13.97
6.50	1	19900.00	-.00	.000040	.000020	13.94
14.50	1	19900.00	-.00	.000082	.000070	13.96
26.50	1	20000.00	-.00	.000211	.000440	14.07
36.50	1	20000.00	-.00	.000480	.002250	14.17
46.50	1	20000.00	1.60	.000970	.009030	14.26
56.50	1	19800.00	3.20	.001680	.027000	14.36
66.50	1	19500.00	5.10	.002540	.062000	14.49
76.50	1	18700.00	6.00	.003480	.115000	14.67
86.50	1	17500.00	5.60	.004210	.167000	15.03
96.50	1	16000.00	4.35	.004550	.190000	15.64
106.50	1	14500.00	3.15	.004340	.172000	16.35
116.50	1	13300.00	2.00	.003860	.133000	16.96
136.50	1	11700.00	1.00	.003160	.087500	17.84
166.50	1	10200.00	.50	.002680	.061300	18.81
196.50	1	9190.00	.10	.002340	.047400	19.56
226.50	1	8450.00	.00	.002040	.035700	20.12
266.50	1	7760.00	-.00	.001770	.028000	20.67
296.50	1	7310.00	-.00	.001840	.029000	21.07
326.50	1	6810.00	-.00	.002080	.036300	21.57
366.50	1	5920.00	-.00	.002580	.046500	22.59
426.50	1	4160.00	-.00	.003070	.077300	24.07
506.50	1	2050.00	-.00	.002870	.076400	27.50
566.50	1	947.00	-.00	.002800	.082400	29.07
606.50	1	453.00	-.00	.002450	.073700	29.08
646.50	1	210.00	-.00	.002160	.059000	29.08
686.50	1	130.00	-.00	.001960	.053000	29.08
710.00	1	100.00	-.00	.000898	.042000	29.08
800.50	1	100.00	-.00	.001290	.240000	29.08
850.50	1	100.00	-.00	.000493	.320000	29.08

ORIGINAL PAGE IS
OF POOR QUALITY

TABLE 21 (CONCLUDED)

(g) Case 7 - Flight AS 501, Body Point 707

TIME (SEC)	PROB OPTN	RECOVERY ENTHALPY (BTU/LB)	RADIATION HEAT RATE (BTU/SQ FT- SECOND)	HEAT COEFF (LB/SQ FT- SECOND)	PRESSURE (ATM)	EDGE MOLECULAR WEIGHT
.00	1	24780.00	-.00	.000033	.000010	12.62
2.80	1	24795.00	-.00	.000040	.000020	12.69
6.80	1	24816.00	-.00	.000059	.000030	12.76
20.80	1	24878.00	-.00	.000244	.000610	12.96
30.00	1	24800.00	-.00	.000560	.003000	13.12
40.00	1	24800.00	4.00	.001300	.014000	13.30
50.80	1	24344.00	13.00	.002900	.078100	13.53
62.00	1	22000.00	49.00	.004300	.150000	13.98
65.00	1	21300.00	41.00	.004500	.153000	14.11
70.00	1	20000.00	26.00	.005000	.190000	14.37
80.80	1	17966.00	9.00	.005210	.252000	14.94
90.00	1	16000.00	4.00	.004300	.170000	15.55
100.80	1	14430.00	2.00	.003760	.129000	16.32
140.80	1	11323.00	-.00	.002770	.068000	18.06
200.80	1	9742.00	-.00	.001520	.020400	19.00
240.80	1	9324.00	-.00	.001270	.013800	19.27
280.80	1	8999.00	-.00	.001220	.012600	19.51
340.80	1	8473.00	-.00	.001540	.020100	20.01
400.80	1	7277.00	-.00	.002780	.064300	21.23
440.80	1	5154.00	-.00	.004040	.134000	23.33
460.80	1	3856.00	-.00	.004260	.152000	24.38
500.80	1	1771.00	-.00	.003460	.115000	28.17
540.80	1	826.00	-.00	.002740	.084000	29.08
600.80	1	180.00	-.00	.002230	.063800	29.08
640.80	1	100.00	-.00	.001590	.035300	29.08
700.80	1	100.00	-.00	.003620	.183000	29.08
760.80	1	100.00	-.00	.005230	.382000	29.08
820.80	1	100.00	-.00	.005550	.428000	29.08
900.80	1	100.00	-.00	.005880	.472000	29.08
1046.80	1	100.00	-.00	.006340	.560000	29.08

TABLE 22

SUMMARY OF FACTORS USED
IN FLIGHT PREDICTIONS

Case*	Nominal Angle of Attack	\bar{S}/R	Convective Heating Factors**				Radiation Heating Factor	Pressure Ratio Factor
			F ₁	F ₂	F ₃	F ₁ F ₂ F ₃ F ₄		
1	18.75	0.947	0.954	1.400	1.02	1.36	1.35	0.845
2	25.0	0.969	0.950	1.615	1.02	1.56	1.17	0.840
3	25.0	0.969	0.950	1.615	1.02	1.56	1.17	0.840
4	18.75	0.430	0.680	1.430	1.01	0.98	1.36	0.878
5	25.0	1.554	0.045	1.615	1.18	0.086	0	0.031
6	25.0	-0.663	0.395	1.615	1.03	0.66	0.50	0.560
7	25.0	-0.663	0.395	1.615	1.03	0.66	0.50	0.560

*For case identification see Table 20

**The convective heating factors presented in this table are for laminar flow ($F_4 = 1.00$). Corrections for turbulent flow applied during portions of Cases 6 and 7 are discussed in Section 6.2.4.

ORIGINAL PAGE IS
OF POOR QUALITY

7. The maximum time step and output intervals - these were typically taken as follows:

Trajectory Time	Maximum Time Step, sec	Output Interval, sec
Through first peak-heating pulse	0.10 or 0.20	5 or 10
Remainder of trajectory	1.0	10

8. Nodal data - these were typically taken as follows, starting from the surface

- 1 node of 0.005 inch thickness
- 5 nodes of 0.010 inch thickness
- 5 nodes of 0.015 inch thickness
- 5 nodes of 0.025 inch thickness
- 9 nodes of 0.060 inch thickness
- 5 to 10 nodes of 0.100 inch thickness, depending on total thickness
- 1 node to supply remaining thickness

6.2 FLIGHT PREDICTION RESULTS

The results of the CMA Apollo flight predictions are presented in the following subsections: in-depth temperature histories are compared to thermocouple data in Section 6.2.1; surface ablation and char penetration histories are presented in Section 6.2.2 and compared to char sensor data and to final surface ablation and char penetration data; final char density profiles are presented in Section 6.2.3 and compared to Apollo core data; and heat transfer predictions including transition to turbulent flow and relaminarization are compared to calorimeter data in Section 6.2.4. The flight prediction results are summarized in Section 6.3.

It is significant that the results presented in this section constitute all of the flight predictions that were generated under the contract: no solutions were discarded because of unfavorable agreement; no solutions were regenerated with changes in material properties, coking model, surface ablation model, convective heating correlations or the like. Therefore, the solutions are equivalent to preflight predictions using the postflight trajectory.

6.2.1 In-Depth and Surface Temperatures

Predicted temperature time histories corresponding to thermocouple locations are compared to thermocouple data for the seven cases (see Table 20) in Figures 41 through 47, respectively. The measured temperature data are shown as solid lines, the corresponding temperature predictions are shown as dashed lines, and the surface temperature predictions are shown as dash-dot lines. In addition, when a thermocouple is predicted to break through the surface (due to surface ablation), the subsequent thermocouple response is shown as a dotted line. As mentioned previously, "consumable" thermocouples were employed on the Apollo heat shield; hence, the thermocouple response subsequent to break-through should be representative of (but not necessarily an accurate indicator of) surface temperature⁵³.

It will be observed that both laminar and turbulent predictions are presented for the last two cases (Body Point 707 for Flights 502 and 501). The criteria for transition to turbulent flow was developed on the basis of the Flight 502 laminar calculation and the same criteria was used for both flights. This will be discussed in Section 6.2.4.

In order to get a better appreciation for the accuracy of these predictions, several representative types of errors are summarized in Table 23, namely, the maximum error which occurs somewhere during the flight, the average error over the flight, and the errors at the end of the flight. Neglecting the laminar Body Point 707 solutions (in favor of the turbulent predictions) and discounting the measured response of a thermocouple after it has been predicted to break through the surface, the disagreement is typically less than 350°R except for some brief periods very early in the trajectory. The errors at the end of the flight average about 130°R. This agreement between predictions and flight measurements is considered to be excellent considering that the solutions are the equivalent of preflight predictions (with the exception of the transition model which was developed on the basis of the present results and the coking model which is based on the evaluation of core data obtained in the same flights). Certainly one could not expect better agreement considering the relatively crude model for char conductivity which was employed and the complexity of the surface ablation phenomena.

Note in particular the substantial improvement obtained in considering transition to turbulent flow. Considering the good agreement for Cases 1-5 for laminar flow, it is quite apparent that transition does occur in Cases 6 and 7 (Body Point 707).

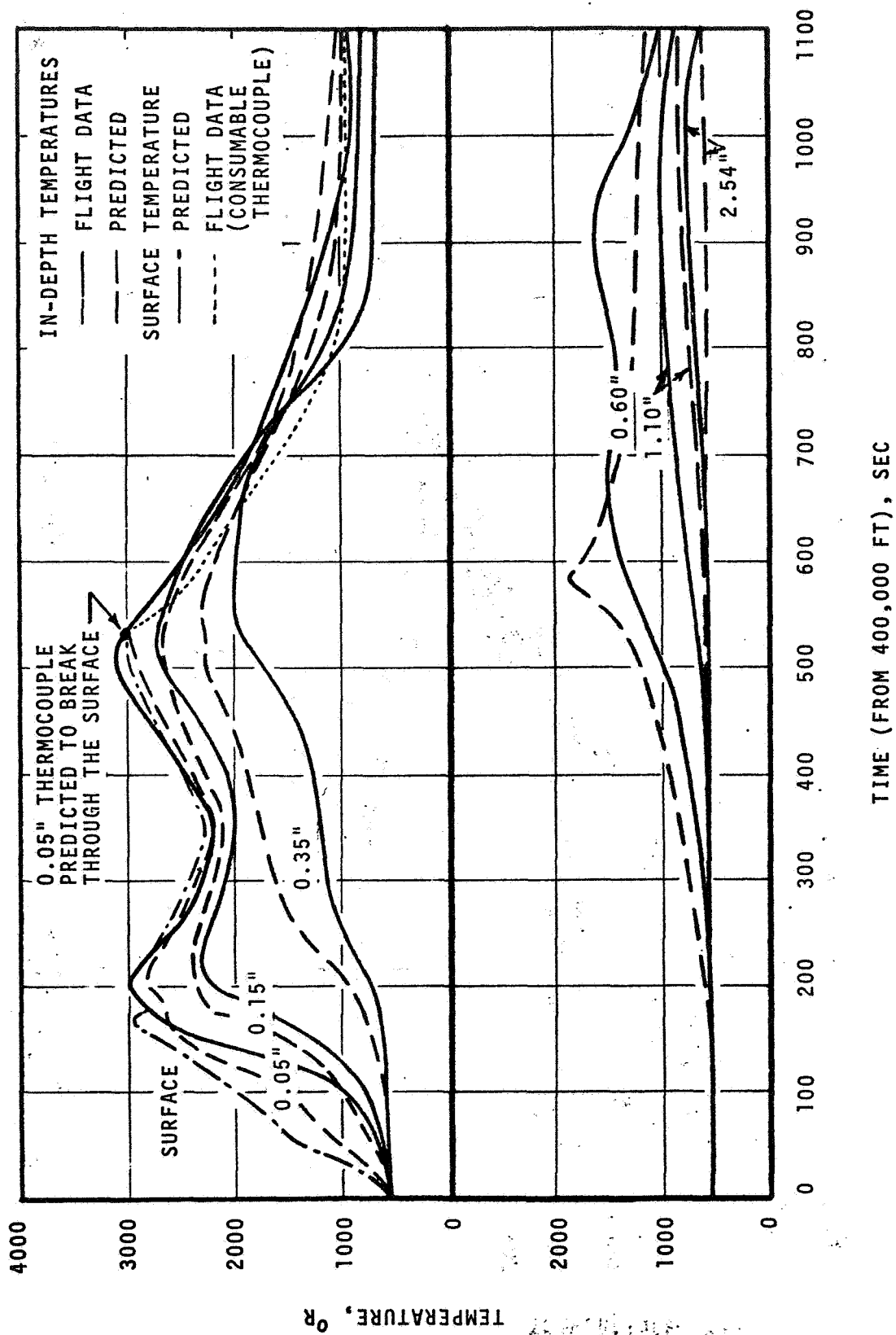


Figure 41. Comparison of Predicted Temperatures with Thermocouple Response for Flight AS 202, Body Point Z71, YO (705)

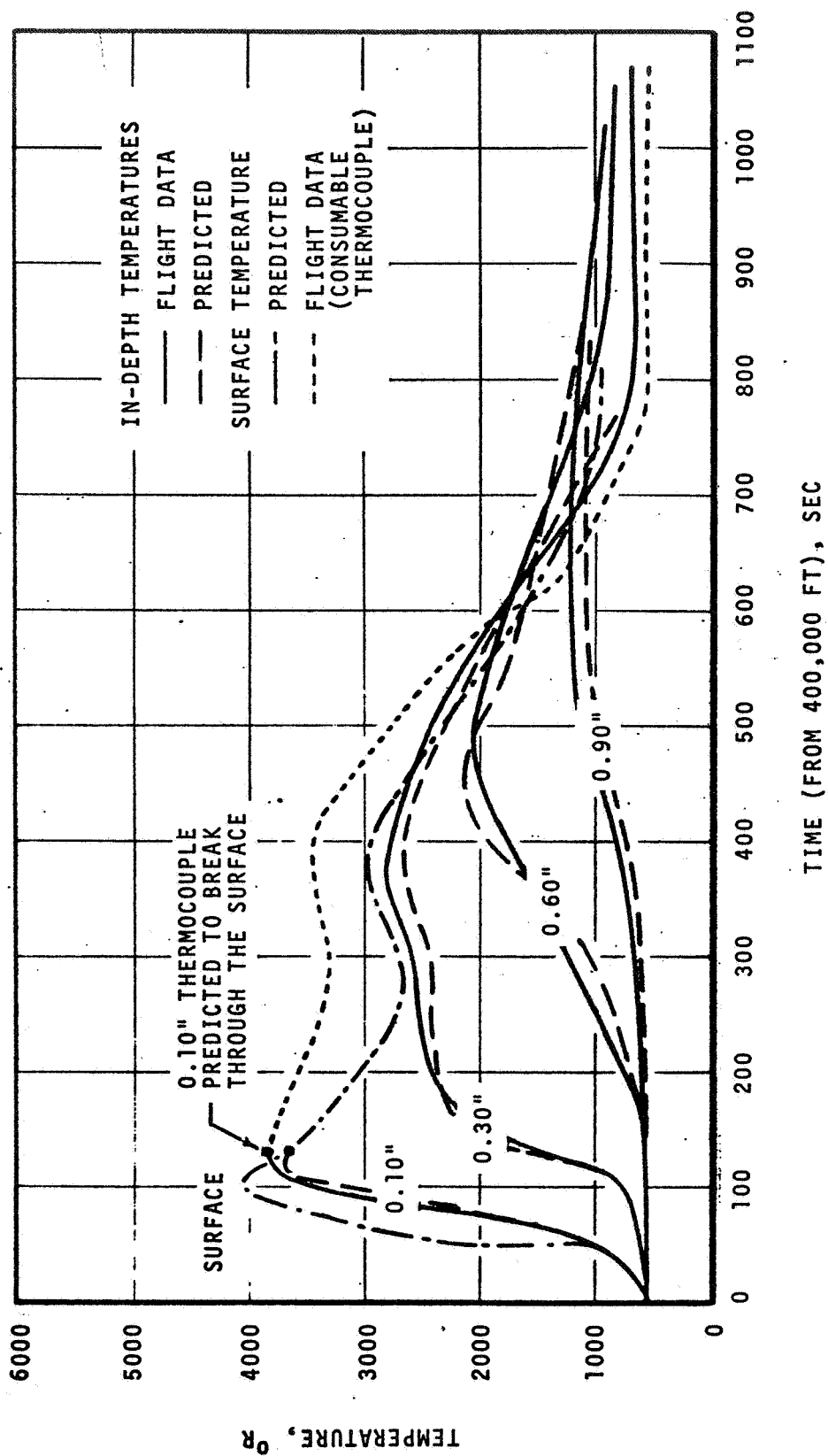


Figure 42. Comparison of Predicted Temperatures with Thermocouple Response for Flight AS 502, Body Point 705

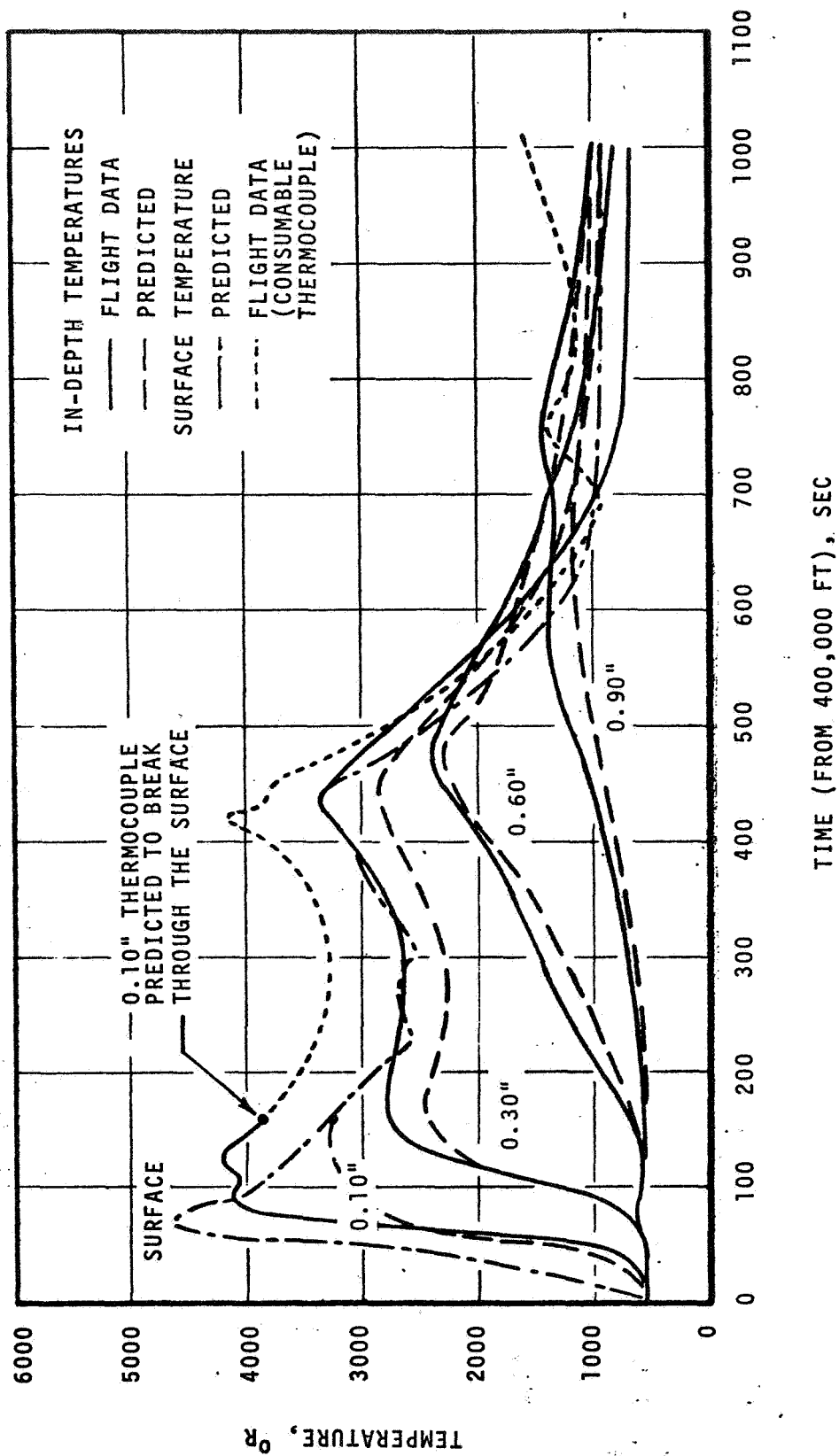


Figure 43. Comparison of Predicted Temperatures with Thermocouple Response for Flight AS 501, Body Point 705

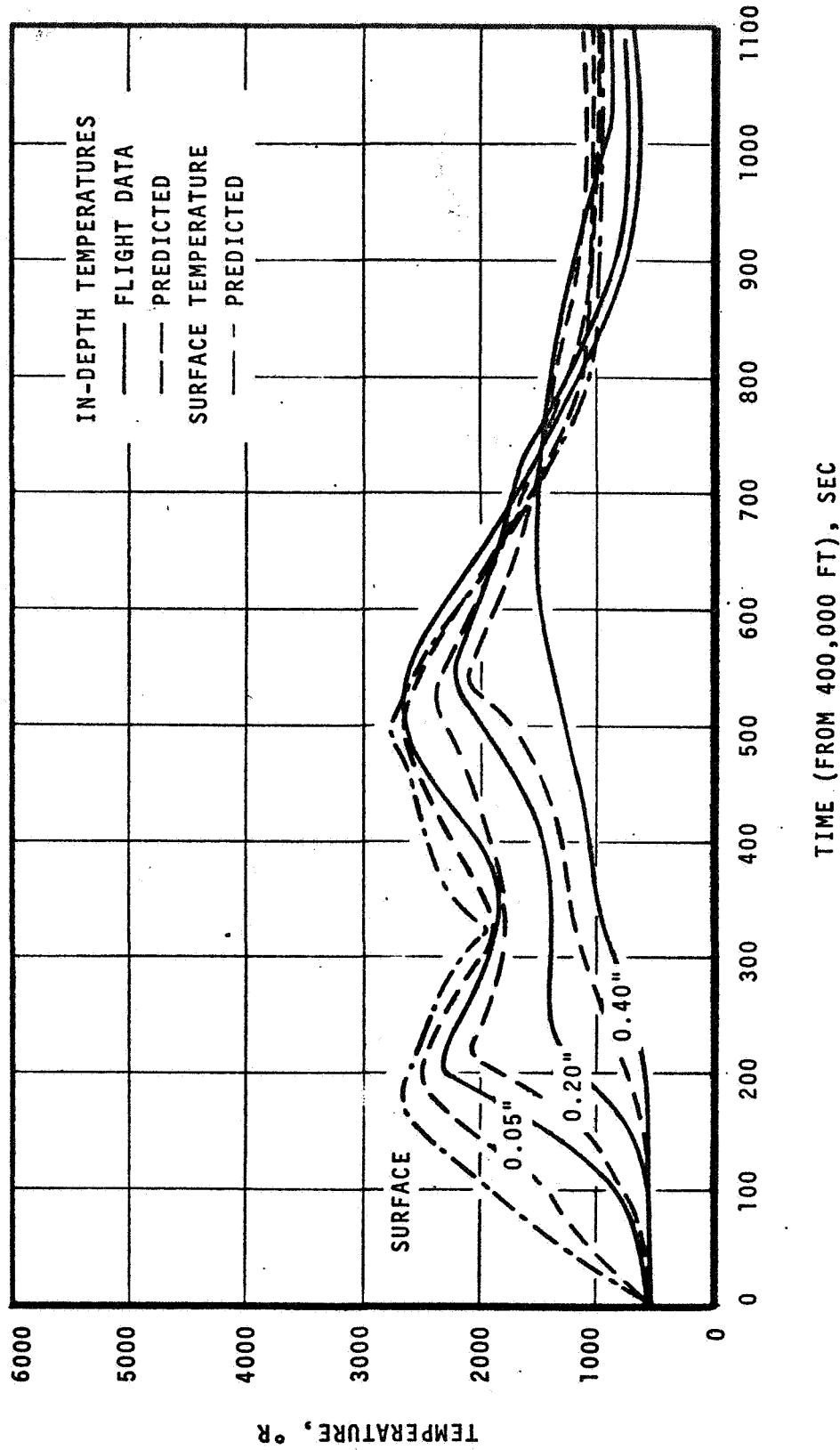


Figure 44. Comparison of Predicted Temperatures with Thermocouple Response for Flight AS 202, Body Point Z0, Y33

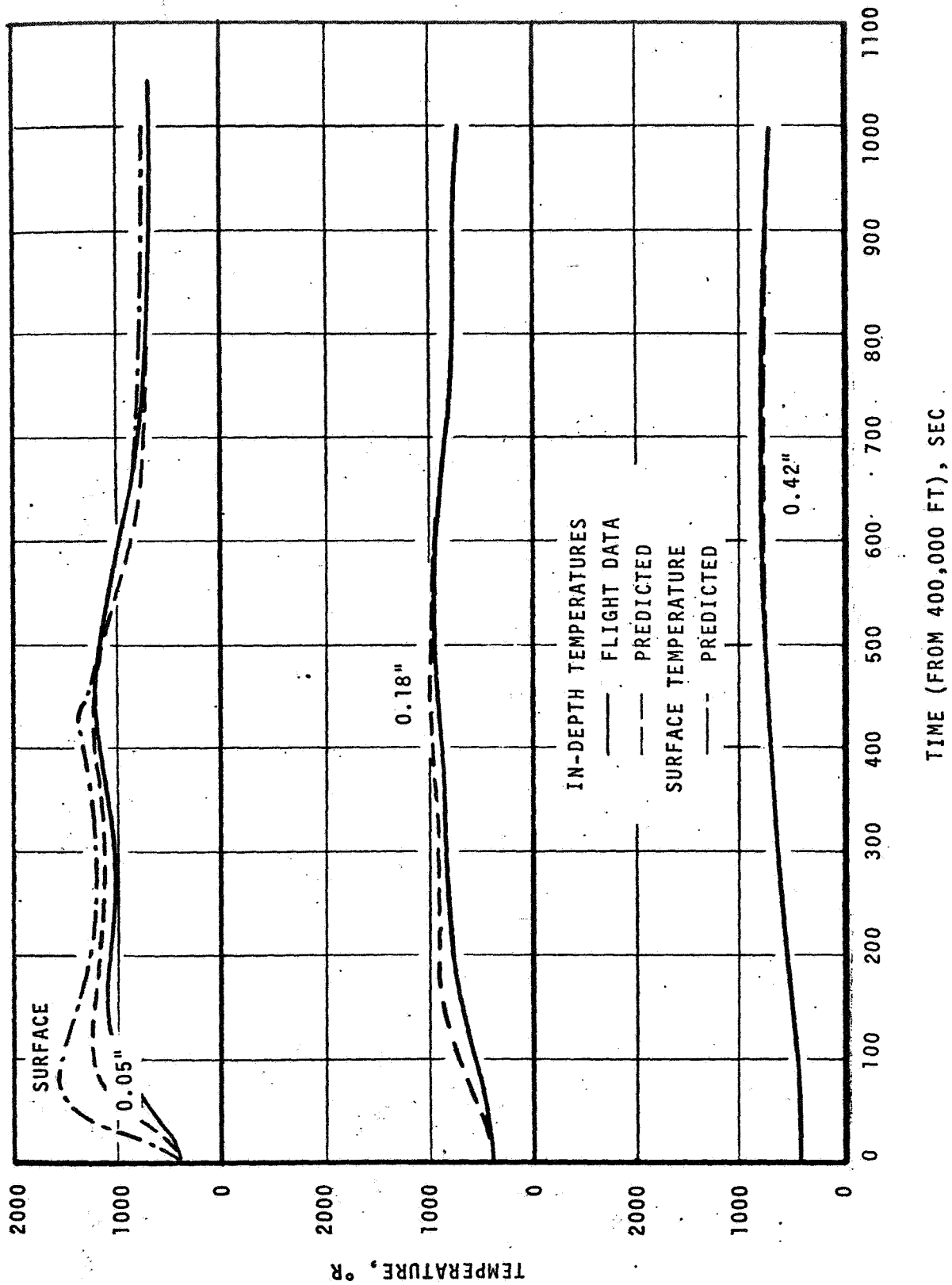
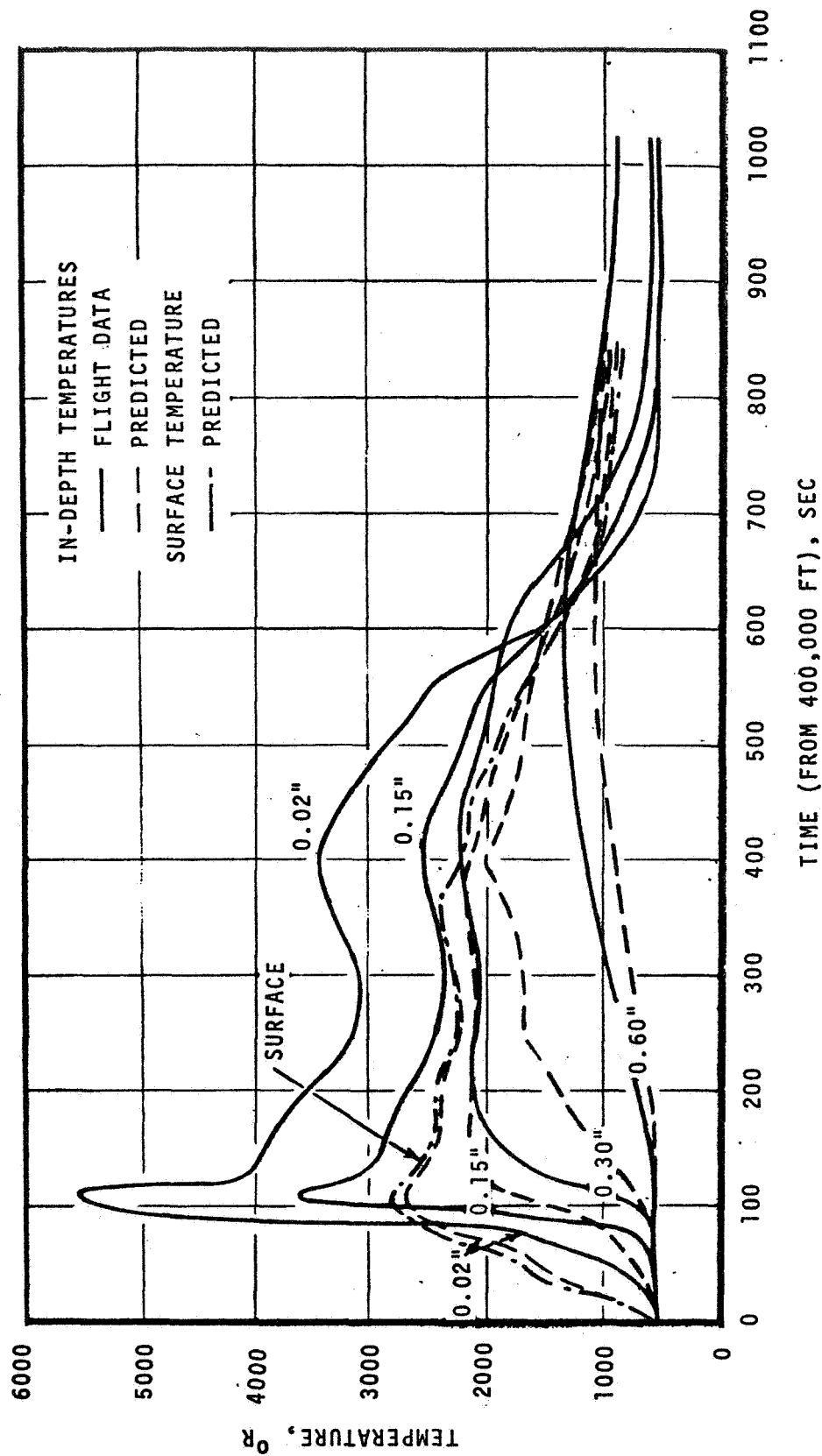
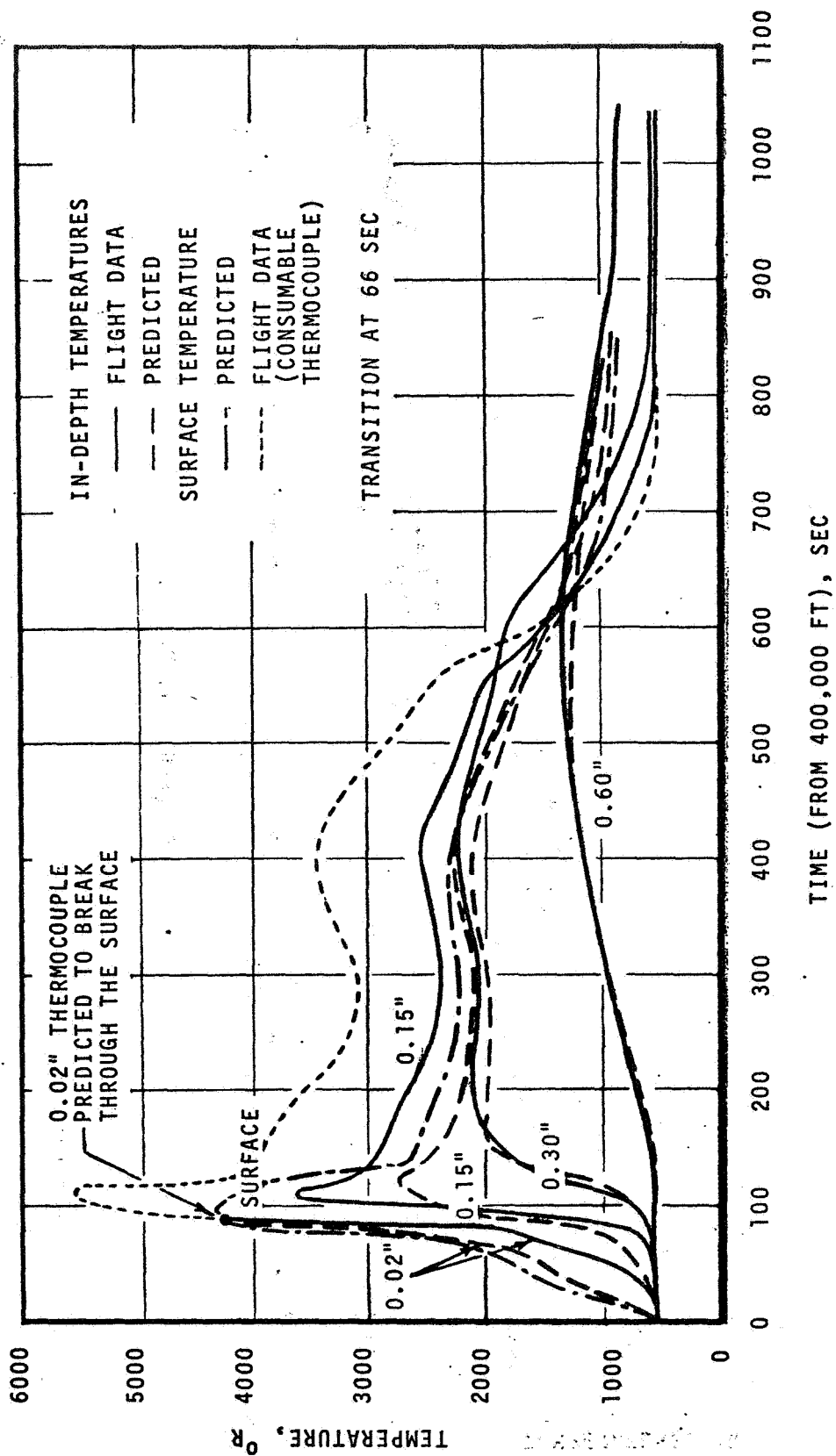


Figure 45. Comparison of Predicted Temperatures with Thermocouple Response for Flight AS 501, Body Point 710



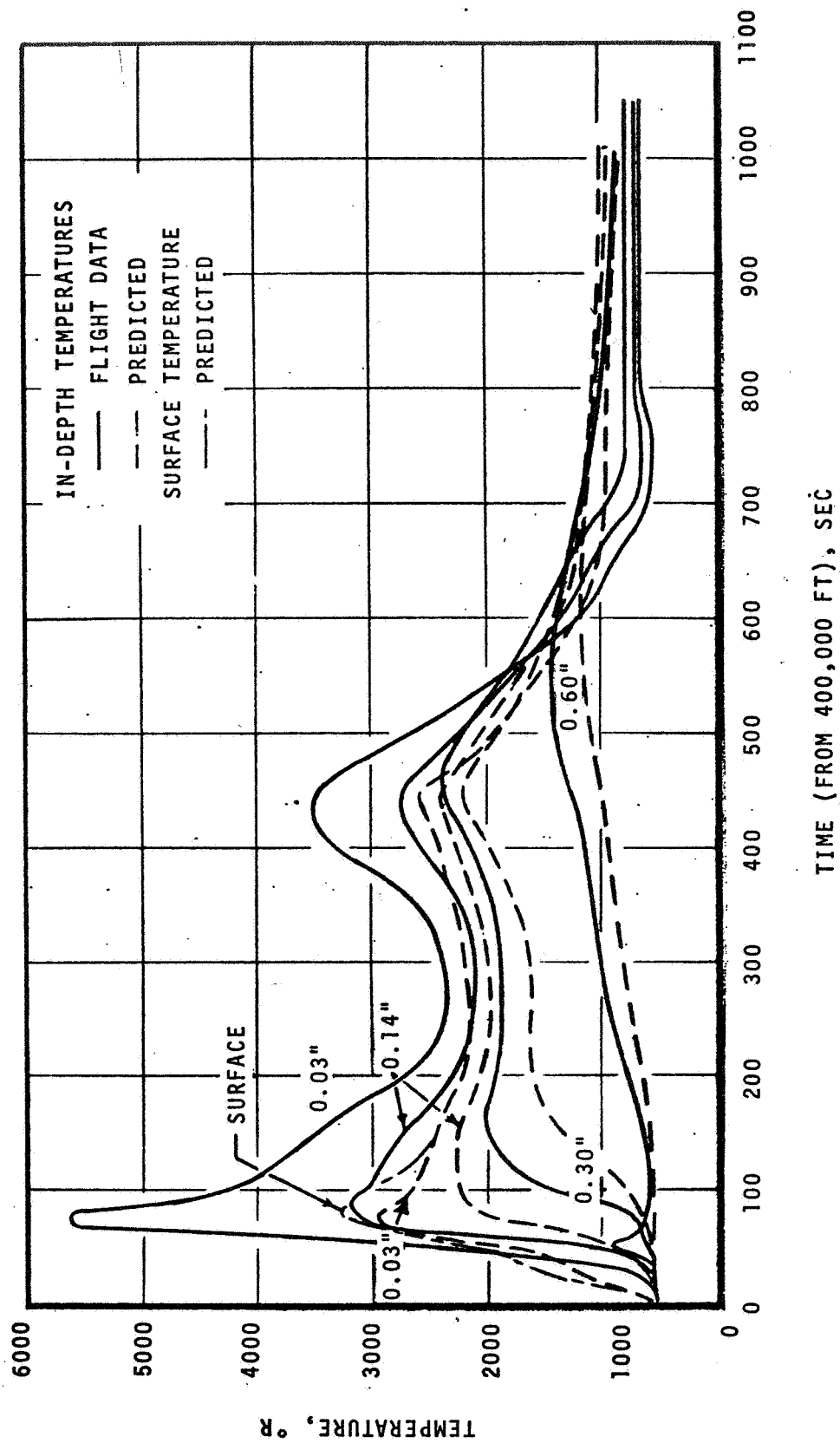
a. Laminar Flow

Figure 46. Comparison of Predicted Temperatures with Thermocouple Response for Flight AS 502, Body Point 707



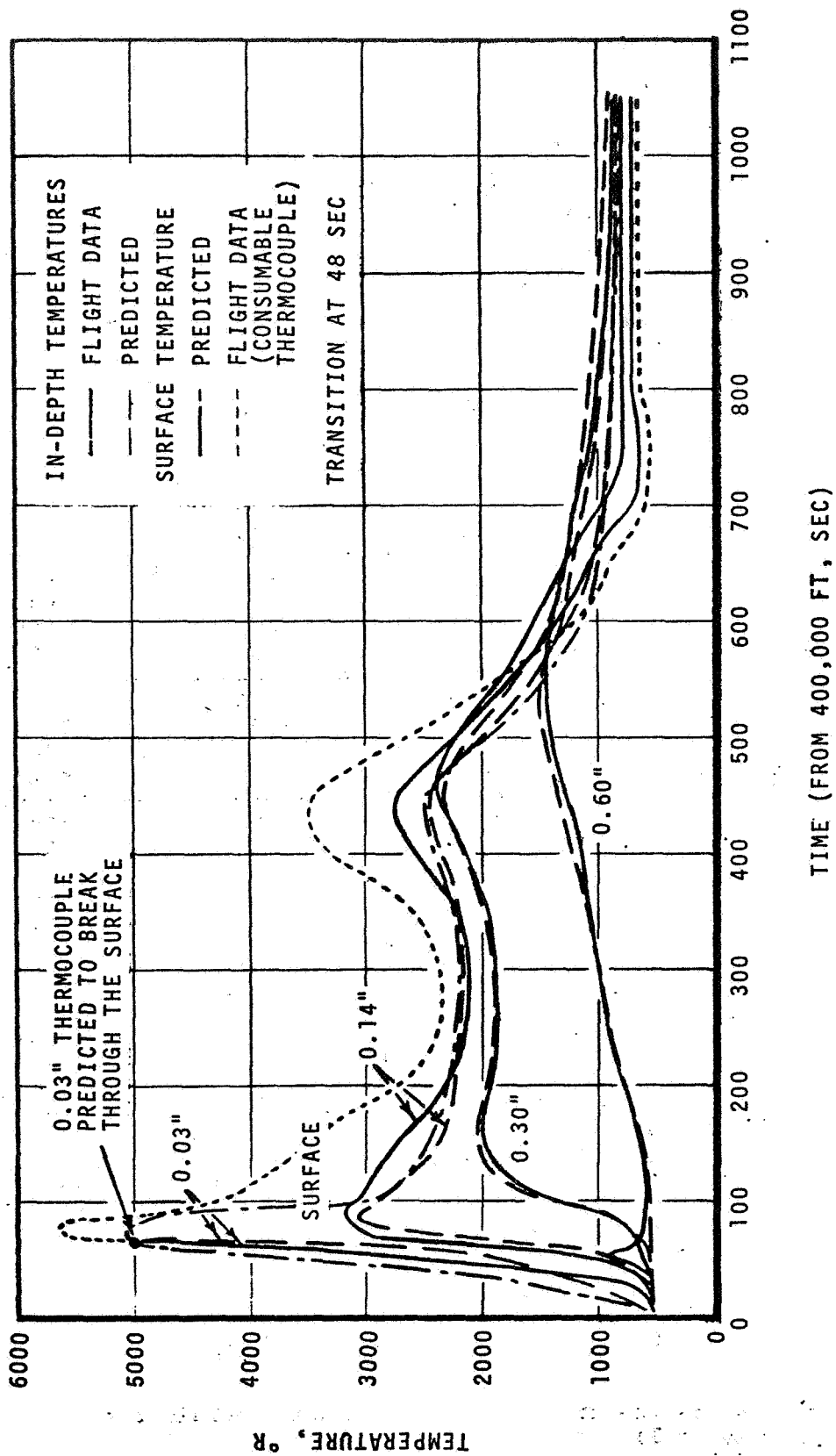
b. Laminar/Turbulent Flow

Figure 46. Concluded



a. Laminar Flow

Figure 47. Comparison of Predicted Temperatures with Thermocouple Response for Flight AS 501, Body Point 707



b. Laminar/Turbulent Flow

Figure 47. Concluded

TABLE 23

SUMMARY OF ERRORS IN PREDICTED IN-DEPTH
TEMPERATURE RESPONSE**

Case	Flight	Body Point	Thermocouple Depth, Inch	Maximum Error °R	Average Error Over the Flight, °R	Error at End of Flight, °R
1	202	Z71,Y0	0.05	+500	+50	*
			0.15	+400	+100	+300
			0.35	+600	+200	+100
			0.60	+500	nil	+150
			1.10	-200	-100	-50
			2.54	-150	-50	nil
2	502	705	0.10	-200	-50	*
			0.30	-150	nil	+50
			0.60	-150	nil	+50
			0.90	-150	-50	-100
3	501	705	0.10	-1,100	-300	*
			0.30	-500	-100	+250
			0.60	-250	-50	+200
			0.90	-300	-100	nil
4	202	Z0,Y33	0.05	+1,100	+250	+300
			0.20	+750	+250	+250
			0.40	+750	+150	+250
5	501	710	0.05	+300	+50	nil
			0.18	+150	+50	nil
			0.42	-50	nil	nil
6	502	707	0.02	-2800/+500 [†]	-350/+200	+300/*
			0.15	-1900/-1000	-150/-100	+400/+350
			0.30	-800/-350	-150/-50	+400/+350
			0.60	-300/-100	-200/nil	nil/nil
7	501	707	0.03	-2700/-500	-300/-150	+200/*
			0.14	-1000/-400	-100/-50	+200/+150
			0.30	-750/+300	-100/+50	+150/+50
			0.60	-300/+100	-100/nil	+150/-50

* Thermocouple predicted to break through the surface.

** A + sign indicates the prediction is higher than the measured data.

[†] 2800/500 represents the errors for laminar and turbulent flow, respectively (typical).

ORIGINAL PAGE IS
OF POOR QUALITY

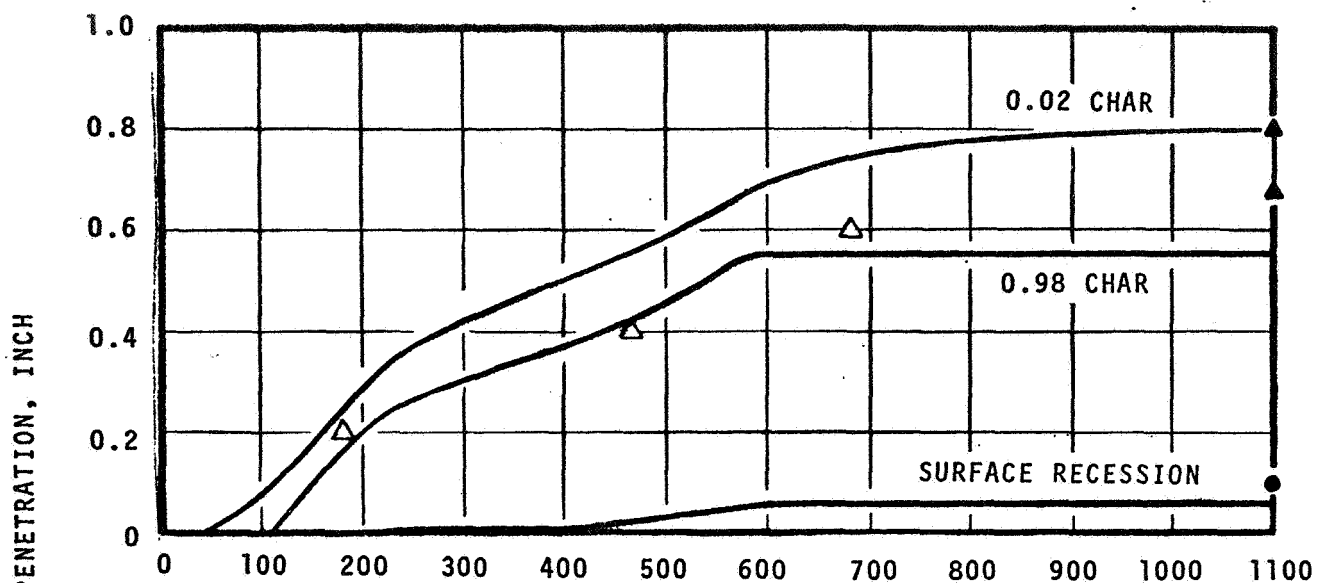
6.2.2 Surface Ablation and Char Penetration

Predicted time histories of surface recession and char penetration (i.e., surface recession plus char depth) are presented for AS 202, AS 501, and AS 502 in Figures 48 through 50. Char sensor data and measured values for final recession and char penetration are also shown. In some cases more than one "measured" value is presented as reported in various sources^{50,52,55,56}.

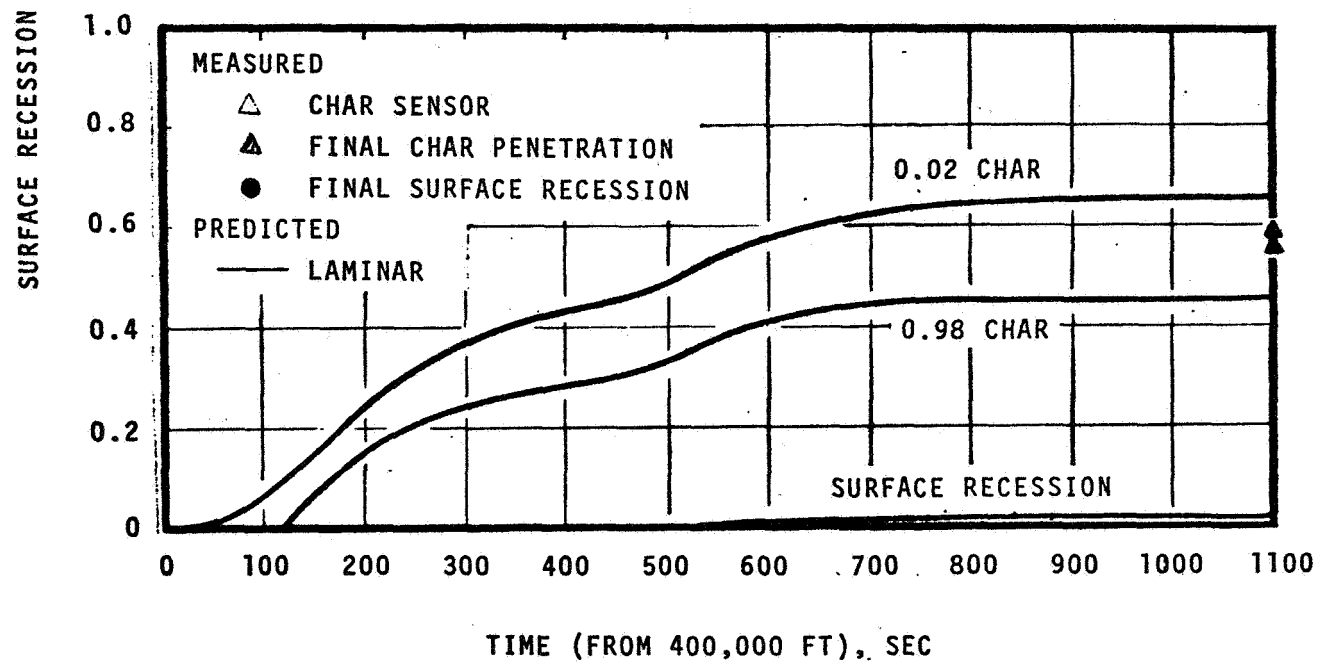
The char penetrations are shown for two conditions - when charring is 2 percent and 98 percent complete. The char sensor data and the measured "char depth" would be expected to correspond to something in between these limits. With this in mind, it can be seen that the char penetration is predicted within 0.10 inch which is about the same as the uncertainty in the measured values as evidenced by the different reported values. This corresponds to a 15 percent uncertainty in predicted char penetration.

Surface recession is predicted within 0.070 inch in all cases. Although this represents a substantial percent of the measured ablation in some cases, it is a small error relative to the overall heat shield thickness. Again, the discrepancy between predicted and measured recession is of the same order as the difference in measured recession at two neighboring core locations or as measured by two different investigators. Another complicating factor not considered in the present calculations is that the char layer of the Apollo material has been observed to shrink in some cases. Therefore, the agreement with surface recession is probably as good as can be expected for the Apollo application due to the small ablation rates and the complexities associated with the Apollo material.

In order to obtain a better appreciation for the nature of the ablation phenomena, time histories of B'_g , B'_c and T_w for Case 3 (Flight AS 501, Body Point 705) are presented in Figure 51. Prior to 60 seconds in the trajectory (see Table 21c), the B'_c (and, hence, the \dot{m}_w (see Eq. (25)) is zero because of the large B'_g coupled with a T_w below 3600°R (see Figure 40). Thus nearly half of the incident radiation pulse and the first part of the convective heating pulse do not contribute directly to surface ablation. When 3600°R is exceeded, the B'_c attains the plateau value of nominally 0.22 where it remains through most of the first peak heating. At about 145 seconds, the surface temperature drops below 3600°R . The B'_c then drops in accordance with the value of B'_g of about 0.5, falling to zero as the T_w reaches a minimum of 2600°R at 280 to 300 seconds. The B'_c then increases again during the second heating pulse, rising nearly to the plateau value, due both to the increasing T_w and the decreasing B'_g during this portion of the trajectory. The B'_c then decreases to zero at 500 seconds, when the T_w drops to 2250°R , and ablation is completed. The total surface recession is divided nearly evenly between the first and second heating



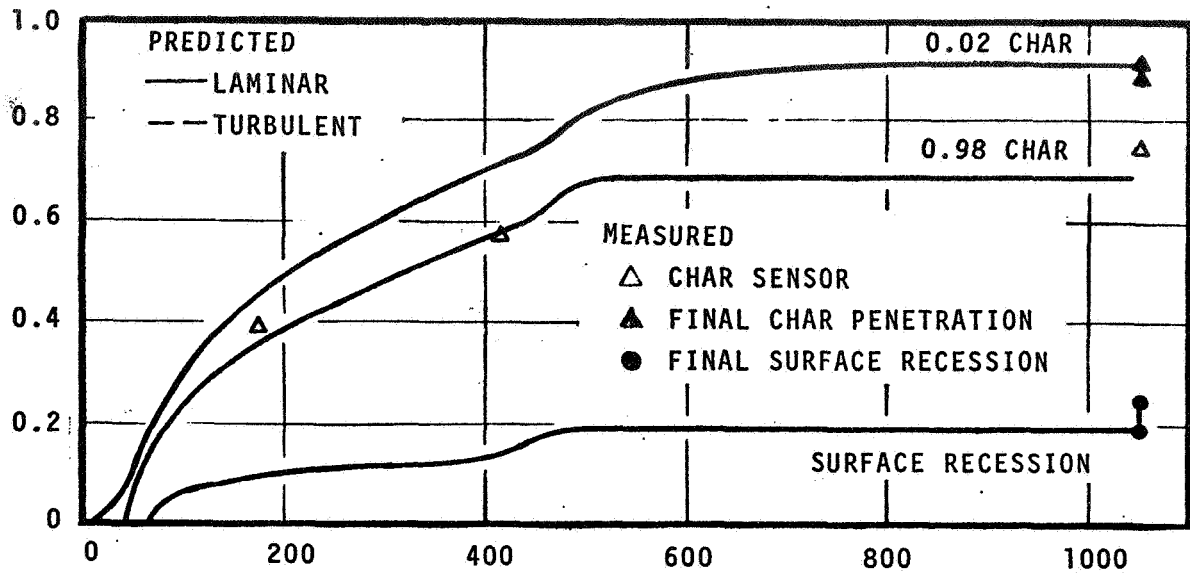
a. Case 1 (Body Point Z71, YO (705).)



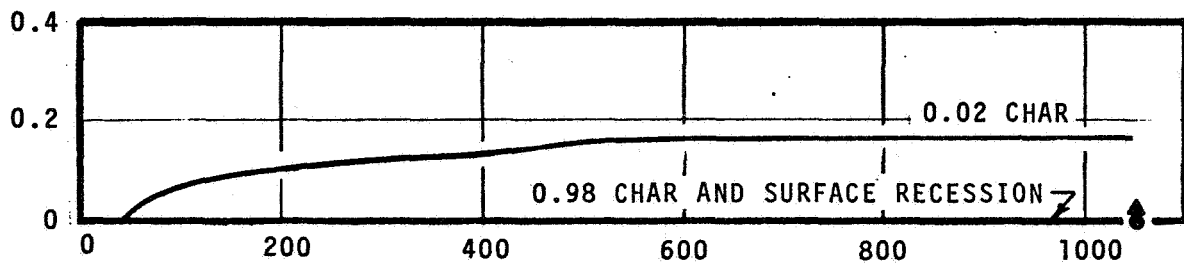
b. Case 4 (Body Point Z0, Y33)

Figure 48. Surface Recession and Char Penetration for Flight AS 202

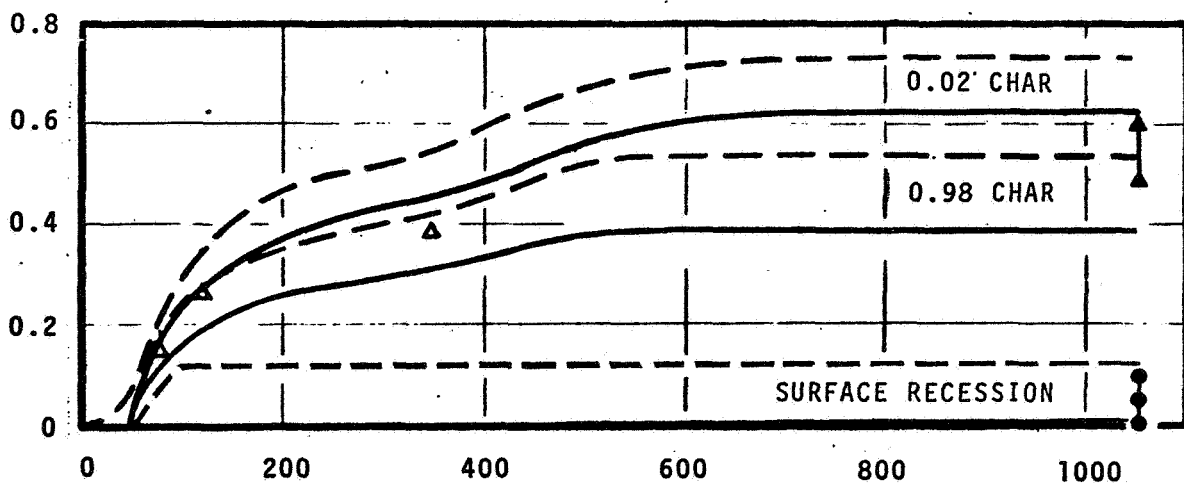
SURFACE RECESSION AND CHAR PENETRATION, INCH



a. Case 3 (Body Point 705)

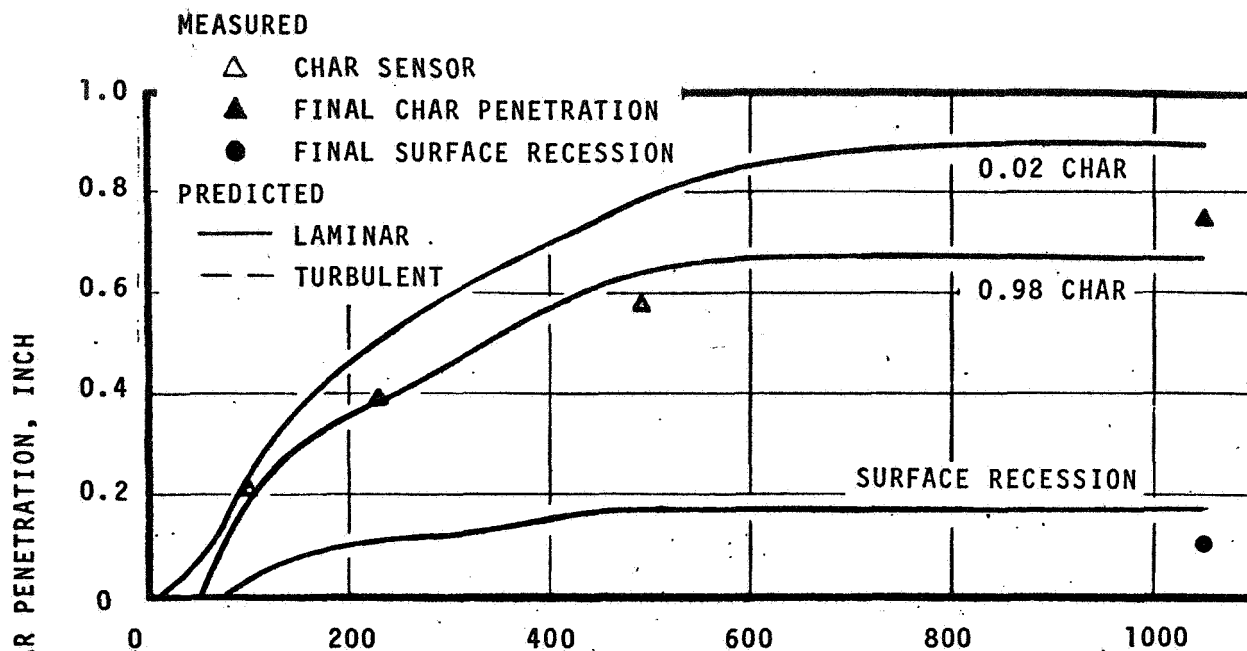


b. Case 5 (Body Point 710)

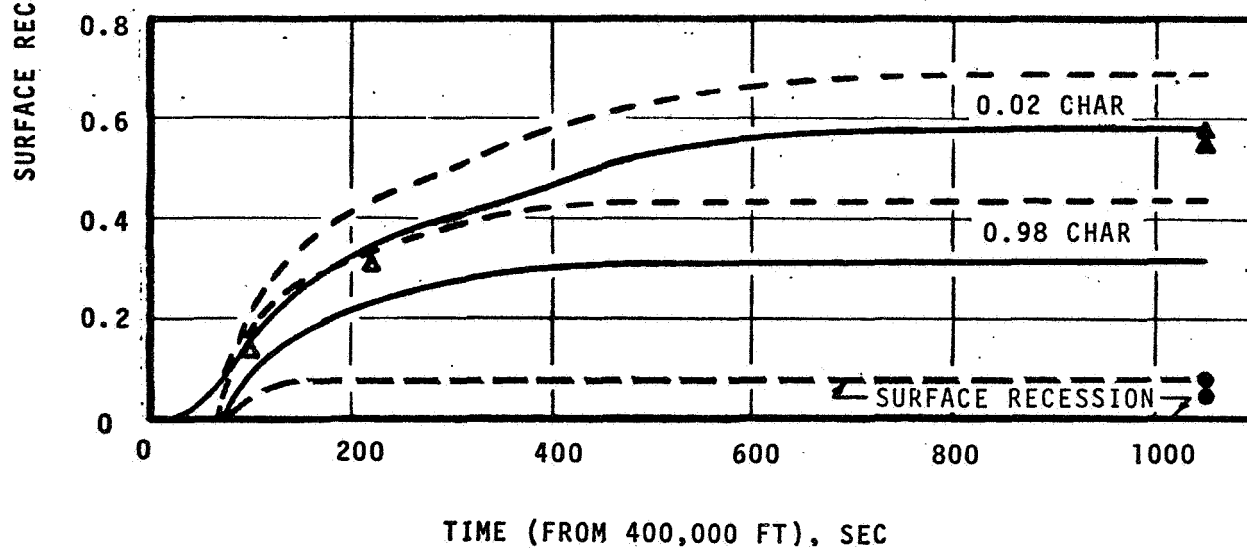


c. Case 7 (Body Point 707)

Figure 49. Surface Recession and Char Penetration for Flight AS 501



a. Case 2 (Body Point 705)



b. Case 6 (Body Point 707)

Figure 50. Surface Recession and Char Penetration for Flight AS 502

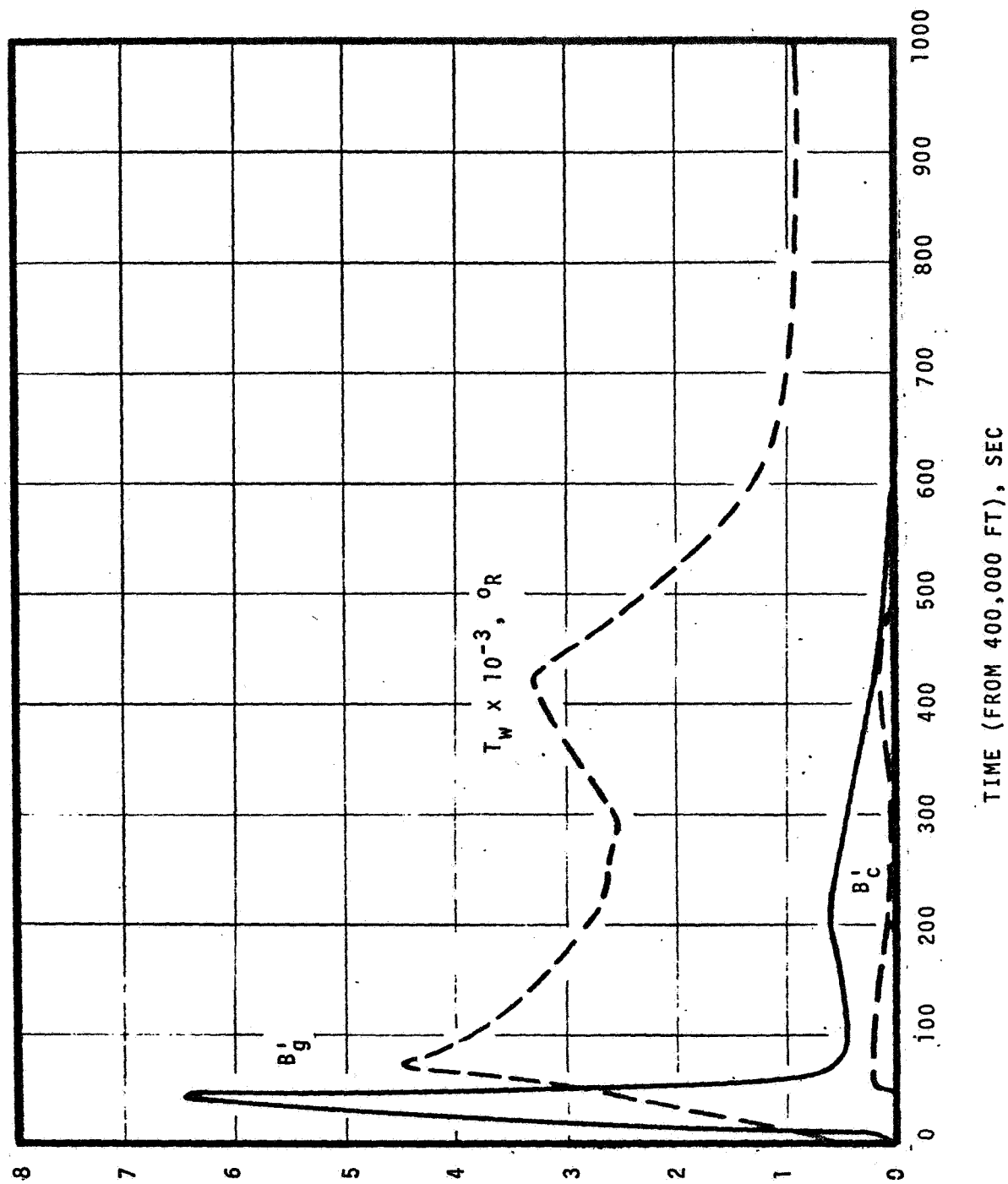


Figure 51. Predicted Blowing Rates and Surface Temperatures for Flight AS 501, Body Point 705

pulses for this flight, since the B_c' , the $\rho_e U_e C_M$, and the time durations are all about the same. (While the total enthalpy, and hence the heat flux, is considerably less during the second heat pulse, the $\rho_e U_e C_{H_O}^i$ - and hence the $\rho_e U_e C_M$ - are about the same.) This behavior is typical of the type of behavior exhibited for the other flights and body points sufficiently severe to experience significant ablation.

6.2.3 Char Density

In order to illustrate the nature of the coking predictions, density of the wall material and surface temperature are presented as functions of trajectory time in Figure 52 for Case 3 (Flight AS 501, Body Point 705). The virgin material initially has a density of 34 lb/ft³. Pyrolysis of the wall material is predicted to start at 10 seconds and to be completed at 35 seconds when the surface density is reduced to 16 lb/ft³. Coking of the surface material starts at 40 seconds and the surface density reaches a maximum of 25 lb/ft³ at 120 seconds. In the mean time, the surface temperature has passed through a maximum of 4500°R so that some internal char erosion is predicted (see Figure 34). The surface density is reduced thereafter until it reaches a final value of 22 lb/ft³ at 520 seconds. This reduction in surface density is the result of surface recession of high-density surface material.

In-depth profiles of material density are presented in Figure 53 for several trajectory times for the same case. Corresponding temperature profiles are also presented in Figure 53. This shows more clearly the events described above. It is particularly interesting to note how the surface density decreases due to surface recession while coking is still taking place. Also, note at early times (e.g., 75 seconds) that the maximum char density does not occur at the surface. This results from the fact that the temperature of the char near the surface is sufficiently hot that coking is completed in depth. In accordance with Equation (60) considered together with Figure 34, the coking rate is reduced to zero when the temperature is slightly in excess of 3600°R.*

Final predicted density profiles are shown for the three flights in Figures 54 through 56. Measured values reported in Reference 2 through 4 are also shown for the six cases where these data are available. It was difficult to obtain an accurate reference for the measured data; hence, these may be mis-plotted by as much as 0.050 inch or so. It can be seen that while the density inversion is predicted qualitatively, the agreement is not always good; the turbulent flow solutions (Cases 6 and 7) are predicted quite well, the Flights AS 501 and 502 stagnation-point solutions (Cases 2 and 3) are predicted fairly well, and the Flight AS 202 (Cases 1 and 4) solutions yield poor agreement.

*At very high char temperatures, internal char erosion would be predicted to occur since K_{C_g} increases with temperature (see Figure 34).

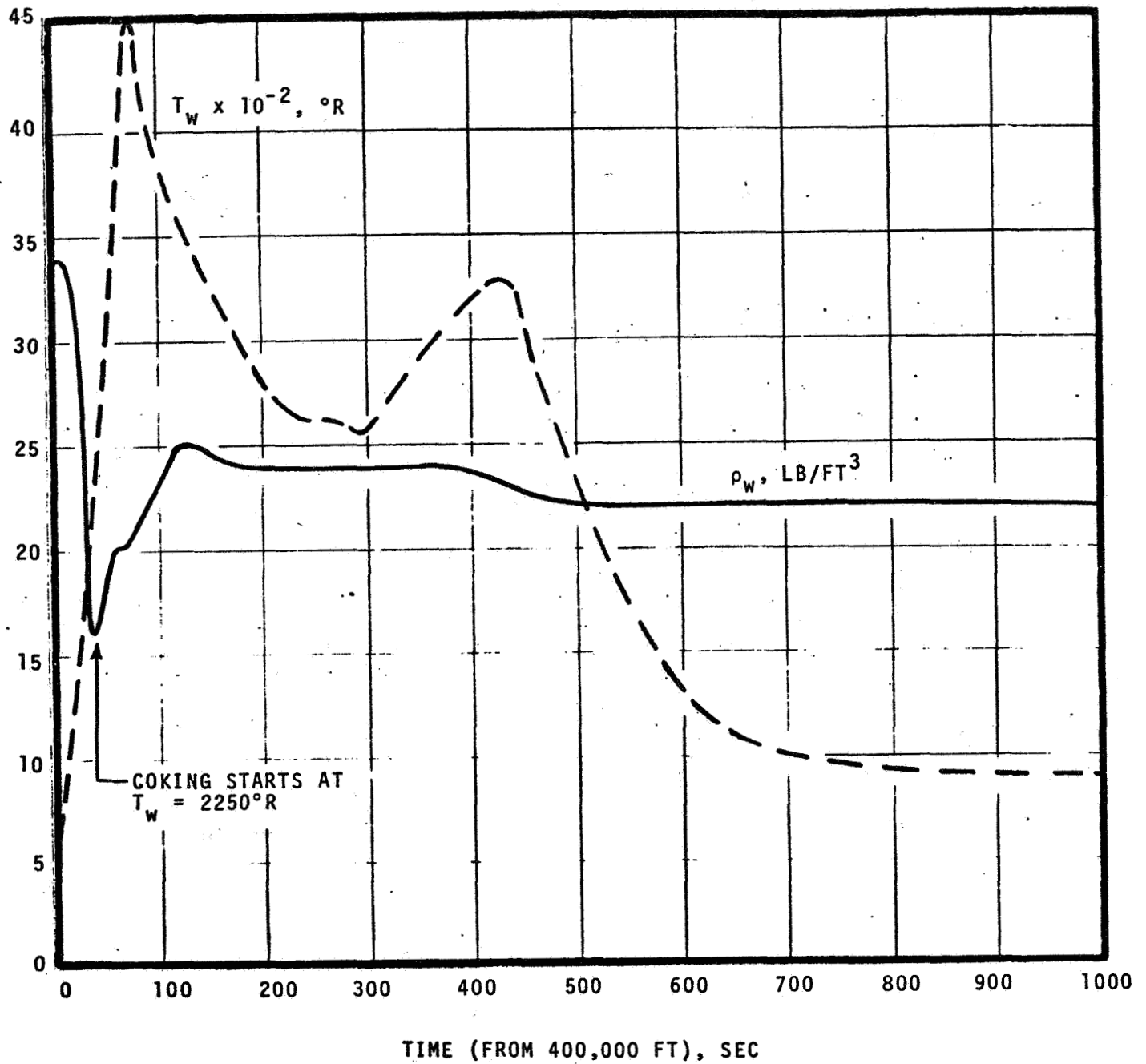
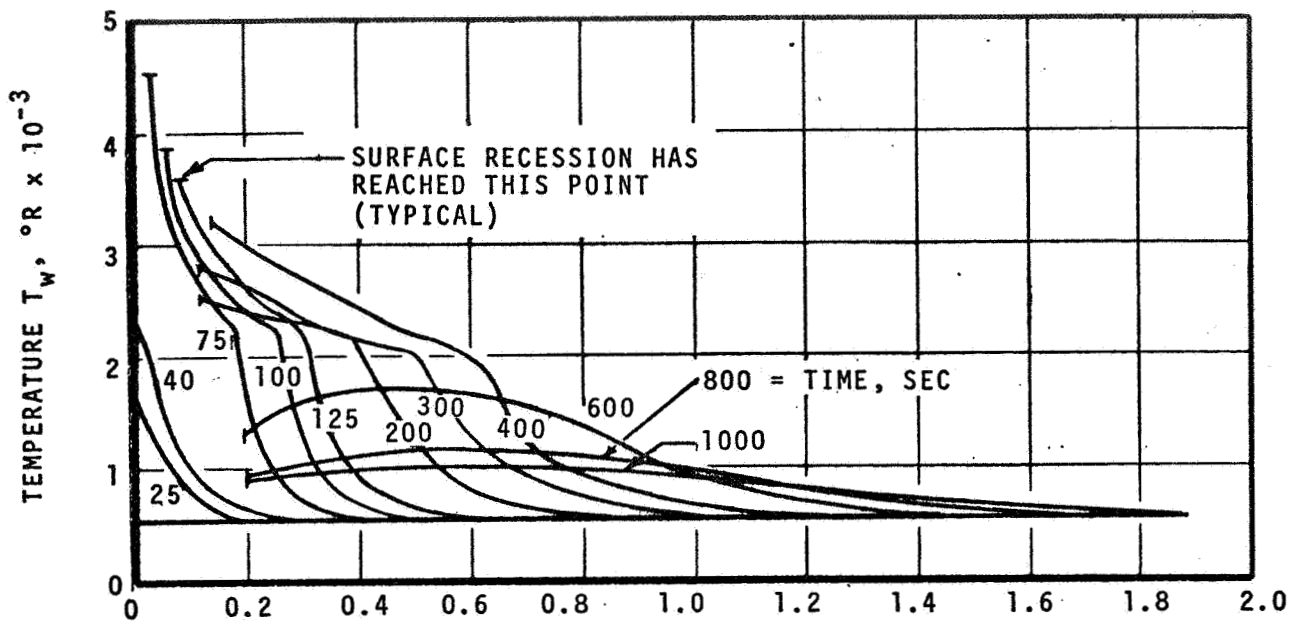
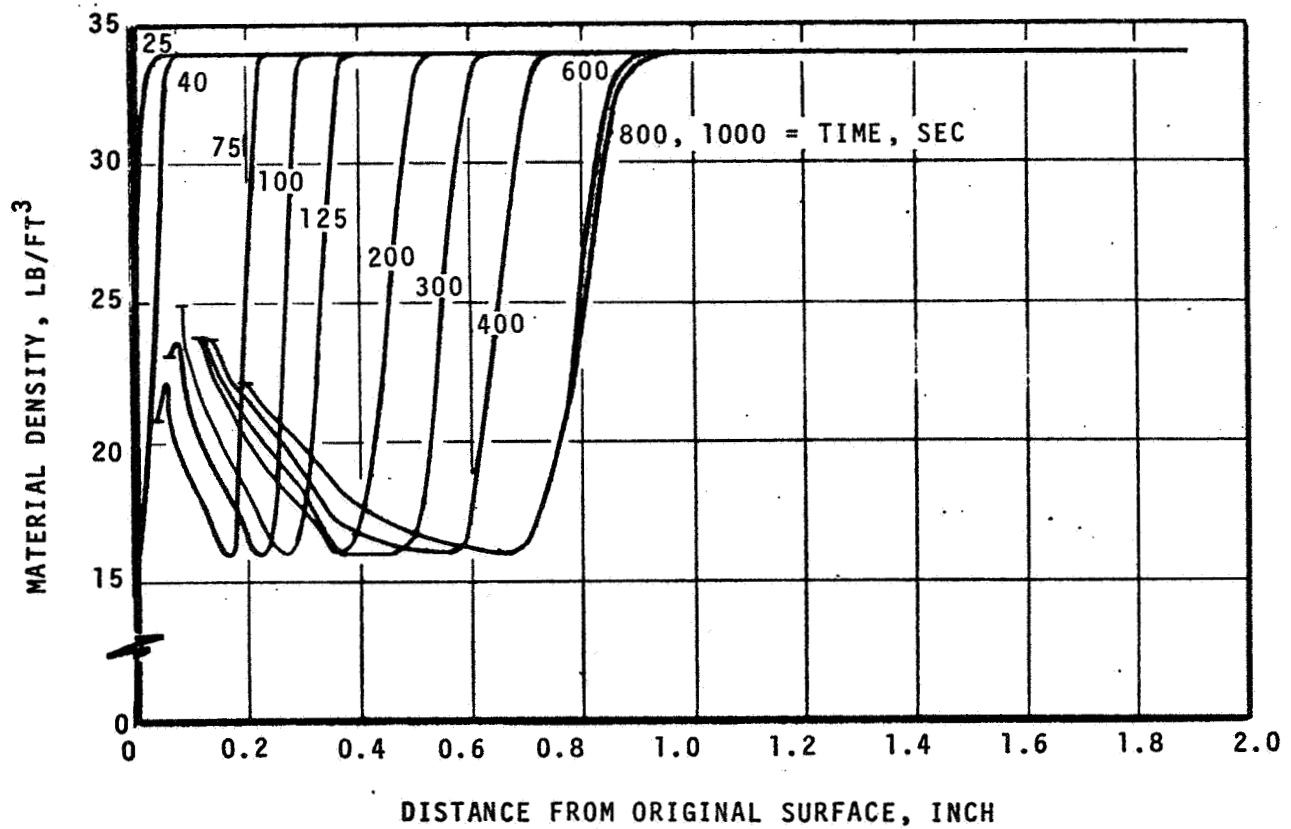


Figure 52. Predicted Density of Surface Material and Corresponding Temperatures for Flight AS 501, Body Point 705

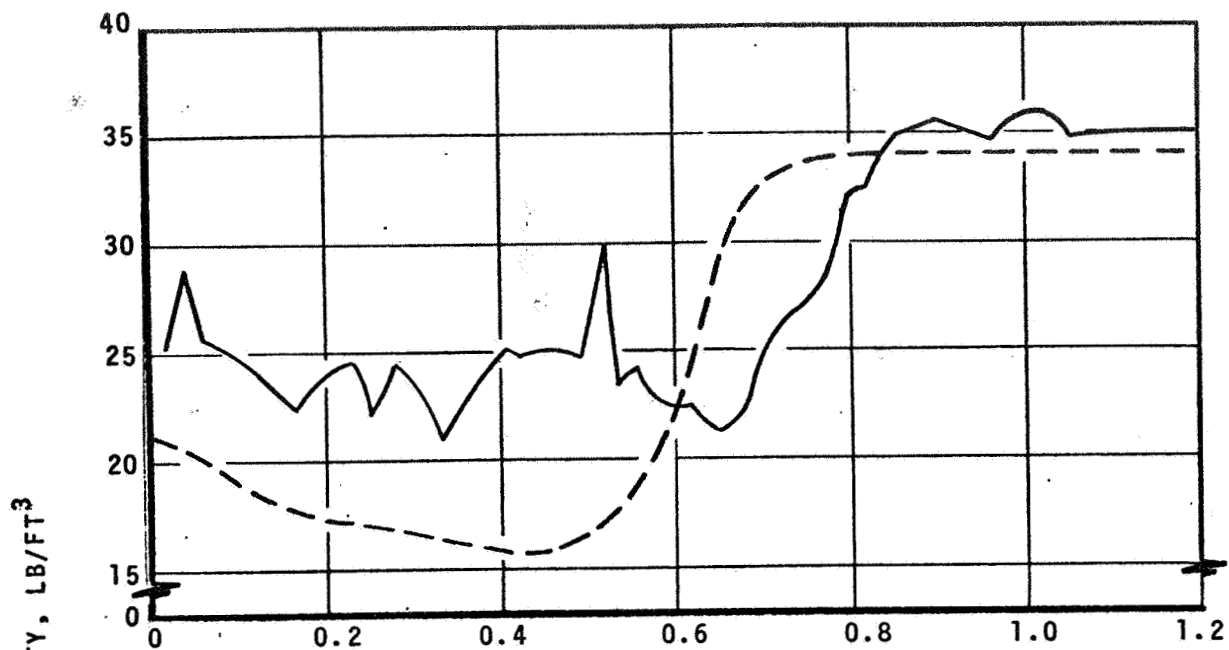


a. Temperature Profiles

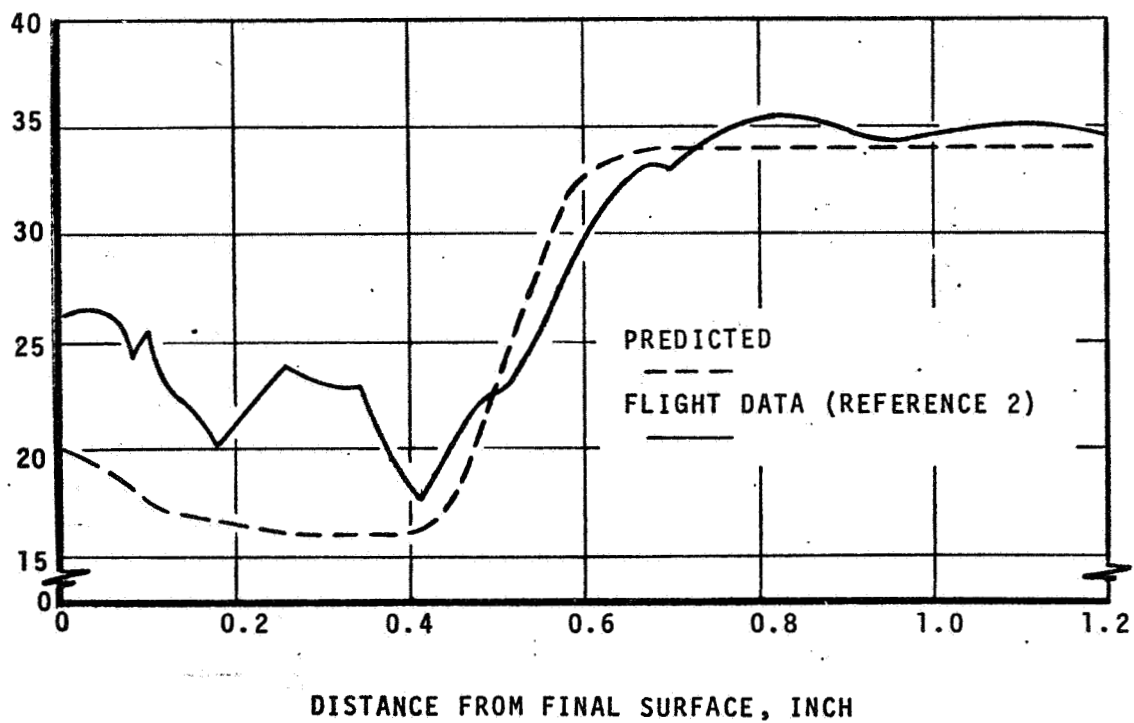


b. Material Density Profiles

Figure 53. In-Depth Temperature and Material Density Profiles for Flight AS 501, Body Point 705



a. Case 1 (Body Point Z71, YO (705))



b. Case 4 (Body Point Z0, Y33)

Figure 54. Material Density Profiles for Flight AS 202

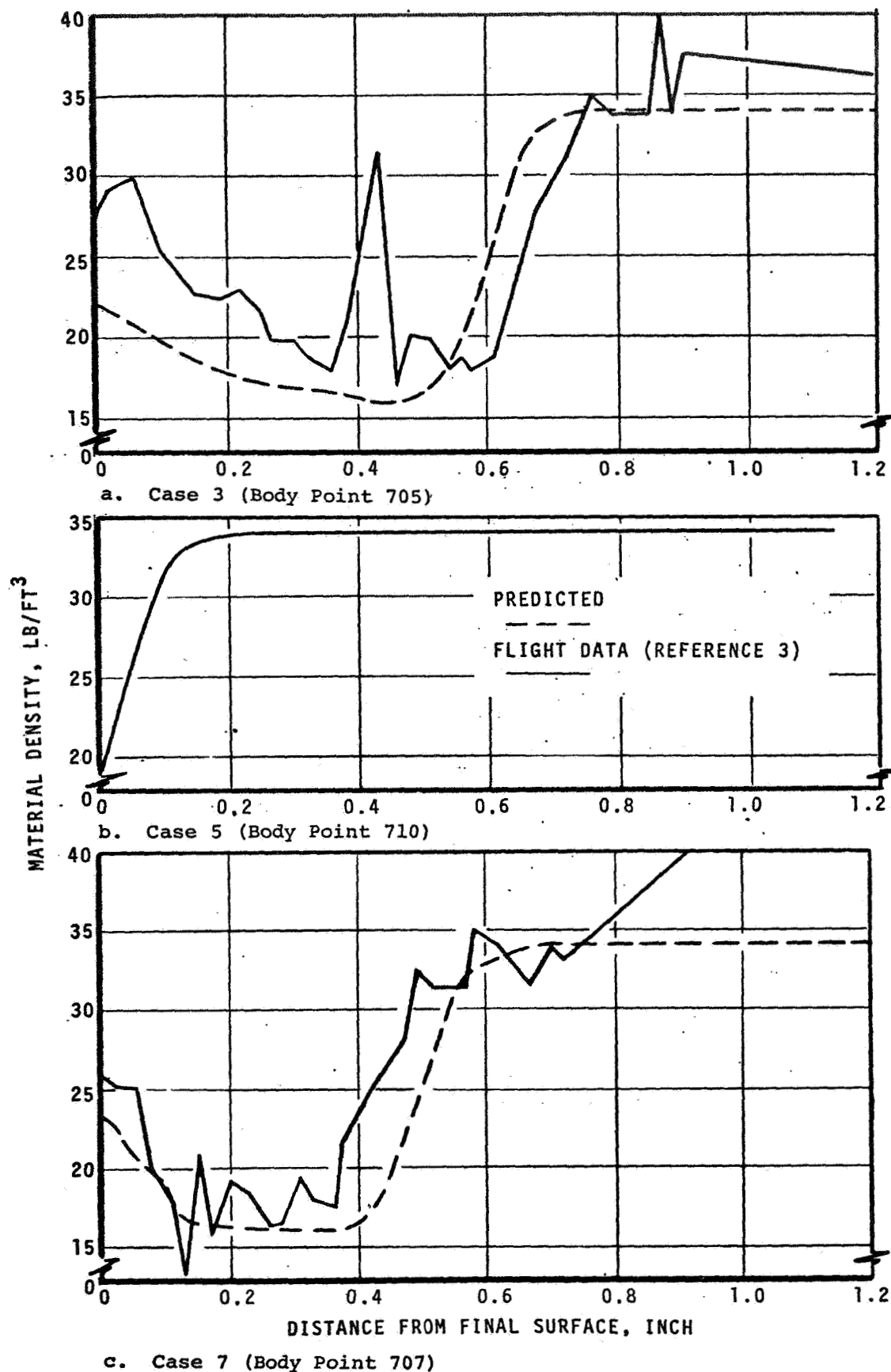
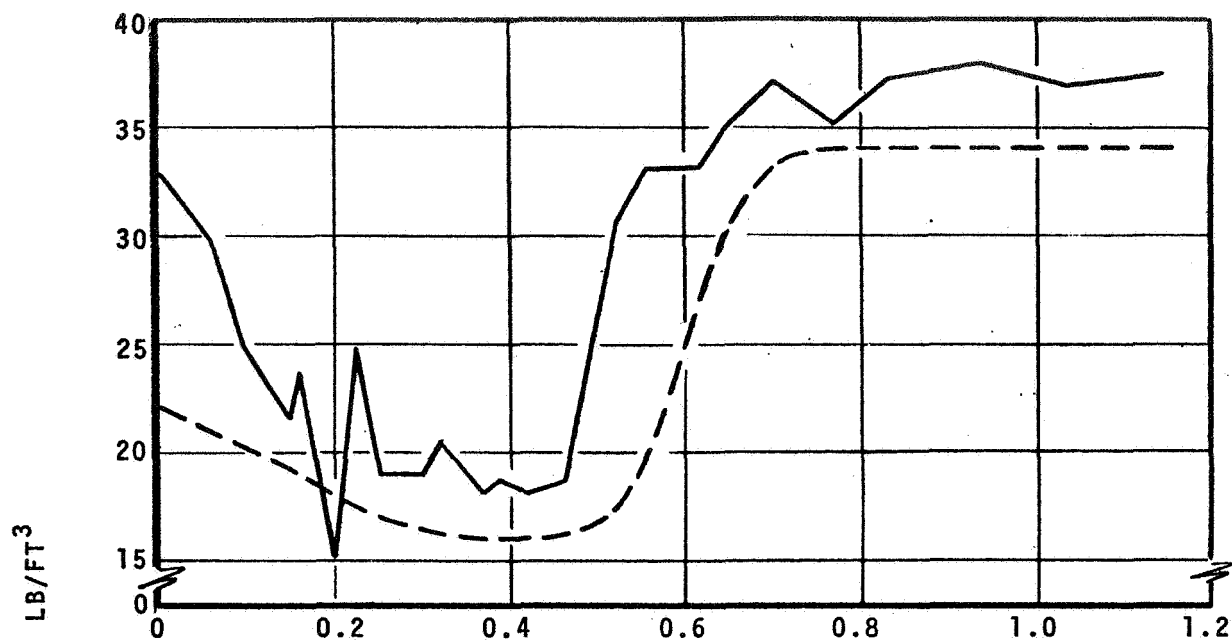
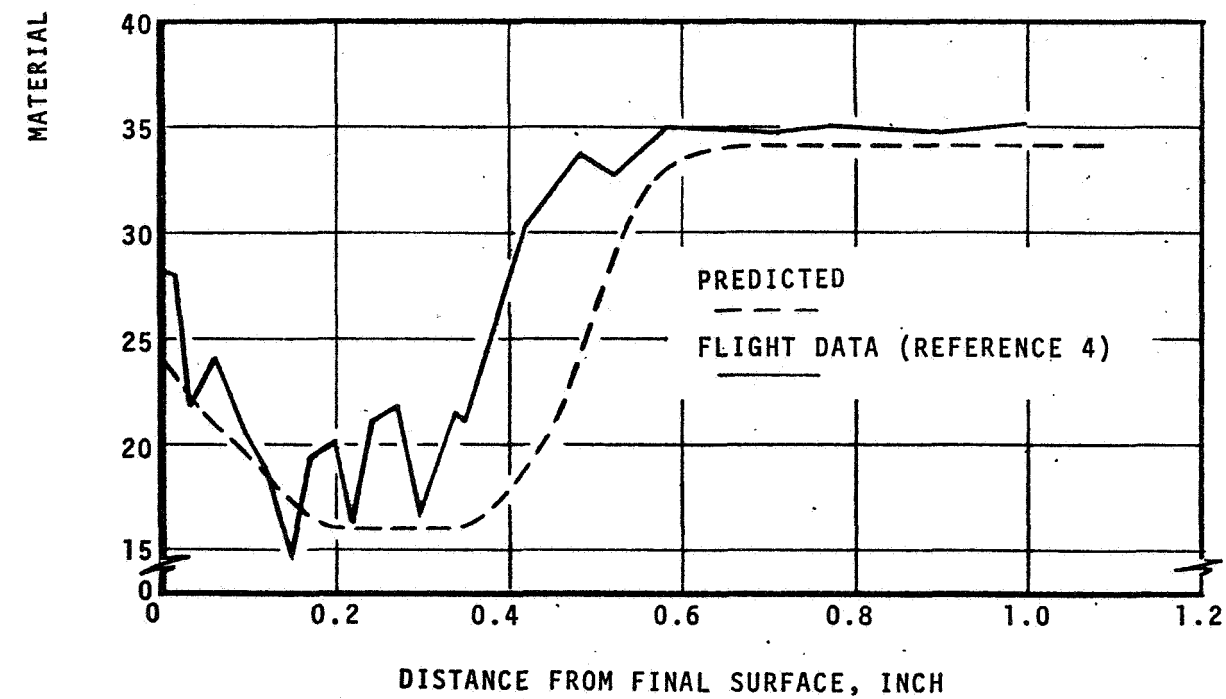


Figure 55. Material Density Profiles for Flight AS 501



a. Case 2 (Body Point 705)



b. Case 6 (Body Point 707)

Figure 56. Material Density Profiles for Flight AS 502

In particular, the measured density is typically higher and does not reduce to a value of 16 lb/ft^3 such as was assumed in the theoretical model for fully pyrolyzed (but uncoked) char (see Section 5.1).

It was also observed in References 2 through 4 that the ash content (presumably silica plus other oxides) typically is higher in the char layer than in the virgin material.* Therefore, a study was made to compare predicted and measured carbon density profiles. This comparison is made in Figures 57 through 59 for the 5 cases for which ash content data were available. Carbon density was obtained simply as the total density minus the ash density. In the case of the predictions, the correction is simple since the ash content is assumed to be constant throughout the char layer at a value of approximately 8 lb/ft^3 . The values reported as measured data were obtained by multiplying a data-smoothed measured total density (also shown in Figures 57 through 59) by a data-smoothed measured percent ash content. It can be seen that the agreement of the prediction and the Apollo flight data is excellent.

In conclusion, assuming the buildup of excess ash in the char layer is indeed primarily silica, the current technique appears to predict carbon deposition very well. Total density profiles are not predicted as well, however, because of the increase in ash content which is not considered in the theoretical model.

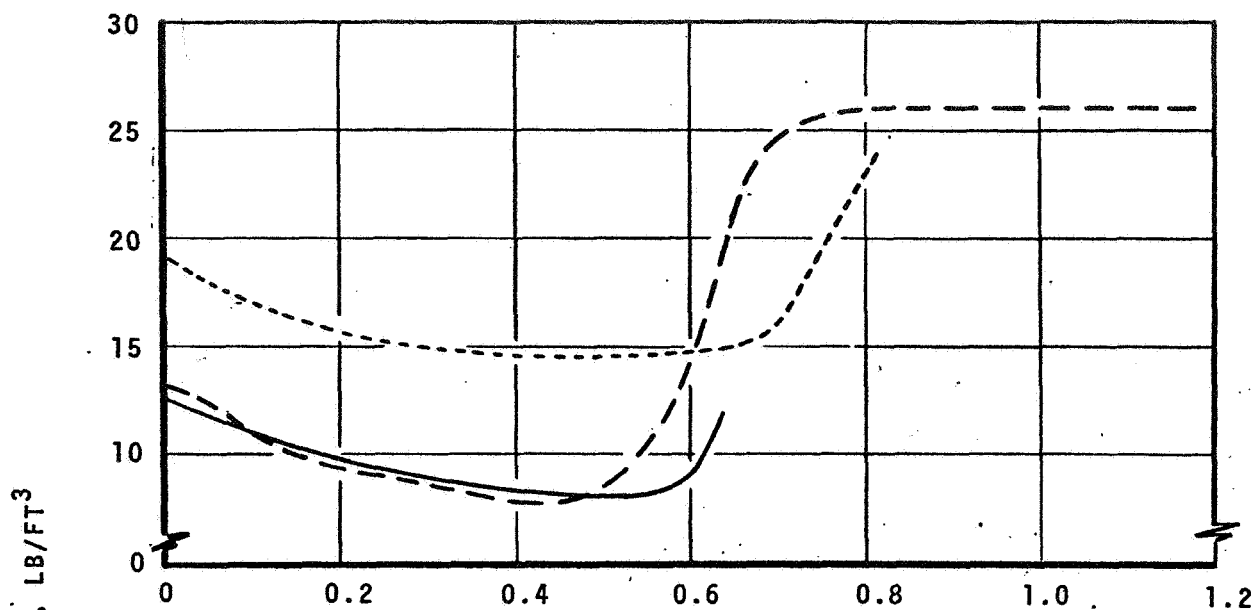
6.2.4 Heat Transfer

The flight predictions which have been generated permit a number of interesting observations and data correlations related to convective heating rates to the surface. Predictions for convective heating rates, the partition of the incident heating into reradiation, conduction, etc., and the further partition of the net energy into the material into decomposition energy, etc., are presented for one of the cases in the first subsection. The blowing corrections predicted to occur in this flight are also presented therein. Available measured convective heating data are compared to predictions in the second subsection. Studies leading to the selection of transition criteria are also presented therein.

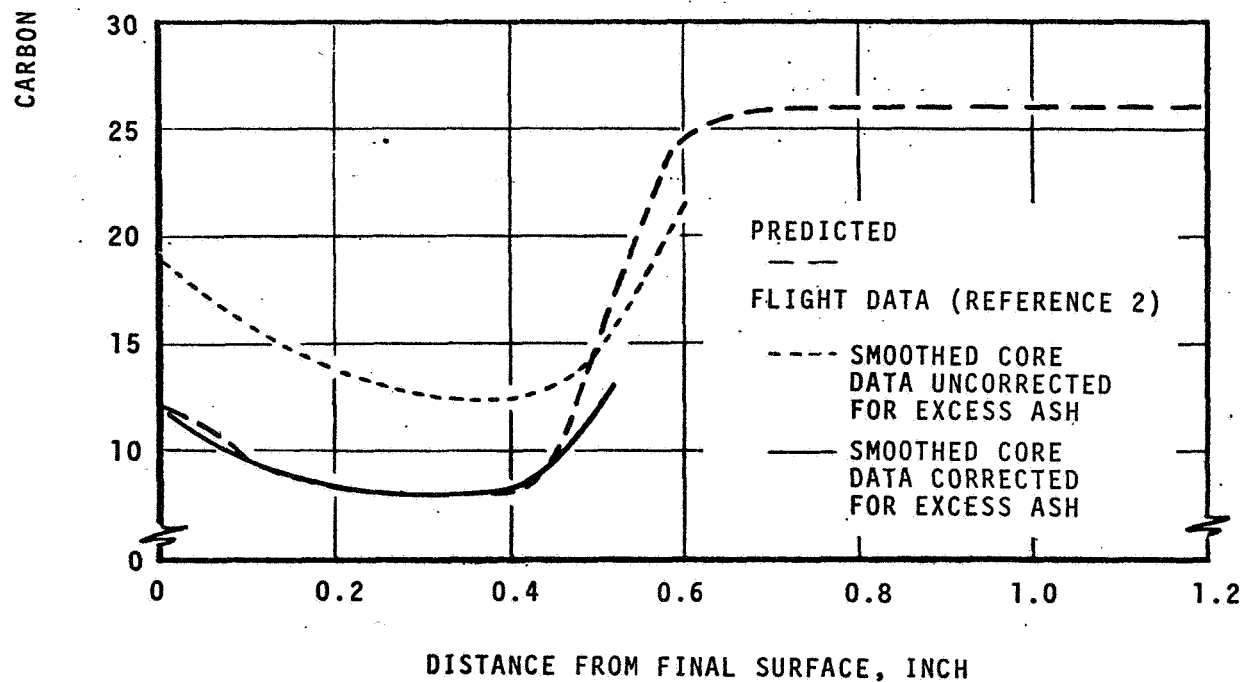
a. Convective Heating Predictions for Flight AS 501, Body Point 705

The predicted convective heating rate for Case 3 (Flight AS 501, Body Point 705) is shown together with the input radiative heat rate and the total

* It was seen in Section 5.2 that this excess ash is often roughly equivalent to the silica corresponding to the ablated depth. On the other hand, it was suggested in Reference 3 that at least part of the excess ash might be the result of unburned carbon.



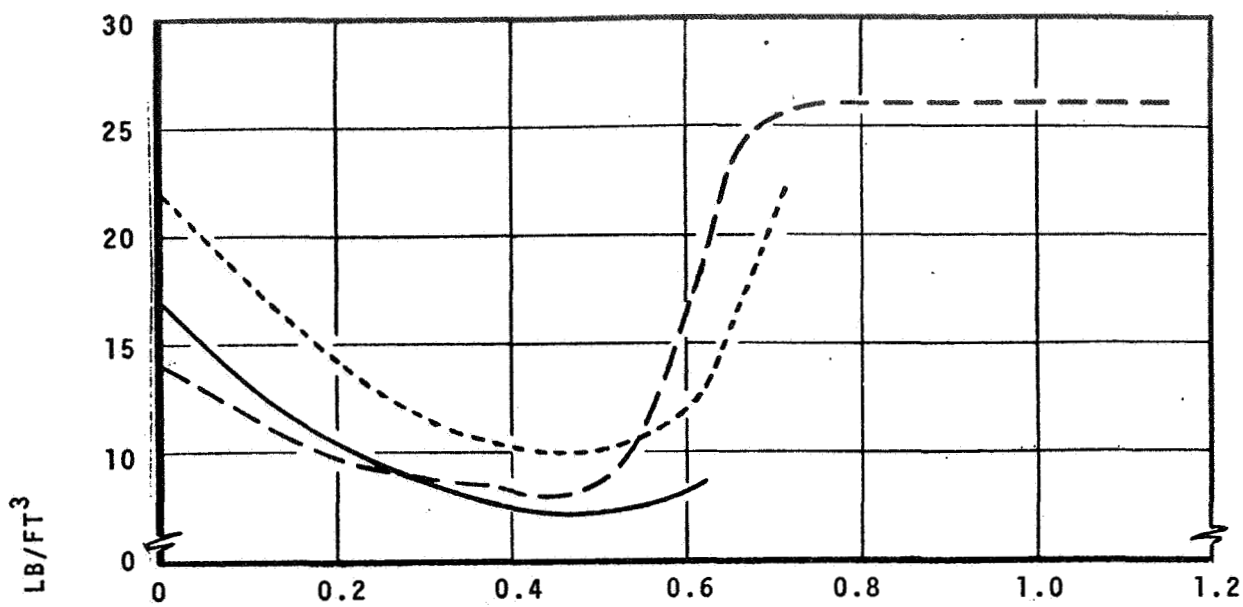
a. Case 1 (Body Point Z71, Y0 (705))



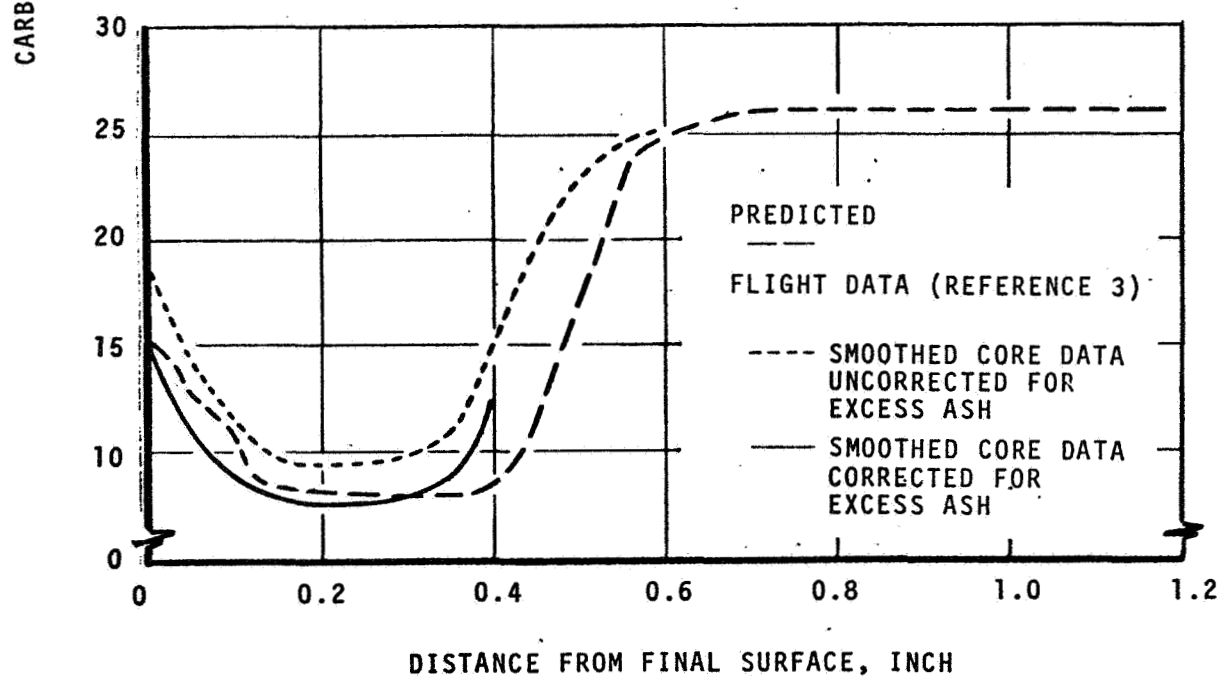
b. Case 4 (Body Point Z0, Y33)

Figure 57. Carbon Density Profiles for Flight AS 202

ORIGINAL PAGE IS
OF POOR QUALITY

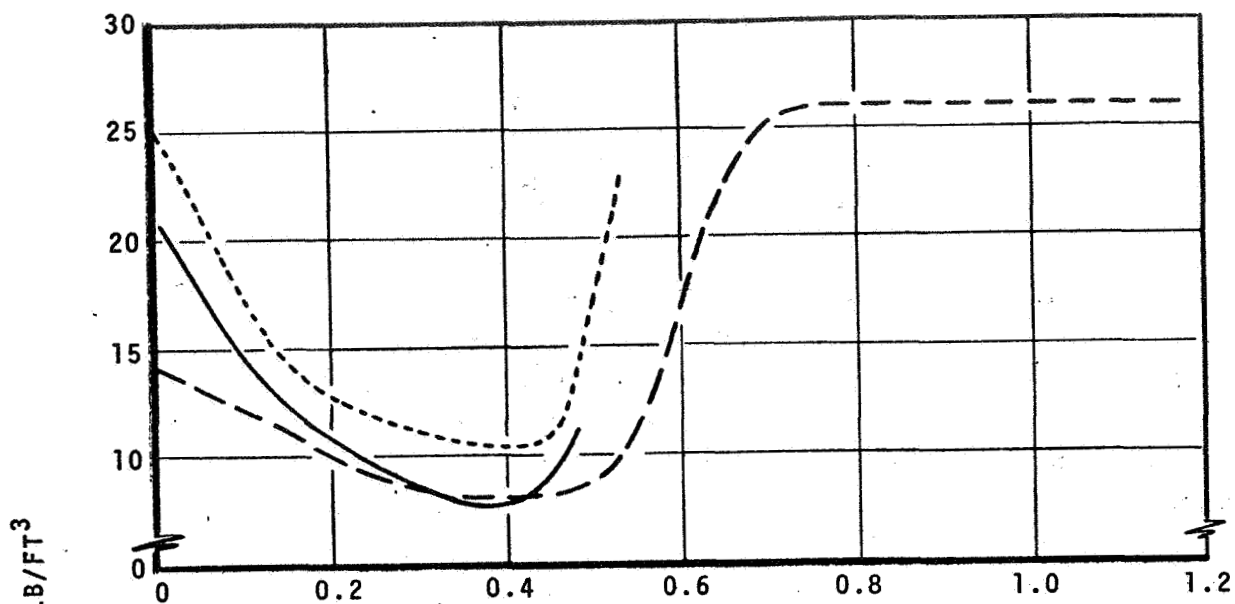


a. Case 3 (Body Point 705)

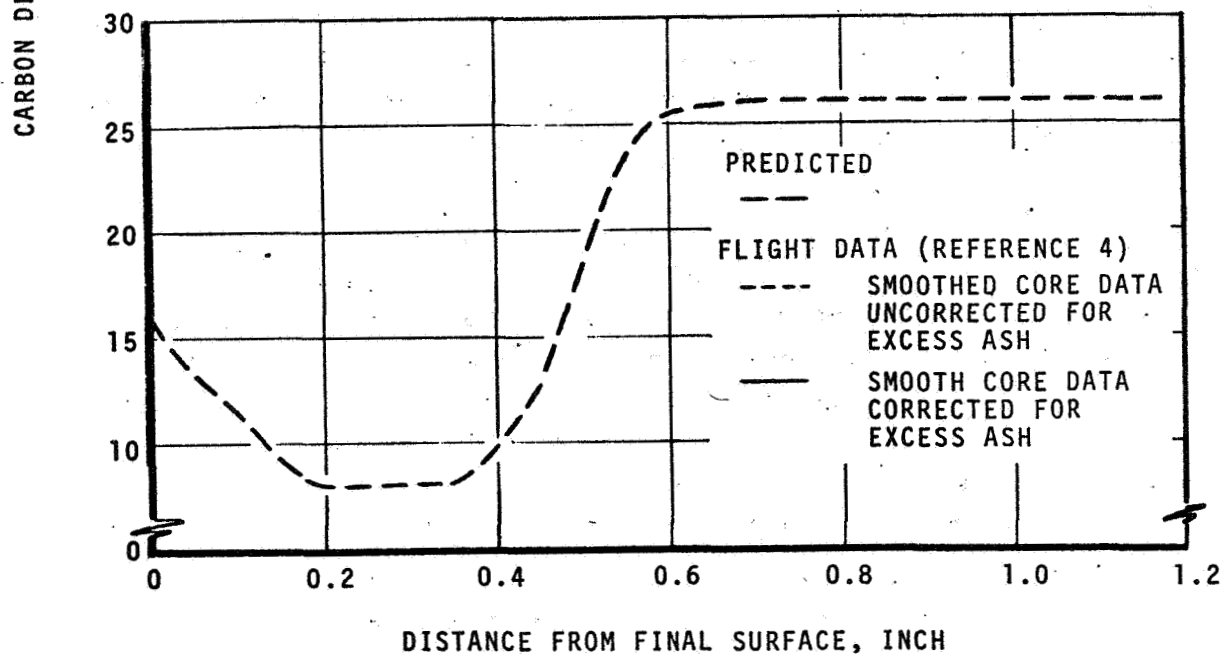


b. Case 7 (Body Point 707)

Figure 58. Carbon Density Profiles for Flight AS 501



a. Case 2 (Body Point 705)



b. Case 6 (Body Point 707)

Figure 59. Carbon Density Profiles for Flight AS 502

(convective plus radiative) heating rate in Figure 60. It can be seen that the peak radiative heating is considerably smaller than and somewhat before the convective heating peak. This particular body point is a short distance downstream of the stagnation point, near the point of maximum convective heating (see Table 22). In the stagnation region, the q_{rad} is 75 percent higher and the q_{conv} is 28 percent lower. Applying these factors to the Body Point 705 results, it is apparent that the peak total heating at the stagnation point is about the same as at Body Point 705 and is evenly divided between convective and radiative heating.

The reduction in convective heat- and mass-transfer coefficients due to ablation processes, C_H'/C_{H_0}' and C_M'/C_{H_0}' as actually predicted for this trajectory are presented in Figure 61. It can be seen that the reduction in $\rho_e U_e C_H'$ is quite small over most of the trajectory, being less than 15 percent except for the region of high B_g' (10 to 60 seconds, see Figure 51), and here the $\rho_e U_e C_H'$ is reduced only by a factor of 2. Note that the reduction in mass-transfer coefficient is considerably larger, being roughly 35 percent over a substantial portion of the trajectory and a factor of five during the high B_g' portion of the trajectory. As mentioned in Section 5.5, this differing behavior of $\rho_e U_e C_M'$ and $\rho_e U_e C_H'$ is very significant in that the effect of mass transfer is to produce a sizeable decrease in surface ablation rate (for a given value of the thermochemical blowing parameter B') with substantially less decrease in heat transfer rate. In previous calculations (e.g., Ref. 44) where $\rho_e U_e C_M'$ and $\rho_e U_e C_H'$ were considered to be much more nearly the same, it was difficult to predict both surface ablation rates and in-depth thermocouple response with a consistent ablation model.

The partition of the total incident heating (convective plus radiative) into other surface energy terms is presented in rate form and integrated form in Figures 62 and 63, respectively. It can be seen that approximately 2/3 of the peak incident heating is reradiated from the surface. It is thus apparent that the surface emittance is very important in determining the surface temperature; as discussed in Section 5.3, a value of 0.65 was used in the present calculations. The majority of the remaining incident energy is absorbed in the various ablation mechanisms; only 15 percent of the incident heat flux is conducted into the body.

Integrated values of the interior energy terms are presented in Figure 64. The major energy absorption mechanisms are the increase in pyrolysis gas energy as the pyrolysis gas heats up and coking occurs and the net energy absorbed in the pyrolysis gas and coking reactions. Storage of energy in the solid is the major energy sink during the first half of the trajectory, but is somewhat less important than the previously mentioned terms in an overall

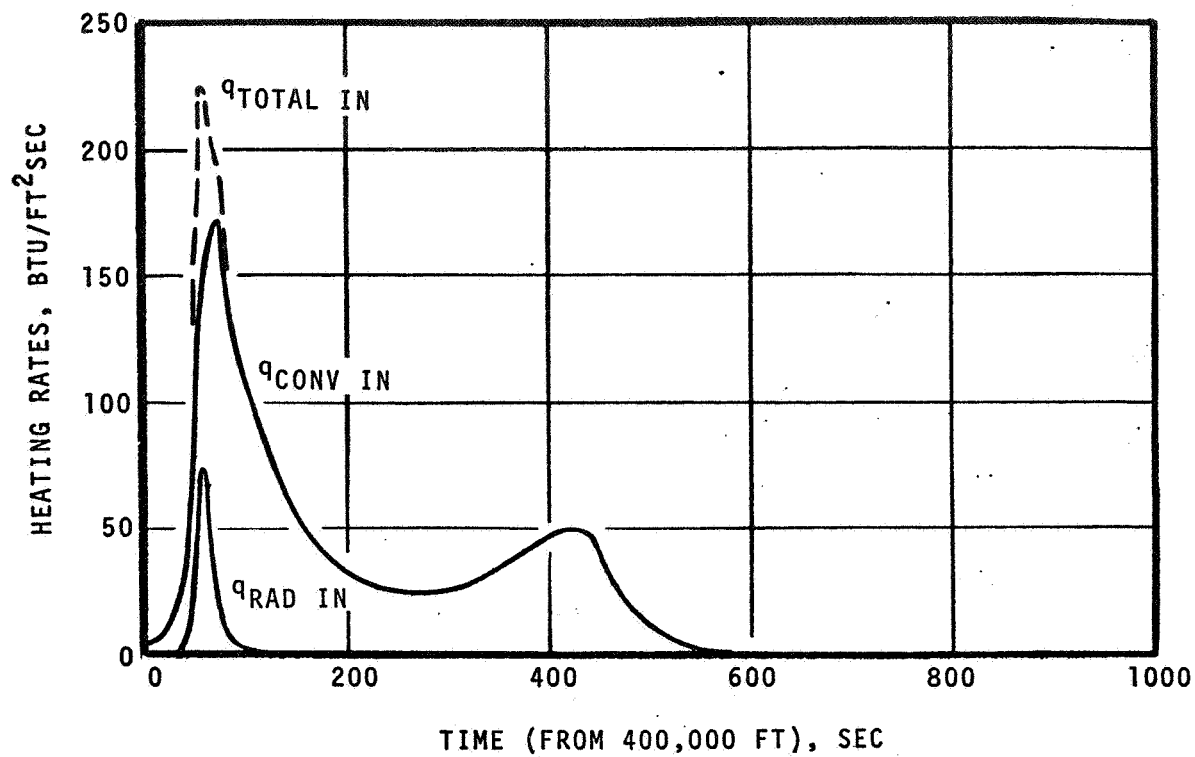


Figure 60. Heating Rate Predictions for Flight AS 501, Body Point 705

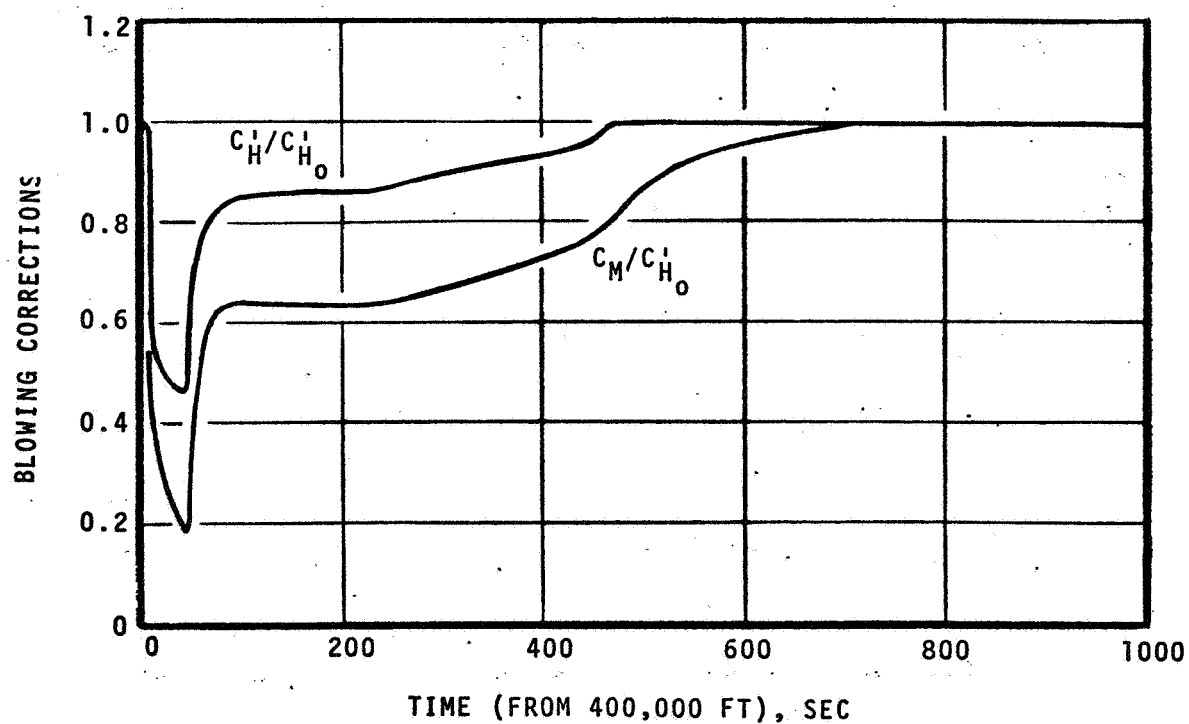


Figure 61. Blowing Reduction Histories Predicted for Flight AS 501, Body Point 705

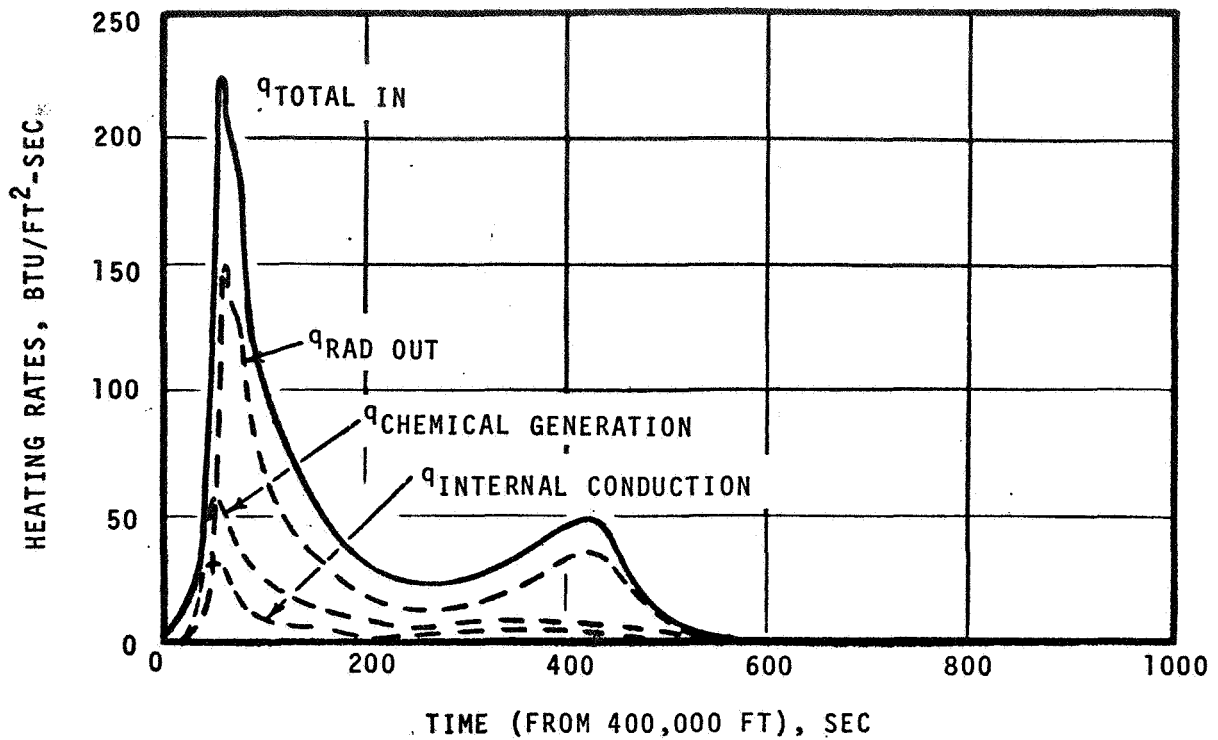


Figure 62. Partition of Surface Heating Rates for Flight AS 501, Body Point 705

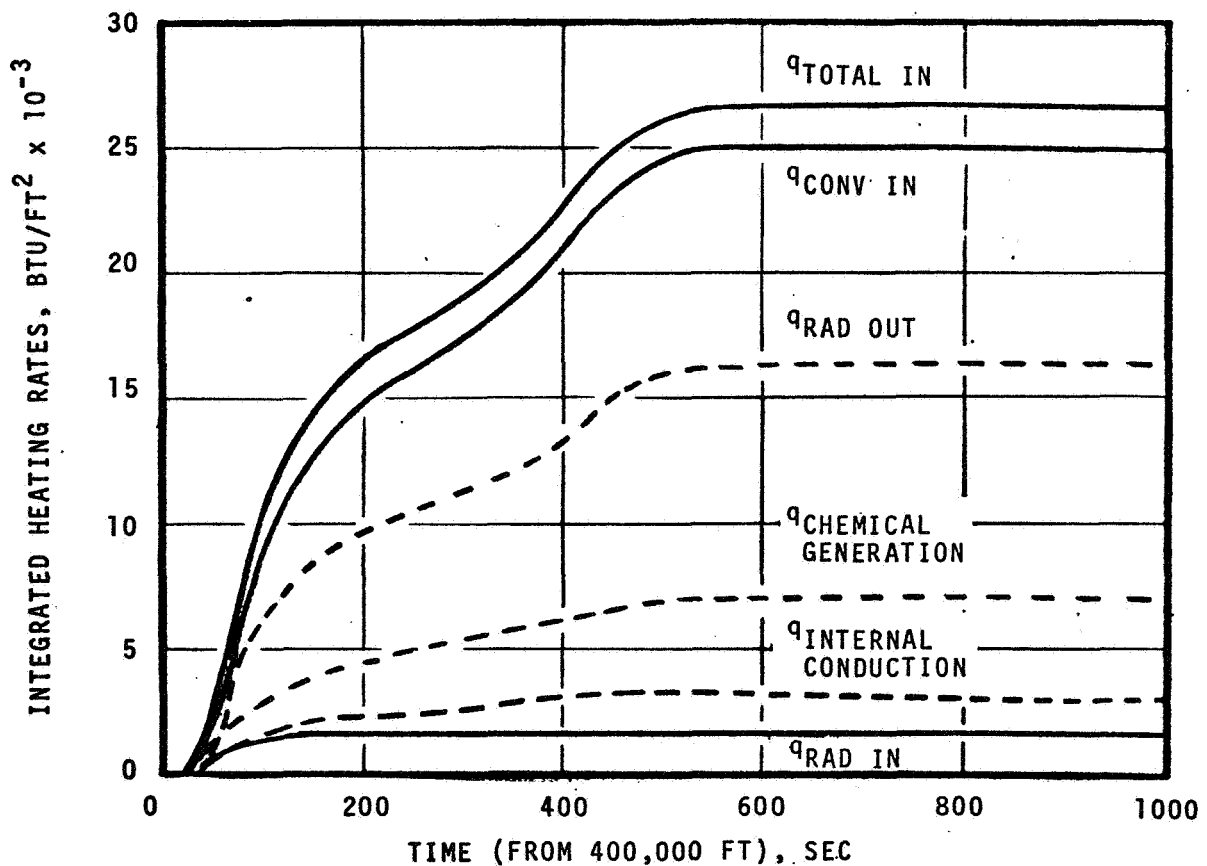


Figure 63. Partition of Integrated Surface Heating for Flight AS 501, Body Point 705

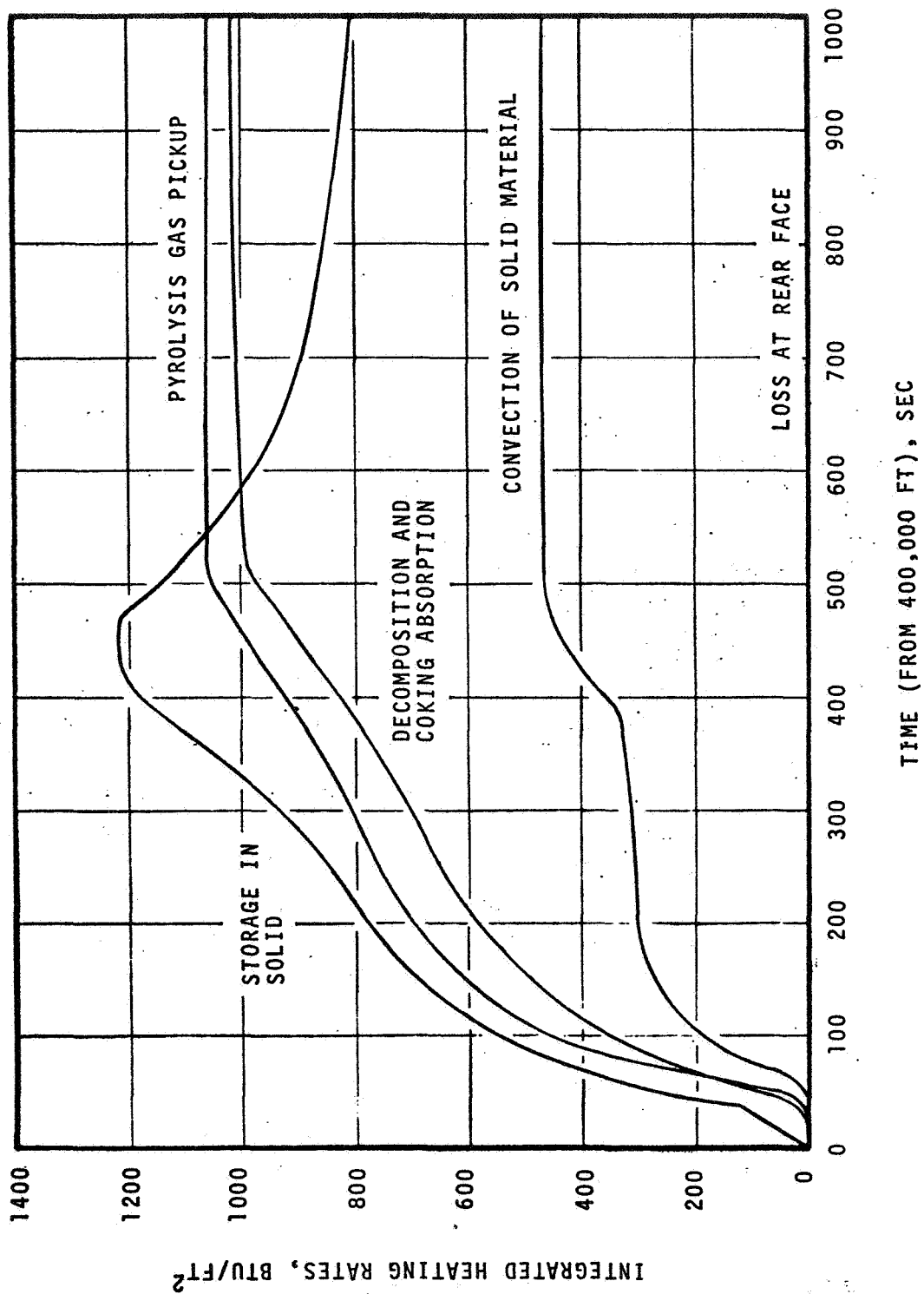


Figure 64. Partition of Interior Energy Terms for Flight AS 501, Body Point 705

integrated sense because substantial energy is lost from the solid during the second half of the trajectory as the ablation material cools down. The energy associated with the moving boundary is small but non-negligible (about 15 percent), while the heat loss at the rear surface is negligible.

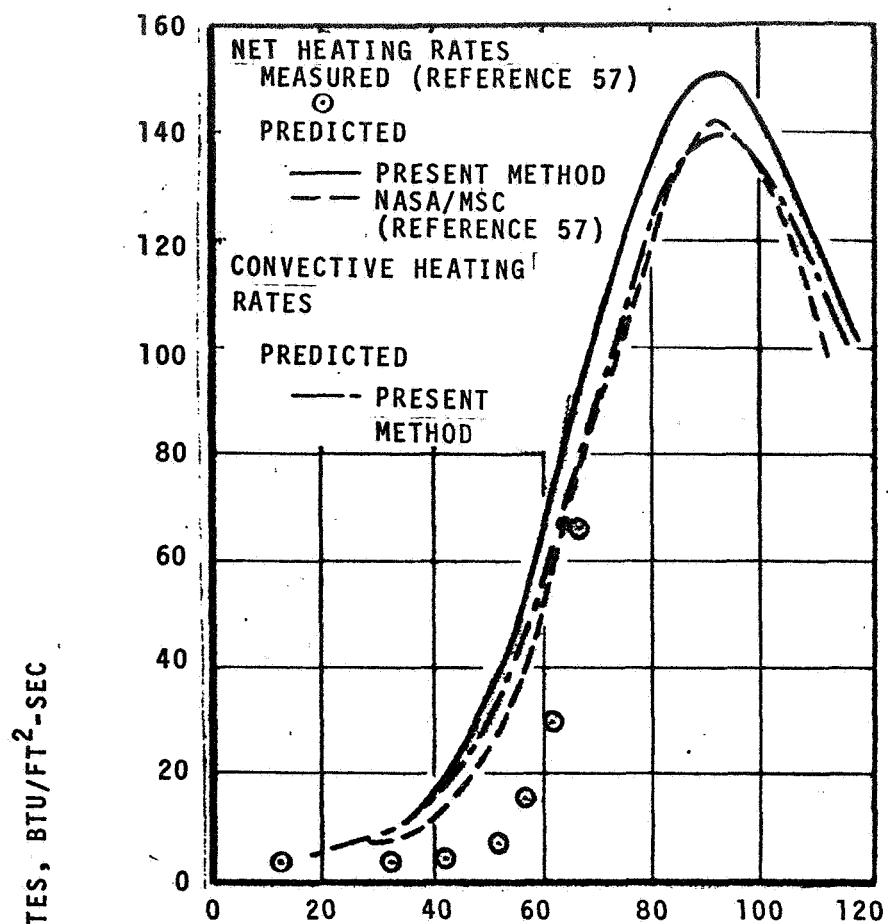
b. Comparison of Measured and Predicted Convective Heating Rates and Development of Transitional Heating Criteria

The Apollo aft heat shield was instrumented with wafer calorimeters while the conical afterbody employed asymptotic calorimeters. The wafer calorimeters consist of stacked graphite wafers designed to allow removal of single wafers by aerodynamic forces as the surrounding heat shield ablates. Thermocouples imbedded in the wafers measure temperature histories from which net heating rates (convection plus incident radiation) can be calculated given material properties and estimates of conduction and reradiation losses. They did not function properly after surface recession started, but did supply fairly smooth temperature responses early in the trajectory. The asymptotic calorimeters, on the other hand, typically performed well throughout the entire reentry mission. As shown in Table 20, 6 of the 7 cases considered in the present study were located on the aft heat shield; of these, the AS 501 and AS 502 flights (Cases 2, 3, 6 and 7) yielded useable early-time wafer calorimeter data. Case 5 (Flight 501, Body Point 710) yielded good asymptotic calorimeter data.

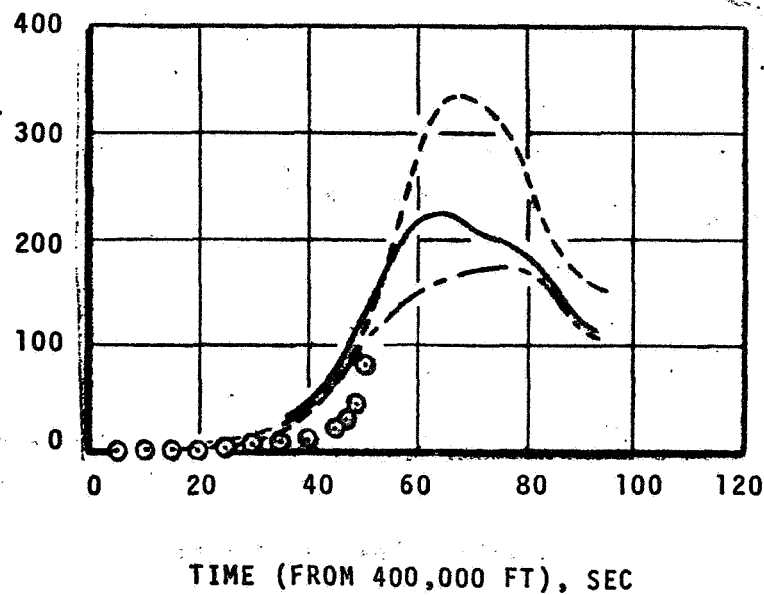
Reduced wafer calorimeter data for Flights AS 502 and AS 501, Body Point 705, are presented in Figures 65a and 65b as net heating rate (convection plus incident radiation).^{*} Also shown are NASA/MSC predictions for net heating rates and the present (CMA) predictions for convective heating rate and net heating rate (employing the values of incident radiation heating used in the CMA calculations, these being based on the NASA/MSC radiation heating factors). The CMA solutions and the NASA/MSC predictions agree reasonably well with each other but do not agree well with the calorimeter data. Since the precise approach for reducing the calorimeter data is not known and the possibility for error is rather large, it is not possible to make any definite conclusions. It is clear, however, that either the data are bad, or the present procedure and the NASA/MSC predictions share similar shortcomings.

The wafer calorimeter data for Flight AS 502 and AS 501, Body Point 707, are presented in Figure 66a and 66b and compared to laminar and turbulent net heating rate predictions. Let us restrict our attention first to Flight AS 502

^{*}These data and NASA/MSC predictions were supplied by NASA/MSC personnel⁵⁷ and differ somewhat from the values reported in the Apollo mission reports.^{51,52}

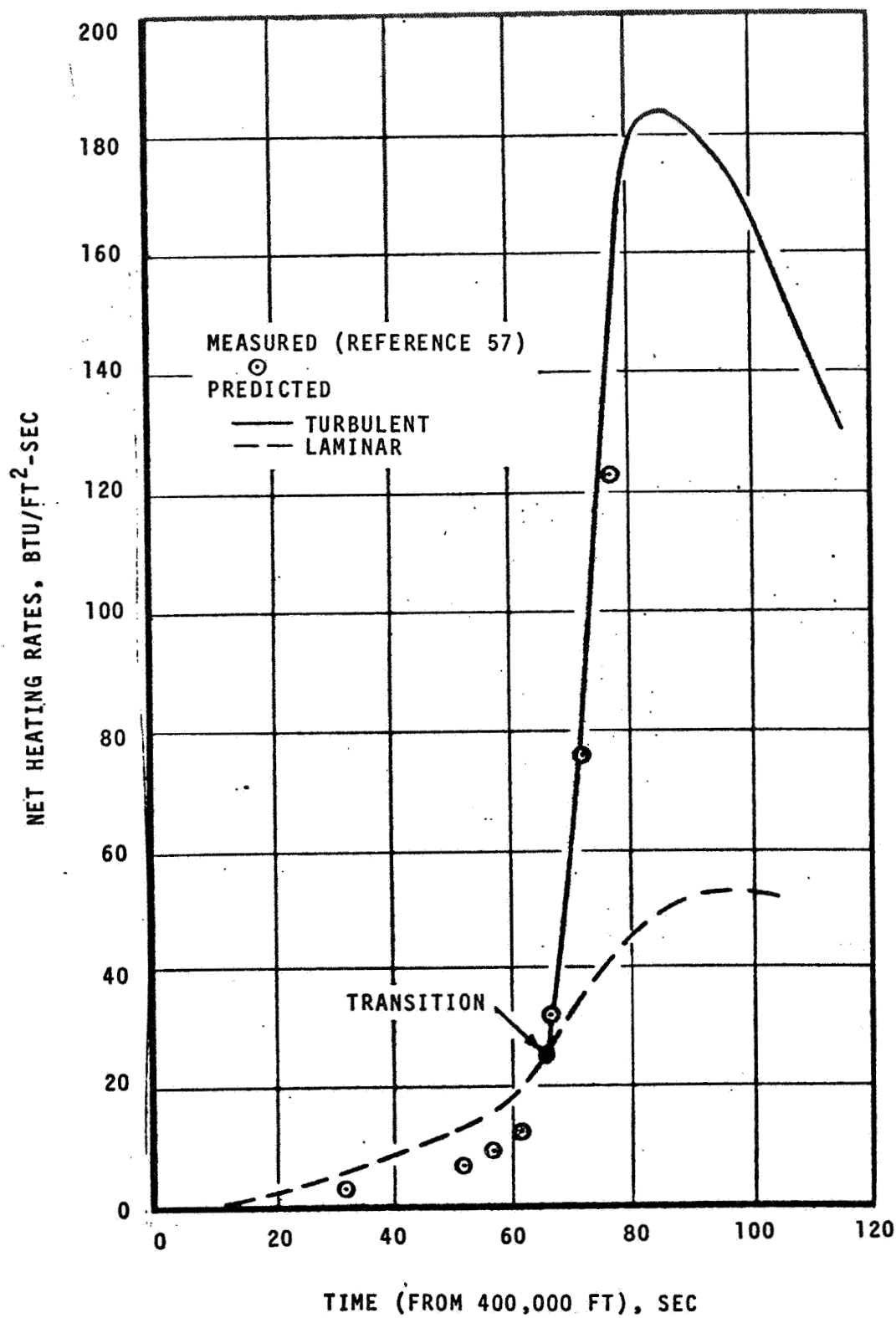


a. Flight AS 502



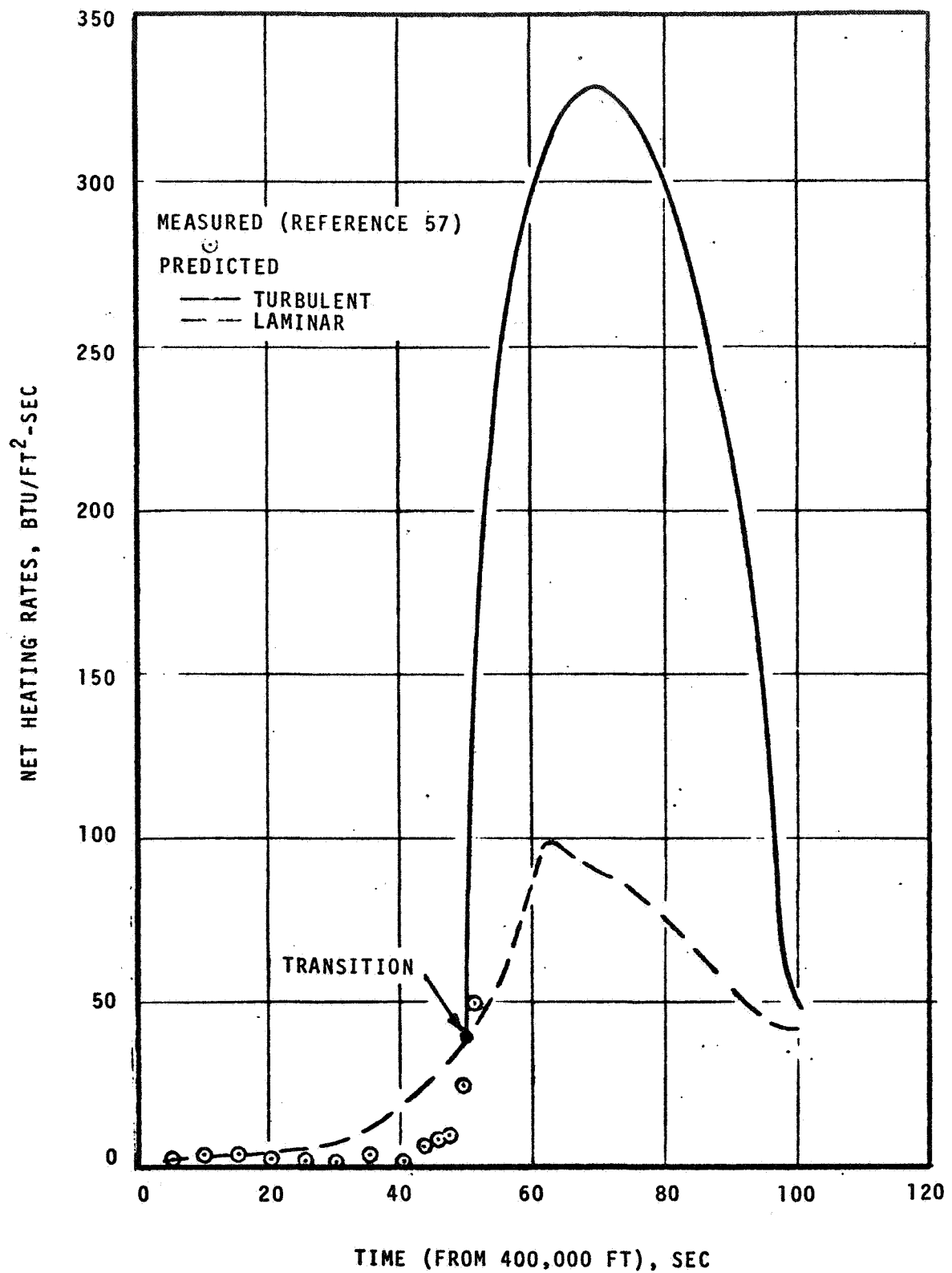
b. Flight AS 501

Figure 65. Comparison of Predicted Heating Rates with Wafer Calorimeter Data for Body Point 705



a. Flight AS 502

Figure 66. Comparison of Predicted Heating Rates with Wafer Calorimeter Data for Body Point 707



b. Flight AS 501

Figure 66. Concluded

(Figure 66a), since this was the approach that was actually employed in the present study. Comparing the measured data with the laminar prediction, transition to turbulent flow appears to occur at a trajectory time of approximately 66 seconds.

It is well known that transition to turbulent flow is strongly dependent upon the momentum thickness Reynolds number Re_{θ} and on surface mass transfer among other things. The momentum thickness Reynolds number for zero ablation Re_{θ_0} and the normalized surface mass-transfer rate B' for this flight and body point are presented in Figure 67.*

Recalling that the calorimeter data suggests transition at 66 seconds, Figure 67 shows that the critical Re_{θ_0} is about 120 and the corresponding B' is about 7 (the actual Re_{θ} is substantially greater than 120, of course). A look at the 0.02 inch thermocouple response for this flight (Figure 46b) suggests that the resumption of laminar flow starts at a trajectory time of about 115 seconds, corresponding to an Re_{θ_0} of 195 and a B' of 1.5, and is probably completed at about 135 seconds, corresponding to an Re_{θ_0} of 150 and a B' of 1.5.** In order to obtain an estimate for the trajectory time when the flow became fully turbulent, Re_{θ_0} versus B' for the trajectory is presented in Figure 68 together with symbols indicating the onset of transition and the initiation and completion of the return to laminar flow. An estimate for the attainment of fully-developed turbulent flow was postulated by presuming that the width of the transitional heating region probably decreases with increasing B' . Assumed straight-line relations separating laminar, transitional, and turbulent regimes are also shown in Figure 68. On the basis of this educated guess, fully turbulent flow was estimated to be attained for this trajectory at 76 seconds (see Figures 67 and 68).

In order to obtain an estimate for the ratio of turbulent to laminar heating from Figure 14 it is necessary to estimate the distance from the onset of transition. This can be obtained from Figures 68 and 13 by comparing the maximum value of the quantity (Re_{θ_0} minus the Re_{θ_0} for the attainment of fully turbulent flow)*** with the slope of Re_{θ} versus distance in the vicinity of the body position of interest (Figure 13). Doing this, it was estimated that the ratio of turbulent to laminar heating for this flight was about 3. In the regions of transitional heating, the value of turbulent to laminar heating was

* The Re_{θ_0} was obtained from Figure 13 while the B' were obtained directly from the CMA solution.

** As demonstrated in References 58 and 59, transitional heating in a boundary layer without mass transfer can persist over a fairly large Reynolds number range.

*** For example, for Flight AS 502, this quantity ΔRe_{θ_0} is $211 - 193 = 18$ (see Figure 68).

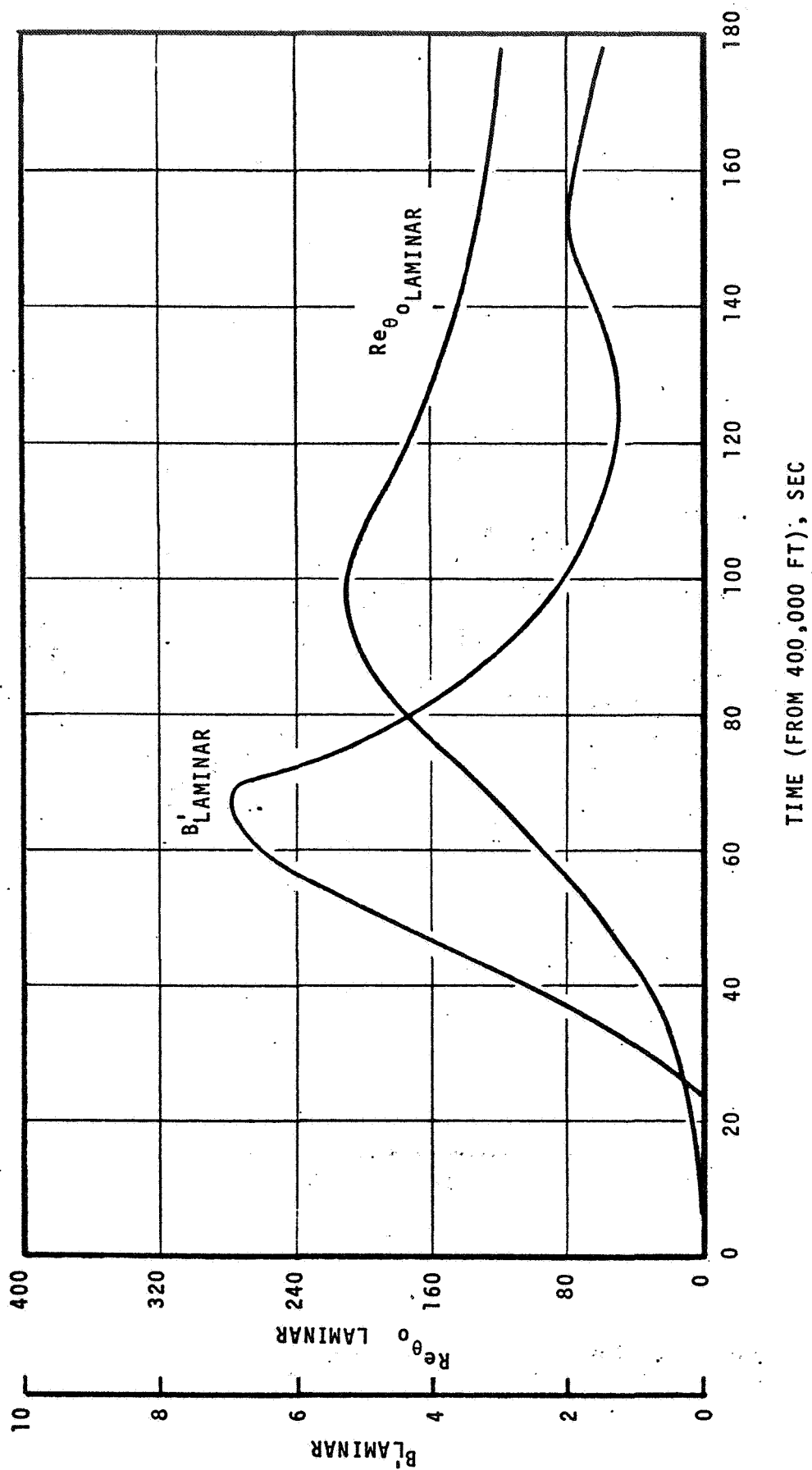


Figure 67. Reynolds Number and Blowing Rate Time Histories for Flight AS 502, Body Point 707

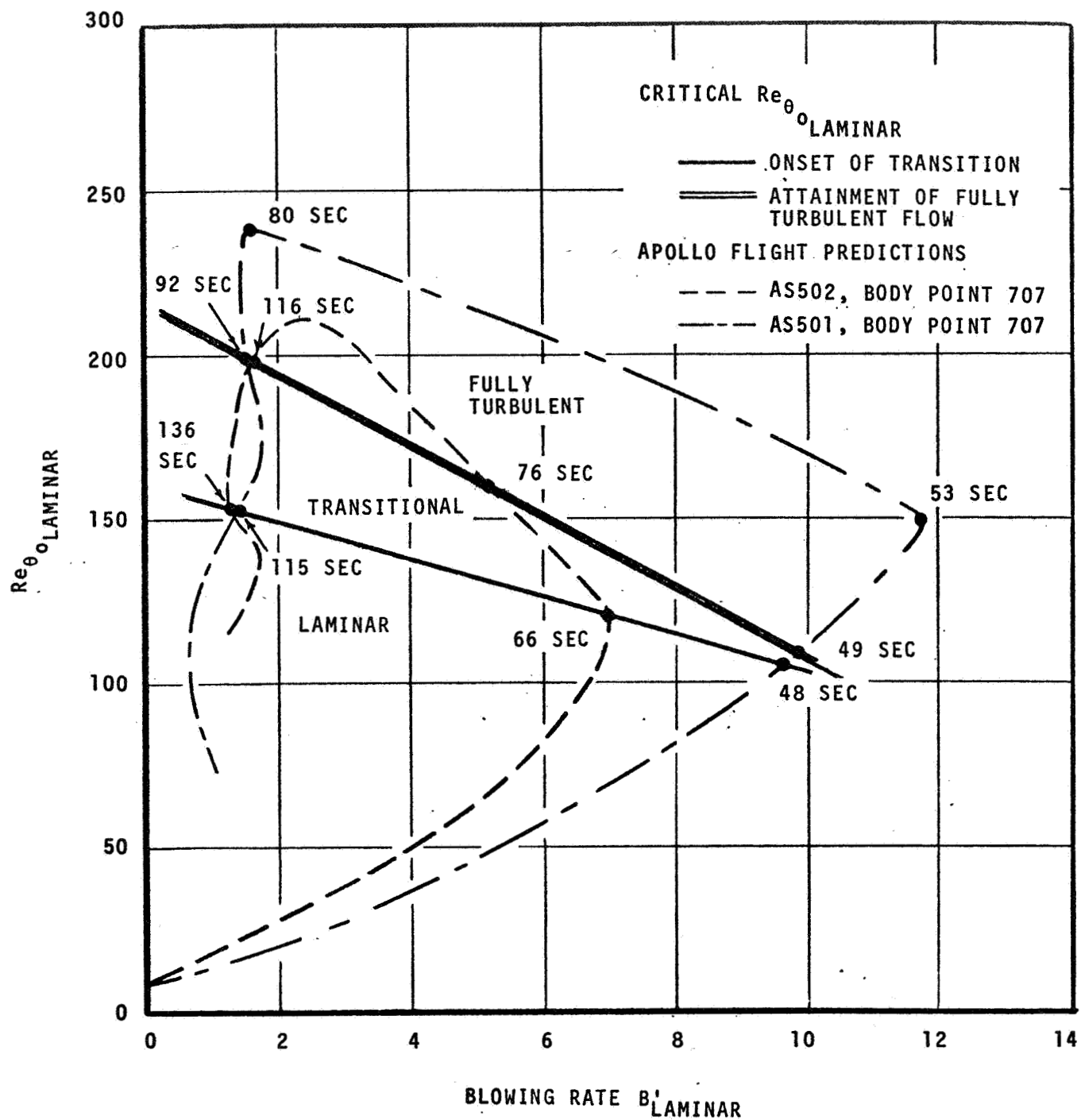
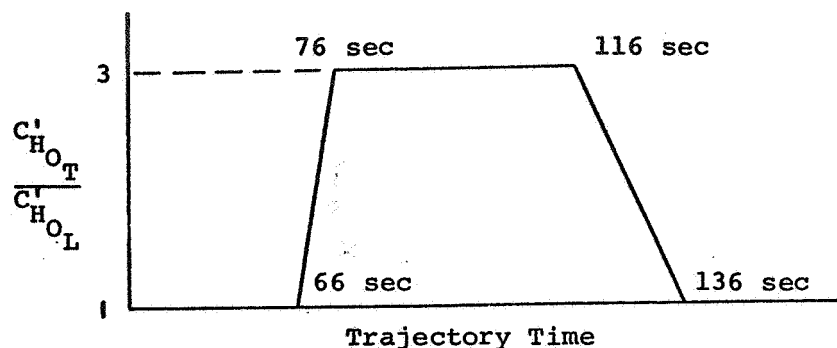


Figure 68. Transition Correlation for Apollo Leeward Aft Heat Shield Applied to Flights AS 502 and AS 501, Body Point 707



Ratio of Turbulent to Laminar Heat-Transfer Coefficient.

considered to vary linearly between unity and 3. This is illustrated in the sketch above. The prediction for convective heating rate predicted with this model is shown in Figure 66a to agree very well with the wafer calorimeter data. With the last calorimeter data at 77 seconds, this actually represents only a correlation of transitional heating. However, recall that good agreement with measured in-depth thermocouple response was obtained with this "turbulent" prediction (see Figure 46b).

The trace of Re_{θ_0} versus B' for Flight AS 501 Body Point 707 is also shown in Figure 68. Applying the transition criteria developed for Flight AS 502 Body Point 707, transition is predicted to occur between 48 and 49 seconds and the return to laminar flow to take place between 92 and 115 seconds. The value of $Re_{\theta_0} - Re_{\theta_0 \text{ critical}}$ is somewhat larger for this flight, with the consequence that the ratio of turbulent to laminar heating was estimated to be about 3.6. The resulting turbulent flow prediction yielded excellent agreement with the measured wafer calorimeter data (Figure 66b) and the in-depth thermocouple response (Figure 47b).

It is recognized that this transition correlation is highly preliminary and may be limited to the leeward side and even to the vicinity of Body Point 707; however, it is very encouraging that a single correlation appears to be satisfactory for both flights. Also, this represents a first (albeit fragmentary) validation of the turbulent heating model employed in the BLIMP program for hypersonic boundary layers with mass addition.

Asymptotic calorimeter measurements reported for Flight AS 501 at a position near Body Point 710⁵¹ are compared to the Body Point 710 predictions in Figure 69. The predictions are seen to agree very well with the data until a trajectory time of nominally 450 seconds, where the measured heating rates indicate that transition to turbulent flow probably occurs. From Figure 13, the Re_{θ_0} at this point is approximately 160; B' is predicted by the CMA program

to be 0.40. It can be seen from Figure 68 that this is in substantial agreement with the transition correlation already developed for the leeward side of the aft heat shield.* Again, it is premature to draw any final conclusions, but the consistency of the Figure 68 transition criteria is certainly encouraging.

6.3 SUMMARY OF FLIGHT PREDICTIONS

A series of seven Apollo flight/body-point combinations have been considered using the CMA program. Convective heating was calculated implicitly using correlations of BLIMP boundary-layer solutions presented in Section 3, radiative heating was input using the NASA/MSC radiation factors evaluated in Section 4, pressure distributions were based on NASA/MSC factors which in turn are based on wind-tunnel data (see Section 2), surface thermochemistry events were represented by a carbon ablation model including chemical interaction with the pyrolysis gases consistent with an in-depth coking and depolymerization model (Section 5). The solutions were all first attempts; that is, the various theoretical models were established (Sections 2 through 5), the solutions were performed, and the results were reported.

The results of these predictions were compared to flight measurements for in-depth temperature profiles, in-depth char density profiles, surface recession and char penetration, and surface heating rates. The agreement of theory and flight data was excellent with the exception of some early-time wafer calorimeter heating data of questionable accuracy. Particularly encouraging is a correlation for transition Reynolds number versus blowing rate which was developed on the basis of one flight and yielded substantial agreement with transition data for two other flights.

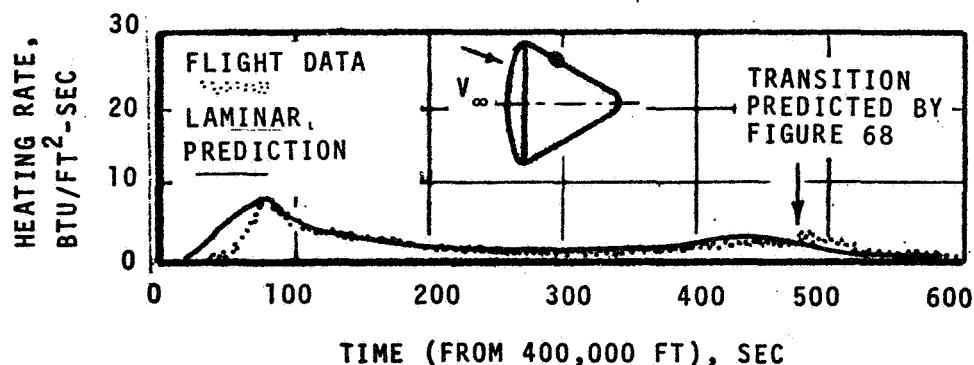


Figure 69. Comparison of Predicted Heating Rates with Asymptotic Calorimeter Data for Flight AS 501, Body Point 710

*The B' is predicted by the CMA program to be about 0.4 at this point in the trajectory (resulting entirely from pyrolysis gas generation).

SECTION 7

RECOMMENDED HEAT-SHIELD DESIGN PROCEDURE

On the basis of the present investigation the following procedure is recommended for preliminary heat-shield design studies for future reentry systems. This procedure is valid for reentry from orbital as well as lunar return velocities and for entry into planetary atmospheres. Furthermore, it is applicable to nonablating as well as ablating heat-shield designs. It does require some experimental data if a high confidence level is desired, but no theoretical prediction procedure could be expected to yield a high confidence level without a certain degree of empiricism for most of the reentry applications for which the recommended procedure is applicable. A more detailed description of the heat-shield design procedure is presented in Reference 10.

1. Obtain wind-tunnel pressure distribution data for the configuration of interest (three-dimensional inviscid flow programs are still not advanced to the stage where they can predict flow fields for blunt capsules of the Apollo class or complex winged vehicles).

2. Use available theoretical procedures and data correlations for radiation heat-transfer rates if the reentry conditions are sufficiently severe that radiation is important.

3. Obtain wind-tunnel nonablating convective heating distributions for the configuration of interest and calibrate these solutions for flight conditions with BLIMP solutions in the pitch-plane.

4. Generate BLIMP turbulent boundary-layer solutions for the configuration of interest and develop correlations of these solutions.

5. Validate material property data using the CMA program in the driver temperature option. This is particularly important if a charring ablation material is used.

6. In the event that surface ablation or other mass transfer phenomena occur utilize the BLIMP program to develop heat- and mass-transfer correlations for the material of interest. The correlations developed for the Apollo material and presented in this report can probably be employed for most charring ablation materials without serious loss of accuracy.

7. In the event that ablation materials are employed, postulate a thermochemical ablation model and generate tables of normalized thermochemical ablation solutions with the EST program. (It should be mentioned in this regard that most materials are not as difficult to analyze as the Apollo material.)

8. In the event that the material type and flight conditions are such that coking may occur, generate quality char density profile data for the material of interest and develop a coking model patterned after the model evaluated in the present study and consistent with the CMA program as modified under the present contract.

9. Generate CMA predictions and correlate with arc-jet test results, modifying the surface thermochemical ablation model (or developing an empirical surface ablation model) until substantial agreement occurs.

10. Predict heat shield response with the CMA program for the flight conditions of interest.

SECTION 8

RECOMMENDATIONS FOR FURTHER ANALYSIS AND PROGRAM IMPROVEMENTS

There are a number of areas where further advancements in heat-shield design procedures are desirable. The following are judged to be of primary benefit. The priorities of the various items listed depend upon the particular applications of interest.

1. Use the BLIMP program to perform a comprehensive evaluation of turbulent heating data from Apollo and other flight programs in order to develop improved transition criteria and to further validate the BLIMP turbulent heating model.
2. Use the BLIMP program to develop stagnation-point heat- and mass-transfer blowing corrections valid for all ablation materials and transpiration concepts of potential interest.
3. Develop a transfer-coefficient approach for correlating nonsimilar boundary-layer solutions and, using this procedure, develop correlations of BLIMP nonsimilar laminar and turbulent boundary-layer solutions for various flow situations of interest.
4. Perform further evaluation of Apollo and other available flight radiometer data using the RABLE radiation coupled viscous shock layer procedure.
5. Extend the GASL/Sandia inviscid flow field program to real gas and modify it so that it will yield useful solutions for Apollo (or other very blunt bodies of interest) at high incidence.
6. Employ the GASL/Sandia program extended under 5. above to evaluate a large body of pressure distribution data for Apollo at incidence and/or other shapes of interest.
7. Extend the BLIMP boundary layer program to consider three-dimensional flow, and build in a capability to treat separated flow.
8. Couple the GASL/Sandia and BLIMP programs extended under 5. and 7. above (long range).

REFERENCES

1. Moen, W. K.: Apollo Engineering Summary Postrecovery Report - Heat Shield Instrumentation, CSM 101. Space Division, North American Rockwell Corporation, Downey, California, Report TDR 68-166, December 1968.
2. Ihnat, M. E.: Evaluation of the Thermophysical Properties of the Apollo Heat Shield. Space Systems Division, AVCO Missiles, Space and Electronics Group, Lowell, Massachusetts, Report AVSSD-0375-67-RR, Volumes I and II, August 1967.
3. Alexander, J. G., et al.: Evaluation of the Thermophysical Properties of the Apollo Heat Shield, AS-501 Flight Core Study. Space Systems Division, AVCO Government Products Group, Wilmington, Massachusetts, Report AVSSD-0206-68-RR, July 1968.
4. Alexander, J. G., et al.: Evaluation of the Thermophysical Properties of the Apollo Heat Shield, AS-502 Flight Core Study, AS-205 Flight Core Study, AS-503 Flight Core Study. AVCO Applied Technology Division, Lowell, Massachusetts, Report AVATD-0198-69-RR, September 1969.
5. Kendall, R. M., Bartlett, E. P., Rindal, R. A., and Moyer, C. B.: Summary Report: An Analysis of the Coupled Chemically Reacting Boundary Layer and Charring Ablator. Aerotherm Corporation, Mountain View, California, Report 66-7, Part I, March 1967 (NASA CR-1060, June 1968).
6. Bartlett, E. P., Nicolet, W. E., Anderson, L. W., and Kendall, R. M.: Summary Report: Further Studies of the Coupled Chemically Reacting Boundary Layer and Charring Ablator. Aerotherm Corporation, Mountain View, California, Report 68-38, Part I, October 1968 (NASA CR-92471).
7. Moyer, C. B. and Rindal, R. A.: Finite Difference Solution for the In-Depth Response of Charring Materials Considering Surface Chemical and Energy Balances. Aerotherm Corporation, Mountain View, California, Report 66-7, Part II, March 1967 (NASA CR-1061, June 1968).
8. Kendall, R. M.: A General Approach to the Thermochemical Solution of Mixed Equilibrium-Nonequilibrium, Homogeneous or Heterogeneous Systems. Aerotherm Corporation, Mountain View, California, Report 66-7, Part V, March 1967 (NASA CR-1064, June 1968).
9. Bartlett E. P. and Kendall, R. M.: Nonsimilar Solution of the Multicomponent Laminar Boundary Layer by an Integral Matrix Method. Aerotherm Corporation, Mountain View, California, Report 66-7, Part III, March 1967 (NASA CR-1062, June 1968).
10. Aerotherm Corporation, Mountain View, California: User's Manual, Aerotherm Charring Material Thermal Response and Ablation Program with Coking (CMAC). Report No. UM-70-19, June 1970.
11. Aerotherm Corporation, Mountain View, California. User's Manual, Aerotherm Equilibrium Surface Thermochemistry Computer Program, Version 4 (EST4). Report No. UM-70-18, June 1970.

12. Aerotherm Corporation, Mountain View, California. User's Manual, Boundary Layer Integral Matrix Procedure, Version C (BLIMPC). Report No. UM-70-20, June 1970.
13. Abbett, M. J.: Studies of the Inviscid Flow Field about Apollo at Incidence by a Time-Dependent Solution Procedure. Aerotherm Corporation, Mountain View, California, Memorandum 6099-1, June 1970.
14. Abbett, M. J. and Fort, R.: Three-Dimensional Inviscid Flow about Supersonic Blunt Cones at Angle of Attack, Part III: Coupled Subsonic and Supersonic Programs for Inviscid Three-Dimensional Flow. General Applied Science Laboratories, Inc., Westbury, New York (Sandia Report SC-CR-68-3728, September 1968).
15. Personal communication, R. C. Ried, Jr., NASA Manned Spacecraft Center, Houston, Texas.
16. Erb, R. B., Lee, D. B., Weston, K. C., and Greenshields, D. H.: Aerothermodynamics - the Apollo Experience. Proceedings of the 1967 Heat Transfer and Fluid Mechanics Institute, edited by P. A. Libby, D. B. Olfe, and C. W. Van Atta, Stanford University Press, 1967, pp. 4-33.
17. Harmel, B. B.: Final AS-501 and AS-502 Pressure Data and Asymptotic Calorimeter Heating Rate Data Analysis. TRW Systems Group, Houston, Texas, TRW IOC 69.4352.10-6, June 1969.
18. Webb, H. G., Jr., Dresser, H. S., Adler, B. K., and Waiter, S. A.: Inverse Solution of Blunt-Body Flowfields at Large Angle of Attack. AIAA Journal, Vol. 5, No. 6, June 1967, pp. 1079-1085.
19. Bohachevsky, I. O. and Mates, R. E.: A Direct Method for Calculation of the Flow about an Axisymmetric Blunt Body at Angle of Attack. AIAA Journal, Vol. 4, No. 5, May 1966, pp. 776-782.
20. Moretti, G.: Inviscid Blunt Body Shock Layers, Two-Dimensional Symmetric and Axisymmetric Flows. Polytechnic Institute of Brooklyn, Report 68-15, June 1968.
21. Cooke, J. C. and Hall, M. G.: Boundary Layers in Three Dimensions. Progress in Aeronautical Sciences: Boundary Layer Problems, edited by D. Küchemann and A. Ferri, Volume II, Pergamon Press, New York, 1962, pp. 221-285.
22. Mager, A.: Three-Dimensional Laminar Boundary Layers. Theory of Laminar Flows, edited by F. K. Moore, Vol. IV of High Speed Aerodynamics and Jet Propulsion, Princeton University Press, Princeton, New Jersey, 1964, pp. 286-394.
23. Hearne, L. F., Chin, J. H. and Woodruff, L. W.: Study of Aerothermodynamic Phenomena Associated with Reentry of Manned Spacecraft. Lockheed Missiles and Space Company, Sunnyvale, California, Report Y-78-66-1, May 1966.
24. Anderson, L. W. and Kendall, R. M.: A Nonsimilar Solution for Multicomponent Reacting Laminar and Turbulent Boundary Layer Flows Including Transverse Curvature. Aerotherm Corporation, Mountain View, California, Report 69-54, October 1969 (AFWL-TR-69-106, March 1970).
25. Bertin, J. J.: Wind-Tunnel Heating Rates for the Apollo Spacecraft. NASA TM X-1033, January 1965.

26. Bertin, J. J.: The Effect of Protuberances, Cavities, and Angle of Attack on the Wind-Tunnel Pressure and Heat-Transfer Distribution for the Apollo Command Module. NASA TM X-1243, October 1966.
27. Nelson, M. L.: Determination of Factors at Heat Shield Body Point Locations. TRW Systems Group, Houston, Texas, TRW IOC 68.3302.13-4, March 1968.
28. Kendall, R. M., Rindal, R. A., and Bartlett, E. P.: A Multicomponent Boundary Layer Chemically Coupled to an Ablating Surface. AIAA Journal, Vol. 5, No. 6, June 1967, pp. 1063-1071.
29. Bartlett, E. P. and Grose, R. D.: An Evaluation of a Transfer Coefficient Approach for Unequal Diffusion Coefficients. Aerotherm Corporation, Mountain View, California, Report 69-50, June 1969 (Sandia SC-CR-69-3270, June 1969).
30. Grose, R. D. and Bartlett, E. P.: An Evaluation of a Transfer Coefficient Approach for Unequal Diffusion Coefficients. AIAA Journal, Vol. 8, No. 6, June 1970, to be published.
31. Spalding, D. B.: Convective Mass Transfer, An Introduction. McGraw-Hill Book Company, New York, New York, 1963.
32. Bartlett, E. P.: Nonsimilar Behavior of Ablating Graphite Sphere Cones. AIAA Journal, Vol. 8, No. 5, May 1970, pp. 948-950.
33. Chin, J. H.: Effects of Non-Grey Self-Absorption and Energy Loss for Blunt Body Flows. JQSRT, Vol. 8, No. 1, Jan. 1968, pp. 503-511.
34. Page, W. A., Compton, D. L., Borucki, W. J., Ciffone, D. L., and Cooper, D. M.: Radiative Transport in Inviscid Nonadiabatic Stagnation-Region Shock Layers. AIAA Paper No. 68-784, June 1968.
35. Nicolet, W. E.: A Nongrey Radiation Transport Model Suitable for Use in Ablation-Product Contaminated Boundary Layers. NASA CR-92473, Aerotherm Corporation, Mountain View, California, October 15, 1968.
36. Nicolet, W. E.: User's Manual - Radiation Transfer Code (RAD). Report No. 68-39, Aerotherm Corporation, Mountain View, California, October 15, 1968.
37. Nicolet, W. E.: Advanced Methods for Calculating Radiation Transport in Ablation-Product Contaminated Boundary Layers. Report No. 69-61, Aerotherm Corporation, Mountain View, California, December 27, 1969.
38. Nicolet, W. E.: User's Manual for the Generalized Radiation Transfer Code (RAD/EQUIL). Report No. UM-69-9, Aerotherm Corporation, Mountain View, California, October 1, 1969.
39. Morris, J. E., Bach, G. R., Krey, R. U., Liebermann, R. W., and Yos, J. M.: Continuum Radiated Power for High-Temperature Air and Its Components. AIAA Journal, Vol. 4, No. 7, July 1966, pp. 1223-1226.
40. Olstad, W. B.: Correlations for Stagnation-Point Radiative Heat Transfer. AIAA Journal, Vol. 7, No. 1, Jan. 1969, pp. 170-172.
41. Bartlett, E. P., Nicolet, W. E., and Howe, J. T.: Heat Shield Ablation at Superorbital Re-Entry Velocities. AIAA Paper No. 70-202, January 1970.
42. Hoshizaki, H. and Wilson, K. H.: Convective and Radiative Heat Transfer During Superorbital Entry, AIAA Journal, Vol. 5, No. 1, Jan. 1967, pp. 25-35.

43. Hoshizaki, H. and Lasher, L. E.: Convective and Radiative Heat Transfer to an Ablating Body, AIAA Journal, Vol. 6, No. 8, Aug. 1968, pp. 1441-1449.
44. Bartlett, E. P. and Anderson, L. W.: An Evaluation of Surface Recession Models for the Apollo Heat Shield Material. Aerotherm Corporation, Mountain View, California, Report 68-38, Part II, October 1968 (NASA CR-92472).
45. Bartlett, E. P., Anderson, L. W., and Curry, D. M.: An Evaluation of Ablation Mechanisms for the Apollo Heat Shield Material. AIAA Paper No. 69-98, January 20-22, 1969.
46. Curry, D. M. and Stephens, E. W.: Apollo Ablation Performance at Super-orbital Entry Velocities. Presented at AIAA Entry Vehicle Systems and Technology Meeting, Williamsburg, Virginia, December 3-5, 1968 (to be published).
47. Personal communication, Donald M. Curry, NASA Manned Spacecraft Center, Houston, Texas.
48. Pope, R. B.: Measurements of the Total Surface Emittance of Charring Ablators. AIAA Journal, Vol. 5, No. 12, December 1967, pp. 2285-2287.
49. Wilson, R. G. and Spitzer, C. R.: Visible and Near-Infrared Emittance of Ablation Chars and Carbon. AIAA Journal, Vol. 6, No. 4, April 1968, pp. 665-671.
50. NASA Manned Spacecraft Center, Houston, Texas: Postlaunch Report for Mission AS-202 (Apollo Spacecraft 011). Report MSC-A-R-66-5, October 1966.
51. NASA Manned Spacecraft Center, Houston, Texas: Apollo 4 Mission Report. Report MSC-PA-R-68-1, January 1968.
52. NASA Manned Spacecraft Center, Houston, Texas: Apollo 6 Mission Report. Report MSC-PA-R-68-9, May 1968.
53. Moen, W. K.: Apollo Heat Shield Thermal Gradient Thermocouple. Space Division, North American Aviation, Inc., Downey, California, Report TDR 67-108, September 1967.
54. Moen, W. K.: Apollo Engineering Summary Postrecovery Report - Heat Shield Instrumentation, CSM 101. Space Division, North American Rockwell Corporation, Downey, California, Report TDR 68-166, December 1968.
55. Gardner, D. C. and Seward, R. E.: Apollo Heat Shield Flight Data Summary. TRW Systems Group, Houston, Texas. Report 11176-H228-RO-00, May 1969.
56. Space Division, North American Rockwell Corporation, Downey, California: Certification Analysis, CAR 027001B, Apollo Block II Heat Shield, Volume III, Heat Shield Thermal Performance. Report SD 68-1004-3, February 1969.
57. Personal communication, Winston Goodrich, NASA Manned Spacecraft Center, Houston, Texas.
58. Masaki, M. and Yakura, J. K.: Transitional Boundary-Layer Considerations for the Heating Analyses of Lifting Re-entry Vehicles. Journal of Spacecraft and Rockets, Vol. 6, No. 9, September 1969, pp. 1048-1053.
59. Schadt, G. H.: Aerodynamic Heating Problems and Their Influence on Earth Orbit Lifting Entry Spacecraft. AIAA Paper No. 68-1126, October 1968.

APPENDIX A

SUMMARY OF COMPUTER CODES CONSTITUTING THE HEAT SHIELD DESIGN PROCEDURE

A.1 GENERAL

A set of mutually compatible computer codes for representing coupled heat conduction, surface ablation, and boundary layer phenomena developed under previous studies^{A-1,A-2} have been extended and synthesized into a heat shield design procedure under the present effort. These are:

- a. Charring Material Ablation (CMAC) program
- b. Equilibrium Surface Thermochemistry (EST4) program
- c. Boundary Layer Integral Matrix Procedure (BLIMPC)

The CMAC program can be operated independently for obtaining the in-depth response of charring (or noncharring) materials for assigned ablation rates and surface temperatures. The EST4 program can be operated independently to determine the equilibrium chemical state for a variety of open and closed systems of arbitrary elemental composition and, in one option, provides surface chemistry and mass-balance tabular data to the CMAC program for transient charring ablation calculations. The BLIMPC program is operated independently to provide nonsimilar laminar or turbulent multicomponent boundary layer solutions for a variety of uncoupled, partially coupled, or coupled steady-state ablation surface boundary conditions. The CMAC program serves as the basic heat shield design procedure, the EST4 program providing the surface thermochemical boundary condition and the BLIMPC program providing correlations of heat- and mass-transfer coefficients.

During the present study, these programs were modified as follows:

- 1) The CMA program^{A-3} was extended to permit coking in-depth and to accept an improved transfer coefficient formulation in the surface energy balance.
- 2) The EST3 program^{A-4} was extended to include an assigned temperature surface equilibrium option and the punched card output format was changed to accommodate the new transfer-coefficient model.

- 3) The BLIMP program^{A-5,A-6} was modified to permit use of the axisymmetric analogy for approximating the three-dimensional boundary layer equations.

In this appendix, the capabilities of the new versions of these codes (CMAC, EST4, and BLIMPC) are briefly summarized, and the modifications performed under the present study are described. User's manuals have been updated to include these and other recent modifications and republished as References A-7 through A-9.

A.2 CHARRING MATERIAL ABLATION WITH COKING (CMAC) PROGRAM

A.2.1 Description of Basic Program

The CMAC program predicts the temperature and density histories of a charring or noncharring material exposed to a hyperthermal environment which supplies heat and which may chemically erode the material surface. The theoretical analysis, finite-difference solution procedure, and characteristics of the basic program (prior to the current modifications) are presented in detail in Reference A-10. A user's manual including the current modifications is available as Reference A-7.

Heat and mass transfer within the charring ablator is considered to be one-dimensional, but the thermal streamtubes are allowed to have arbitrary cross-sectional area. The complex phenomena associated with the decomposition of the virgin material into a char and a pyrolysis gas are considered to be represented by the conventional "simple physics" model



The virgin material is permitted to decompose while considering parallel Arrhenius type rate laws for three different constituents. The pyrolysis gases which form are considered to be in thermal equilibrium with the char. The program has been extended under the current effort to permit coking of the pyrolysis gas to deposit carbon on the char. The coking model which is employed is discussed in Section 5.2 of this report; the specific program changes are summarized in Section A.2.2.

The CMAC program permits up to eight different backup materials of arbitrary thicknesses. The back wall of the composite material may transfer energy by convection and radiation or may be insulated. Three options exist for the ablating surface boundary condition when CMAC is operated as a main program:

Option 1 - Transfer-coefficient model for convection-radiation heating with coupled heat and mass transfer considering detailed surface chemistry events.

Option 2 - Specified surface temperature and surface recession rate

Option 3 - Specified radiation view factor and incident radiation flux, as functions of time, for a stationary surface.

Any combination of these options may be used for a single computation. Option 1 is used when it is desired to predict ablation rates and surface temperatures as well as in-depth response. This option utilizes tabular data supplied by the EST4 program (see Section A.3) and is discussed later in this section. Option 2 is useful for evaluating in-depth thermocouple data. Option 3 is appropriate to cooldown after termination of convective heat input and is often useful in conjunction with Options 1 and 2. During the present effort, the transfer-coefficient approach used in Option 1 has been modified. The basis for these changes is discussed in Section 3.3 of this report; the specific program changes are summarized in Section A.2.2.

Material properties such as thermal conductivity, specific heat, and emissivity are input as functions of temperature for virgin plastic and char. For partially decomposed or coked materials, the program performs an appropriate averaging to determine effective material properties.

The CMAC/EST4 approach provides an economical means for obtaining transient charring ablation predictions while considering detailed surface thermochemical events. The CMAC and EST4 programs are mechanically decoupled, punched card output from EST4 being used as input to the CMAC program (see Section A.3). However, the final result can be effectively a coupled solution if appropriate steps are taken as discussed below. The EST4 data provides the surface mass balance and surface equilibrium constraints while the CMAC program provides the pyrolysis gas rate and conduction term and solves the surface energy balance. The surface heating boundary condition is expressed in terms of nonablating heat-transfer coefficients and heat- and mass-transfer blowing-reduction relationships supplied by the user. The degree to which this represents a coupled procedure depends upon the generality and accuracy of the transfer coefficient correlations employed. In Sections 3.2 and 3.3 of the present report, correlations are developed which are accurate over the entire anticipated range of Apollo flight conditions, char removal rates and pyrolysis gas rates. These are then used as input to the CMAC program in a series of flight predictions presented in Section 6.

An implicit finite difference solution procedure is employed in the CMA program. The principles of differencing and nodal sizing which are employed are summarized below. Further details regarding these considerations can be found in References A-2 and A-10.

- 1) The nodes have a fixed size.
- 2) Nodes are dropped from the back (nonablating) face of the material.
- 3) The difference forms of derivatives are kept simple and are formed so as to provide a direct physical analog of the differential event leading to the derivative.
- 4) The difference equation for energy is formulated in such a way that it reduces to the difference equation for mass conservation when temperature and enthalpies are uniform.
- 5) The difference energy equations are written to be "implicit" in temperature.
- 6) In contrast to Point 5), the decomposition and coking relations are written as "explicit" in temperature.
- 7) Mass balance operations are performed in a different, tighter network than that used for the energy balance equations.

The storage requirements for the CMAC program depend strongly upon the coupling mode in use. Coupling to a film coefficient model for the surface energy balance (Option 1) involves considerable table storage; hence the program barely fits a 32,000-word machine with full table sizes adequate to treat a wide variety of problems. With use of Option 2 or Option 3, the need for storing extensive boundary condition tables is eliminated. In these cases, the CMAC program requires less than 8,000 words of storage.

Option 2 has been used extensively without difficulty in the evaluation of material thermal properties models from in-depth thermocouple data. A study of the Apollo material thermal properties model is reported in Section 5.4 of this report.

The coupled computation procedure constituted by CMA (Option 1) and EST has been applied to a wide variety of materials of technical interest. The approach is fully checked out and operational for the physical and chemical models currently employed. Computation time depends, of course, on the problem being computed, but experience to date indicates that CMA computations run roughly two to three times faster than real time for "typical" charring material problems for machines of the Univac 1108 speed class. Predictions generated for recent Apollo superorbital reentry missions are compared to measured data in Section 6 of this report.

A.2.2 Summary of CMAC Program Modifications

a. In-Depth Coking Model

The implementation of the coking model, described in Section 5.2 of this report, into the existing CMA code had four tasks:

1. The provision of input of the $\tilde{K}_{C_g}(T,p)$ and $h_g(T,p)$ functions
2. The addition of the coking density change rate equation
3. The incorporation of the appropriate change to the in-depth energy equation when coking is occurring
4. The addition of provisions for input and use of coked zone properties.

These changes, summarized below, are described in detail in Reference A-7.

Input of $\tilde{K}_{C_g}(T,p)$ and $h_g(T,p)$

These two functions are input as simple tables of \tilde{K}_{C_g} and h_g values as a function of discrete temperatures at a number of discrete pressures.

Coking Density Change Rate Calculation

The input \tilde{K}_{C_g} function, when chosen to match core coking data as related to local temperatures, does not allow coking to begin until 1250°K. This temperature is sufficiently high that coking for all practical purposes only occurs in "mature char" parts of the material.

The coking calculation begins with the usual pyrolysis calculation, which develops a total \dot{m}_g evolved by pyrolysis throughout the material. The coking mass transfer calculations follow, beginning at the deepest char node and proceeding toward the heated surface. The function \tilde{K}_{C_g} is evaluated at the current boundary-layer pressure for each nodal temperature in turn, and any coking or erosion is computed. Suitable checks are incorporated for total removal of carbon from the gas and from the char matrix.

Energy Events

As discussed in Section 5.2 of this report, the only change here substitutes h_{C^*} for \bar{h} in nodes where coking is occurring.

Coking Zone Properties

In the coking zone, the char properties are considered to be functions of both density and temperature. New input tables, similar to the properties tables used for other materials in CMA, give the temperature dependence of the

thermal conductivity for a sequence of densities. The specific heat is computed as a simple mass weighted average of the specific heats of silica and carbon, which are interpreted from the char specific heat and a special table of carbon specific heat.

Interaction with Surface Thermochemistry Tables

As noted in Section 5.2 of this report, the implementation of the coking model has necessitated a change in surface thermochemistry parameters from the P , B'_g , B'_C used in CMA to P , B'_g , and T_w . This makes it more convenient to use T_w as the independent variable in the surface energy balance iterations, requiring minor changes in this portion of the code logic. The surface recession \dot{s} is computed as B'_C/ρ_C^* where ρ_C^* is the local density of carbon.

b. New Transfer-Coefficient Model

Prior to the present study, the CMA program obtained diffusive heat and mass fluxes in the following manner:

1. The $\rho_e U_e C'_{H_2O}$ was obtained by any available means.
2. The $\rho_e U_e C'_H$ (defined implicitly by Eq. (21) of this report) was obtained from $\rho_e U_e C'_{H_2O}$ and a blowing correction for C'_H/C'_{H_2O} in the form of Eq. (26) of this report with the value of λ input by the user.
3. The $\rho_e U_e C'_M$ was obtained from $\rho_e U_e C'_H$ and Le in accordance with $C'_M/C'_H Le^{2/3} = 1$.

The results of the present study indicate the following approach is preferable:

1. The $\rho_e U_e C'_{H_2O}$ is obtained from a nonablating BLIMPC solution.
2. The $\rho_e U_e C'_H$ (Eq. (23) of this report) is obtained from $\rho_e U_e C'_{H_2O}$ and a blowing correction for C'_H/C'_{H_2O} in the form of Eq. (30) with λ_H given by Eq. (31).
3. The $\rho_e U_e C'_M$ is obtained from $\rho_e U_e C'_H$ and a blowing correction for C'_M/C'_H in the form of Eq. (26) with λ_M given by Eq. (29).

These changes have been made in the CMAC coding and are described in detail in Reference A-7, together with other modifications required to permit consideration of coking (see Section A.2.2.a).

A.3 EQUILIBRIUM SURFACE THERMOCHEMISTRY PROGRAM VERSION 4 (EST4)

A.3.1 Description of Basic Program

The EST4 code solves for equilibrium chemical composition for a variety of open or closed systems of arbitrary chemical composition. The EST program is a streamlined and simplified version of the proprietary Aerotherm Chemical Equilibrium (ACE) program.^{A-11} The theory upon which the EST4 program is based is presented in Reference A-12 and summarized in the EST4 manual.^{A-8}

The EST4 program has the following major options:

1. Evaluation of chemical state for assigned pressure, elemental composition of several component mixtures which can be defined arbitrarily, and either enthalpy or temperature.
2. Calculation of surface mass balances to determine a relationship between normalized char recession rate, normalized pyrolysis gas rate, surface temperature, and pressure while considering equilibrium between the char and gases adjacent to it.

These options are formulated for completely general chemical systems. Consideration of any molecular, atomic, ionic, or condensed species requires only the inclusion of the basic thermodynamic data appropriate for that species. These data are obtained, for example, from the JANAF Thermochemical Data Tables and include heat of formation and curve fit constants for entropy and specific heat.

The EST4 program uses general Newton-Raphson iteration to solve the set of simultaneous nonlinear equations governing chemical equilibrium. Very elaborate convergence damping and rescue procedures have been developed over the period of years with a result that the program is very reliable. The solution procedure is discussed in some detail in Reference A-12.

For most options, a rather complete state of the system is generated which includes compositions, thermodynamic properties, and property and composition derivatives (available as a consequence of the Newton-Raphson solution procedure). The surface state option provides additional information as discussed below.

The surface state option of the EST4 program contains a number of features which make it useful in the analysis of ablation data. In the first place, one does not have to choose a priori the surface species. For example, in the case of the Apollo material, the program will determine from the surface equilibrium relationships whether the char surface is SiO_2^* , C^* , SiC^* , Si^* or Si_3N_4^* .

Secondly, it is possible to chemically isolate species or component gas mixtures from the system. A third major capability of the EST4 program is that it permits consideration of unequal diffusion coefficients as well as unequal heat and mass-transfer coefficients through application of an approximation for binary diffusion coefficients described in Reference A-13.

The surface state options of the EST4 program provide char recession rate normalized by a mass-transfer coefficient, and other information needed to perform an energy balance on the surface of a charring ablation material, as a function of pyrolysis gas rate normalized by the same mass-transfer coefficient, surface temperature, and pressure. It thus does not by itself constitute an ablation prediction tool. In the first place, it is necessary to specify the mass-transfer coefficient and this cannot be done precisely without solving the boundary-layer equations. Secondly, the determination of surface temperature requires the solution of a surface energy balance. The recommended procedure for ablation predictions is to generate surface state solutions with the EST4 program in the form of punched card output. This is then used as input to the CMAC program (Option 1) which performs the surface energy balance. The requisite transfer coefficients are then obtained from correlations of boundary layer solutions obtained with the BLIMPC program described in Section A.4. The CMAC/EST4 approach is described further in Section A.2.1 above.

The EST program has been used extensively in all of its options for a wide variety of problems and is thoroughly checked out. It takes 10 to 60 milliseconds per chemistry iteration depending upon the size of the chemical system under consideration, and usually converges in 5 to 15 iterations.

A.3.2 Summary of EST4 Program Modifications

a. Changes to Accommodate the CMAC In-Depth Coking Model

In order to accommodate the new CMAC in-depth coking model (see Section 5.2 of this report), the EST3 program^{A-4} was extended to include an option to compute surface equilibrium with assigned temperature (in lieu of assigned B'_c). This change was necessary to create surface thermochemistry tables for use with CMAC since the chemical composition of the pyrolysis gas must be tailored as a function of P and T_w to harmonize with the $\tilde{K}_c(P, T_w)$ function used in the coking calculations. This new option is described in the EST4 user's manual.^{A-8}

b. Changes to Accommodate the New CMAC Transfer-Coefficient Model

The requirement for wall-gas molecular weight, m_w , not needed with the old CMA approach, necessitated a change in the EST4 punched-card data. The m_w is now provided in the place formerly used to supply information for the calculation of $\rho_e U_e C_H$ which is no longer needed with the new transfer-coefficient approach. This minor change is also described in the EST4 user's manual. A-8

A.4 BOUNDARY LAYER INTEGRAL MATRIX PROCEDURE VERSION C (BLIMPC)

A.4.1 Description of Basic Program

The BLIMPC program solves the nonsimilar two-dimensional or axisymmetric laminar or turbulent boundary layer including transverse curvature effects by a novel procedure which is capable in a practical limit of yielding "exact" solutions for the equations considered. The equations which are solved, the solution procedure which is utilized, and the characteristics of the program are described in detail in References A-14 and A-15. A comprehensive up-to-date user's manual is available as Reference A-9. The program is virtually unchanged since the writing of Reference A-15 with regard to the physical and chemical models which are considered and the basic solution procedure which is utilized with the exception that an option has been added which permits use of the axisymmetric analogy to the three-dimensional boundary-layer equations. The basis for this modification is discussed in Section 2.2 of this report; the specific program changes are summarized in Section A.4.2.

The BLIMPC program applies to general, ionized, chemical systems, considering equilibrium with the exception that selected species or component mixtures can be considered to be frozen, and rate-controlled surface reactions or surface-catalyzed homogeneous reactions can be taken into account. Unequal diffusion and thermal diffusion coefficients for each species can be considered through the use of convenient approximations for these coefficients described in Reference A-13. Relations of the Sutherland-Wassiljewa type are used for mixture molecular viscosity and conductivity.

At the wall it is possible to assign temperature and mass fluxes of various component gas mixtures defined by the user, to require the surface to be in equilibrium with whatever condensed species is predicted by the program to be the surface species, to permit rate-controlled surface reactions specified by the user, and to perform a steady state energy balance at the wall (in which case the boundary layer is completely coupled to the wall response). A candidate surface species can be considered to be removed mechanically in the event it wants to appear as the surface above a "fail temperature" prescribed by the

user (e.g., the fail temperature for silica might be selected as its melt temperature). Such boundary conditions as mass addition, ablation material, and body shape can be varied discontinuously around the body, and the type of wall boundary condition can be altered in different regions over the body.

The BLIMPC program calculates its own boundary-layer edge condition by performing an isentropic expansion given stagnation conditions and pressure distribution around the body. An incident radiation flux can be taken into account when a surface energy balance is considered. This incident flux is considered to enter into the surface energy balance without being attenuated in the boundary layer. (A procedure for obtaining radiation-coupled boundary layer solutions, termed the RABLE code, is described in Reference A-2.)

For turbulent flows, the time-averaged equations of motion are solved utilizing an eddy viscosity model to describe the "Reynolds stress" term, plus constant turbulent Prandtl and Schmidt numbers in the energy and species conservation equations. Eddy viscosity is related to a variable mixing length in the region very near the wall, and to global parameters of the flow in the outer portion of the boundary layer. Turbulent transport terms in the equations of motion are considered only after the transition criterion, an input transition Reynolds number on momentum thickness, has been satisfied.

The numerical solution procedure which is employed, termed an integral-matrix method, was developed specifically for the chemically reacting boundary layer application. The integral matrix approach uses spline interpolation functions across the boundary layer and quadratic finite differences in the streamwise direction to reduce the nonsimilar boundary-layer equations to algebraic form. These equations are then integrated across the boundary layer with step weighting functions to obtain a proper set of linear and nonlinear algebraic equations. These equations are solved by general Newton-Raphson iteration in a fully coupled manner. This approach has proven itself to be economical (due to the small number of nodes required to achieve essentially exact solutions), to converge rapidly and reliably even for highly-blown boundary layers, and to be readily extendable to include new physics, new boundary conditions, and the like.

The BLIMPC program contains approximately 5,000 instructions. The number of nodal points and the number of elements are the most critical dimensioned variables, in regard to both storage requirements and computational speed. The BLIMPC program is currently dimensioned for 15 nodal points, seven elements plus electrons, 60 species, and 40 streamwise stations. The BLIMPC program with these dimensions requires overlay on the Univac 1108.

The BLIMPC program takes two to three seconds per iteration on the Univac 1108 computer for a 7 node, 5 element, 30 species problem. The number of iterations required differs substantially according to the severity of the problem (the nonlinearity introduced by the chemistry events) and the first guesses. Typically 10 to 20 iterations are required for stagnation point solutions involving complex chemistry starting with built-in, uninspired first guesses, while downstream solutions require 2 to 6 iterations depending upon streamwise spacing. Thus a solution for a stagnation point plus 12 additional stations (this is sufficient to go around most bodies) would typically require 60 to 80 iterations corresponding to 2-1/2 to 3 minutes on the Univac 1108.

The BLIMPC program has been checked out for the Apollo heat shield material in all of the applicable options. Solutions for typical Apollo conditions are presented in Section 3 of this report. Results for very high speed reentry (e.g., 50,000 feet per second) are presented in References A-2 and A-16. The BLIMP program has also been used extensively for the ablation of carbon, carbon-phenolic, nylon-phenolic, and teflon in air; graphite in a Venusian atmosphere; and discontinuous injection of exotic transpirants through a graphite surface. Though the BLIMPC program is complex and contains a large number of options, the program input is quite simple, and the program is very reliable for the experienced user.

A.4.2 Summary of BLIMPC Program Modifications to Permit Use of Axisymmetric Analogy

The changes in the BLIMP program^{A-6} to permit use of the axisymmetric analogy are very simple. First, provision is made to input the velocity gradient ratio i (see Eq. (12) of this report) for use at the stagnation point. The stagnation point pressure gradient parameter β_{stag} is then computed using Eq. (13). Finally, the integration of the streamwise variable ξ and the wall stream function f_w in the stagnation region (see Appendix C of Reference A-14) are changed in accordance with the s^i behavior of the spreading factor h_2 . It is up to the user to obtain a solution to the differential equation for the spreading factor (Eq. (11)) for use with this option.

REFERENCES FOR APPENDIX A

- A-1 Kendall, R. M., Bartlett, E. P., Rindal, R. A., and Moyer, C. B.: Summary Report: An Analysis of the Coupled Chemically Reacting Boundary Layer and Charring Ablator. Aerotherm Corporation, Mountain View, California, Report 66-7, Part I, March 1967 (NASA CR-1060, June 1968).
- A-2 Bartlett, E. P., Nicolet, W. E., Anderson, L. W., and Kendall, R. M.: Summary Report: Further Studies of the Coupled Chemically Reacting Boundary Layer and Charring Ablator. Aerotherm Corporation, Mountain View, California, Report 68-38, Part I, October 1968 (NASA CR-92471).
- A-3 Aerotherm Corporation, Mountain View, California: User's Manual, Aerotherm Charring Material Ablation Program, Version 2. Second Edition, January 1969.
- A-4 Aerotherm Corporation, Mountain View, California: User's Manual, Aerotherm Equilibrium Surface Thermochemistry Computer Program, Version 3. Report Number UM-70-13, Volumes I and II, April 1970.
- A-5 Bartlett, E. P. and Deblaye, C.: User's Manual, Boundary Layer Integral Matrix Procedure. Aerotherm Corporation, Mountain View, California, Report 68-42, October 1968.
- A-6 Anderson, L. W., Bartlett, E. P., and Kendall, R. M.: User's Manual, Boundary Layer Integral Matrix Procedure (BLIMP). Air Force Weapons Laboratory, Kirtland Air Force Base, New Mexico, Report AFWL-TR-69-114, Volumes I and II, March 1970.
- A-7 Aerotherm Corporation, Mountain View, California: User's Manual, Aerotherm Charring Material Thermal Response and Ablation Program with Coking (CMAC). Report No. UM-70-19, June 1970.
- A-8 Aerotherm Corporation, Mountain View, California. User's Manual, Aerotherm Equilibrium Surface Thermochemistry Computer Program, Version 4 (EST4). Report No. UM-70-18, June 1970.
- A-9 Aerotherm Corporation, Mountain View, California. User's Manual, Boundary Layer Integral Matrix Procedure, Version C (BLIMPC). Report No. UM-70-20, June 1970.
- A-10 Moyer, C. B. and Rindal, R. A.: Finite Difference Solution for the In-Depth Response of Charring Materials Considering Surface Chemical and Energy Balances. Aerotherm Corporation, Mountain View, California, Report 66-7, Part II, March 1967 (NASA CR-1061, June 1968).
- A-11 Powars, C. A. and Kendall, R. M.: User's Manual, Aerotherm Chemical Equilibrium (ACE) Computer Program. Aerotherm Corporation, Mountain View, California, May 1969.
- A-12 Kendall, R. M.: A General Approach to the Thermochemical Solution of Mixed Equilibrium-Nonequilibrium, Homogeneous or Heterogeneous Systems. Aerotherm Corporation, Mountain View, California, Report 66-7, Part V, March 1967 (NASA CR-1064, June 1968).
- A-13 Bartlett, E. P., Kendall, R. M., and Rindal, R. A.: A Unified Approximation for Mixture Transport Properties for Multicomponent Boundary-Layer Applications. Aerotherm Corporation, Mountain View, California, Report 66-7, Part IV, March 1967 (NASA CR-1063, June 1968).

- A-14 Bartlett, E. P. and Kendall, R. M.: Nonsimilar Solution of the Multicomponent Laminar Boundary Layer by an Integral Matrix Method. Aerotherm Corporation, Mountain View, California, Report 66-7, Part III, March 1967 (NASA CR-1062, June 1968).
- A-15 Anderson, L. W. and Kendall, R. M.: A Nonsimilar Solution for Multicomponent Reacting Laminar and Turbulent Boundary Layer Flows Including Transverse Curvature. Aerotherm Corporation, Mountain View, California, Report 69-54, October 1969 (AFWL-TR-69-106, March 1970).
- A-16 Bartlett, E. P., Nicolet, W. E., and Howe, J. T.: Heat-Shield Ablation at Superorbital Re-entry Velocities. AIAA Paper No. 70-202, January 19-21, 1970.